PIEZOELECTRIC THIN FILMS FOR BULK ACOUSTIC WAVE RESONATOR APPLICATIONS: FROM PROCESSING TO MICROWAVE FILTERS

THÈSE N^{O} 2991 (2004)

PRÉSENTÉE À LA FACULTÉ SCIENCES ET TECHNIQUES DE L'INGÉNIEUR

Institut des matériaux

SECTION DES MATÉRIAUX

ÉCOLE POLYTECHNIQUE FÉDÉRALE DE LAUSANNE

POUR L'OBTENTION DU GRADE DE DOCTEUR ÈS SCIENCES TECHNIQUES

PAR

Roman LANZ

ingénieur en science des matériaux diplômé EPF
de nationalité suisse et originaire de Wiedlisbach (BE)

acceptée sur proposition du jury:

Prof. N. Setter, directrice de thèse
Prof. H. Bleuler, rapporteur
Dr P. Muralt, rapporteur
Dr V.P. Plesski, rapporteur
Prof. R.W. Whatmore, rapporteur

Lausanne, EPFL
2004

Abstract

Bandpass filters for microwave frequencies realized with thin film bulk acoustic wave resonators (FBAR) are a promising alternative to current dielectric or surface acoustic wave filters for use in mobile telecommunication applications. With equivalent performance, FBAR filters are significantly smaller than dielectric filters and allow for a larger power operation than SAW filters. In addition, FBARs offer the possibility of on-chip integration, which will result in substantial volume and cost reduction. The first passive FBAR devices are now appearing on the market. They mainly cover needs in miniaturized RF-filters for the new bands around 2 GHz.

A FBAR is essentially a thin piezoelectric plate sandwiched between two electrodes and acoustically isolated from the environment for energy trapping purposes. If the isolation is effectuated by an acoustic Bragg reflector, one speaks of solidly mounted resonators (SMR). Piezoelectric aluminum nitride (AlN) thin films are predominantly used in the emerging FBAR technology because AlN exhibits a sufficient electromechanical coupling coefficient k_t^2, low acoustic losses at microwave frequencies, a low temperature coefficient of frequency, and its chemical composition is compatible with CMOS requirements.

This thesis has two research directions. In the first part, FBAR structures based on AlN thin films were investigated for applications at X-band frequencies (7.2-8.5 GHz), i.e. operating at much higher frequencies than the ones used for present products. The goal was to identify property limitations related to such high frequencies, and to demonstrate to industry high performing SMR filters at 8 GHz. In the second part, a new material for FBAR devices was studied. The motivation is that AlN allows for a restricted filter bandwidth only, limited by its coupling factor of maximal 7%. Monocrystalline $KNbO_3$ appears as an ideal alternative with its high coupling factor k_t^2 of 47%, and relatively large sound velocity of 8125m/s for longitudinal waves along the [101] direction. Piezoelectricity of $KNbO_3$ films grown on electrodes has never been characterized. Single crystal results indicate that the optimal film texture would be (101). In this thesis, the growth of $KNbO_3$ films on Pt electrodes was studied with the goal to achieve this texture uniformly, and to characterize piezoelectric properties.

X-band FBAR's were first studied with numerical simulations based on a one-dimensional theory of the thickness-extensional bulk acoustic wave (BAW). Thickness, acoustic properties and electrical conductivity of the electrodes have a large impact on the resonator characteristics. There are conflicting requirements with respect to optimum acoustic and electrical properties of the electrode materials. An optimum thickness was calculated for 8GHz FBARs that use Pt bottom and Al top electrodes. The characteristics of ladder filters have been calculated based on the impedances of single resonators. The adjustable filter parameters, i.e. the areas of series and shunt resonators, frequency de-tuning between series and parallel resonators, and number of π-sections were screened for a process window

offering maximum filter bandwidth with lowest ripple and low insertion loss for a given out-of-band rejection. An important result of the numerical simulations was that the bandwidth of ladder filters can be doubled by de-tuning the series and parallel resonators by more (1.3 times) than the difference of resonance and anti-resonance frequency. This also leads to a flatter passband while keeping the ripples below ±0.2dB.

Solidly mounted resonators and filters were fabricated using an acoustic multilayer reflector consisting of AlN and SiO_2 $\lambda/4$ layers. All films were sputter deposited in a high vacuum sputter cluster system with 4 process chambers. The films were patterned using standard photolithography and dry etching processes. The SMR exhibited a strong and spurious-free resonance at 8GHz with a high quality factor of 360 and electromechanical coupling coefficient of 6.0%. The temperature coefficient of frequency was -18ppm/K, and the voltage coefficient of frequency was -72ppm/V. Passband ladder filters with T- and π-topology consisting of 3 to 14 SMR were successfully demonstrated with a center frequency of 8GHz. These filters were optimized for maximum bandwidth and exhibited an insertion loss of 5.5dB, a rejection of 32dB, a 0.2dB bandwidth of 99MHz (1.3%), and a 3dB bandwidth of 224MHz (2.9%). There was good correspondence between measured and simulated filter and resonator characteristics. For perfect agreement, parasitic elements needed to be taken into account. These were a series resistance of 5Ω and a parallel conductance of 2mS in case of single resonators. The series resistance can be explained with resistive losses in the electrodes, whereas the parallel conduction was due to conduction along the surface. For π-filters, an additional series inductance of 100pH was needed to obtain a satisfactory fit. This inductance increased the out-of band rejection and insertion loss. Besides the group delay variation, all industrial specifications were met.

$KNbO_3$ was in-situ sputter deposited at 500 to 600°C using a rf magnetron source. A dedicated sputter chamber with load-lock and oxygen resistant substrate heater was built for this purpose. The high volatility of potassium oxide requires a potassium enrichment of the target. Targets with several excess concentrations (in the form of K_2CO_3) were studied. Stoichiometric $KNbO_3$ films were obtained with targets containing 25 and 40% excess K. Zero and 10% excess yielded K deficient films, whereas 100% and 200% excess K led to highly unstable targets with K accumulation on the target surface, resulting in K rich second phases. The potassium-to-niobium ratio in the films depends strongly on sputter pressure and substrate temperature. Dense films, nucleated with cubic {100} texture, were obtained on platinized silicon substrates with a 10nm thick IrO_2 seed layer at substrate temperatures of 520°C. At lower temperatures the films were amorphous, and at higher temperatures the films were composed of individual and facetted $KNbO_3$ grains. The cubic high-temperature {100} texture results in a mixed (101)/(010) texture in the orthorhombic room temperature phase. The measured relative permitivity of 420 indicates that both orientations are equally present. Micro-Raman confirms the orthorhombic line splitting. Piezoelectrical and ferroelectrical activity were verified by means of a piezoelectric sensitive atomic force microscope. A very large piezoelectric activity was observed on some of the grains, and the polarization could be switched on most of the grains. However, the average $d_{33,f} = e_{33}/c_{33}$, as measured by means of laser interferometry, showed a modest value of 24pm/V. The effective coupling factor is derived as k_t^2=2.8%, which is small relative to the theoretical value of 47%. The high dielectric constant and the absence of piezoelectric activity along the [010] direction are responsible for the reduction of the k_t^2 factor. Film roughness, complexity of deposition process and open poling issue make $KNbO_3$ integration into BAW devices a difficult task.

Kurzfassung

Bandpassfilter für Mikrowellenfrequenzen bestehend aus akustischen Raumwellen-Dünnschichtresonatoren (FBAR) sind eine vielversprechende Alternative zu den aktuellen Dielektrik-, und Oberflächenwellenfiltern (SAW) für den Einsatz in mobilen Telekommunikationsanwendungen. Bei gleichwertiger Funktionen sind FBAR Filter erheblich kleiner als dielektrische Filter und ermöglichen einen grösseren Leistungsdurchsatz als SAW-Filter. Zusätzlich bieten FBARs die Möglichkeit der on-chip Integration, die erhebliche Volumen- und Kosteneinsparungen ergibt. Die ersten passiven FBAR Bausteine, welche gegenwärtig auf dem Markt erscheinen, decken hauptsächlich den Bedarf von RF-Filter für die neuen Bänder um 2 Gigahertz ab.

Ein FBAR ist im Wesentlichen eine dünne piezoelektrische Platte zwischen zwei Elektroden, die zum Energieeinschluss von der Umgebung akustisch isoliert ist. Wenn die Isolierung durch einen akustischen Bragg Reflektor erfolgt, spricht man von substrat-fixierten Resonatoren (SMR). Piezoelektrische dünne Schichte aus Aluminiumnitrid (AlN) werden bevorzugt in der aufkommenden FBAR Technologie eingesetzt. AlN zeichnet sich aus durch eine ausreichenden elektromechanische Kopplung, niedrige akustische Verluste bei Mikrowellenfrequenzen, einen tiefen Frequenz-Temperaturkoeffizienten, und gute chemische Kompatibilität mit CMOS Anforderungen.

Diese Doktorarbeit hat zwei Forschungsrichtungen: Im ersten Teil wurden FBAR Strukturen, die auf AlN Dünnschichten basieren, für Anwendungen bei X-Band Frequenzen (7.2-8.5 Gigahertz) untersucht, d.h. bei viel höheren Frequenzen als gegenwärtig in der mobilen Telefonie verwendet werden. Das Ziel war, die Funktionalität begrenzenden Eigenschaften zu identifizieren, und der Industrie einen funktionstüchtigen 8GHz SMR Filter zu demonstrieren. Im zweiten Teil wurde ein neues Material für den Einsatz in FBAR Vorrichtungen studiert, welches die durch seinen Kopplungsfaktor von maximal 7% eingeschränkte Filterbandbreite von AlN, erweitern könnte. Mit seinem hohen Kopplungsfaktor k_t^2 von 47% und verhältnismässig grosser Schallgeschwindigkeit von 8125m/s für Longitudinalwellen in [101] Richtung erscheint einkristallines $KNbO_3$ als ideale Alternative. Piezoelektrizität von $KNbO_3$ Dünnschichten, die auf Elektroden gewachsen werden, ist bisher nicht untersucht worden. In dieser Doktorarbeit wurde das Wachstum von $KNbO_3$ Dünnschichten auf Pt Elektroden mit dem Ziel studiert, diese optimale (101)-Textur gleichmässig aufzuwachsen, und die piezoelektrischen Eigenschaften zu charakterisieren.

X-Band FBARs wurden zuerst mit numerischen Simulationen studiert, die auf einer eindimensionalen Theorie der longitudinalen akustischen Raumwelle (BAW) basieren. Schicht-

dicke, akustische Eigenschaften und elektrische Leitfähigkeit der Elektroden haben eine grosse Auswirkung auf die Resonatoreigenschaften. Optimale akustische und elektrische Eigenschaften stellen entgegengesetzte Anforderung an die Dicke der Elektroden.

Die optimalen Schichtdicken für 8GHz FBARs wurden bestimmt, wobei Al fü die obere und Pt für die untere Elektrode verwendet wurden. Die Eigenschaften der Bandpassfilter wurden Aufgrund der Impedanzen von einzelnen Resonatoren berechnet. Die wählbaren Filterparameter sind die Flächen der seriellen und parallelen Resonatoren, deren Frequenzdifferenz und die Anzahl π-Kreise. Optimale Kombinationen wurden ermittelt, die eine maximale Filterbandbreite mit niedrigster Welligkeit (Ripple) und limitierter Dämpfung bei einer gegebenen Signalunterdrückung ermöglichen. Als wichtiges Resultat ergab sich, dass die Bandbreite der Filter verdoppelt werden kann, falls die seriellen und parallelen Resonatoren um mehr (1.3mal) als der Differenz der Resonanz- und Antiresonanzfrequenz verstimmt werden. Dieses führt auch zu einem flacheren Durchlassbereich und limitiert die Rippel unter $\pm$0.2dB.

Substrat-fixierte Resonatoren und Filter wurden auf einem akustischen mehrschichtigen Reflektor fabriziert, der aus AlN und SiO_2 $\lambda/4$ Schichten besteht. Alle Schichten wurden mittels Kathodenzerstäubung in einem UHV Clustersystem mit 4 Prozesskammern hergestellt. Die Strukturierung erfolgte mit Standardphotolithographie und Trockenätzprozessen. Die SMR zeigten eine starke und rippelfreie Resonanz bei 8GHz mit einem hohen Qualitätsfaktor von 360 und elektromechanischem Kopplungskoeffizienten von 6.0%. Der Frequenz-Temperaturkoeffizient betrug -18ppm/K, und der Frequenz-Spannungskoeffizient -72ppm/V. Bandpassfilter mit T und π-Schaltungen, die aus 3 bis 14 SMR mit einer Mittenfrequenz von 8GHz bestehen, wurden erfolgreich demonstriert. Diese Filter waren für eine maximale Bandbreite optimiert und zeigten eine Dämpfung von 5.5dB, eine Signalunterdrückung von 32dB, eine 0.2dB Bandbreite von 99MHz (1.3%) und eine 3dB Bandbreite von 224MHz (2.9%). Für die vollkommene Übereinstimmung zwischen den gemessenen und simulierten Filter- und Resonatoreigenschaften mussten parasitäre Elemente hinzugefügt werden. Diese bestanden aus einem Serienwiderstand von 5Ω und einer parallelen Leitfähigkeit von 2mS für die einzelnen Resonatoren. Der Serienwiderstand kann mit Widerstandsverlusten in den Elektroden erklärt werden, während die parallele Leitfähigkeit entlang der Oberfläche erfolgt. Für π-Filter war eine zusätzliche Serieninduktanz von 100pH erforderlich um eine zufriedenstellende Übereinstimmung zu erreichen. Diese Induktanz erhöht die Signalunterdrückung und die Signaldämpfung. Ausser der Gruppenverzögerungsänderung wurden alle industriellen Spezifikationen erfüllt.

$KNbO_3$ Schichten wurde in-situ mit Kathodenzerstäubung (RF Magnetron) zwischen 500 und 600°C abgeschieden. Zu diesem Zweck wurde eine spezielle Anlage mit Schleuse und oxydierungsresistenter Substratheizung gebaut. Die hohe Flüchtigkeit des Kaliumoxids erfordert eine Kaliumanreicherung des Targets. Targets mit mehreren Überschusskonzentrationen (in Form von K_2CO_3) wurden studiert. Stöchiometrische $KNbO_3$ Schichten wurden mit Targets von 25, respektive 40% Kaliumüberschuss erreicht. Null und 10% Kaliumüberschuss führte zu kaliumarmen Schichten, während 100% und 200% Kaliumüberschuss zu einer K Anreicherung auf der Targetoberfläche und zu kaliumreichen Zweitphasen in der Schicht führte. Das Kalium zu Niobium Verhältnis in den Schichten hängt weiter stark von

Prozessdruck und Substrattemperatur ab.

Dichte, mit einer {100} Textur gekeimte Schichten wurden auf platinbedeckten Siliziumsubstrates mit einer 10nm dicken IrO_2 Nukleationsschicht bei 520°C abgeschieden. Bei niedrigeren Substrattemperaturen wurden amorphe Schichten, und bei höheren Substrattemperaturen wurden stark fazetierte quasi freistehende $KNbO_3$ Körner erzeugt. Die kubische Hochtemperaturtextur {100} führt zu einer gemischten (101)/(010) Texture in der orthorhombic Raumtemperaturphase. Die gemessene relative Dielektrizitätszahl ϵ_r=420 weist darauf hin, dass beide Texturen gleichmässig vorhanden sind. Mikro-Raman Lichtstreuung bestätigt die orthorhombische Aufspaltung. Die piezoelektrische und ferroelektrische Aktivität wurden mittels eines piezoelektrisch empfindlichen Kraftmikroskops überprüft. Eine sehr grosse piezoelektrische Aktivität wurde auf einigen der Körner beobachtet, und die Polarisation konnte bei den meisten Körnern umgeschaltet werden. Die piezoelektrischen Konstante $d_{33,f} = e_{33}/c_{33}$, die mittels der Laserinterferometrie gemessen wurde, zeigt jedoch einen tiefen Wert von 24pm/V. Der effektive Kopplungsfaktor wird somit als k_t^2=2.8% berechnet, was im Verhältnis zum theoretischen Wert von 47% sehr klein ist. Die hohe Dielektrizitätskonstante und das Fehlen piezoelektrischer Aktivität entlang der [010] Richtung sind für die Reduzierung des k_t^2 Faktors verantwortlich. Schichtrauhigkeit, Kompliziertheit des Zerstäubungsprozesses und die ungelöste Schichtpolung machen die $KNbO_3$ Integration in BAW Filter zu einer schwierigen Aufgabe.

Acknowledgements

I acknowledge Professor Nava Setter, my thesis director, for providing me with the necessary means to do the present research.

I would like to thank my thesis advisor, Dr. Paul Muralt, for teaching me the techniques of thin film processing, for being a constant source of inspiration, for providing a lot of freedom, as well as his support and explanations.

I would also like to thank Dr. Dragan Damjanovich for his disponibility on questions about ferroelectrics and experimental set-ups. Many thanks also to Dr. Enrico Colla for help on LabView programming.

I would like to thank Simon Bühlmann for piezo-AFM and piezoelectric laser interferometry measurements, fruitfull discussions and his excellent Sushi dinners; Kyle Brinkman for RTA anneals, moral support and fruitful discussions, be it about science, golf, skiing or enjoying life; Matthew Davis for english-corrections, tensor calculations, how-to-tie-a-tie-knot demonstrations and his british humor; Dr. Stephane Hiboux and Dr. Brahim Belgacem for help on the Nordico but also excellent after-work hours.

More thanks to other members of the Ceramics Laboratory: Dr. David Martrou for critical discussions and helping in assembling the sputtering tool, Lino Olivetta for support with all sorts of electrical problems and electric wiring of the sputtering machine. Gregor Kissling also provided a helpful hand when needed, Dr. Fabrice Martin for laser-interferometer measurements, but also discussions about AlN and ZnO deposition details. Dr. Marco Cantoni for high-quality TEM images and EDX analyses, Dr. Marlyse Demartin Maeder for SEM-EDX analyses, Jacques Castano for the powder target processing, Dr. Pedro Möckli and Dr. Igor Stolitchnov for having a high uptime of the X-ray machines, Dr. Sandrine Gentil, Evelyn Hollenstein, and Maxime Morozov for help on experimental problems.

Thanks go also to my two diploma students, Samuel Rey-Mermet and Patrick Carazzetti, for their contribution to my work.

All the other members of the Ceramics Laboratory for comfortable work environment.

A big thanks goes to Nicolas Xanthopoulos for in-numerous XPS analyses which were performed in the shortest of times possible.

I am also very grateful for training and access to all the machines at CMI, which were always perfectly maintained and which allowed for efficient process execution. Especially Dr. Philippe Flückiger, Dr. Cyrille Hibert, Roberto Mancini, Guy Clerc and Irene Magnenat.

Many thanks to the machine shop for the precise and prompt machining of all the self-

designed parts of the sputtering tool. Special thanks to Werner Brönnimann and Louis-Henri Masson for their flexibility and fast execution times.

I would also like to thank Dr. Klaus Leitner at UMICORE (former UNAXIS) for the target fabrication, Dr. Eduart Kügler and Dr. Stanislav Kadlec at UNAXIS for AlN depositions within a diploma work.

I also acknowledge gratefully the help of Prof. Arvind Shah, Dr. Evelyne Vallat and Fanny Meillaud at University Neuchatel for the Micro-Raman analysis.

I am indebted to the members of the jury who agreed to be co-examiners: Prof. H. J. Mathieu (EPFL), Prof. H. Bleuler (EPFL), Prof. R. W. Whatmore (Cranfield University) and Dr. V. P. Plesski.

I acknowledge the funding of the Swiss Office for Education and Research and the inputs from and fruitful discussions with the partners of the European MEDCOM project.

I want to thank topNano21 for their financial support and the Ceramics Laboratory for providing the flight for my participation in the Korea-Swiss Symposium 2002. I would also like to thank the korean side which paid for all the local expenses.

I also want to acknowledge the *student travel support* of 1000USD from the 2003 Ultrasonics Symposium (USS) in Honolulu, USA. Without this contribution I could not have afforded to travel privately to Hawaii, and to participate and present my paper in the oral session of the conference, which was the only opportunity presenting my results of BAW filters at the USS.

Special thanks to Dr. Colin Sanctuary, Marie-Soleil Rouillard and Dr. Simon Rolshoven for moral support, but especially the numerous hours spend together in the snow.

I especially thank Caroline Ballebye for all her support and understanding during the sometimes tough and long PhD years.

Nomenclature

AFM	Atomic force microscope
AlN-LC	Single chamber single target sputter tool without load-lock
BAS450	Single chamber multi-target batch sputter tool without load-lock
BAW	Bulk acoustic wave
BPF	Bandpass filter
BW	Bandwidth
CMOS	Complementary metal-on-oxide semiconductor
CVD	Chemical vapor deposition
EDX	Energy dispersive X-ray spectroscopy
FBAR	Film bulk acoustic resonator
FWHM	Full width at half maximum
GPS	Global positioning system
IC	Integrated circuit
k_t^2	Electromechanical thickness-extensional coupling factor
KN-ratio	[K]/[Nb] atomic concentration ratio
MBE	Molecular beam epitaxy
MCF	Monolithic crystal filter
MMIC	Monolithic microwave integrated circuit
MOCVD	Metal-organic chemical vapor deposition
MSP	Magnetron sputtering
NORDICO	Single chamber multi target sputter tool without load-lock
PCS	Personal communications band
PLD	Pulsed laser deposition
PS-ratio	Parallel-to-series surface area ratio
Q	Quality factor
RF	Radio frequency
SAW	Surface acoustic wave
SCF	Stacked crystal filter
SMR	Solidly mounted resonator
Spider	UHV sputter cluster tool with 4 process chambers and load-lock
SZM	Structure zone model
TCF	Temperature coefficient of frequency
TEM	Transmission electron microscope
TFR	Thin film resonator
VCF	Voltage coefficient of frequency
VCO	Voltage controlled oscillator
XPS	X-ray photoelectron spectroscopy
XRD	X-ray diffraction

Contents

Abstract **iii**

Kurzfassung **v**

Acknowledgements **ix**

Nomenclature **xi**

1 Introduction **5**
1.1 Film bulk acoustic resonators and derived filters 7
1.2 Piezoelectrics used for film bulk acoustic resonators 9
1.3 Aim of this thesis 11
1.3.1 Fabrication and characterization of solidly mounted resonators and thin film bulk acoustic wave resonators working at 8GHz 11
1.3.2 Modeling, fabrication and characterization of SMR based ladder filters working at 8GHz 12
1.3.3 Study of the growth of $KNbO_3$ thin films 12
Bibliography 13

2 Bulk Acoustic Wave Resonators **17**
2.1 Introduction 17
2.2 Analytical models of bulk acoustic wave resonators 18
2.2.1 1-dimensional model of thickness-extensional modes in thin piezoelectric plates 18
2.2.2 Analytical model of resonator with finite thickness electrodes 19
2.2.3 Equivalent circuit 21
2.2.4 2-dimensional models 23
2.3 State of the art of BAW resonators 24
2.3.1 Thin film bulk acoustic resonator obtained by surface micromachining 26
2.3.2 Solidly mounted resonator 28
2.4 Review on AlN thin films for BAW applications 29
2.4.1 AlN properties 29
2.4.2 AlN thin film growth 31

2.4.3 Frequency (non)-uniformity and frequency trimming of BAW resonators 39
2.5 Numerical model simulation results 41
2.5.1 Material data used for numerical simulations 41
2.5.2 Effect of reflector layers on mechanical properties of Bragg stack . . 41
2.5.3 Effect of reflector layers on resonator properties 43
2.5.4 Implications of different electrodes on resonator behaviour 43
2.6 Growth and properties of AlN, Pt and Mo thin film 46
2.6.1 Film patterning and characterization 46
2.6.2 Deposition process for Pt electrodes 47
2.6.3 Deposition process for Mo electrodes 48
2.6.4 AlN deposition process 48
2.6.5 AlN wet etching 52
2.7 Solidly mounted resonators 53
2.7.1 Bragg reflector fabrication 53
2.7.2 Design of resonators 56
2.7.3 Resonator fabrication 57
2.7.4 Characterization of SMR microwave properties 58
2.7.5 Comparison of measured resonator admittance vs. numerical model simulations 62
2.7.6 Frequency dependency on temperature and applied dc-field. 63
2.8 Film bulk acoustic resonators 66
2.8.1 Sacrificial layer fabrication 66
2.8.2 Characterization of FBAR microwave properties 74
2.9 Summary and Conclusions 77
Bibliography 80

3 Passband Filters **93**
3.1 Introduction 93
3.1.1 State of the art of FBAR ladder filters 95
3.2 Theory of passband ladder filters 96
3.3 Numerical simulations of ladder filters 98
3.3.1 The transmission ($ABCD$) matrix 99
3.3.2 Numerical simulation results 100
3.4 Ladder filter fabrication 104
3.4.1 Design of ladder filters 105
3.4.2 Fabrication method 105
3.4.3 Frequency shifting 106
3.5 Characterization of 8GHz SMR ladder filters 110
3.6 Measured vs. numerical ladder filters simulations 112
3.7 Summary and Conclusions 115
Bibliography 117

4 $KNbO_3$ thin films **121**
4.1 Introduction . . . 121
4.2 Properties of $KNbO_3$ . . . 123
4.2.1 Phase diagrams . . . 123
4.2.2 Chemical stability and decomposition . . . 124
4.2.3 Dielectric, elastic and piezoelectric properties . . . 125
4.2.4 Literature review on $KNbO_3$ thin film synthesis . . . 127
4.2.5 Literature review on $Na_{0.5}K_{0.5}NbO_3$ thin film synthesis . . . 130
4.3 Substrates, targets and tools . . . 132
4.3.1 Preliminary study . . . 132
4.3.2 Rf magnetron sputter tool . . . 133
4.4 Characterization of the sputter process . . . 139
4.4.1 Effect of process parameters on target voltage . . . 139
4.4.2 Effect of pressure and substrate temperature on deposition rate . . . 142
4.5 Film stoichiometry analyzed with XPS . . . 142
4.6 Film crystallography analyzed with XRD and Micro-Raman . . . 145
4.6.1 Crystallographic phases and textures observed with XRD . . . 145
4.6.2 Effect of excess K in targets on film crystallography . . . 146
4.6.3 Phase determination by Micro-Raman measurements . . . 147
4.7 $KNbO_3$ film deposition on (100) $SrTiO_3$ substrates . . . 149
4.8 $KNbO_3$ film deposition on (111) Pt/Si substrates . . . 151
4.8.1 $KNbO_3$, K_3NbO_4, $K_3Nb_7O_{19}$ and $K_4Nb_6O_{17}$ film microstructure . . . 151
4.8.2 Phase segregations of $KNbO_3$-$K_3Nb_7O_{19}$-$K_4Nb_6O_{17}$ films . . . 153
4.8.3 Effect of seed layers on $KNbO_3$ film growth . . . 155
4.8.4 Effect of sputter pressure and substrate temperature on film stoichiometry . . . 158
4.8.5 Effect of sputter pressure and substrate temperature on film crystallography . . . 159
4.8.6 TEM plane view bright field and diffraction images . . . 161
4.8.7 Film outgrows-nanorods observed in the Nb_2O_5-K_2O system . . . 162
4.9 Dielectric and piezoelectric characterization . . . 164
4.9.1 Macroscopic $d_{33,f}$ measurements with double beam laser interferometer 164
4.9.2 Microscopic measurement of piezoelectric activity with AFM . . . 168
4.10 Summary and Conclusions . . . 172
Bibliography . . . 175

Conclusions and outlook **183**

List of publications **187**

Curriculum vitae **189**

Chapter 1

Introduction

The growing use of mobile communication systems that operate at radio frequencies (RF) of 0.9-5.5GHz call for ever smaller, better and cheaper bandpass filters. These bandpass filters are required to transmit or receive signals within a certain bandwidth at a specified frequency and suppress all other signals. Global positioning systems (GPS, Galileo), mobile telecommunication systems (GSM, PCS, UMTS), data transfer (Bluetooth, Wireless Local Area Network WLAN), satellite broadcasting and future traffic control communication are examples of such applications. Wireless networks are especially advantageous in some rural and semi rural areas.

An architecture for the microwave section of a portable communications transceiver is shown in figure 1.1. One of the largest passive components is the dielectric resonator-based bandpass filter (BPF) at the exit of the transmit path. Bandpass filters can potentially be integrated on-chip in wireless communication, resulting in significant performance and functionality enhancement, size reduction by reducing the number of parts and by eliminating large passive components.

Bandpass filters for RF signal treatment are today fabricated using different technologies: i) ceramic filters based on dielectric resonators, ii) filters using Surface Acoustic Wave (SAW) resonators, and iii) filters using thin film Bulk Acoustic Wave (BAW) resonators. High electric losses prevent the use of lumped elements which are widely used at lower frequencies for signal filtering.

The biggest impact of the thin Film Bulk Acoustic Resonators (FBAR) technology is in providing miniature high performance resonators and filters over a wide frequency range for conventionally designed RF systems and as an enabling technology for more advanced system architecture (SiP system in package, SoC system on chip). In general these filters are approximately ten to one hundred times smaller than ceramic filters or SAW devices performing the same function. The largest constraint for SAW technology at one gigahertz and above, in addition to it being a non-monolithic integratable technology, is that the filter technology requires submicron metallization. High dielectric constant filters based on titanates and zirconates have dielectric constants in the 10 to 100 range. This results in size reductions ranging from 3 to 10. However, at one gigahertz, the size of a quarter wave resonator is still approximately 0.8mm for a dielectric constant of 100.

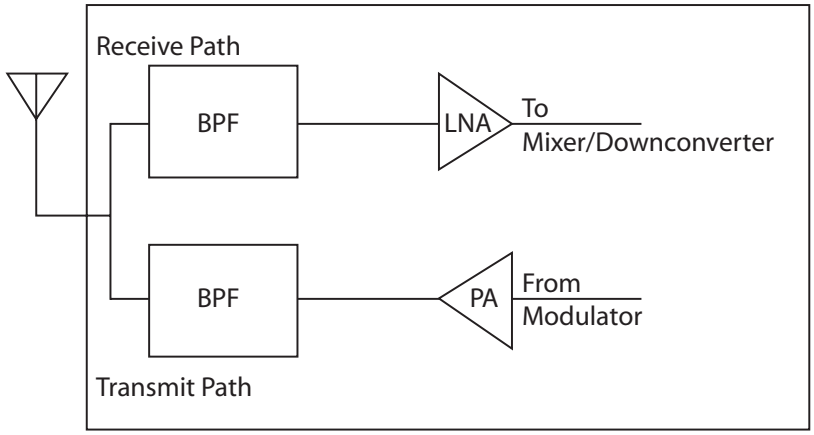

Figure 1.1: Schematic of the rf section of a portable communications receiver. BPF Bandpass filter, LNA Low noise amplifier, PA Power amplifier.

Another advantage of the FBAR technology is its CMOS compatibility which allows the integration into monolithic microwave integrated circuits (MMIC). Ceramic resonators, SAW resonators, and SAW filters are relatively large compared to MMIC, and because they are constructed from special piezoelectric materials, they cannot be integrated on-chip.

In summary, the FBAR structure has several unique properties which makes it extremely useful for certain types of filter design: i) size, ii) monolithic implementation allowing large scale integration of MMIC devices, iii) high mechanical quality (Q) performance, iv) large power handling capabilities, and v) series and parallel resonance usable for bandpass filters by providing two transmission poles.

The final goal of semiconductor companies such as Intel, ST Microelectronics, and Motorola is above chip integration of FBAR to provide complete solutions or modules for rf signal processing. There are few companies that have developed sufficient knowledge to start the commercialization of the first FBAR based devices: TFR Technologies, USA, was founded in 1989 by K.M. Lakin who was one of the pioneers of the FBAR and later SMR technology. Agilent, USA, started developing their technology in 1994 [29]. In 2000 they reported a pilot run production of FBAR based duplexers for 1.9GHz (1/10 the volume of commercial units - ceramic filters) [19], and in 2001 the volume production on 4" wafer and development work on 6" [3]. Sanyo is producing currently a CDMA phone using Agilent FBAR duplexers. Infineon Technologies, D, started volume production of SMR devices in mid 2002. The estimated number of fabricated FBAR related devices per year was near three billion in 2002 [34]. In 2000 the European MEDCOM project (IST-1999-11411 - OFES-No: 99.0661) was started to develop european knowledge of FBAR technology. The present work was tightly involved with this project, and bandpass filters for use in a test-subsystem were successfully produced.

1.1 Film bulk acoustic resonators and derived filters

The concept of the Film Bulk Acoustic Resonators derives from the original composite crystal resonator of Sliker and Roberts [31] in 1967 in which a thin film of evaporated CdS served as a transducer on a resonant piece of bulk quartz crystal. Page [27] demonstrated in 1968 that the quartz can be replaced by a thin (75μm) substrate of single crystal silicon. Lakin and Wang [15], Grudkowski et al. [8] and Nakamura et al. [24], more than a decade later, fabricated ZnO and AlN based *composite* film bulk acoustic resonators by using a 6μm thin silicon membrane, respectively a 2.5μm thick SiO_2 temperature compensated membrane, obtained by anisotropic etching of the silicon substrate. Lakin et al. [18] demonstrated later the *edge-supported* FBAR resonator by removing the Si membrane. Kline and Lakin [12] fabricated the first wafer top side planar processed FBAR by using an under-cut edge on GaAs substrates. Satoh et al. [30] presented in 1985 the first surface-micromachined FBAR. The latter two approaches allow the integration with integrated circuits (IC).

Another milestone for BAW technology was the re-introduction of the Solidly Mounted Resonator (SMR) by Lakin et al. [14] in 1995, which is also integratable. The air interface of the FBAR is replaced by a Bragg reflector, consisting of several quarter-wavelengths thick layers with large acoustic impedances ratios, to acoustically isolate the resonator from the substrate. An important effect of the reflector layers, as demonstrated by Newell in 1965 [25], is the partial lateral stiffening of the piezoelectric plate that minimizes displacements associated with plate wave generation and consequent spurious resonances normally observed in free plates. Lakin et al. [14] demonstrated the feasibility and lack of spurious signals in AlN based SMR, and realized ladder filters working at 1.6GHz with an insertion loss of 2.9dB and an out-of-band rejection of 40dB.

FBARs can be used in filter design as bandpass filters or image rejection filters (narrow passband with signal rejection at adjacent lower frequencies). Passband filters may be realized with electrically coupled FBARs using a ladder or lattice topology. Another way of realizing BPF is by lateral acoustic coupling in thickness- or shear-mode resonance. Grudkowski et al. [8] demonstrated in 1980 the laterally coupled, thin film Monolithic Crystal Filter (MCF) with 8.5dB insertion loss and 40dB rejection. BPF can also be realized by stacking two resonators which couple acoustically in the thickness mode. A large out-of-band rejection is achieved because of the grounded middle electrode. Lakin et al. [17] introduced in 1986 the thin film Stacked Crystal Filter (SCF), as well as the electrically coupled ladder filter.

The FBAR technology can potentially be used as a chemical sensor (Burns et al. [4] and Hsieh et al. [10]): The FBAR can be used as gravimetric sensing device, due to its high Q, similar in principe to the quartz balances used for deposition rate control in evaporation systems. By coating the FBAR surface with a protein-specific receptor, a frequency shift due to marginal mass-loading (in the order of monolayers) of the electrode should occur when the protein attaches to the receptor. The feasibility and extremely high sensitivity of such a device was demonstrated in a diploma work [28] supervised within this thesis.

The increasing interest on FBAR related devices is graphically shown in figure 1.2: A

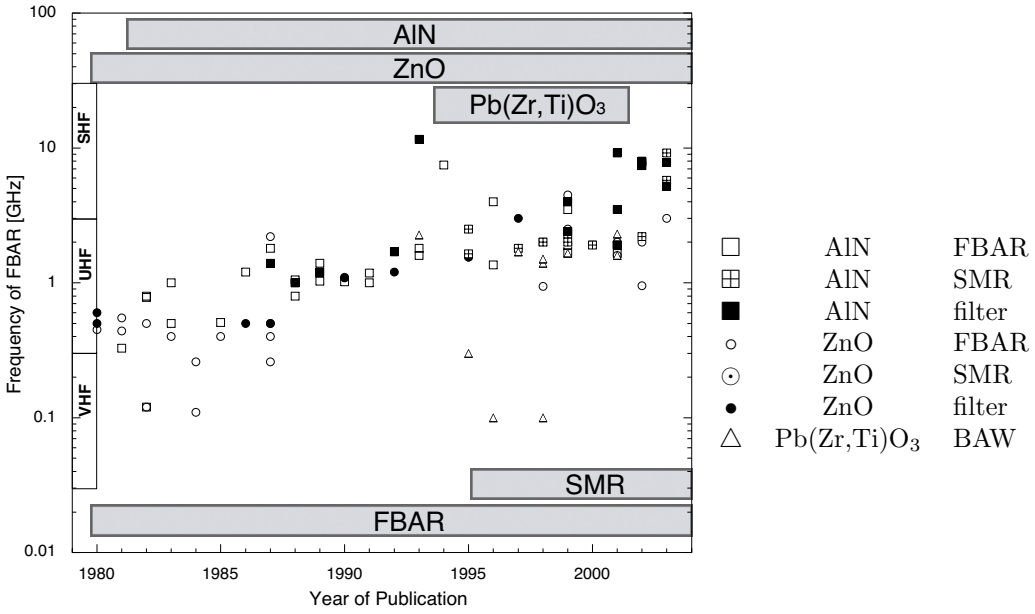

Figure 1.2: FBAR and SMR related publications with achieved resonance frequencies over the past 25 years. AlN and ZnO based thin film BAW have been demonstrated since 1980/81. A few reports on $Pb(Zr,Ti)O_3$ based FBAR/SMR have been published since 1993, showing large electromechanical coupling but very low mechanical quality factors. Recently some interest has turned to the high coupling and lead-free $KNbO_3$. To our knowledge no publications exist on $KNbO_3$ based BAW devices. A reliable process to grow $KNbO_3$ on metallized Si substrates needs to be developed first.

growing number of publications address theoretical and fabrication issues of FBAR derived applications. Most publications are concerned with the Ultra High Frequency (UHF) range of 0.3-3GHz, in which most current consumer mobile communication products are using bands (L, S). The C and X-band frequency range (5.8-8.5GHz) within the Super High Frequency (SHF) range is dedicated to radar, point-to-point, and ground-satellite communication. One of the aims of this work is to evaluate the limitations and feasibility of FBAR/SMR technology for X-band frequencies

In spite of the growing success of the FBAR technology problems and unanswered questions remain: The drive for optimizing the resonator characteristics quality factor Q and electromechanical coupling factor k_t^2 may be solved by improving the film quality of the piezoelectric material, but they are also influenced by the design of the resonator and the layer properties of the materials surrounding the piezoelectric film. Eliminating ripple or "suck out" associated with lateral mode excitation is a big problem for pass-band filters. It requires 2-dimensional simulations to understand these phenomena. Solutions are needed for maintaining a uniform film thickness for frequency control and a means to target frequency to $< 0.1\%$ over the whole wafer area. This may be achieved either by improving the

deposition tools or by developing techniques for individual resonator and filter trimming. Different electrode materials are used by the various groups working on FBARs. What is the influence and advantage of certain metals over others? How can the filter bandwidth be trimmed? What is the best design and how many FBAR elements are needed to implement ladder filters. How can the frequency drift due to temperature variations be reduced or oppressed? What is the upper frequency limit for FBAR and how can it be increased? These issues are just a few examples of ongoing research.

1.2 Piezoelectric materials used for film bulk acoustic resonators

FBAR use piezoelectric films to convert electrical into mechanical energy and vis-versa. This film is sandwiched between two electrodes on which the electric field is applied. For microwave BAW devices, emphasis has been mainly on polar materials of the hexagonal wurtzite crystal class, e.g. CdS, ZnO, and AlN. Thin films of these compounds can possess a strong oriented polycrystalline fibered structure, and the key problem is to control the film texture, together with physical properties, on various electroded surfaces. Ferroelectric materials are also polar (and piezoelectric), but in these materials the polarization can be switched and reversed by an applied electric field. The largest class of ferroelectric materials is the perovskite-type oxide group based upon solid solutions of $BaTiO_3$, $SrTiO_3$, $Pb(Zr,Ti)O_3$ (PZT), $LiNbO_3$, $LiTaO_3$, $NaNbO_3$, and $KNbO_3$. Low temperature processing methods compatible with the needs of integrated circuits would lead to the choice of non-refractory materials, e.g. KNO_3, SbSI, etc. Unfortunately, these materials are often chemically or electrically unstable. The more refractory materials such as perovskites mixed oxides require higher growth temperatures (500-700°C) to stabilize the desired ferroelectric phase. Side effects may occur, associated with thermal expansion and chemical interaction relative to the substrate [7].

AlN and ZnO FBAR devices posses material properties that make them suitable for current front-end filters for global positioning system (GPS) receivers and RF components in current personal communications systems (PCS) handsets, such as duplexers, and voltage controlled oscillators (VCO). However, the low electromechanical coupling in AlN and ZnO leads to low-bandwidth filters ($< 3.5\%$), making it difficult to meet the requirements for broad-band access and large data transmission in future mobile applications. It is apparent that materials with higher coupling coefficients are required beyond AlN unless some other means of bandwidth enhancement are used, such as integral inductors to pull the resonators to higher effective k_t^2. That bandwidth is well short of the requirement for full bandwidth filters in the PCS (3.2%) and ISM (3.5%) bands [13]. The material properties listed in table 1.1 suggest that ZnO might be an ideal piezoelectric for use in these wider bandwidth filters. However, other factors must be considered such as intrinsic Q at high frequencies and potential fabrication constraints. Ferroelectric materials in the PZT series can have high electromechanical coupling coefficients but their drawback are the high acoustic losses at microwave frequencies.

AlN and ZnO based FBARs have dominated over the last two decades (c.f. figure 1.2). The thin film growth of these materials by very large scale integration (VLSI) and CMOS (only AlN) compatible rf or dc sputtering was first demonstrated in the 1970s, and developed specifically for FBAR fabrication in 1980 by a number of groups. These films are now readily produced with optimized piezoelectric properties and very high thickness uniformity on 4-8" substrates with standard industrial sputtering machines.

The search for new materials is fed by practical demands for devices with improved characteristics, e.g. lower loss (higher Q, less insertion loss), higher piezoelectric coupling (increased bandwidth), better temperature stability, greater miniaturization, and higher acoustic velocity, which leads to easier fabrication of high-frequency devices.

Table 1.1 compares the different FBAR materials used to date. Aluminum nitride is one of the promising thin-film piezoelectric materials due to its high ultrasonic velocity and fairly large piezoelectric coupling factors. Furthermore AlN is CMOS compatible, a key consideration for on-chip integration of electronics with MEMS devices. The high ultrasonic velocity is useful in BAW for higher frequencies because of the reduced film thickness corresponding to the fundamental mode $\lambda/2$ thickness which scales with $1/f$ and is only a few hundred nanometers above 5GHz. The longitudinal material coupling coefficient for c-axis oriented AlN was estimated by Lakin [16] as 6.5-7%, respectively 7.8% for ZnO. The slightly higher coupling coefficient of ZnO is offset by its higher temperature coefficient of frequency (TCF) and low acoustic velocity. The use of CdS has not been reported recently because of its low electromechanical coupling.

Microstructural and stoichiometric considerations limit the use of PZT to high deposition temperatures, while CMOS contamination requirement limit the use of ZnO in CMOS compatible processes. PZT has a very high dielectric constant compared to AlN, ZnO and (101) oriented $KNbO_3$. To fabricate 50Ω impedance matched resonators or filters, the surface area has to be chosen significantly smaller, which increases the width-to-thickness ratio and hence renders the resonators more prone for plate wave spurs. Su et al. [32] demonstrated PZT FBARs with Q=54 and k_t^2=19.8% showing strong ripple due the the small width-to-thickness ratio of 6. They also demonstrated PZT FBAR ladder filters exhibiting 6.5dB insertion loss and a large 3dB bandwidth of 120MHz (7.5%) at 1.6GHz. Further materials not listed are for example the AT cut quartz which has a very small coupling coefficient of only 0.8% but a TCF of 0ppm/K. $LiNbO_3$ and $LiTaO_3$ both have coupling coefficients k_t^2 in the range 13-27% and sound velocities comprised between 4.5-7.3km/s depending on the cut.

$KNbO_3$ has recently roused some interest for BAW and SAW applications because of its high acoustic phase velocity (c.f. table 1.1) and its very high electromechanical coupling coefficient. In order to use $KNbO_3$ for BAW applications, this perovskite material needs to be deposited on metal electrodes with a controlled crystalline texture at temperatures above 500°C. During the cool down to room temperature, the material undergoes two phase transitions from the high-temperature cubic, to the tetragonal and finally orthorhombic phase. The final crystalline orientation at room temperature needs to have the polar direction out-of-plane for piezoelectric activity in the thickness direction. The thickness-extensional coupling factor will be maximum when the polarization vector is at

Table 1.1: Summary of important material properties of the most widely used and potential thin film piezoelectric ceramics for low loss and high coupling bulk acoustic wave application.

Property		AlN [33, 5]	ZnO [9, 26, 1]	CdS [9, 11]	$PZT_{52/48}$ [2]	$KNbO_3$ [35, 36]
ρ	[kg/m^3]	3260 [33]	5665 [9]	4820	7550 [2]	4620
TCF	[ppm/K]	-25 [13]	-60 [13]	-108	-	-
$V_{(001)}$	[m/s]	11550 [5]	6080 [13]	4500	5400 [22]	8125 [23]
$k^2_{t,film}$	[%]	6.5-7.8 [6, 20]	7.5 [13]	2.4	25 [22]	49 [23]
Q	[-]	> 1000	> 1000	-	67 [21]	-

an angle of approximately 45° with respect to the surface normal. This corresponds to a (101) orthorhombic texture ((100) pseudo-cubic) which is readily obtained in $KNbO_3$ thin films deposited onto mono-crystalline substrates. To our best knowledge, no reports on $KNbO_3$ based BAW devices exist. This may be explained with the little knowledge of thin film growth which is available, especially on polycrystalline substrates, as well as reported problems with stoichiometry control.

1.3 Aim of this thesis

The aim of this thesis is to develop an understanding of the fundamental parameters which govern the behavior of bulk acoustic wave resonators and filters working above 5GHz. Today, numerous research groups and industries work on BAW devices that operate in the frequency range 1-5GHz which is currently used by mobile communication systems. New BAW applications working at higher frequencies will eventually be limited by the thinness of the layers that constitute the BAW resonators and the increasing sensitivity towards thickness deviations of these layers. Another important point of research is the drive for higher effective electromechanical coupling of the BAW devices, which may be achieved by improving the currently used piezoelectric materials, by improving the design of the resonator, or by developing a new high coupling piezoelectric thin film material. This thesis is divided into 3 parts which lead towards these different goals:

1.3.1 Fabrication and characterization of solidly mounted resonators and thin film bulk acoustic wave resonators working at 8GHz

The basis for fabricating BAW resonators and filters is the knowledge of how to fabricate and pattern acoustic reflectors, thin film electrodes and piezoelectric thin films. This chapter treats these practical aspects and concentrates on the fabrication and characterization of resonators working at 8GHz. Numerical simulation results will identify the important materials and geometrical parameters to be optimized for ladder filters. Different metal electrodes will be studied with numerical 1-dimensional simulations to point out how they compare at rf frequencies between 1 and 10GHz and what their advantages and limitations

are. The emphasis will be put on how to increase the effective coupling coefficient of resonators which is one of the limiting factors of the current FBAR/SMR filter technology. The growth of AlN on a new promising electrode will be studied for the same purpose.

1.3.2 Modeling, fabrication and characterization of SMR based ladder filters working at 8GHz

One goal of this work is to present a theoretical feasibility study, to optimize the resonator and filter design, and finally to realize passband filters working beyond the frequency of commercial products. At the beginning of this thesis the chosen frequency of 8GHz was very advanced: Numerical simulations of the ladder filter topology will help to understand the different parameters which determine the filter characteristics. Practical methods of shifting resonance frequencies for ladder filter trimming, or generally for frequency trimming will be studied and discussed. Different ladder filter topologies using 3-14 SMR elements will be simulated, fabricated and characterized.

1.3.3 Study of the growth of $KNbO_3$ thin films

The potential of $KNbO_3$ as new high-coupling BAW material has been discussed above. The development of novel lead-free $KNbO_3$ thin films deposited on metallized substrates will be presented: a major point of the $KNbO_3$ development in this thesis is to build an adequate deposition tool, and to find process conditions which allow the reproducible fabrication of stoichiometric, crystalline, dense, textured and piezoelectric films on platinized silicon. According to our literature study, few publications exist describing the sputter deposition of $KNbO_3$ thin films. Even less report on the growth on polycrystalline electrodes which are a prerequisite for BAW resonators on silicon. Because of the contaminating nature of potassium, with respect to other thin films grown in this laboratory, a specially dedicated and fully computer controlled rf magnetron sputtering tool was built by the author. Special points are the load-lock and a non-contact, oxygen-resistant heater which achieves substrate temperatures of up to 600°C. To compensate for expected potassium loss in deposited films, different target compositions are studied, using various potassium excess contents in self-fabricated 4" ceramic targets. Several thermally and chemically stable Pt electrodes are developed, as well as nucleation layers. The influence of the before-mentioned parameters as well as the sputter process parameters (O_2:Ar ratio, pressure, temperature, rf power) will be studied. Results include the study of film morphology by SEM, chemical analysis by XPS, crystallographic and phase information by X-ray diffraction, phase information by Raman analysis and piezoelectric measurements by interferometry and piezo-AFM.

Bibliography

[1] B. A. Auld. Properties of materials. In *Acoustic Fields and Waves in Solids*, volume 1, pages 122,131,247,357. John Wiley & Sons, New York, 1973.

[2] D. A. Berlincourt, C. Cmolik, and H. Jaffe. Piezoelectric properties of polycrystalline lead titanate zirconate compositions. In *Proceedings of the IRE*, volume 48, pages 220–229, 1960.

[3] P. Bradley, R. Ruby, J. Larson, Y. Oshmyansky, and D. Figueredo. A film bulk acoustic resonator (FBAR) duplexer for USPCS handset applications. In *Ultrasonics Symposium*. IEEE, 2001.

[4] S. G. Burns, R.J. Weber, and S.D. Braymen. High frequency oscillators using cointegrated BAW thin-film piezoelectrics with microwaves. In *45th Annual symposium on frequency control*, pages 207–211, 1991.

[5] G. Carlotti, F. S. Hickernell, H. M. Liaw, L. Palmieri, G. Socino, and E. Verona. The elastic constants of sputtered aluminum nitride films. In M. Levy, S. C. Schneider, and B. R. McAvoy, editors, *IEEE Ultrasonics Symposium*, volume 1, pages 353–356, Seattle, WA, 1995. IEEE.

[6] G.G. Fattinger, J. Kaitila, R. Aigner, and W. Nessler. Thin film bulk acoustic wave devices for applications at 5.2GHz. In *Ultrasonics symposium Proceedings*, Hawaii, USA, 2003. IEEE.

[7] M. H. Francombe and S. V. Krishnaswamy. Growth and properties of piezoelectric and ferroelectric films. *Journal of vacuum science & technology A*, 8:1382–1390, 1990.

[8] T. W. Grudkowski, J. F. Black, T. M. Reeder, D. E. Cullen, and R. A. Wagner. Fundamental-mode VHF-UHF miniature acoustic resonators and filters on silicon. *Appl. Phys. Lett.*, 37(11):993–995, 1980.

[9] J.G. Gualtieri, J.A. Kosinski, and A. Ballato. Piezoelectric materials for acoustic wave applications. *IEEE Transactions on Ultrasonics, Ferroelectrics and Frequency Control*, 41(1):53 –59, 1994.

[10] P. Hsieh, R. Reif, and B. Cunningham. Dc magnetron reactive sputtering of low stress AlN piezoelectric thin films for MEMS application. In *Materials Science of Microelectromechanical Systems (MEMS) Devices*, pages 165–170. Mater. Res. Soc., Warrendale, PA, USA, 1999.

[11] H. Jaffe and D. A. Berlincourt. Piezoelectric transducer materials. *Proceedings of the IEEE*, 53(10):1372–1386, 1965.

[12] G. R. Kline and K. M. Lakin. 1.0-GHz thin-film bulk acoustic wave resonators on GaAs. *Appl. Phys. Lett.*, 43(8):750–751, 1983.

[13] K. M. Lakin. Thin film resonators and filters. In *IEEE Ultrasonics Symposium*, volume 2, pages 895–906, 1999.

[14] K. M. Lakin, G. R. Kline, and K. T. McCarron. Development of miniature filters for wireless applications. *IEEE Transactions on Microwave Theory and Techniques.*, 43(12):2933–2939, 1995.

[15] K. M. Lakin and J. S. Wang. UHF composite bulk wave resonators. In *Ultrasonics symposium proceedings*, pages 834–837. IEEE, 1980.

[16] K.M. Lakin. Fundamental properties of thin film resonators. In *Frequency Control, 1991., Proceedings of the 45th Annual Symposium on*, volume 1, pages 201 – 206, 1991.

[17] K.M. Lakin, G.R. Kline, R.S. Ketcham, and S.G. Burns. Thin film resonator based low insertion loss filters. In *IEEE 1986 Ultrasonics Symposium Proceedings*, volume 1, pages 371–375, 1986.

[18] K.M. Lakin, J.S. Wang, G.R. Kline, A.R. Landin, Y. Y. Chen, and J. D. Hunt. Thin film resonators and filters. *Ultrasonics symposium*, pages 466–475, 1982.

[19] J. III. Larson, R. Ruby, P. Bradley, J. Wen, S.-L. Kok, and A.l. Chien. Power handling and temperature coefficient studies in FBAR duplexers for the 1900 MHz PCS band. In *IEEE Ultrasonics symposium*, volume 1, pages 869–874, 2000.

[20] H. P. Löbl, M. Klee, C. Metzmacher, W. Brand, R. Milsom, and P. Lok. Piezoelectric thin AlN films for bulk acoustic wave (BAW) resonators. *Materials Chemistry and Physics*, 79:143–146, 2003.

[21] H. P. Löbl, M. Klee, C. Metzmacher, W. Brand, R. Milsom, P. Lok, and F. van Straten. Piezoelectric materials for BAW resonators and filters. In *Ultrasonics Symposium*, pages 807–811. IEEE, 2001.

[22] H. P. Löbl, M. Klee, O. Wunnicke, R. Kiewitt, R. Dekker, and E. v. Pelt. Piezoelectric AlN and PZT films for micro-electronic applications. *Ultrasonics symposium*, 2:1031–1036, 1999.

[23] K. Nakamura and Y. Kawamura. Electromechanical coupling factor of $KNbO_3$ single crystal. In *IEEE Ultrasonics Symposium*, volume 2, pages 1013 –1018, 1999.

[24] K. Nakamura, H. Sasaki, and H. Shimizu. ZnO/SiO_2-diaphragm composite resonator on a silicon wafer. *Electronics Letters*, 17(14):507–509, 1981.

[25] W.E. Newell. Face-mounted piezoelectric resonators. *Proceedings of the IEEE*, 53:575–581, 1965.

[26] S. Ono, K. Wasa, and S. Hayakawa. Surface-acoustic wave properties in ZnO-SiO_2-si layered structure. *Wave Electronics*, 3:35–49, 1977.

[27] D.J. Page. A cadmium sulfide-silicon composite resonator. In *Proceedings of the IEEE*, pages 1748–1749. IEEE, 1968.

[28] S. Rey-Mermet. *Resonateurs films minces piezoelectriques utilises comme biocapteurs.* Diploma, EPFL, 2003.

[29] R. Ruby and P. Merchant. Micromachined thin film bulk acoustic resonators. In *Proceedings of the 1994 IEEE International Frequency Control Symposium*, pages 135–138, 1994.

[30] H. Satoh, Y. Ebata, H. Suzuki, and C. Narahara. An air-gap type piezoelectric composite thin film resonator. In IEEE, editor, *Proceedings of the Annual symposium on frequency control*, volume 39, 1985.

[31] T. R. Sliker and D. A. Roberts. A thin-film CdS-quartz composite resonator. *J. Appl. Phys.*, 38(5):2350–2358, 1967.

[32] Q.X. Su, P. Kirby, E. Komuro, M. Imura, Q. Zhang, and R. Whatmore. Thin-film bulk acoustic resonators and filters using ZnO and lead-zirconium-titanate thin films. *IEEE transactions on microwave theory and techniques*, 49(4):769–778, 2001.

[33] K. Tsubouchi and N. Mikoshiba. Zero-temperature-coefficient SAW devices on AlN epitaxial films. *IEEE Trans. on Sonics and Ultrasonics*, SU-32(5):634–644, 1985.

[34] R. Weigel, D.P. Morgan, J.M. Owens, A. Ballato, K. M. Lakin, K. Hashimoto, and C.C.W. Ruppel. Microwave acoustic materials, devices, and applications. In *IEEE Transactions on Microwave Theory and Technique*, volume 50-3, pages 738–749, 2002.

[35] E. Wiesendanger. Dielectric, mechanical and optical properties of orthorhombic $KNbO_3$. *Ferroelectrics*, 6:263–281, 1974.

[36] M. Zgonik, R. Schlesser, I. Biaggio, E. Voit, J. Tscherry, and P. Günter. Materials constants of $KNbO_3$ relevant for electro- and acousto-optics. *J. Appl. Phys.*, 74(2):1287–1297, 1993.

Chapter 2

Bulk Acoustic Wave Resonators

2.1 Introduction

Film bulk acoustic resonators consist of a piezoelectric plate sandwiched between two electrodes. The fundamental thickness-extensional resonance occurs when the thickness of the plate corresponds to half a wavelength, and higher order resonances occur for odd numbers of half-wavelengths of the standing wave. For large bandwidth applications, the fundamental mode resonance is best suited because the effective coupling decreases with increasing mode number (overtones). Thickness-shear modes may also be excited, although with lower resonance frequencies than thickness-extensional modes. High quality factors are obtainable with an excellent acoustic isolation that traps and confines the acoustic energy of the resonator. High quality factors and quite high coupling coefficient microwave resonators may be synthesized with piezoelectric AlN and ZnO films. The fundamental mode resonance for frequencies of 1-10GHz corresponds to film thicknesses of 6-0.3μm.

In this thesis work emphasis will be put on BAW resonators and filters working in the C- and X-band (5.8-8.5GHz): most publications focus on BAW devices in the frequency range between 1-5GHz, which are used by current GSM, UMTS, GPS, WLAN and numerous other wireless professional and consumer applications. Future applications will certainly also exploit higher frequencies. However, many issues and problems of FBAR/SMR resonators and filters that are not significant at lower frequencies, become accentuated or even prevailing when using C- & X-band frequencies: material acoustic losses, e.g. dissipated power, are expected to be greater at higher frequencies, proportional to frequency squared, the absolute thickness requirement of the individual FBAR layers are higher, e.g. electrode thicknesses are limited to approximately 50nm and the piezoelectric film thickness to less than 500nm. These constraints increase parasitic electrical resistances. Furthermore, piezoelectricity deteriorates below 500nm film thickness.

2.2 Analytical models of bulk acoustic wave resonators

There are both similarities and substantial differences between thin film resonators and conventional single-crystal resonators used at low frequencies. For most applications the thin film resonator is fabricated with lateral dimensions in excesss of 50 to 100 times the thickness and as such can be considered a one-dimensional device for the purpose of wave propagation and circuit modeling. Border effects can be neglected, and the fundamental Lamb-wave modes will be at a much lower frequency.

The nature of a specific wave type can be rather comlex even if we consider linear relationships and a homogeneous piezoelectric insulator as a propagation medium (characterized by stiffness, piezoelectric, permittivity tensor, and mass density), which is normally sufficient for practical applications.

2.2.1 1-dimensional model of thickness-extensional modes in thin piezoelectric plates

Consider a thin piezoelectric plate of thickness t with electroded major faces of area A normal to the z- or 3-direction (fig. 2.1 (a)). If its lateral dimensions are large compared with thickness, the plate can be considered as laterally infinite and laterally clamped (strain $S_1 = S_2 = S_4 = S_5 = S_6 = 0$) for plane wave propagation in the thickness direction. Similarly for an insulating dielectric medium with no electric flux leakage $D_1 = D_2 = 0$ and $\partial D_3/\partial z = 0$. These suggest that the extensive variables charge density D and strain S be chosen as independent variables, and stress T and electric field E as dependent variables [83]

$$T_3 = c_{33}^D S_3 - h_{33} D_3 \tag{2.1}$$

$$E_3 = -h_{33} S_3 + \frac{1}{\epsilon_{33}^S} D_3 \tag{2.2}$$

where c_{33}^D is the elastic stiffness at constant electric displacement, h_{33} is the piezoelectric stress constant, and ϵ_{33}^S is the clamped dielectric constant. The longitudinal displacement ξ along z obeys the wave equation for constant-D

$$\frac{\partial^2 \xi}{\partial t^2} = \frac{c_{33}^D}{\rho} \frac{\partial \xi}{\partial z^2} \tag{2.3}$$

where ρ is the mass density. The general solution for the particle displacement ξ is given by

$$\xi = \left(A \sin \frac{\omega z}{v^D} + B \cos \frac{\omega z}{v^D} \right) e^{i\omega t} \tag{2.4}$$

where $v^D = \sqrt{c_{33}^D/\rho}$ is the sound velocity, and $\omega = 2\pi f$ the angular frequency. The constants A and B can be evaluated from the boundary conditions ($T_3 = 0$ at $z = 0, t$) at the free faces using equations 2.1 and 2.4 noting that $S_3 = \partial \xi/\partial z$. For a harmonic excitation $D_3 = D_0 e^{i\omega t}$.

$$\xi = \frac{v^D h_{33} D_3}{\omega c_{33}^D} \left(\sin \frac{\omega x_3}{v^D} - \tan \frac{\omega t}{2 v^D} \cos \frac{\omega x_3}{v^D} \right) \tag{2.5}$$

By substituting equation 2.5 into equation 2.2 the electrical admittance is obtained

$$Y = \frac{i\omega A D_3}{\int_0^t E_3 dx_3} = \frac{i\omega C_0}{1 - k_t^2 \frac{\tan(\omega t/2v^D)}{\omega t/2v^D}} \tag{2.6}$$

$$\text{with } k_t^2 = h_{33}^2 \frac{\epsilon_{33}^S}{c_{33}^D} \tag{2.7}$$

$$\text{or } k_t^2 = \frac{e_{33}^2}{c_{33}^D \epsilon_{33}^S} \tag{2.8}$$

where $C_0 = A\epsilon_{33}^S/t$ is the clamped capacity of the transducer plate, and e_{33} is the piezoelectric constant. Equation 2.8 is derived when starting with the mixed independent variables strain S and electric field E for the piezoelectric relations (equations 2.1, 2.2). In principle, resonance f_r and anti-resonance f_a are obtainable from the maximum and minimum admittance using equation 2.6 and the assumption that losses are negligible, i.e. that $f_r = f_m, f_a = f_n$. f_m, f_n are defined at maximum and minimum absolute admittance, whereas f_r, f_a are defined at the frequency of zero susceptance [34].

$$Y = 0 \rightarrow \tan\frac{\omega t}{2v^D} = \infty \rightarrow f_a = \frac{v^D}{2t} \tag{2.9}$$

$$1/Y = 0 \rightarrow k_t^2 = \frac{\pi}{2}\frac{f_r}{f_a}\cot\frac{\pi}{2}\frac{f_r}{f_a} \tag{2.10}$$

In practice, because of superposed spurious responses, the frequencies of minima and maxima of admittance f_a, f_r may be difficult to identify without ambiguity. For small $k_t^2 \rightarrow f_r \approx f_a$, and the electromechanical coupling coefficient of the resonator, equation 2.10, simplifies to

$$k_t^2 = \frac{\pi^2}{4}\frac{f_a - f_r}{f_a} \tag{2.11}$$

The effective coupling coefficient of a resonator with finite electrode thicknesses, other acoustic loads, or parasitic electric loads may differ from the k_t^2 derived from material parameters. We will call effective coupling coefficient the value calculated with f_n, f_m from the absolute admittance.

2.2.2 Analytical model of resonator with finite thickness electrodes

At microwave frequencies thin film resonators are only approximately described by the admittance relation in equation 2.6. To take into account electrode metal thicknesses, and associated losses, a method using transmission line concepts and matrix algebra can be used to analyze relatively complex geometries [62, 53]. The piezoelectric plate is essentially a three port network having two acoustical and one electrical port. By solving the boundary value problem an equation for the electrical port impedance in terms of arbitrary mechanical

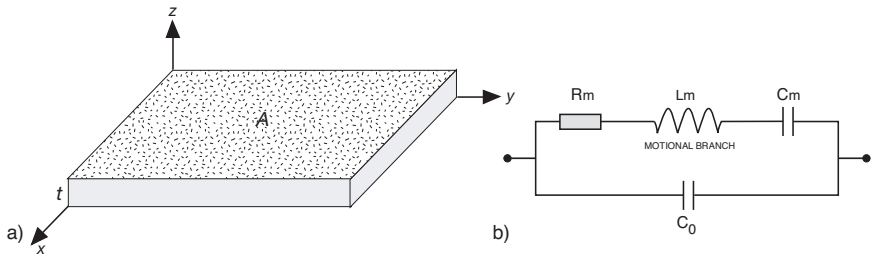

Figure 2.1: (a) Thickness mode resonator with electroded major faces of area A, and lateral dimensions much larger than its thickness t in z-direction. (b) Electrical equivalent circuit model, also Butterworth-Van Dyke model (BVD), of harmonic oscillator.

loads is obtained:

$$Z = \left(\frac{1}{iwC_0}\right)\left(1 - k_t^2 \frac{\tan\phi}{\phi} Z_{in}\right) \tag{2.12}$$

$$Z_{in} = \frac{(z_r + z_l)\cos^2\phi + i\sin 2\phi}{(z_r + z_l)\cos 2\phi + i(z_r z_l + 1)\sin 2\phi} \tag{2.13}$$

where z_r and z_l denote load impedances of the electrodes on either side of the resonator, normalized by the piezoelectric film impedance, and $\phi = \frac{\theta}{2} = \frac{\pi}{2}\frac{f}{f_p}$, $\theta = kd$ is the phase across the piezoelectric film.

For more complex geometries, as for example in the SMR (fig. 2.2), the effective load impedance of the substrate can be found from an ABCD matrix cascading of equivalent transmission line sections or by successive use of the transmission line equation:

$$Z_{in} = Z_0\left(\frac{Z_l\cos\theta + jZ_0\sin\theta}{Z_0\cos\theta + jZ_l\sin\theta}\right) \tag{2.14}$$

Here Z_{in} is the input impedance, Z_0 the characteristic impedance, θ the phase across the delay section, and Z_l the load impedance attached to the line section.

Loss in the resonator equation is modeled by a finite Q through a complex phase $\phi_{loss} = \phi_{lossless}(1 - j\frac{1}{2Q})$, or as proposed by Naik et al. [93] adding complex terms to the real material stiffness $c = c_{real} + i2\pi f\eta$ where η is the acoustic viscosity, or Nakamura and Kanbara [96] defining $c = c_{real} + i\frac{1}{Q}$.

The reflection coefficient R is defined using the impedance mismatch ratio $Z = Z_{ac,2}/Z_{ac,1}$ on the interface between two solids 1 and 2 ([83], page 70):

$$R = \frac{Z-1}{Z+1} = \frac{Z_{ac,2} - Z_{ac,1}}{Z_{ac,2} + Z_{ac,1}} \tag{2.15}$$

where the acoustic impedance $Z_{ac} = \rho \cdot V$ is defined with the product density times acoustic velocity.

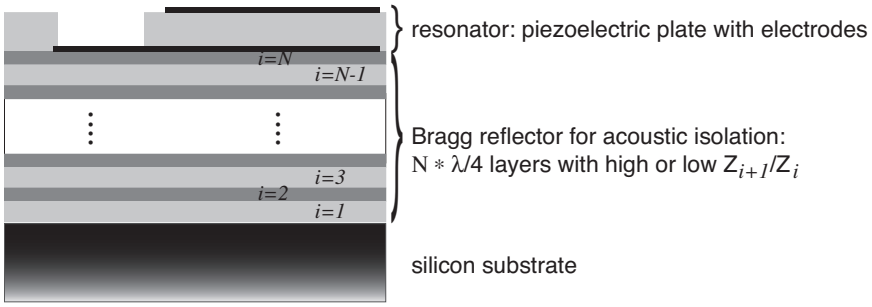

Figure 2.2: Schematic drawing of the SMR: the piezoelectric plate which is sandwiched between two electrodes, deposited onto N $\lambda/4$ layers for acoustic isolation, and supported by a silicon substrate.

Several authors proposed models for the resonator admittance simulation: Lakin [61] proposed a more general form of the one-dimensional theory for general quasi-mode composite resonators taking into account the film orientation. It uses matrix multiplication to cascade various sections. Yamada et al. [143] proposed also a formulation for the piezoelectric plate thickness vibration. Nowotny and Benes [100] formulated a general one-dimensional transfer matrix description for layered piezoelectric structures with two electrodes which connects the fundamental physical parameters at the termination surfaces as a result of the fundamental piezoelectric differential equations without using any acoustoelectrical analogies. As a consequence of the full vector description of the mechanical termination parameters, the obtained resonance-determining equations contain 3x3 matrices and allow the analysis of arbitrary crystallographic orientations of the plates within the sandwich structure. Mansfeld et al. [81, 79, 80] treated theoretically the one-dimensional case for BAW composite resonators-filters and the acoustic isolation from the substrate using quarter wavelength layers.

2.2.3 Equivalent circuit

A lumped element circuit model often used by low frequency crystal filter designers is the Butterworth Van Dyke (BVD) model shown in figure 2.1 (b). The merits of this model are the easy introduction of losses due to finite quality factors and the few parameters needed for circuit modeling. The BVD model does, however, not predict harmonic responses. The impedance of the series motional branch is defined as

$$Z_m(\omega) = R_m + i\omega L_m + \frac{1}{i\omega C_m} \tag{2.16}$$

and the admittance of the total circuit equals

$$Y(\omega) = i\omega C_0 + \frac{1}{Z_m(\omega)} \tag{2.17}$$

where C_0 is the the clamped capacity, R_m the motional resistance, L_m the motional inductance, and C_m the motional capacity. The series resonance frequency is defined at zero impedance in the motional branch at $\omega_s^2 = \frac{1}{L_m C_m}$. The parallel resonance is defined at zero admittance $\omega_p^2 = \omega_s^2 \left(1 + \frac{C_m}{C_0}\right)$

Electro-mechanical resonators are characterized by 2 quantities: the electro-mechanical coupling coefficient k_t^2 which is a measure of the ratio of stored mechanical energy to supplied electrical energy, and the quality factor Q which can be defined as of the ratio of the reversibly stored energy to the dissipated energy. The quality of a material as a medium for wave propagation is described in terms of its mechanical Q, defined as the ratio of the energy carried by a wave to the dissipated energy. At the series resonance the stored energy in the motional branch is $1/\omega_s C_m * I_{\text{rms}}^2$ and the dissipated energy is $R_m * I_{\text{rms}}^2$, where I_{rms}^2 is the current passing through the branch. The series quality factor is therefore defined in terms of the equivalent circuit

$$Q_s = \frac{1}{\omega_s R_m C_m} \tag{2.18}$$

For the characterization of measured resonators it is more convenient to use the slope of the impedance phase ϕ at series resonance. Separating equation 2.16 into resistance and reactance

$$Z_m(\omega) = R_m + i\frac{\omega}{C_m}\left(L_m C_m - \frac{1}{\omega^2}\right) = R_m + i\frac{\omega}{C_m}\left(\frac{1}{\omega_s^2} - \frac{1}{\omega^2}\right) \tag{2.19}$$

yields the impedance phase angle ϕ

$$\tan\phi = \frac{\omega}{R_m C_m}\left(\frac{1}{\omega_s^2} - \frac{1}{\omega^2}\right) \tag{2.20}$$

The slope of the phase at the series resonance is then

$$\left.\frac{\partial \tan\phi}{\partial\omega}\right|_{\omega_s} = \frac{2}{\omega_s^2 R_m C_m} \tag{2.21}$$

which can be used to define Q_s in terms of the impedance phase slope using equation 2.18 and knowing that at $\omega_s : \phi \to 0$

$$Q_s = \frac{\omega_s}{2}\left.\frac{\partial \tan\phi}{\partial\omega}\right|_{\omega_s} = \frac{\omega_s}{2}\left.\frac{\partial\phi}{\partial\omega}\right|_{\omega_s} = \frac{f_s}{2}\left.\frac{\partial\phi}{\partial f}\right|_{f_s} \tag{2.22}$$

The same equation can equally be used to determine the quality factor at the parallel resonance frequency ω_p by measuring the phase slope at that frequency.

The quality factor Q_s may also be expressed as a function of the full width at half maximum (FWHM) of the conductance peak at ω_s. Expressing equation 2.17 in terms of conductance and susceptant $Y(\omega) = G + iB$ yields

$$Y(\omega) = \underbrace{\frac{R_m}{R_m^2 + \frac{\omega^2}{C_m^2}\left[\frac{1}{\omega_s^2} - \frac{1}{\omega^2}\right]^2}}_{G} + i\,\omega\underbrace{\left[C_0 - \frac{\frac{1}{C_m}\left[\frac{1}{\omega_s^2} - \frac{1}{\omega^2}\right]}{R_m^2 + \frac{\omega^2}{C_m^2}\left[\frac{1}{\omega_s^2} - \frac{1}{\omega^2}\right]^2}\right]}_{B} \tag{2.23}$$

The maximum of conductance is found at the series resonance frequency

$$\omega = \omega_s :\rightarrow G_{\max} = \frac{1}{R_m} \tag{2.24}$$

For a resonator with a high quality factor, the expression in brackets for G in equation 2.23 in proximity of ω_s simplifies to

$$\left[\frac{\omega^2 - \omega_s^2}{\omega_s^2 \omega^2}\right]^2 = \frac{1}{\omega_s^4 \omega^4}\left[\underbrace{(\omega - \omega_s)}_{\Delta\omega}\underbrace{(\omega + \omega_s)}_{\approx 2\omega_s}\right]^2 = \frac{4\Delta\omega^2}{\omega_s^2 \omega^4} \tag{2.25}$$

Substituting this equation back into equation 2.18 we obtain for G

$$G = \frac{1}{R_m\left(1 + \frac{4\Delta\omega^2 Q_s^2}{\omega^2}\right)} \tag{2.26}$$

and substituting $G_{\max}$ we can express the quality factor as

$$Q_s = \frac{\omega}{2\Delta\omega}\left(\frac{G_{\max}}{G} - 1\right) \tag{2.27}$$

Using the definition of FWHM one finds finally

$$Q_s = \left.\frac{\omega}{\mathrm{FWHM}_G}\right|_{\omega_s} \tag{2.28}$$

which is valid for a resonator with high quality factor ($Q_s > 10$). The two resonator models can be linked by doing a mathematical expansion of equation 2.6 about the series resonance to obtain another expression of the coupling coefficient

$$k_t^2 = \frac{\pi^2}{8}\frac{C_m}{C_0} \tag{2.29}$$

2.2.4 2-dimensional models

A finite differences formulation of the general two dimensional coupled piezoelectric wave equation was derived by Lakin [48, 63, 55, 52, 64] to investigate plate waves which cause spurious resonances.

The transverse waves are generated at the electrode edges, which presents a large gradient in force in the transverse direction, and where the discontinuity produces an uncompensated transverse motion via the Poisson effect. The transverse wave energy thus generated may propagate away from the resonator (un-trapped and lower Q) or if external propagation is cut-off or limited in the plate then the energy is confined to the electrode area and is trapped (high Q). Plate waves will propagate throughout the plate reflecting off any material or electrical discontinuity. The trapped transverse wave components are generally weak for the higher transverse mode numbers and the subsidiary resonances are unequally

spaced in frequency (an-harmonic) because the velocity of the transverse wave is dispersive. Plate waves generated at the electrode edge propagate in the plate and produce a normal displacement current that is summed by the electrode area. The transverse periodic variations of displacement current from the plate waves is averaged to a relatively small value by large electrodes. In contrast, the uniform displacement current of the primary thickness mode increases in total current with electrode area. The effect of the plate waves is therefore diminished by large diameter-to-thickness ratios.

Typical width-to-thickness ratios for AlN resonators used in 50Ω filters might be as high as 100:1 creating a large mode number for the lateral resonance. The result is a spurious resonance ripple superimposed on the desired resonator impedance response.

Results show that when the width-to-thickness ratio of the resonator approaches 200, the resonance is nearly that of a one-dimensional resonator. Smaller area resonators have proportionally higher degrees of plate mode propagation and therefore more spurious resonances. Simulation results of 60:1 and 240:1 width-to-thickness ratio AlN resonators about the primary thickness mode resonance are compared. The many spurs in the former resonator are due to overtones of standing plate resonances caused by reflections from the abrupt edge of the plate. The latter shows in contrast the decrease of spurious resonances when the thickness-to-width ratio is increased to 240:1. In both cases, the plate is abruptly terminated beyond the electrode region to maximize plate wave reflections for analysis purposed. Simulations also show that below a 20:1 width-to-thickness ratio large ripples result using AlN resonators with both Al or W electrodes. When comparing these electrodes with the same thickness-to-width ratio of 72:1, less ripples are observed with the W electrode. The use of an AlN/SiO_2 reflector in SMR, as opposed to the free standing membrane in the FBAR, also reduces significantly the plate wave response.

2.3 State of the art of BAW resonators

The minimum requirements for a thickness mode electro-acoustic BAW resonator are parallel and reflecting surfaces for energy trapping, a means of exciting the acoustic wave, e.g. using a piezoelectric film, and a set of electrodes which are photolithographically defined metal film patterns used to apply the electric field.

The first thin film BAW devices emerged in the late 1960's: a sputter deposited piezoelectric ZnO film on sapphire or quartz substrates served as delay line transducer [20], an evaporated thin film piezoelectric CdS on quartz substrate [125], respectively single crystal silicon substrate [105], led the way for the composite resonator, and piezoelectric AlN thin film acoustic transducers were fabricated by evaporation of Al in a dissociated N_2 atmosphere [123]. These first resonators operated at a fundamental mode frequency of some hundred megahertz and the figures of merit, e.g. quality factor Q in excess of 1000, coupling factor k_t^2 of 6.2%, were very high (ZnO [10]).

The extra layers in composite resonators, that are piezoelectrically inactive and act as the mass loading layer on the FBAR, lower the effective coupling coefficient. This inactive layer may however increase the overall quality factor of the resonator if the acoustic quality

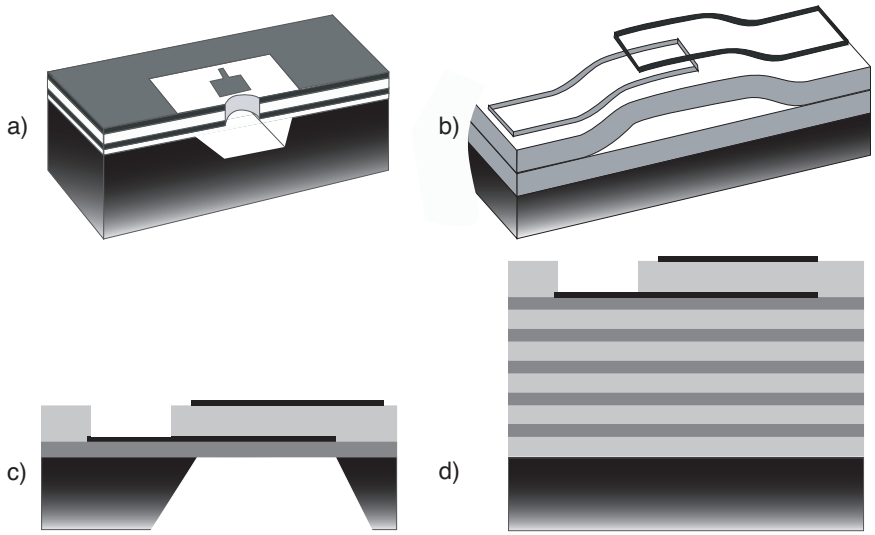

Figure 2.3: 4 different types of thin film bulk acoustic resonators: (a) through-the-hole under-cut FBAR, (b) air-gap or bridge under-cut FBAR, (c) edge-supported FBAR, and (d) solidly mounted resonator SMR.

factor of the inactive layer is superior to the piezoelectric film material. Overmoded AlN resonators on sapphire, $LiNbO_3$ and quartz substrates can reach for example Q's as high as 70000 [43], because most of the energy is stored in the substrate and not in the transducer which only occupies a small fraction of the resonator volume.

Although conventional thickness mode resonators may be operated at odd order overtones, the effective electromechanical coupling coefficient decreases proportional to the overtone order. Early attemps at composite resonator development employed CdS films, which subsequently resulted in monolithic filter devices. Resonators in these earlier works were essentially overmoded. However, for many other applications a single response is desired, and that requires fundamental mode resonators.

The four possible types of thin film bulk acoustic wave resonators are schematically presented in figure 2.3. These are the bulk micromachined composite (AlN/Si or AlN/SiO_2 membrane) or edge-supported (AlN membrane only) resonator (c), the through-the-hole under-cut FBAR with no defined etch cavity (a), the air-gap or also bridge under-cut FBAR with a predefined etch cavity (b), and the solidly mounted resonator SMR (d) which was only presented in 1995 in contrast to the first 3 which were presented in the beginning of the 1980's.

The requirements on the piezoelectric candidate material used in the FBAR/SMR, which are basically large width-to-thickness ratio devices, are thin films in the range of 0.1 to 10μm with a high degree of orientation and large piezoelectric coupling. Additional material requirements include high resistivity, good breakdown strength, low dielectric permitivity, and reproducibility of film deposition. Materials that satisfy a number of these requirements

include CdS, ZnO, AlN, $LiNbO_3$, $LiTaO_3$, $KNbO_3$ and PZT. While CdS films have inherently a low electromechanical coupling, thin film deposition of $LiNbO_3$, $LiTaO_3$ and $KNbO_3$ suffer from stoichiometry control. Oriented films of PZT used in SMR exhibited very low quality factors. Although all these materials have been investigated in the past few decades ZnO and AlN have attracted the most attention for FBAR applications. Magnetron sputtered ZnO and AlN films, which are deposited on a variety of substrates including silicon, metallized silicon and gallium arsenide, meet most of the material requirements described earlier. They have mostly been used for the piezoelectric layer over the past two decades. The predominating deposition method was reactive rf or dc magnetron sputtering, because it allows for a much lower process temperature in the range of 200-500°C which is CMOS compatible, lower than the temperature required by alternative techniques such as CVD [142, 56] or molecular beam epitaxy [29]. AlN can be synthesized by MOCVD techniques at temperatures as low as 400°C, however no good piezoelectric properties were reported for such films [119].

AlN films are of significant interest for high-frequency bulk-acoustic wave devices because of their high acoustic wave velocity and fairly high electromechanical coupling coefficient, but also chemical stability favoring eventual integration with other device fabrication techniques. The acoustic wave velocity v^D is proportional to the thickness of the piezoelectric resonator plate at a given resonance frequency. The piezoelectric volume, where the resonance is established, is therefore larger for high v^D materials which may increase the effective coupling of the resonator. Another important advantage of maximizing the thickness of the piezoelectric layer is due to the thickness dependency of the piezoelectric coefficient, as for example observed in AlN thin films [82].

2.3.1 Thin film bulk acoustic resonator obtained by surface micromachining

The thin film bulk acoustic resonator technology employs an additive way to realize high frequency resonators, contrary to the crystal resonators. The latter are thinned from a thick bulk crystal to the required thickness, whereas the former are grown or deposited until the desired thickness is achieved. The basic ideas and technologies of FBARs (fig. 2.3 a)-c)) were developed in the beginning of the 1980's. The bulk micromachined FBARs were the first solution to realize thin film resonators because of the ease of fabrication of the membrane and the c-axis growth of the wurtzite ZnO and AlN on the monocrystalline Si or GaAs substrate. Surface micromachined FBARs were developed shortly afterwards driven by the prospective compatibility with IC processing.

The current nomenclature has its roots from; thin film resonator TFR [66], film bulk acoustic resonator FBAR [137], or semiconductor bulk acoustic resonator SBAR [8].

Bulk micromachined FBARs

FBARs were the first type of additive bulk acoustic wave (BAW) resonators presented by three different groups in 1980/81: Lakin and Wang [58], Grudkowski et al. [23, 24]

and Nakamura et al. [97]. They fabricated ZnO/Si *composite* fundamental mode *bulk* micromachined resonators and *acoustically* coupled resonators filters, but also ZnO/SiO_2 *temperature compensated* resonators. ZnO and AlN were both used as piezoelectric material. Silicon bulk micromachining (anisotropic etching of the silicion substrate using heavily boron-doped Si as etch stop) was used to release the composite ZnO/Si membranes (6μm silicion thickness) on which the resonator was defined using patterned aluminum electrodes. The p^+ layer acts as seed layer for the AlN growth, etch stop, bottom electrode since it is a good conductor, and as compensation for the temperature coefficient of frequency (TCF, p^+ Si 8ppm/K). This last point was demonstrated using an AlN/Si composite membrane structure with a fundamental mode frequency at 330MHz and a TCF of less than 4ppm/K over the temperature range from -20 to +120°C [140].

FBAR configurations include edge-supported resonators, in which the piezoelectric layer is supported on its edge, and membrane-supported composite resonators (c.f. figure 2.3 c). Both Si and SiO_2 have been used as membrane materials for Si-based composite FBARs, while AlN and SiO_2 have been used in GaAs based FBARs. Edge-supported membranes may be realized (Lakin et al. [66] in 1982) by removing the supporting p^+ Si membrane material.

Surface micromachined FBARs

Longitudinal and shear AlN resonators on an Al/GaAs substrate were proposed in 1983 by using wafer top side planar processing only [42]. The air interface underneath the resonator was achieved by removing the substrate locally with an undercut etch (c.f. figure 2.3 a). In this example the bottom electrode contact is realized with capacitive coupling over a large surface area.

A new approach with *surface micromachining* was proposed two years later by Satoh et al. [115, 116]: A very thin air gap under each self-supported resonator for acoustic insulation was fabricated by using a sacrificial layer (c.f. figure 2.3 b). The resonator size and the required lateral space are almost identical, which results in very small die areas. Compared with the bulk micromachined approach, the wafers are not rendered fragile, and only single side mask alignment is necessary. Furthermore, there are no through wafer holes which interfere with integrated circuits (IC) on the same wafer, so FBARs can be fabricated on top of premanufactured ICs. The Au/Ti/ZnO(2.6μm)/Au/Ti resonator was deposited on top of a flat silicon nitride passivation film, using a 100nm thick ZnO or SiO_2 sacrificial layer. These resonators were not only integrated with bipolar ICs as one-chip oscillator for 400MHz but composite SiO_2/ZnO/SiO_2 FBARs were also integrated as voltage controlled oscillator (VCO). This new air-gap structure enables thin film resonators to be fabricated easily on a multitude of substrates: Si or GaAs substrate, glass, ceramic or SOS substrates, and on a flat dielectric passivation film on top of an IC. The characteristic properties of such early surface micromachined air-gap resonators were very promising: A FBAR composed of SiO_2/Al/ZnO and working at 2GHz had a Q of 300 and a k_t^2 of 5% [144], and AlN based air-gap FBARs exhibited Q's also in the range of 500 and k_t^2 between 5.5-6.5% [51]. Thin film stacked crystal filters using the same technology achieved insertion losses of 2dB.

Seabury et al. [117] fabricated low stress ZnO FBARs by PLD using dry surface machining to avoid stiction and low yield. The fabricated multi-pole filters yielded -7dB insertion loss and 28dB rejection at 1.5GHz.

An alternative method for air-gap resonators, is to use wafer bonding to fabricate a free standing membrane which avoids the use of wet etching to release the membranes and related stiction problems [78].

Composite resonators are expected to have a higher Q, since the single-crystal Si membrane is likely to have a higher Q than the sputtered AlN or ZnO [59]. The composite structures of FBARs provide temperature stabilization by utilizing materials with alternately positive and negative temperature coefficients. Temperature compensation to zero ppm/K with double sided SiO_2 layer on ZnO FBARs were demonstrated [97, 89, 120, 90, 118]. SiO_2 has a positive temperature coefficient of elastic constants and is easily fabricated in thin film form. The drawback of composite resonators is their lower coupling factor because only a fraction of the resonator is active. Therefore applications requiring large filter bandwidth are necessary realized with edge-supported or air-gap FBARs.

Control over film stress in the piezoelectric AlN and ZnO films was inevitable as soon as edge-supported and air-gap FBARs were realized. The successful demonstration of these FBARs, and therefore film stress control inferior to a few 100MPa which prevents film rupture or film buckling, was accomplished in the 1980's. The main stress controling parameters pressure, N_2/Ar gas mixture and substrate bias are all related to ion bombardment of the growing AlN film (c.f. paragraph 2.4.2).

2.3.2 Solidly mounted resonator

The SMR technology uses adjacent quarter-wavelength layers of materials, having large effective transmission-line impedance ratios, to form a reflector between the resonator and substrate (Newell [98]). The result is an acoustical isolation of the resonator from the substrate which produces a high-Q resonator rather than a low-Q transducer. Both free and clamped interfaces can be obtained using the quarter wavelength thick transformation layers.

The concept of the SMR was re-introduced by Lakin et al. [54, 57] in 1995, and by a patent of Motorola [17]. The former proposed SiO_2/AlN, SiO_2/Si_3N_4, respectively W/SiO_2 quarter wavelengths (wavelengths are referred to the center frequency of the resonator in this paper) layers for the acoustic isolation. Reflectors consisting of conductive materials, such as W/SiO_2, need to be patterned in complex filter structures to avoid capacitive coupling and other parasitic effects between resonators through the mirror [36]. Acoustic reflectors made by CVD tungsten and PECVD SiO_2 were for example patterned using a CMP method [19].

In addition to the above mentioned materials used for acoustic reflectors, SiO_2/ZnO reflectors for ZnO based SMR were fabricated [101], and a comparison of 3 different acoustic reflectors using AlN/SiO_2, Al/Ti and Ta_2O_5/SiO_2 yielded the best overall resonator performance on the SiO_2/AlN reflector [106].

The use of SiO_2 in most proposed reflectors is a result of its positive TCF, which is

of opposite sign compared to all other mentioned reflector materials, of its low acoustic impedance, and of its high mechanical quality factor. By adding additional SiO_2 below, or on top, of AlN and ZnO based SMR, the TCF can be engineered to zero, not without reducing the coupling coefficient though [101].

SiO_2/AlN and SiO_2/W reflectors have attracted the main attention and have yielded SMRs with very high quality factors: Lakin et al. [54] demonstrated for example in 1995, at the same time as they proposed the theoretical model, SiO_2/AlN SMR based ladder filters working at 1.6GHz with 2.9dB insertion loss and 40dB rejection for use in GPS systems.

The model simulation [54, 98] (c.f. also paragraph 2.2), which takes into account all layers used for the SMR, yields a lower *effective* coupling for the SMR when compared to the FBAR because a fraction of the acoustic energy is stored outside the resonator in the reflector. Furthermore, the reflection characteristics of a quarter wavelength reflector using a 2:1 (2.8 for AlN:SiO_2), respectively a 10:1 (7.6 for W:SiO_2) acoustic impedance ratio yields a total reflection (reflection coefficient $R = 1$) over a wider frequency, as well as a slightly higher coupling coefficient for the high impedance ratio couple [36]. The particle displacement after the 3^{th} reflector pair is reduced to less than 10% of the displacement of the first reflector layer, assuming a 10:1 impedance ratio.

Unlike the FBAR, the SMR has the advantage of being less sensitive to film stress. Furthermore, the SMR fabrication requires less process steps, i.e. the sacrificial layer definition, VIA opening to access the sacrificial layer and sacrificial layer removal are avoided. Another important effect of the reflector layers, as demonstrated by Newell [98], is the partial lateral stiffening of the piezoelectric plate that minimizes displacement associated with plate wave generation and consequent spurious resonances normally observed in free plates (FBAR). Nevertheless, plate waves responsible for spurious resonances around the main thickness mode resonance may still occur. These were for example optically observed by laser probing [133, 132] on circular and square 1GHz SMR, using 2 pairs of reflective W/SiO_2 layers.

The main difficulty with SMRs is at low frequencies obtaining films of the required thickness in a finite period of time such that the process is economical, and at high frequencies the requirement of a higher degree of absolute film thickness control. Furthermore, when comparing the SMR to the FBAR, the thick acoustic reflector deposited on the substrate makes interconnects to underlying ICs more complicated.

2.4 Review on AlN thin films for BAW applications

2.4.1 AlN properties

Aluminum nitride (AlN) is a III-V compound with a wurtzite crystal structure. The lattice constants are $a = 3.112\mathring{A}$, $c = 4.982\mathring{A}$. AlN has some outstanding physical properties that have attracted much interest [129]: AlN has a wide band gap of 6.2eV. Its hardness (stiffness constants slightly inferior to those of diamond films) and low density 3260kg/m^2 result in a very high longitudinal ultrasonic velocity v_{LA} of 11550m/s [5, 4]. This and the low acoustic losses make AlN preferable over ZnO at frequencies higher than 5GHz for BAW

Table 2.1: Physical properties of aluminum nitride [135].

Property		Unit	Value
Density	ρ	kg/m^2	3260
Elastic stiffness	c_{11}^E	$10^{11}N/m^2$	3.45
	c_{33}^E	$10^{11}N/m^2$	3.95
	c_{12}^E	$10^{11}N/m^2$	1.25
	c_{13}^E	$10^{11}N/m^2$	1.20
	c_{44}^E	$10^{11}N/m^2$	1.18
Piezoelectric constant	e_{31}	C/m^2	-0.58
	e_{33}	C/m^2	1.55
	e_{15}	C/m^2	-0.48
	d_{33}	$10^{-12}C/N$	5.53
Dielectric constant	ϵ_{11}^S	$10^{-11}F/m$	8.0
	ϵ_{33}^S	$10^{-11}F/m$	9.5
Thermal expansion	α_{11}	10^{-6} 1/K	5.27
	α_{33}	10^{-6} 1/K	4.15

applications.

The elastic, dielectric and piezoelectric tensor constants of epitaxial thin film AlN grown by MOCVD on Al_2O_3 and Si substrates were determined using SAW characterization [136, 134, 135], respectively by Brillouin light scattering on dc reactive sputtered AlN films deposited on Si_3N_4/Si substrates [5, 4] (c.f. table 2.1). The films grown by MOCVD had an oxygen content of approximately 1-5% [135], which might explain why recent results from [77, 19, 82] present a higher coupling coefficients (k_t^2=7.8-9.6%) than the calculated value of 6.4% using values from table 2.1 (c.f. paragraph 2.4.2, page 39 for influence of oxygen in AlN films).

The high thermal conductivity of 3.2W/cmK (Si: 1.5W/cmK, Al: 2.36W/cmK) allows for high power operation [38], the high chemical stability and a reasonable thermal match to Si and GaAs, also makes AlN an attractive material for semiconductor and MEMS devices. The index of refraction is 2.15. The electric breakdown field is very high with 5MV/cm as well as the electrical resistivity $5 - 6\ 10^{13}\Omega$cm [139]. AlN has a resistance to high temperature in air up to at least 1500°C, a decomposition temperature of 2490°C [31], and a melting point of 2800°C [87].

The high ultrasonic velocity, a low acoustic loss and a fairly large piezoelectric coupling factor are reasons why AlN thin films have drawn attention as one of the more promising piezoelectric materials for the generation and detection of surface and bulk acoustic waves. Furthermore, on the basis of its superior optical qualities AlN has been considered favorably for optical waveguide and for acousto-optic applications.

The clamped piezoelectric constant $d_{33,f}$ determines together with the stiffness constant and the dielectric permittivity the electromechanical coupling coefficient of the film. Numerous reports on the clamped piezoelectric constant of AlN film state scattered values within -3.5 and +5.2pm/V, which are summarized in table 2.2.

Table 2.2: Reported values of the piezoelectric constant d_{33} for AlN thin films.

Deposition method	Substrate	Piezoelectric constant	Reference
epitaxial film		[pm/V]	
MOCVD epitaxial	(0001) Al_2O_3	d_{33}=5.53	[135]
(002) textured films			
rf MSP	Si	d_{33}=3.2	[146]
rf MSP	WC-Co	d_{33}=1.7	[146]
rf MSP	SiO_2/Si	d_{33}=1.6-2.3	[84]
ab-initio calculation		d_{33}=6.72	[37]
pulsed dc MSP	Pt/Ta/SiO_2/Si	$d_{33,f}$=-3.9	[15]
rf MSP	Ru/Ti/SiO_2/Si	$d_{33,f}$=-3.5 to +4.2	[113]
PECVD/LACVD	SiO_2/Si	$d_{33,f}$=3.2/4.0 $\rightarrow d_{33}$=5.6	[25]
pulsed dc MSP	Pt/Ta/SiO_2/Si	$d_{33,f}$=3.4	[13]
pulsed dc MSP	Pt/Ta/SiO_2/Si	d_{33}=3.7	[14]
pulsed dc MSP	Pt/Ti/SiO_2/Si	$d_{33,f}$=5.15 $\rightarrow d_{33}$=6.8	[82]

The magnitude of d_{33} was strongly influenced by the electrode material and process conditions. The most important parameter determining the piezoelectric coefficient d_{33} (c.f. paragraph 2.4.2 on page 35 and 38) was the substrate potential during MSP deposition which is directly responsible for the ionic bombardment of the growing film.

2.4.2 AlN thin film growth

Growth methods

Growth of nitrides is typically oriented along a polar axis of the material, i.e. c-axis normal to the substrate surface. This orientation occurs on many different substrates, even if the substrate is amorphous (Hellman [30]). C-axis orientation can be changed though from normal to in-plane by adding H_2 to the N_2 sputtering gas [28] or increasing the particle bombardment [26].

AlN thin film growth has been reported by thermal evaporation [123], chemical vapor deposition CVD [56, 142], metal-organic CVD [134, 119], ECR Dual-ion beam or molecular-beam epitaxy MBE [29, 103], pulsed laser deposition PLD [74, 139], rf diode sputtering [99], r.f. [121, 122, 124] and d.c. [28, 140, 99, 60] magnetron sputtering (MSP), and dual ion beam sputtering [31, 103]. Magnetron sputtering is a relatively inexpensive and simple method for film depositions on large substrates and can easily be scaled up for volume production.

Noreika et al. [99], 1969, employed reactive rf diode sputtering to deposit AlN films on Si, sapphire, SiO_2 and tantalum covered substrates. The substrate temperature was 900°C, the gas mixture was Ar-N_2 and the base vacuum was $< 10^{-9}$T. These films were (002) textured with an average grain diameter of 60nm. The resistivity was measured as

$10^{13}\Omega$cm, the relative dielectric permittivity as 8.5, and the dissipation factor as <0.5%. Rutz [114] reports in 1976 on the growth of epitaxial AlN by reactively rf sputtering at 1000°C on (111) tungsten and (0001) sapphire substrates, and the piezoelectricity of rf sputtered epitaxial AlN on (0001) sapphire substrates was shown in 1974 by Shuskus et al. [124] using a SAW delay line.

The reactive diode sputtering technique was replaced by reactive rf or dc planar MSP in the beginning of the 1980's because of its higher deposition rate and lower target voltage. In 1998 Jagannadham et al. [35], as well as Dubois and Muralt [15, 13] reported on pulsed dc MSP, which reduces the risk of arcing. The following paragraphs summarize the process details and relevant AlN film properties measured in those early papers. The process details up to the present date have not been significantly modified.

Shiosaki et al. [122, 121, 123] report in 1980 on either highly textured or epitaxial (002) AlN films with a FWHM rocking curve of less than 3° grown using reactive rf planar MSP (4" pure Al target, Ar-N_2 gas with pressures of 3-10mT) on sapphire, glass, Si without or with an oxide, nitride or gold film, and substrate temperatures as low as 50-500°C. Piezoelectricity was demonstrated with SAW filters. The FWHM rocking curve values decrease from 100 to 200°C substrate temperature and thereafter remain constant up to 500°C.

Wang and Lakin [140, 60, 141] published in 1981-83 in detail their reactive AlN dc planar MSP process (5" target size, 0.4-4mT pure N_2, 200-500°C, $5\,10^{-8}$T base pressure), emphasizing the importance of a low oxygen content in the AlN film (O_2<0.5ppm in N_2 sputter atmosphere), and use process control for the film stress control. X-ray results show the highly oriented structure with the c-axis parallel to the surface normal of the substrate. Si, Al film, Ta sheet, and sapphire were used as substrates. A rocking curve FWHM for AlN/Si of approximately 2.1° was measured. Composite and edge-only supported plate configurations (FBAR) are presented showing piezoelectricity: a composite resonator working at the fundamental frequency of 0.3GHz exhibited a coupling factor k_t^2 of 0.06% and a quality factor of 7300. The third overtone exhibited 1500 for the quality factor and a coupling of 0.36%. Note that the overtone coupling is higher than the fundamental in accordance with the composite resonator theory. FBAR membranes (edge supported) obtained by removing the p^+ layer were flat, indicating stress control to a few hundred megapascals or tensile stress, and exhibited a Q of 1200 and a k_t^2 of 1.1%. The TCF was -20ppm/K for a resonator working at a frequency of 0.8GHz. Longitudinal and shear AlN resonators were proposed on an Al/GaAs substrate by using wafer top side planar processing only [42]. The same group demonstrated in 1989 both bulk- and surface micromachined FBARS and SCF [51]. A quality factor of 300-500 and a coupling coefficient of k_t^2 5.5-6.5% characterized these AlN based FBARs. To reduce the partial pressure of water and oxygen during the sputtering process, they conducted reactive rf magnetron sputtering in a ultrahigh vacuum system ($5\,10^{-10}$T) with a load-lock. The sputter pressure was 4mT. A k_t^2 of 6.4% is reported using 40% N_2 and a substrate temperature of 150°C. Using 275°C and 20%N_2, a material k_t^2 of 7.5% was attained. Strain control is realized by changing the N_2:Ar ratio. Wafer up to 6" size could be handled [85].

Ruby and Merchant [111] produced perfectly textured (002) AlN films on Mo by reactive

rf MSP (5mT , 1:1 N_2:Ar) in a vacuum chamber fitted with a load lock system to achieve a base pressure of 1 10^{-8}T which reduces the oxygen contamination. The rocking curve FWHM is 3.3° and the films show low stress $< \pm$200MPa.

Summarizing the above paragraphs, it can be concluded that high quality, piezoelectric, purely (002) textured AlN films with a narrow rocking curve FWHM can be grown on Si, GaAs, sapphire and metallized substrates. Prerequisites are reactive rf or dc planar magnetron sputtering in a pure Ar-N_2 atmosphere using a high purity aluminum target, a low oxygen and low water contamination inside the process chamber and a substrate temperature in excess of 200°C. Film stress, which has to be limited to a couple of hundred megapascals for air-gap or edge-supported resonators, may be controlled by modifying the Ar-N_2 mixture, gas pressure or ion bombardment as will be discussed below.

Possible substrates and their influence on the growth

(002)-textured AlN was grown epitaxially on various monocrystalline substrates, e.g. on sapphire by MOCVD [135] and PLD [139], and on (111) monocrystalline tungsten [114]. Rocking curve FWHM as narrow as 0.21° were measured [139].

For the first composite FBARs, (002) textured AlN was directly grown onto monocrystalline Si and GaAs substrates. Al electrodes were post-deposited on top of the AlN film and from the backside, after p^+ Si removal, for the bottom electrode.

Growth of AlN on electrodes and not only single crystal Si or GaAs substrates became an unavoidable issue as soon as air-gap FBARs, SCF and SMR devices started emerging. Al (111) was the material of choice starting from 1981 [140, 21], later also AlCu2%/Ti [126] and AlSi1% [78] was employed. In the 1990's Pt, Mo, Ti, Hf, W, Ru/Ti [113] and Cr [40] were proposed and developed as bottom electrodes for AlN. FBARs at microwave frequencies require low parasitic electric losses. This restricts the use of metals to Al (2.65), Mo (5.3), W (5.3), Pt (10.5), Ir (4.7), Au (2.2), Cu (1.7), Ru (7.1) and Ag (1.59), where the electric resistivity is given in parenthesis in units of $\mu\Omega$cm. Hf (33), Cr (12.5) and Ti (39) possess too high a resistivity. The need of a high ultrasonic phase velocity is a further requirement and rules out the use of Au and Ag which have velocities below 4000m/s. Ru with 7100m/s, Al with 6500m/s, Mo with 6400m/s, Ir with 5560m/s, W and Cu with 5200m/s, and Pt with 4230m/s are therefore the ideal choices from the mechanical and electrical point of view. The electrical resistivities of thin film electrodes will have higher than bulk values due to crystal lattice imperfections. The sound velocity[1] [2] is calculated with material data from [73].

The growth of (002) textured AlN films are strongly affected by the various types of substrates: on (111) Al, Pt or Ir the AlN orientation has excellent quality, because the hexagonal AlN structure matches well with the Al, Pt or Ir (111) plane (Zhang et al. [145]).

Perfectly (002) textured AlN films with a FWHM rocking curve of 3.3° were obtained

[1] sound velocity in [110] direction in bcc crystals is $v_{l,[110]} = \sqrt{\frac{c_{11}^{D\,\prime}}{\rho}} = \sqrt{\frac{c_{11}^D + c_{12}^D + 2c_{44}^D}{2\rho}}$ [3], page 83

[2] sound velocity in [111] dir. in ccp crystals $v_{l,[111]} = \sqrt{\frac{c_{33}^{D\,\prime}}{\rho}}$ with $c_{33}^{D\,\prime} = \left(\frac{1}{3}c_{11}^D + \frac{2}{3}c_{12}^D + \frac{4}{3}c_{44}^D\right)$

on Mo bottom electrodes [111, 69, 112]. Mo, as well as W, has a body-centered cubic (bcc) structure that grows preferentially in (110) direction. Unlike the (111) oriented cubic close-packed (ccp) structure, the (110) texture results in a rectangular arrangement of the atoms at the surface which is not compatible with hexagonal AlN structure and may complicate (002) AlN nucleation (c.f. paragraph 2.6.3). Such nucleation problems and hindered c-axis growth were observed on Mo but not on Si, SiO_2 and Pt (111) coated Si substrates [71]. Mo electrodes for AlN growth were studied and FBARs with k_t^2=5.6% demonstrated. W and Mo are more easily wet etched, compared to Pt, and have better acoustic wave propagation properties due to the higher acoustic velocity.

AlN film growth was compared on Pt, Al, Ti and Hf electrodes using a reactive pulsed dc magnetron sputtering process. It was observed that the substrate rf induced bias or self-induced bias due to pressure or Ar:N_2 mixture, and hence ionic bombardment on the substrate has a major influence on film properties like film stress and piezoelectricity [14, 12]. No correlation between the piezoelectricity and the electrode/AlN lattice misfit was observed. Unfortunately, the crystalline quality, e.g. rocking curve FWHM, of the electrodes was not investigated which plays a major role in aligning the c-axis of the growing AlN film (c.f. paragraph 2.4.2 on page 38).

Films of AlN with a thickness of 100nm, grown by MBE on (0001) Al_2O_3, are dominated by the presence of grains with the primary orientation, aligned as (0001)AlN||(0001)Al_2O_3. The almost complete domination of this orientation is rather surprising, since an initial 25-nm thick film was found to have a number of different crystallographic alignments. The misoriented AlN grains persist at the AlN/Al_2O_3 interface in the thick AlN film. These small grains were not observed to propagate more than a few nanometers away from the interface, c.f. figure 2.4. The observation of the alignment of the 100nm-thick film suggests that islands of AlN, that are aligned with the primary orientation during the initial stages of growth, grow faster than the misaligned grains. This observation is consistent with the microstructure of the initial AlN film, where grains of AlN with the primary alignment were found to be generally larger in size than grains of other orientations [29].

AlN thin films growth, always exhibiting the preferential (002) texture, is possible on a large number of various mono-crystalline, textured and amorphous substrates. Different signs and magnitude of the piezoelectric coefficient of AlN films deposited on Ru/Ti electrodes with differing surface/interface properties seem to suggest that the relative fraction of polarization directions (up or down) depends on the substrate surface. Another explanation for different magnitudes of the piezoelectric coefficient as a function of film thickness may be the random crystal orientation during initial growth (25nm) which then becomes predominantly (002) with increasing thickness. Another reason, namely plane tilt distribution inherited from the substrate during initial film growth, which plays a major role for the magnitude of the piezoelectric coefficient, will be discussed below.

The above paragraphs may be summarize as follows: Different mono-crystalline and polycrystalline metal covered substrates may be used for (002)-textured AlN film growth. The cubic-close-packed (ccp) (111) texture of e.g. Pt, Al and Ir, or hexagonal metals like Ti and Ru favor (002)-textured AlN growth because both have the same symmetry. Body-centered cubic (bcc) metals, e.g. Mo and W grow preferentially with a (110) texture that

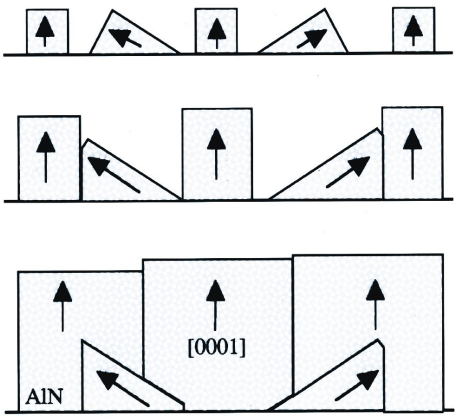

Figure 2.4: Schematic growth of AlN film on sapphire. The preferred and faster growth direction along [0001] AlN dominates the film microstructure, misoriented grains are localized on the interface region [29].

has a rectangular arrangement of atoms at the surface which might inhibit or make c-axis AlN growth difficult.

Importance of ion-bombardment on crystalline structure

The energy delivered to the growing AlN film through film bombardment by energetic species is a key point in MSP because of the low substrate temperatures <500°C. This represents a homologous temperature $T_{growth}/T_{melting}$ of 0.25, which corresponds to zone 1 according to the structure zone model (SZM) proposed by Thornton [131, 130]. Activation energies for surface, grain boundary, and bulk diffusion are typically in the ratio 1:2:4 so that at $T_g/T_m < 0.5$ surface and grain boundary diffusion rates can be orders of magnitude larger than bulk diffusion rates. In the case of sputter deposition, the transport step is controlled by parameters such as the apparatus geometry, substrate surface morphology, and working gas pressure, while the diffusion steps are controlled largely by the substrate temperature, but may be significantly influenced by energetic particle bombardment. All of these parameters influence the coating atom arrival directions and the energy and momentum delivered to the surface by the sputtered species and/or other energetic bombarding species. It is well established that intense energetic ion bombardment during deposition can largely suppress the development of open zone 1 structures at low T_g/T_m. The relevant parameters are the ion energy and the ion flux relative to the coating flux.

Messier et al. [88] modified the SZM proposed by Thornton to include the substrate film bias V_s as another parameter controlling ion bombardment. Its effect on the morphology can be compared with a reduction of the sputtering pressure. Films prepared under conditions of low adatom mobility (zone 1) are characterized by highly anisotropic columnar structures. The V_s induced mobility (by bombardment), which affects the physical struc-

ture, is accompanied by other effects with decreasing sputtering gas pressure, such as an increase in the average energy of the sputtered species as they arrive at the growing film surface.

Harper et al. [26] prepared AlN films by a dual-ion beam deposition process in which aluminum films were deposited by Ar^+ ion beam sputtering with simultaneous bombardment by N_2^+ ions of the growing films. They find that for impinging N_2^+ ions of 100-200eV the AlN films are oriented with the c-axis perpendicular to the film plane whereas for N_2^+ ions of 400-500eV the c-axis is parallel to the film plane. Thus the incident ion beam energy is of importance for the film texture.

The N_2^+ concentration in the plasma discharge increases when the N_2 concentration increases in the Ar-N_2 gas mixture in rf diode sputtering [2]. The higher ion concentration results in a more intense bombardment of the negatively biased substrate, and hence in better crystalline film quality [31, 46].

Lee and Lee [70] examined the effect of N_2 concentration and pressure on reactively rf MSP films. The (002)-texture index increases for decreasing sputter pressures and increasing nitrogen concentrations. This is explained with increased kinetic energy which is delivered to adatoms at the growing film surface when the pressure is reduced (increased free mean path of particles). This bombardment causes film densification due to the energy transfer to adatoms, which results in higher mobility. At higher pressures (>10mT) or lower N_2 concentration (<25%), which is equivalent with reducing the energy transfered to adatoms by energetic species, the c-axis changed from out-of-plane to in-plane.

Kusaka et al. [47], 1996, found that the rocking curve FWHM and stress of AlN films decreases with decreasing sputtering pressure in reactive planar MSP. Furthermore, the c-axis orientation is improving with increasing film thickness.

Rodriguez-Navarro et al. [107] identified the ion-bombardment energies, incidence angle and deposition rate as the main factors controlling the preferential orientation of AlN thin films during reactive rf diode sputtering. Positive ions are accelerated towards the substrate with energy proportional to the substrate floating potential V_s, which is the difference between self-bias potential and plasma potential. V_s decreases in negative value as pressure decreases below 10mT, whereas for higher pressures it is almost constant. V_s also increases in negative value with decreasing N_2 percentage. Values of V_s were -40eV at 100W plasma power and 5mT pressure, respectively -60eV at 200W. Furthermore, they attribute the dependence of film orientation on deposition rate with the importance of surface free energy which controls the film crystallography. The ion-bombardment (90-95% of positive ions are N_2^+ [103, 11]) induces adatoms mobility and selects the orientation of crystal grains. Increasing energy bombardment increases crystallinity, density, and flattens the film surface, favoring orientation of densely packed planes, i.e. (002). At lower pressure, 5 mT, when the energy of bombarding ions may be in excess of 60eV, crystal structure damage is caused by particle penetration in the subsurface of the films and then a lower crystallinity and a decrease in preferred orientation results.

Muhl et al. [91] presented in 1997 a detailed process description of reactively dc and rf magnetron sputtering. Good quality AlN films were obtained at 250°C, 70% N_2, and 620W_{dc} on a 4" target. Quartz, glass, silicon and Ti-coated Pyrex were used as substrates.

Among many film properties the grain size was evaluated at 45nm and the Al/N composition was 0.98. The morphology and crystallinity of the film depend on a combination of nitrogen species bombardment and substrate temperature. Because of the low homologous substrate temperature T_g/T_m <0.25 (400°C) during the deposition, dense and oriented crystalline films can only be explained by the existence of considerable bombardment with ions and energetic neutrals.

Ohuchi and Russell [102] deposited AlN by rf MSP and obtained (002) textured films with a columnar structure when the deposition rate was limited to 4nm/min in 75-100% N_2 atmosphere. Above this rate, other crystal orientations were obtained which is explained by the limited ad-atome mobility.

Dubois and Muralt [14] confirmed the importance of ion-bombardment for obtaining highly textured films which exhibit high piezoelectric activity. A minimum substrate threshold bias of -40V must be attained using a high N_2:Ar flow ratio, a low pressure, or rf induced substrate biasing to achieve highest d_{33} values. This threshold value is dependent on sputter geometry.

The successful deposition of dense, crystalline and (002)-textured AlN films requires sufficient adatom mobility. This must be achieved by providing sufficient ion-bombardment because the available thermal energy is too low at a homologous temperature of only 0.25 used for AlN depositions. This energy may be added by i) increasing the substrate rf biasing, ii) higher kinetic energy of the bombarding species by reducing the pressure, iii) increasing the density of N_2^+-ions by increasing the nitrogen concentration in the sputter gas, iv) reducing the deposition rate which reduces the ratio of arrival atom flux to bombardment flux. The supplied energy should however not exceed a threshold value to limit damage to the crystal structure.

Stress control

Film stress control in edge-supported or air-gap FBAR is important. The stress needs to be adjusted to less than ±200MPa to avoid membrane buckling or film rupture [21, 111]. Film stress control is also of importance in SiO_2/AlN reflectors of SMR, especially at frequencies below 5GHz where the reflector thickness is >4μm thick. The compressive stress of SiO_2 can be compensated with a tensile stress in AlN. Numerous authors have investigated stress control in AlN films which is achieved by pressure (compressive-tensile transition at around 4mT), N_2:Ar flow rate ratio [85], or rf induced substrate bias [14, 16] adjustment:

Este and Westwood [18] examined AlN and TiN thin film stress produced by RF reactive MSP on Si substrates with Ar/N_2 gas mixture and pressure being the process variables. The AlN film stresses measured ranged from -19GPa compressive to +2.5GPa tensile as the pressure increased from 1.5 to 38mT. Zero stress was found at 7.5mT sputter pressure. At 3mT the film stress could be changed from -5GPa compressive to tensile by increasing the Ar percentage in the sputter gas. The compressive film stress is attributed to bombardment by N atoms. This bombardment didn't lead to excess nitrogen incorporation [26].

Meng et al. [87] conducted in-situ measurements of intrinsic stress during reactive sputter deposition of polycrystalline and epitaxial AlN thin films on Si (111) substrates

using scanning laser reflection to measure the substrate curvature. The tensile-compressive stress transition was estimated at 3.7mT using a N_2-to-Ar ratio of 1.3. The measurements indicate that the initial stress for all pressures in the range 2.3-9.2mT is compressive. No significant stress relaxation occurred during film growth even at substrate temperatures as high as 800°C.

Dubois and Muralt [14] introduced the rf-induced substrate potential as an easily controllable parameters for film stress and piezoelectric activity control.

Drüsenau et al. [11] measured the total energy per atom impinging on the growing AlN film during rf magnetron sputtering. At the metallic-reactive transition the energy input increases by more than a factor 3 to 300-500eV. A maximum in the AlN texture coefficient (002)/(100) and the grain size was observed when increasing the N_2 content in the sputtering gas corresponding to a total energy input of about 250eV per atom.

The compressive stress in AlN films produced at low pressures, high N_2:Ar flow ratios, or rf-induced substrate potential, is due to the increased particle bombardment from energetic plasma species (ion peening [47]) which not only controls the film texture as seen before, but also densifies the growing film and renders it compressive. Tensile stress on the other hand may be explained by attractive forces between open grains-boundaries which are created at higher pressures. Higher pressures enhance the particle scattering and in turn lower the energy of striking particles [44].

Crystal structure and coupling coefficient

Hickernell et al. [32], Hsieh at al. [33], Naik et al. [94] and the thesis of Naik [12, 92] found a correlation between the FWHM of the rocking curve of the (002) AlN peak and the effective electromechanical coupling coefficient: For FWHM values of less than approximately 3.5°, k_t^2 saturates at approximately 6.5%. For FWHM values larger than 3.5°, k_t^2 gradually decreases to approximately 2.5% at a FWHM of 7.5°. [32, 33] also noted that there is a similar relationship between the FWHM and x-ray diffractometry peak intensity. Chubachi [7] established in 1976 a relationship between the rocking curve FWHM of dc diode sputtered ZnO films and the effective electromechanical coupling coefficient for longitudinal bulk waves measured by SAW.

Naik et al. [95] obtained perfectly (002) textured AlN films on Si with a rocking curve FWHM of 2.3°, respectively 5.7° on Al/Si. These results were obtained after modifying their deposition system to reduce the oxygen containing species (H_2O and O_2 partial pressure) to less than $1\ 10^{-10}$T. These films exhibited tensile stresses of 300-600MPa. The influence of target power, sputter pressure and substrate-target distance was analysed in terms of $\Theta - 2\Theta$, texture index and rocking curve measurements.

Löbl et al. [76, 75] also found a relationship between rocking curve FWHM and the coupling coefficient. Their highest reported value of k_t^2 is 7.8% at a rocking curve FWHM of 1.4°, independent of temperature in the interval between 300 and 500°C. They also found an improvement of the (002) orientation with film thickness [77]: A coupling coefficient k_t^2 of 7.8% was obtained with a 2.8GHz SMR (AlN thickness $>1\mu$m) compared to only 4.0-4.8% at 8GHz (460nm AlN thickness).

Martin et al. [82] find a close correlation between the rocking curve FWHM of the (002) AlN peak and the clamped piezoelectric coefficient $d_{33,f}$. A maximum of 5.15pm/V for $d_{33,f}$ was measured on the best oriented film with a rocking curve FWHM of 1.0°.

Practically, FWHM for polycrystalline, textured AlN films are measured from anywhere between 1.3 and 12° [76]. Epitaxial AlN films on Pt or Ir coated sapphire substrates yielded 0.67° FWHM rocking curves [145]. A prerequisite for highly (002) textured AlN films with small FWHM rocking curve values in reactive sputtering are low oxygen contents [72] in the sputter chamber and for example low deposition pressure (Naik et al. [95]) to increase film bombardment. Carlotti et al. [4] observed a correlation between oxygen content and normalized (002) X-ray intensity. We have seen above that the normalized X-ray intensity is related to the rocking curve FWHM and also with the coupling coefficient. Harris et al. [27], and later McNeil et al. [86], suggested that there is a change in the structure of the oxygen defect (e.g. inversion domain boundaries) as the concentration increases above 0.75%at. The oxygen incorporation in AlN results in a noticeable change in unit cell volume. Below the threshold value, N is substituted by O and an $Al_{0.33}$ vacancy is created. Hickernell et al. [32] also observed a threshold value of 0.5%at oxygen, below which the normalized X-ray intensity of the (002) AlN peak saturates. We can conclude that a low oxygen content in the AlN films is of uppermost importance. A sputter system for AlN fabrication should have an extremely low base pressure ($< 1\,10^{-7}$T) and should be equipped with a load-lock to prevent moisture uptake during sample introduction.

The coupling coefficient can be related to the piezoelectric coefficient $d_{33,f}$, measured with laser interferometry. The film piezoelectric coefficient $d_{33,f}$ is lower than the bulk piezoelectric coefficient d_{33} because of film clamping. The measured $d_{33,f}$ may be expressed as [108]:

$$d_{33,f} = \frac{e_{33}}{c_{33}^E} = d_{33} - \frac{2s_{13}^E}{s_{11}^E + s_{12}^E} d_{31} \tag{2.30}$$

where s_{ij}^E are the mechanical compliances of the piezoelectric film and d_{31} is the transverse piezoelectric coefficient. This definition of $d_{33,f}$ may be used in equation 2.8 to determine the piezoelectric coupling coefficient or vise versa. Because $c_{33}^E = c_{33}^D(1 - k_t^2)$ and $\epsilon_{33}^S = \epsilon_{33}^{\text{film}}(1 - k_t^2)$ we may rewrite equation 2.8 as

$$k_t^2 = \frac{d_{33,f}^2 c_{33}^E}{\epsilon_{33}^{\text{film}}} \tag{2.31}$$

2.4.3 Frequency (non)-uniformity and frequency trimming of BAW resonators

Frequency uniformity

The frequency of a FBAR is most dependent upon the thickness of the piezoelectric film and, to a lesser extend, surrounding layer thicknesses. In most integrated circuit (IC) manufacturing, lateral feature geometries are critical and film thickness is less important. In FBAR manufacturing, lateral features are not so important, but film thickness primarily determines the resonance frequency.

Non-uniformity of the resonance frequency over the substrate directly translates into wafer yield and thus profitability. The resonance frequency dependence on film thickness, also called sensitivity, depends on the individual film thicknesses and materials composing the FBAR or SMR. The active piezoelectric layer has the highest sensitivity, followed by the uppermost layer in the acoustic reflector, which has the highest sensitivity of all reflective layers in the SMR [104]. The sensitivity of the piezoelectric layer is smaller for the SMR compared to the FBAR. The piezoelectric AlN layer has a 10 times higher sensitivity than the Al electrodes, and 5 times more than the topmost SiO_2 layer in the reflector [49]. The sensitivity of the 3^{th} reflective layer is already reduced to 4% of the AlN sensitivity.

Every deposition method, machine configuration and deposition material results in a characteristic thickness distribution on the substrate. As indicated above, the resulting thickness variation over the wafer has a direct influence on the resonance frequency of the SMR. It is not only important to deposit the exact absolute thickness for each layer, but equally important to get the best possible substrate uniformity to increase the yield. Once the resonators are fabricated they can still be trimmed by adding or removing material locally on the resonators, for example with a stepper and a lift-off technique. A good deposition uniformity is nevertheless required to obtain highly reproducible filters over the whole wafer

High wafer uniformity was already an issue when the first FBAR emerged in 1982: 8" diameter ZnO target [66], or 5" Zn or Al targets [140] were used to reactively magnetron sputter ZnO or AlN for edge-supported FBAR. In 1995 Lakin et al. [54] reported on a sputter tool which enabled them to obtain a 4" wafer uniformity of the midband frequency in AlN ladder filters, e.g. including all resonator material thicknesses, of $\pm 0.65\%$ [43]. Two years later, they reported also on ± 0.1dB insertion loss distribution over a 4" wafer using SMR based ladder filters [54].

Frequency trimming

Frequency trimming is required for hitting the central frequency of the passband exactly, and for adjusting the two pairs of resonators to each other as needed in ladder filters (c.f. chapter 3). In ladder filters it is most convenient to decrease the frequency of the shunt resonator by adding an additional loading layer. The passive trimming of shunt resonators is a very delicate and difficult step.

Passive overall trimming is achieved by measuring individual zones on a wafer and adding for example a dielectric layer over that zone to decrease the resonance frequency by a certain amount. This kind of tuning, using SiO_2 was already used for crystal resonators in the 1960's [45], and is also used in this work for passband ladder filter tuning [67]. The SiO_2 was sputter deposited. This low temperature process yields low stress and high acoustic quality filters [41]. Kaitila et al. [36] used Cu to tune shunt resonators in ladder filters to the desired frequency, on top of Al electrodes. Another approach is the local removal or thinning of the resonators, for example piezoelectric crystals can be thinned by plasma etching with a precise control of frequency: The impedance of the thinning resonator is used to control the etch rate. An almost zero etch rate should be obtained when the resonance

frequency of the plate/crystal approaches the plasma generator frequency during etching. This self limiting etching was successfully demonstrated on quartz crystals, but may be implemented one day for FBAR tuning [65].

Agilent built an automated probing station for wafer mapping which allows control of FBAR figure of merit and frequency uniformity needed for trimming [68]. A ±0.5% uniformity for the resonance frequency over the central 2" diameter of a 3" wafer is reported.

For channel selection, it would be desirable to be able to tune the resonance frequency during operation. The standard solution in *LC*-circuitry uses voltage controlled oscillators (VOC). Attempts have been made to achieve the tuning also with BAW resonators. A tungsten resistivity micro-heater, which serves at the same time as bottom electrode, integrated into an AlN FBAR was tested for frequency tuning purposes. The frequency could be changed by 50-80ppm/°C and a maximum temperature without degrading the resonator of 580°C was supported [111, 109]. This heater-tuner may be used to tune the frequency up to ∼2%.

2.5 Numerical model simulation results

2.5.1 Material data used for numerical simulations

The numerical simulation of resonator admittance in this thesis are written with MatLab code, based on equation 2.12. A resonance frequency of 8GHz serves as reference frequency for all subsequent simulation results, with a resolution of 5MHz. The SMR is modeled as electrode/AlN/electrode resonator on top of an acoustic Bragg reflector, built up of 5 pairs of $\lambda/4$-thick SiO_2 (187 nm) / AlN (355nm), deposited on an infinitely thick Si susbstrate.

The intrinsic AlN material data are assumed as: relative dielectric permittivity $\epsilon_r = 10.5$, dielectric loss $\tan\delta = 0.2\%$, and thickness mode electromechanical coupling coefficient $k_t^2 = 5.8\%$. k_t^2 is assumed lower than the maximum value of 6.5% calculated for epitaxial films due to the reduced piezoelectric coefficient $d_{33,f}$ for AlN films thinner than 500nm [82]. The size of the clamped capacity area for 50Ω matching is dependent on the ratio of the metal electrode thickness to piezoelectric thickness and must therefore be always adjusted. In our model simulations we will introduce loss in the acoustic velocity as $v^D = v_0^D(1 - i\frac{1}{Q})$. Parasitic losses like electrode resistance, inductances and stray capacities are neglected. Material data used for the simulation are listed in table 2.3.

2.5.2 Effect of reflector layers on mechanical properties of Bragg stack

As noted in paragraph 2.3.2 different pairs of materials have been proposed for the acoustic reflector fabrication. We choose to use the combination SiO_2/AlN because both materials may be fabricated in a single run in our Nordico 2000 multitarget sputtering tool, and compared to the SiO_2/W combination, no complicated reflector patterning needs to be performed. The following simulation results suggest the use of 5 pairs of SiO_2/AlN will be appropriate to achieve sufficient high acoustic isolation for SMR applications.

Table 2.3: Material parameters used for numerical 1-D BAW thickness extensional resonator simulations.

Material	Density [kg/m^3]	Sound velocity [m/s]	Quality factor [-]	Ac. impedance [10^7 kg/m^{2}s]
Si	2328	8433	500	1.96
SiO_2	2200	5970	500	1.31
AlN	3260	11354	2000	3.70
Al	2700	6490	500	1.75
Pt	21500	4230	200	9.09
Mo	10230	6408	300	6.56

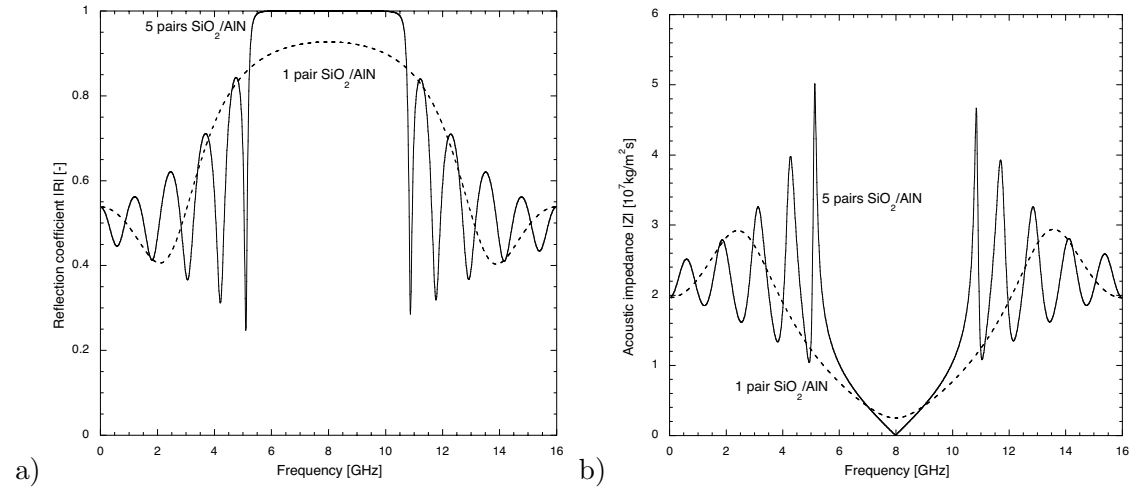

Figure 2.5: Numerical simulation results for the absolute reflection coefficient $|R|$ (a) of a Bragg reflector using 1 and 5 pairs of SiO_2/AlN layers deposited on an infinitely thick Si substrate, respectively the absolute acoustic impedance $|Z_{ac}|$ (b) seen by the resonator.

The absolute reflection coefficient $|R|$ (eq. 2.15) and absolute acoustic impedance $|Z_{ac}|$ (eq. 2.14) seen by the resonator are represented in figure 2.5 as function of frequency for 1 pair, respectively 5 pairs of SiO_2/AlN. The acoustic impedance of the reflective layer stack, as seen from the resonator electrode, decreases with increasing number of reflective layers at the center frequency. The substrate impedance of 1.96 10^7kg/m^{2}s is hence reduced to 8% for 1 reflector pair and virtually zero for 5 reflector pairs. The value of the reflection coefficient $|R|$ is at the same time increased from 92% to 100%. Furthermore, a large frequency band of $\pm$25% around the center frequency maintains a reflection coefficient of close to 100%. The total reflection bandwidth of the reflector would be even more enhanced if AlN was replaced with the higher impedance material W.

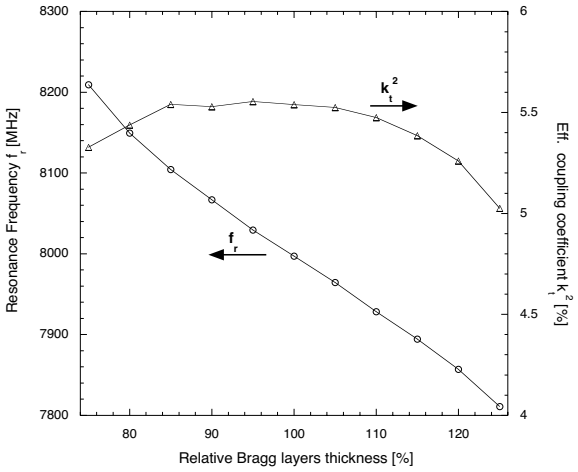

Figure 2.6: Resonance frequency variations of a 8GHz SMR relative to $(SiO_2/AlN)_5$ Bragg layer thickness variations. The sensitivity is -6.8MHz/% or -850ppm/%. The effective coupling coefficient, reported to the right axis, is almost constant in the range 100±10%.

2.5.3 Effect of reflector layers on resonator properties

Thickness deviations in the Bragg reflector layers from the ideal $\lambda/4$ thickness influence the resonator characteristics. As seen in figure 2.6, variations in the acoustic layer thickness directly influence the resonance frequency of the resonator. For the examined 8GHz SMR a dependency of -6.8MHz/% or -850ppm/% is observed. A 12% thickness deviations from the ideal $\lambda/4$ thickness of the Bragg layers results therefore in a 1% variation in the resonance frequency. For the same interval of thickness deviation the effective coupling coefficient remains almost unaffected.

Numerical simulations show that the effective coupling of the SMR is lower than the FBAR, reduced from 6.5% to approximately 6.0% when using SiO_2/W reflectors, and reduced even more to 5.85% when using the SiO_2/AlN reflector. The effective coupling increases with the impedance ratio of the reflective layers because less acoustic energy is stored outside of the resonator. The low impedance layer, SiO_2, needs to be directly below the resonator instead of the higher impedance layer to achieve a high effective coupling. The materials in the reflector not only have an effect on k_t^2 but also on the quality factor of the resonator [93].

2.5.4 Implications of different electrodes on resonator behaviour

We investigated the effective coupling properties of SMR with Al, Pt or Mo electrodes as a function of frequency from 1 to 10GHz, using k_t^2 =6.5% as AlN material coupling coefficient. The top and bottom electrode were assumed to be of the same material and its thickness was fixed to 100nm. The frequency dependency of the coupling coefficient and the AlN thickness for the 3 metals are represented in figure 2.7.

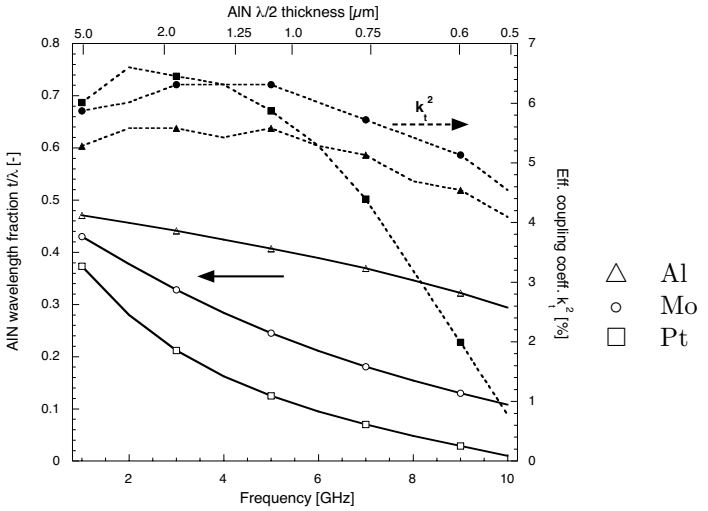

Figure 2.7: Thickness of AlN layer expressed as a fraction of its wavelength λ assuming 100nm thick electrodes for the frequency range of 1 to 10GHz. For infinitely thin electrodes the AlN thickness would be equal to $\lambda/2$, reported on the top x-axis. The full symbols represent the effective coupling coefficient reported to the right axis.

Aluminum has the lowest mass loading effect of the three investigated metals. This results in the largest absolute and relative thickness of AlN, when reported to the ideal $\lambda/2$ resonator thickness for infinitely thin electrodes. The wavelength fraction of AlN for molybdenum electrodes is reduced to 0.11 at 10GHz, respectively 0.01 for the platinum electrodes and 0.29 for the aluminum electrodes. In absolute thickness, as reported on the top x-axis, the AlN thickness at 10GHz is reduced to a mere 20nm for the Pt electrodes, 123nm for the Mo electrodes and 334nm for the Al electrodes.

Between 1 and 5GHz, all 3 metals show a more or less constant effective coupling coefficient. Pt and Mo have a k_t^2 of approximately 6%, Al on the other hand has a maximum of only 5.5%. Above 5GHz the Mo SMR continues to excel over the Al SMR with respect to the effective coupling coefficient. Pt based SMR suffer a sharp decrease of their k_t^2 above 5GHz, which is due to the sharply reduced driving AlN volume in the resonator relative to the 100nm thick electrodes.

The reduction in coupling coefficient found with these simulations is only due to geometrical and acoustic constraints. Additionnaly, one has to take into account a reduction of the material coupling coefficient, due to a reduced $d_{33,f}$, below approximately 500nm [82]. Another disadvantage of Pt electrodes at higher frequencies is the smaller absolute thickness of the AlN, and hence higher capacity. To maintain a 50Ω matching of the resonators, the resonator area needs to be reduced accordingly. At 10GHz, the 50Ω resonator area is ideally 42x42μm^2. For the Pt resonator with only 0.01λ instead of 0.5λ AlN thickness, the area is reduced to 6x6μm^2 which is close to the conventional resolution limit of photolithography.

To maximize the effective coupling coefficient of SMR at 8GHz, its dependency on the

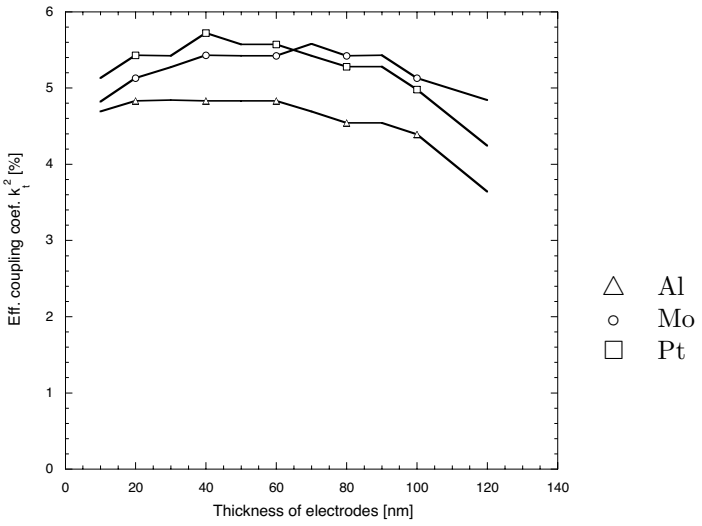

Figure 2.8: Effective coupling coefficient of SMRs at 8GHz for 3 different bottom electrode materials and Al top electrodes of the same thickness. The AlN thickness ranges from 230 to 675nm for the metals and thickness range tested.

electrode thickness was evaluated. Both top and bottom electrode thicknesses were varied at the same time. Again we investigated Al, Mo or Pt bottom electrodes, the top electrode was always Al because of its low electric resistivity and it allows for a thicker AlN layer at 8GHz so that the absolute thickness can be achieved more precisely. The material coupling coefficient was assumed to be 5.8%, in accordance with the lower $d_{33,f}$ value for films below 500nm thickness.

The result of this optimization, figure 2.8, indicates that for both Pt and Mo bottom electrodes a high effective coupling in excess of 5.5% may be achieved at 8GHz for electrode thickness between 30 and 70nm. Above 70nm electrode thickness, the effective coupling is decreasing. The effective coupling coefficient for Al electrodes is always below 4.9%, which is lower compared to the other two metals. No pronounced maximum of the coupling coefficient is observed either. To reduce the electrical resistance and to assure high quality electrodes with sputter deposition, a thickness of 60nm seems to be appropriate. Al-Pt SMR achieve the maximum effective coupling for a slightly lower thickness than the Al-Mo SMR.

Lakin et al. [50] also compared different electrode materials (Al, W, Au, Cu), with numerical simulations in view of their electrical and acoustic qualities: The effective coupling coefficient of resonators increases initially with increasing electrode/piezoelectric AlN ratio and then starts decrease. This coupling enhancement, which translates into enhanced filter bandwidth, is more pronounced for the high acoustic impedance materials W, Cu and Au. The increase in coupling coefficient is due to the improved match in the distribution of acoustic standing wave to the linear distribution of applied electric potential. Gold and

copper electrodes are not suitable for microwave acoustic applications because they are mechanically soft and present a low Q factor. Tungsten has double the electrical resistivity of aluminum. To combine the advantages of Al and W, a sandwich structure Al/W/AlN/W/Al was proposed for 0.85GHz bandpass filters. Fabricated SMR confirmed the higher effective k_t^2 of 6% compared to 5.2% for the ideal resonator with zero thickness electrodes.

2.6 Growth and properties of AlN, Pt and Mo thin film

The fabrication, patterning and characterization of thin films needs a wide range of equipment. In order to avoid particle contamination of the thin films all wafers were processed in clean room environment of class 100. Some of the tools are located in EPFL in the Center of MicroNanotechnology, others are at the clean room facility of the Ceramics Laboratory. Single-side 4" (100)-Si wafer were used as substrates.

2.6.1 Film patterning and characterization

Photolithography The positive photoresists Shipley 1805, 1813 and 1818 were used for the photolithography process, depending on the required thickness. They were applied on the wafer either with a manual Karl Süss RC8 spin coater or a RiteTrack coater and backed at 115°C for 60sec. The 5" mask was aligned with a Karl Süss MA6 and exposed with a UV dose appropriate for the thickness of the photoresist. The resist was developed in either Shipley 351 with a 7:1 dilution, or Shipley CD26. The post-bake was at 115°C for 30sec, and a short oxygen plasma etch with a Tepla 300 at 500W for 30sec ensured complete removal of the photoresist in the non-covered areas. The quality of the photolithographic process (resolution, flank, homogeneity, reaction of substrate, etc) is checked with an optical microscope. To remove the photoresist after the etching or lift-off step, a bath of Shipley 1165 Remover at 70°C was used for 20min and remaining traces of photoresist were removed in the Tepla 300 asher during 4min.

Film thickness measurements Film thickness and roughness were measured with a alpha-step 200 which measures the surface profile with a stylus and offers a vertical resolution of one nanometer and a horizontal resolution of 40nm. A fast and non-contact spectroscopic-reflectometry method of measuring the thickness and its wafer distribution of transparent films is accomplished with a Nanospec 6100 from Nanometrics. Optionally a Plasmos SD2300 ellipsometer was used for film thickness measurements.

Film stress measurements The in-plane stress measurement technique for thin films uses the effect of substrate bending induced by stress in the film. The Stoney equation [127] relates the average stress σ of a thin film deposited on a substrate to the change in the radius of curvature: $\sigma = \frac{E_s h^2}{(1-\nu)6t} \cdot (\frac{1}{R_2} - \frac{1}{R_1})$ where h is the substrate thickness, t the film thickness, $\frac{E_s}{(1-\nu)}$ the biaxial elastic modulus of the substrate (1.81e11 Pa for (100) silicon wafers) and R_1, R_2 the bending radius of the sample before and after the application of

the film. This relation is valid for $t << h$. The changes in the radius of curvature of the substrate is measured with a Tencor FLX-2900 stress measurement setup using a sweeping dual wavelength laser beam that is reflected on the sample surface.

Film resistivity measurement The sheet resistivity of continuous films are measured with a 4 point resistivity meter, OmniMap RS75 from KLA Tencor. The resistivity may be measured as a function of the position on the wafer to yield the thickness distribution. Alternatively, the electrical resistivity was also measured on predefined metal strips on integrated test structures with an Ohm-meter.

Film cristallography - $\Theta - 2\Theta$ X-ray diffraction and rocking curves The Bragg-Brentano diffraction method using the angle Θ between incident X-ray and sample surface, respectively 2Θ for the incident beam and detector when the source and detector are on the same periphery of a circle with the sample placed in the center is used to measure the out of plane lattice spacing of a crystalline film. The Bragg conditions for diffraction are fulfilled when $2d \sin\Theta = n\lambda$ with d distance between reticular planes, λ the X-ray source Cu-Kα radiation wavelength of 1.54$\mathring{A}$, and n an integer. The X-ray diffraction machine used is a Kristallflex from Siemens. This method measures the in plane crystallographic orientation. Peaks are indexed with the JCPDS Powder diffraction file database. Rocking curves of certain reticular planes were measured by fixing the angle source-detector at 2Θ corresponding to the lattice spacing and rotating the sample around the angle $[\Theta - \delta, \Theta + \delta]$. The FWHM of the rocking curve is a measure of the tilt distribution of the reticular planes.

2.6.2 Deposition process for Pt electrodes

The (111) Pt/Ta bottom electrodes used as substrates for AlN depositions are either deposited in the BAS450 sputter tool or the Spider tool. The Balzers BAS450 is a single chamber multi-target and multi wafer sputtering tool without load-lock, providing 2 dc and 1 rf magnetrons (size 127x254 mm) and 1 etch station. The cylindrical substrate holder may be loaded with 9 wafers and may be rotated at a maximum of 24rpm. The maximum attainable substrate temperature is 300°C.

The deposition process for 100/10nm thick Pt/Ta films is the following: After reaching a base pressure of 4.10^{-7}T, the substrates are heated to 300°C. The deposition pressure is approx. 4.5mT with a 20sccm Ar flow (throttle valve). The substrate are presputtered for 1min with an rf etch of 500W. 10nm of tantalum nucleation and adhesion layer is deposited (6sec, 8.7W/cm^2, 12rpm) before 100nm of platinum are deposited (1min, 3.1W/cm^2, 4rpm). The Pt exhibits a pure (111) texture with a rocking curve FWHM of 3.2°.

The Spider high vacuum sputter cluster tool from Pfeiffer Vacuum with 4 process chambers and load-lock allows for higher quality and more reproducible film depositions compared with the BAS450. The substrate dimensions can be either 4" or 6", and the target diameter is 8". We transfered the Pt/Ta process from the BAS450 to the SPIDER because of its better functionality: The wafer introduction time is greatly reduced due to a load lock, the base pressure is better ($<5.10^{-8}$T), deposition chambers are only used for a few elements

Table 2.4: Studied parameters for growth of (110)-textured Mo electrodes in the Nordico tool.

Base Pressure	3.10^{-6}	Torr
Target Power	25-50	W_{dc}
Temperature	440-600	°C
Pressure	4	mT
gas	Ar: 30	sccm
Substrate bias	0-25	W_{rf}
Seed layers on Pt	Ta, Ti, TiO_x	

(less contamination), the uniformity is very good (2-5%) and the whole deposition process is done fully computer controlled. 100/10nm of Pt/Ta are deposited in 38/9sec at 300°C and 1.6/3.2W/cm^2 (500/1000W) of target power in 3.75mT Ar. The resulting Pt film is perfectly (111) textured with a rocking curve FWHM of 3.2°. The electrical resistivity of 100nm thick Pt films are 16±1$\mu\Omega$cm (bulk value: 10.6$\mu\Omega$cm).

2.6.3 Deposition process for Mo electrodes

Molybdenum is an promising alternative for platinum electrodes for SMR applications because of its better acoustic and electric properties. Because Mo is body-centered cubic, Mo films grow with a (110)-texture. (110)-planes correspond to the densest packing and the lowest free surface energy [11]. We developed a process to grow perfectly textured (110) Mo films in the Nordico 2000 sputter tool on Si and passivated SiO_2/Si wafer substrates from a 4" 99.95% pure Mo target. The parameters studied are detailed in table 2.4.

$\Theta - 2\Theta$ X-ray results of Mo films grown on different substrates are shown in figure 2.9 (a). When using no or a Ta adhesion layer, the films were mostly (110) textured but had a significant amount of (200) and (211) texture. The use of Ti as adhesion layer reduced the unwanted orientations. Using the Ti nucleation layer, followed by an oxidation step finally yielded perfectly textured (110) Mo electrodes. The electrical resistivity of the 240nm thick Mo film was 7.7$\mu\Omega$cm (bulk value: 5.3$\mu\Omega$cm). The Mo film stress was +580MPa tensile.

2.6.4 AlN deposition process

AlN growth on Pt electrodes

We used an already established reactive pulsed-dc growth process of AlN on Pt electrodes for the SMR and FBAR fabrication [12]. The sputter tool without load-lock (AlN-LC) is in-house built. It reaches a base pressure of 5.10^{-7}T with a 250l/s Pfeiffer turbo-molecular pump, high purity Ar and N_2 can be admitted with massflow meters. The pure 4" target (99.999%) is attached to a magnetron, which is operated in pulsed-dc mode to avoid arcing. The 4" substrate holder can be heated to 400°C with halogen lamps, and an external rf-bias may be applied. The process details used for the AlN depositions are given in table 2.5. The

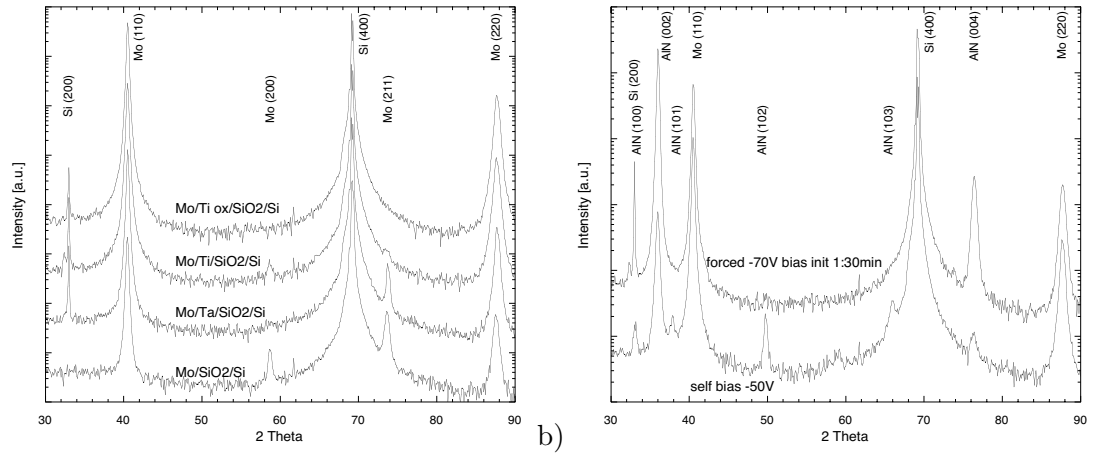

Figure 2.9: (a) $\Theta - 2\Theta$ x-ray scan of Mo film electrodes deposited at 530°C, 50W$_{dc}$, 25W$_{substr.}$, 30sccm Ar, 4mT on 4 different substrates. Pure (110)-texture is obtained on the oxidized Ti nucleation layer. (b) 750nm thick AlN film deposited in the AlN-LC sputter tool on Mo/Ti/SiO_2/Si substrates at a substrate self bias of -50V showing random AlN growth, respectively using a rf substrate bias of -70V resulting in perfect (002)-texture.

Table 2.5: Process conditions for the deposition of AlN films in the AlN-LC sputter tool.

Base Pressure	5.10^{-7}	Torr
Target Power	500	W$_{dc,pulsed}$
Temperature	400	°C
Pressure	3.5-5.0	mT
gas	N_2: 20	sccm
Substrate bias	0-5W → 35-70	V

substrate bias, which controls the piezoelectricity and stress in the deposited AlN films was either adjusted using an external rf power source, or by adjusting the sputter pressure. The deposition rate is approximately 21nm/min, and a maximum $d_{33,f}$ of 3.9pm/V is achieved on Pt substrates. The relative dielectric permittivity is ϵ_r=10.8 and the dielectric losses are $\tan\delta$=0.3%.

Alternatively to the AlN-LC sputter tool, the SPIDER sputter tool with far better base vacuum ($5\,10^{-8}$T) and better uniformity[3] (1-3%) was also used to produce AlN films. With this equipment, $d_{33,f}$ values of up to 5.15pm/V are achieved routinely for AlN film thicknesses of 1μm, deposited on (111) Pt electrodes. $\Theta-2\Theta$ x-ray measurements of AlN/Pt deposited in the SPIDER tool are shown in figure 2.11 (a).

[3]the film thickness uniformity is defined as $\frac{t_{max}-t_{min}}{2t_{average}}$ where t is the local film thickness

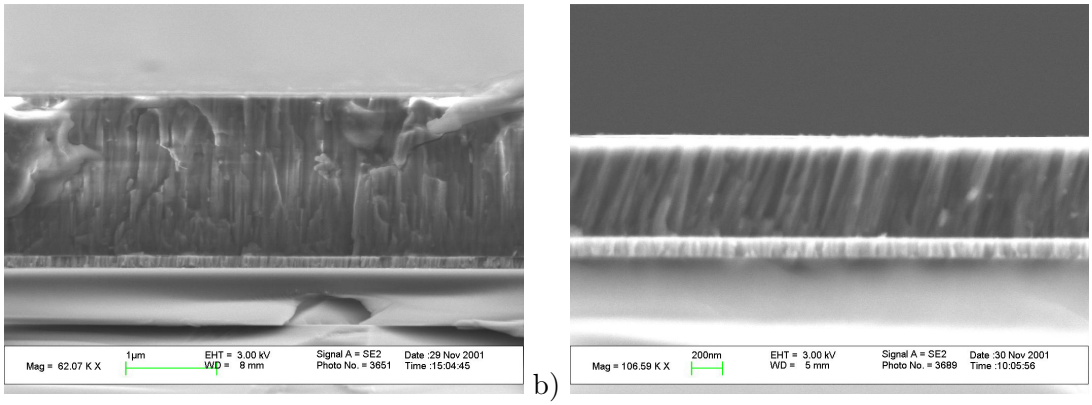

a) b)

Figure 2.10: SEM cross-section images of (002) textured AlN grown on (110) Mo using -70V initial substrate bias (a), respectively -50V self bias (b).

AlN growth on Mo electrodes

AlN films were deposited in the AlN-LC tool on $Mo/Ti/SiO_2/Si$ substrates using the process conditions given in table 2.5 at 4mT without substrate bias. We observed an initial substrate self bias of -50V at the deposition start. With these deposition conditions a perfect (002) texture is obtained on Pt (111) substrates. However on the (110) textured Mo substrates, a randomly oriented AlN film resulted, c.f. figure 2.9 (b). By polarizing the substrate with $5W_{rf}$, corresponding to -70V, for the initial 28nm thick AlN deposited, and then reducing to -40V self-bias, a perfectly textured (002) AlN could be obtained. The rocking curve FWHM of the (002) AlN peak was 4.0° compared with 4.6° for the (110) Mo peak of the underlying electrode.

This result shows that the AlN growth is influenced by the substrate and the growth process. By increasing the energy of the ion bombardment in the initial stages of AlN film growth, the random growth is replaced with the dominating (002) textured grains because of enhanced adatom mobility. Furthermore, non-(002) orientations become either instable and are re-sputtered, or their growth rate is reduced with respect to the (002) growth rate. A comparison of the microstructure of the AlN/Mo films obtained with different bias, cross-section SEM images in figure 2.10, show that the fibrous grain growth is perpendicular to the substrate for the sample with the -70V substrate bias, and inclined for the randomly textured film. The inclined grain-growth is not due to border effects on the substrate, because both samples were placed on the same position on the substrate holder.

AlN depositions on 60/10nm thick $Mo/Ti/SiO_2/Si$ (Nordico) substrates in the Spider tool with -100V initial substrate bias for the first minute and a bias of -80V for the next 8min yielded also perfectly (002) textured AlN films. The X-ray $\Theta - 2\Theta$ of 500nm thick AlN films deposited on Pt/Ta and Mo/Ti bottom electrodes, figure 2.11 (a) show the pure texture. The rocking curves (b) of the (002) AlN, (110) Mo, and (111) Pt peaks are represented in figure 2.11 (b). The rocking curves FWHM for (110) Mo/Ti used for 8GHz SMR was 4.6°.

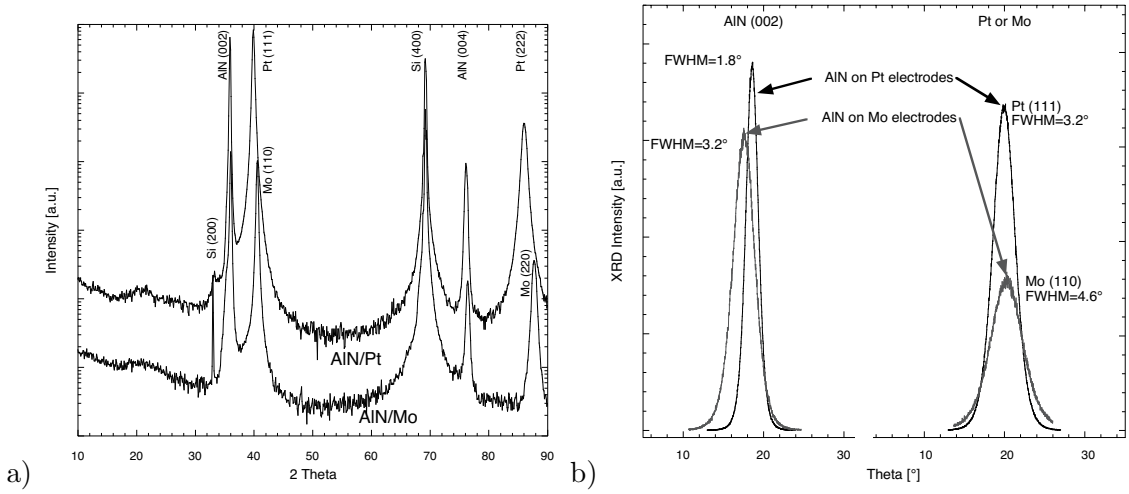

Figure 2.11: (a) $\Theta - 2\Theta$ X-ray scans show the perfect (002) texture of AlN films deposited in the Spider tool on both the Mo/Ti and Pt/Ta electrodes. (b) The corresponding rocking curves of the (111) Pt, (110) Mo, and (002) AlN diffraction peaks show a correlation between the electrode and AlN FWHM. Furthermore the AlN FWHM is larger on the Mo electrode than on the Pt electrode.

The rocking curve FWHM of 500nm thick AlN film grown with the Spider tool on top of this electrode was 3.2°. AlN grown on Pt/Ta (all Spider) exhibited, due to the better Pt rocking curve of 3.2°, a rocking curve FWHM of only 1.8°. The $d_{33,f}$ value measured on the AlN/Mo film was only 3.1pm/V compared to 4.0pm/V for AlN grown on Pt [67]. $d_{33,f}$ interferometric measurements on SMR devices were done according to [39].

The discrepancy in $d_{33,f}$ values of AlN grown on Pt and Mo electrodes is best explained with the difference in lattice plane tilts as indicated by FWHM rocking curve values. The correlation between $d_{33,f}$ and FWHM of the rocking curve was shown in [82]. We observed that the rocking curve FWHM of AlN grown on Mo was higher than on Pt electrodes. Three effects might be responsible for the higher FWHM values: i) AlN grows with a local epitaxy on the substrate and inherits therefore its lattice plane tilt. According to our rocking curve measurements the (110) textured Mo has a higher lattice plane tilt compared to the (111) textured Pt electrode. ii) the Mo films might have a higher roughness compared with Pt films and promotes AlN nuclei with the wrong orientation [71] iii) the body-centered cubic Mo (110) lattice plane has a rectangular atom arrangement, unlike the cubic close-packed Pt (111) lattice plane with its hexagonal atom arrangement (fig. 2.12), and does therefore hinder local epitaxy of the hexagonal AlN and rather promote nuclei with a random orientation as we have observed with XRD. Another interesting point to note is that the AlN FWHM values are generally better than the FWHM of the underlying electrode.

At a frequency of 8GHz the AlN film thickness used in the SMR is below 500nm and may even be as low as 250nm depending on the bottom electrode material used. Below 500nm

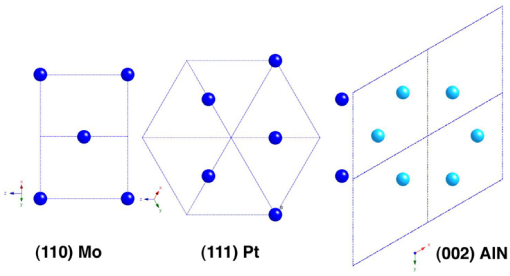

Figure 2.12: Arrangement of atoms within the reticular planes of (110) textured Mo, (111) textured Pt and (002) textured AlN. The hexagonal symmetry of the atom arrangement in Pt favors the (002) nucleation of AlN, whereas AlN nucleates and grows with the same process conditions with a random texture on the rectangular atom arrangement of the (110) Mo.

the crystalline orientation, e.g. rocking curve FWHM and hence the coupling coefficient degrade: Löbl et al. [75] measured for example an effective coupling coefficient of 5.3% at 2.6GHz where the AlN thickness is 1.4μm, respectively 2.9% coupling at 9.2GHz where the AlN is only 240nm thick. At the same time the rocking curve FWHM for these films degraded from 2.4 to 3.5°.

Problems of growing c-axis textured AlN on Mo has been previously reported, even though it grows perfectly on Si, SiO_2 and Pt(111) [71]. In that work it was attributed to a higher surface roughness: smooth Mo surfaces were obtained when reducing the sputtering pressure from 10 to 1mT (showing high compressive stresses as a consequence). A randomly inclined columnar structure was observed in the AlN films grown on the rough Mo surface, whereas on the smooth Mo surface a purely textured (002) AlN film was obtained. Reducing the roughness of the Mo films resulted in a decrease of the rocking curve FWHM of the AlN film from 12 to 2.4°. The authors, however, do not relate the rocking curve information of the AlN and Mo films.

2.6.5 AlN wet etching

AlN films have an excellent chemical stability favoring eventual integration with other device fabrication techniques. AlN is found to be unaffected by concentrated acids such as HNO_3, H_3COOH and HF, but is etched by basic solutions such as NaOH, KOH, NH_4OH [44], or AZ400K developer [138] which is KOH based. AlN can be etched in hot H_3PO_4 [119]. For device processing it is important to have a precise knowledge of AlN wet and dry etching possibilities:

We conducted etch test in hot concentrated H_3PO_4 on 500nm thick AlN films deposited on Pt/Si substrates. A thermally activated etch rate, fig. 2.13, was found for this particular etch system. Below a certain threshold temperature of approximately 90°C, the films were only partially etched. At the highest tested temperature of 103°C, limited by the degradation temperature of the masking photoresist, a thickness etch rate of 100±5nm/min was

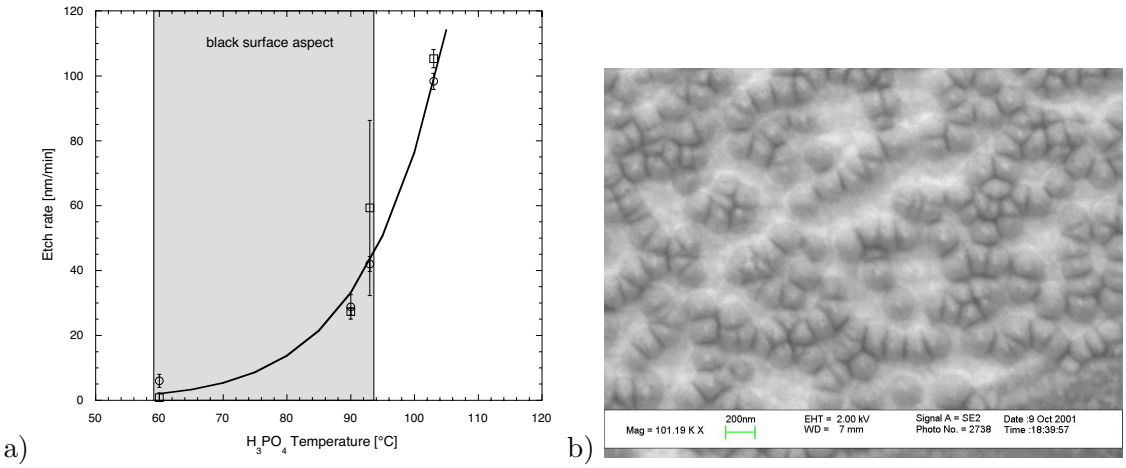

Figure 2.13: Thickness etch rate of (002) AlN films as a function of H_3PO_4 temperature. The black surface aspect seen during initial etch corresponds to preferential grain boundary etching, which is also evident in the SEM picture of a partially etched AlN/Pt film that reveals the individual AlN grains. □ represent 50x50μm^2 features, respectively ◯ for 200x200μm^2. The curve represents an Arhenius fit, relating the etch rate with thermal activation energy.

found. The AlN film gets preferentially attacked on the grain boundaries (c.f. fig. 2.13 (b)), which results in the black surface aspect observed on partially etched films.

2.7 Solidly mounted resonators

Bragg reflectors consisting of pairs of SiO_2/AlN were developed as starting point for the SMR and SMR ladder filter fabrication. At 8GHz the $\lambda/4$ thicknesses are 187nm for SiO_2 and 355nm for AlN. The compressive SiO_2 film stress may be compensated with the AlN film stress by carefully engineering the process parameters.

2.7.1 Bragg reflector fabrication

Multilayer stacks of SiO_2 and AlN, which were deposited in a single run in the NORDICO 2000 sputter tool, turned out to be difficulty to control with respect to a constant level of deposition rate and stress level. A stringent control of the stress level is important to obtain low level stress reflectors avoiding cracks and excessive wafer bending. Obviously, a high reproducibility of the deposition rate for successive layers in the reflectors is of paramount importance. The acoustic isolation of the reflectors depends mostly on the thickness of the topmost layer. When calibrating the deposition rate using the Nanospec or ellipsometry, only the film thicknesses of maximum 2 layers can be assessed with precision. After depositing 5 pairs of SiO_2/AlN films, the topmost layer thickness may only be characterized

Table 2.6: Sputter conditions used in NORDICO for the acoustic Bragg reflector fabrication.

Film	Gas	Flux [sccm]	Pressure [mT]	Temperature [°C]	Power [W]
AlN	Ar/N_2	30 total, 44-67%N_2	4-5	330	500 dc_{pulsed}
SiO_2	Ar	25	10	330	300 rf

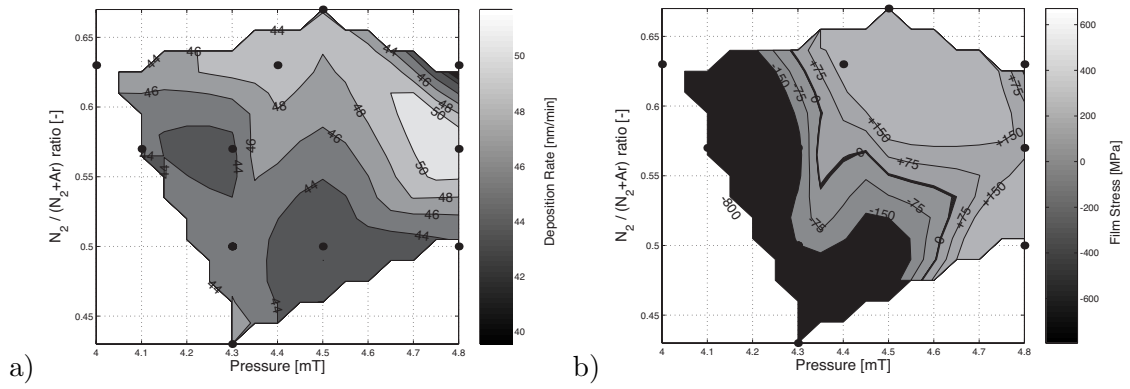

Figure 2.14: Deposition rate (a) and film stress dependency (b) of AlN films fabricated in Nordico for reflector fabrication.

after complete SMR fabrication with a destructive method.

SiO_2 was sputter deposited from a 99.995% pure 4" SiO_2 target in an Ar atmosphere. The stress level of SiO_2 was in general -200±50MPa compressive. The relevant sputter conditions are given in table 2.6. The deposition rate was measured as 14±1nm/min with a wafer uniformity of ±29%.

The pulsed dc reactive AlN deposition was very sensitive to small variations of pressure, gas mixture and vacuum time of the substrate: In order to obtain a low average stress in the reflector, a tensile stress of a few hundred Megapascal was aimed for. For this reason the gas mixture $N_2/(Ar+N_2)$ was varied between 0.44 and 0.67 (poised mode) and the pressure was varied between 4 and 5mTorr. The deposition rate was 41-50nm/min for the conditions studied. The film thickness uniformity was ±22%. AlN film thickness was measured by a) nanospec, or b) by chemically etching with hot H_3PO_4, or c) using a cache during the deposition to provide a mechanical step. A summary of stress and deposition rate achieved for the AlN deposition by varying the pressure and gas mixture is given in figure 2.14.

The AlN film stress shows a steep transition from tensile to compressive stress for small variations of pressure or N_2:Ar gas mixtures. It was not possible to control the pressure to more than ±0.2mT because of Baratron zero drifts of ±0.2mTorr. They are due to relaxation phenomena in the Baratron measurement membrane due to frequent chamber vents. Nonetheless, Bragg reflectors were fabricated and working SMR exhibited acceptable

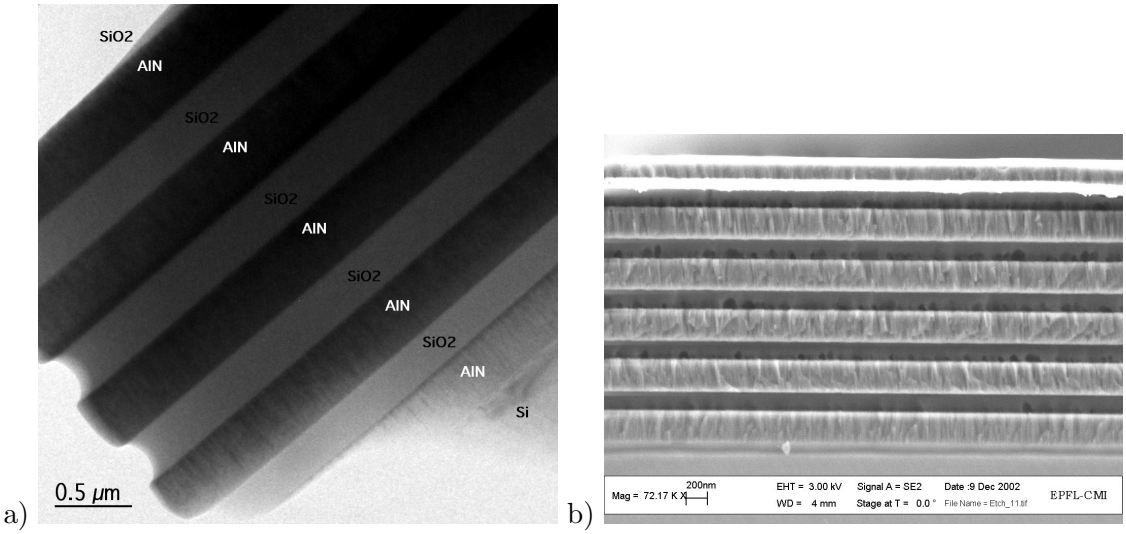

Figure 2.15: Bragg reflectors fabricated in 2 different sputtering tools. TEM cross section image of reflectors fabricated in NORDICO for 8GHz (a), and a SEM cross section showing a finished 8GHz SMR fabricated in the SPIDER tool (b) which has been attacked in BHF for 10sec to obtain a better contrast.

but not satisfying figure of merits (c.f. paragraph 2.7.3). A TEM cross section image (fig. 2.15 (a)) of a reflector fabricated in Nordico shows the 5 pairs of SiO_2 and AlN. The layers become increasingly thick for each successive layer, both for the AlN and SiO_2 films. More detailed analysis showed that the AlN thickness is initially exactly 350nm as needed for 8GHz, but increases to 420nm for the last layer. The SiO_2 on the other hand reaches 320nm instead of the 190nm aimed for. This large deviation from the $\lambda/4$ thickness was the cause for the complete failure of the first SMR batch. The increase of thickness, due to an increase of deposition rate, (deposition time was kept constant), is related to the Nordico sputter tool which lacks a load-lock. For the first depositions, the base vacuum and contaminations with H_2O and O_2 are high. After several depositions, these contamination are reduced. A 1% oxygen addition during sputtering from a SiO_2 target with Ar reduces the deposition rate by a factor of 3. Oxygen may also cause an Al_2O_3 formation on the Al target during reactive AlN sputtering that will result in a pronounced sputter rate decrease. The reduced chamber contamination with oxygen species over time is a possible explanation, why the sputter rate increases over several successive depositions. Other sources for the sputter rate increase might be target heat-up during the process, or depositions on the anode rings which change the plasma characteristics.

Sensitivity simulations have shown that the uppermost layer in the Bragg reflector is the one with the most stringent thickness tolerances [104]. Knowing that the Bragg reflectors fabricated in the Nordico exhibit a variable deposition rate, it is impossible to use these reflectors for SMR fabrication. Later attempts of Bragg reflector fabrication using the same

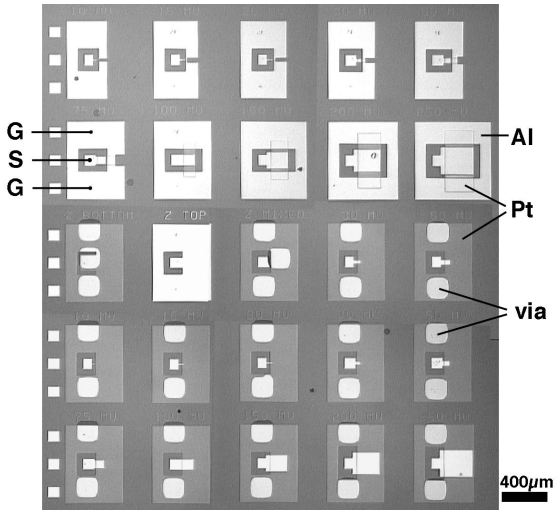

Figure 2.16: Finished single (bottom) and double (top) SMR test structures with sizes varying from 10x10μm^2 to 250x250μm^2. The contact for vertical GSG coplanar probes is left of the center in each structure, the bright areas represent the Al top electrode, and the dark rectangular areas represent the Pt bottom electrodes. Wet etched vias trough AlN for bottom electrode contact are seen as bright circular shapes.

reflector materials were conducted in the Spider tools which has a better base vacuum due to the load-lock. The resulting Bragg reflectors (cross section in fig. 2.15 (b)) are perfectly flat, dense and show a homogenous thickness for all layers.

2.7.2 Design of resonators

Resonators were designed with different surface areas of the electrodes between 10x10 and 250x250μm^2 with a logarithmic increase in 10 steps usable for frequencies from 1 to 10GHz. All resonators were square, because the thickness-to-width ratio is usually larger than 100, so that border effects are negligible, and because it facilitates the pattern generation and allows for a denser packing when using in ladder filter configurations. The distance between the 100x100μm^2 large and 250μm spaced contact pads for GSG coplanar probing and the resonator was minimized to 10μm to reduce parasitic resistances and inductances. Single resonators need via's across the AlN film to contact the bottom electrode. Via's may be avoided by arranging 2 resonators in series, then the two electrode contacts can be established on the top electrodes only. Another advantage of double over single resonators is that they have a larger surface area, which is an important aspect at 8GHz, and they have a better power handling because of the doubling in size to maintain the 50Ω impedance. Figure 2.16 shows an image of fabricated single (bottom of picture, with via) and double (top) SMR. The double resonators are framed with the grounded top electrode to reduce external electrical noise sources.

2.7.3 Resonator fabrication

2 types of resonators will be presented. The first SMR prototypes, identified as *Nordico*, were fabricated with sputtering tools (Nordico, BAS450, AlN-LC) which are multi-purpose machines and have no load-lock. The resulting chamber base vacuum is therefore not very pronounced and is generally in the upper 10^{-7}T range. The second type of resonator, identified as *Spider*, which will later also be used for SMR ladder filter fabrication, is completely fabricated in the Spider tool. This tool is a specially dedicated machine with superior base vacuum due to its load-lock, and high thickness wafer uniformity. The substrates were 4" single side polished Si wafers with a resistivity of 0.1-100Ωcm.

Nordico

The prototype SMR are fabricated on a $(SiO_2/AlN)_5$ reflector on 4" Si wafer as described in paragraph 2.7.1. The reflector layers are deposited with sputter conditions so that the compressive stress of the amorphous SiO_2 film is compensated by an adjustable tensile stress in (002) textured AlN. Because of the known problems of deposition rate drift during the single run multi-layer deposition a new approach was chosen: To increase the thickness precision of the reflector pair closest to the resonator, 4 pairs are deposited first, then the stress and deposition rate of SiO_2 and AlN were re-calibrated before applying the last reflector layer in Nordico. With this approach, the topmost Bragg layer was deposited with a precision estimated as approximately 15%. The (non)-uniformity of films deposited in Nordico is quite pronounced. Deposition tests on AlN and SiO_2 films revealed a concentric parabolic thickness profile with the maximum about 1cm off-center. At a distance of 2cm from the maximum, a 10% decrease in thickness is observed, and 18% at a distance of 3cm. These large variations will inevitably influence the SMR properties like coupling coefficient and quality factor, but also center frequency.

The 85/10nm thick (111) Pt/Ta bottom electrode was sputter deposited in BAS450. The uniformity of depositions realized in this machine are quite homogeneous as the substrates rotate on a drum across the rectangular magnetrons. The properties of this electrode are an electrical resistivity of $\rho_{85nmPt} = 16.5 \pm 0.7\mu\Omega$cm (bulk value 10.6) and a tensile stress of +274±31MPa. The bottom electrode is patterned by dry etching in the STS. Etch residues on the sides of Pt patterns were observed after the Shipley strip resin remover, but could be removed with an ashing process. Then the piezoelectric 310nm thick (002) AlN is deposited in the AlN-LC sputter tool. Vias accross the AlN film for bottom electrode access are opened in 95°C H_3PO_4 for 3min. The 105nm thick top Al electrode is then e-beam evaporated in an Alcatel EVA600. The electrical resistivity measured again with a 4-point-resistivity meter was 2.91$\mu\Omega$cm, slightly higher than the bulk value of 2.65. The top electrode is patterned by dry etching in the STS.

Spider

The fabrication of material and thickness optimized SMR in the new Spider tool followed basically the same process flow as mentioned with the prototype Nordico SMR. However,

this time all layers were fabricated in the Spider tool, i.e. 5 SiO_2/AlN reflector pairs, the 60/10nm thick Pt/Ta bottom electrode, the 380nm thick active AlN film and the 60nm thick AlSi1% top electrode. The bottom and top electrode were patterned by dry etching in a STS Multiplex ICS tool using a Cl_2-Ar chemistry, respectively a BCl_3-Cl_2 chemistry.

We developed a program in the Spider tool to deposit exactly 60/10nm of (111) textured Pt/Ta (300°C, 500W, 15sccm Ar, approx 4mT). The deposition time with these conditions is 24/9s, which is extremely short considering there is no cache to shield the substrate during the time that the plasma is ramped to full power and during which the deposition rate is increasing. The electrical resistivity of 60/10nm thick Pt/Ta was measured with the 4-point method as 19.3$\mu\Omega$cm. 4" wafer uniformity is inferior to ±4% for AlN and better than ±2.5% for SiO_2.

2.7.4 Characterization of SMR microwave properties

Microwave properties of resonators and filters were measured with a network analyzer NA HP8722 D from Hewlett Packard which has a frequency range from 50MHz to 40GHz. Air coplanar GSG probes from Cascade Microtech with 250μm pitch are used to establish contact with the resonators by means of integrated contact areas. The coplanar probes are attached to Cascade Microtech microprobe holders that allow for precise xyz displacement and contacing of the resonators. The samples or wafer are placed on a chuck which can be heated to 100°C. The 1-port S_{11} reflection coefficient of SMR/FBAR, respectively 2-port S_{21} transmission coefficients of SMR passband filters, measured with the NA are transfered to a MAC GBIP acquisition system using a Labview program. The one-port or full two-port measurement is calibrated with an impedance standard substrate from Cascade Microtech Inc. 101-190B with open/short/50Ω on each port, and open/short for the transmission calibration. The complex resonator admittace Y is calculated from the complex S_{11} parameter as

$$Y = \frac{1}{Z_0}\frac{1 - S_{11}}{1 + S_{11}} \tag{2.32}$$

where $Z_0 = 50\Omega$ is the characteristic impedance of the system. The resonator characteristics quality factor Q and coupling coefficient k_t^2 are extracted from the measured admittance curve using equations 2.22, 2.28, and 2.11 and a Matlab program which treats the measurements automatically.

Some of the 1-port S_{11} measurements were carried out using a superposed dc bias. For this purpose a Bias Tee EP-62 (4-18GHz, 200V breakdown voltage) from KDI Triangle was inserted into the electric circuit. This permits injection of a dc voltage into the rf circuit without affecting the flow of the rf signal through the main transmission path.

Nordico

The admittance measured on a double (2 series) 50x50μm^2 sized SMR, which matches 50Ω, is shown in figure 2.17 (a). The effective coupling coefficient is determined as 3.95%, and the series quality factor as 264. The mean frequency of resonators over this 4" wafer was 7.8GHz with a large frequency distribution between 7.2-8.7GHz due to large film thickness

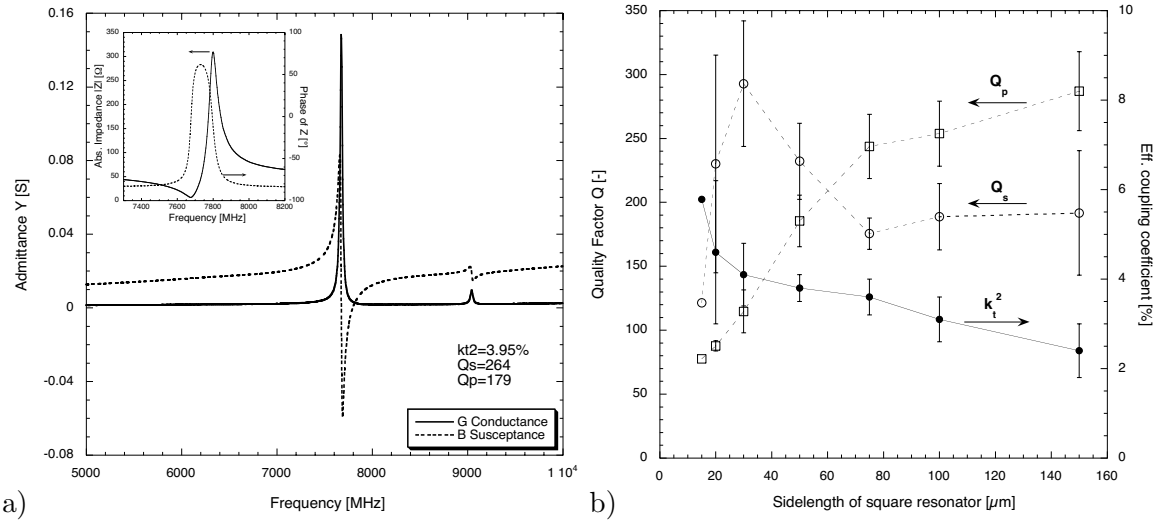

Figure 2.17: (a) Admittance of a double SMR (Nordico) with 50x50μm^2 surface. The inset shows the absolute impedance along with the phase of the impedance around the resonance. Between the series and parallel resonance, the phase changes from capacitive to inductive. The quality factors derived are Q_s=264 and Q_p=179 with an effective coupling coefficient of 3.95%. (b) Effect of resonator areas (2 series resonators with the side-length of square resonators as parameter) on the quality factor □=Q_p, ○=Q_s and coupling coefficient measured on a large number of SMR distributed over a 4" wafer.

variations. The relative dielectric constant was $\epsilon_r = 10.8 \pm 0.8$ with a loss tangent of $< 0.2\%$ at 10kHz.

A spurious resonance is observed at 9GHz. As previously mentioned, the reflector layers SiO_2/AlN were too thick with respect to the target frequency of 8GHz. Numerical simulations taking into account the increase of reflective layer thickness yield the same spurious response. These spurious resonances are aggravated when the layers are not only off-centered but also when each layer has a different thickness. The increased reflector layer thickness shifts the resonator center frequency downwards, and also causes spurious resonances at the high frequency side. Furthermore, the effective coupling coefficient will also be reduced, according to our numerical simulations.

The impedance phase, given in the inset, shows a slight asymmetry, which is also manifested by the difference of the series $Q_s = 264$ and parallel $Q_p = 179$ quality factor. This reduction of Q_p of 32% was also observed by Ruby et al. [112], who stated a difference of typically 20-50%. They were able to level the difference by changing the design of the resonators. We also compared the behavior of the quality factor as a function of resonator size, which is equivalent to an electrical mismatch (fig. 2.17 (b)): The series quality factor increases up to 30x30μm^2 and then decreases, whereas the parallel quality factor increases over the whole resonator size range observed. Q_s matches Q_p at approximately 60μm. The effective coupling coefficient becomes smaller when increasing the resonator size. The deter-

mination of Q and k_t^2 for resonators smaller than 30x30μm^2 is difficult because of spurious resonances.

BVD model simulations with parasitic elements might explain these results: The bottom electrode resistance is calculated, based on the metal film resistivities and geometry of electrode, as approximately 2Ω for the 50x50μm^2 double resonator, respectively 1Ω for the top electrode. Introducing a series resistance of this magnitude into the BVD model simulation results in a slight increase of the effective coupling coefficient and a decrease in the parallel quality factor. This observation is contradictory to the observed behavior. Hence an increase in parallel resistance due to larger electrodes does not explain the observed trends. When further investigating the influence of the possible parasitics parallel resistance, parallel capacity, and series inductivity, only the parallel capacity leads to a reduction of the effective coupling coefficient. An increase in parasitic parallel capacity reduces the parallel resonance frequency and thus the effective coupling coefficient, which corresponds to our observations. The increased parasitic parallel capacity may be explained with the resonator design, i.e. for larger top electrodes, there is an increased parallel gap between signal and ground electrode which acts like a parallel plate capacity.

The ohmic losses introduced by the electrodes reduce the quality factor of the resonator: Simulation results show that a 3Ω loss results in a decrease of the series quality factor of -64%, respectively -78% for 6Ω resistance.

Spider

The microwave admittance of SMR completely fabricated in the Spider tool exhibit a very strong and spurious-free resonance. Measured coupling coefficients are between 5.0 and 6.0% whereas the quality factor Q_s varies between 200 and 360. Figure 2.18 shows two examples of such resonators: (a) 30x30μm^2 double SMR which has too high an impedance (approx. 150Ω) and shows some spurious ripples on the high frequency side of f_a. The quality factor and coupling coefficient are nonetheless very high with 360 and 5.9%. The 50x50μm^2 double resonator (b) is perfectly impedance matched and shows very little spurious signals. The coupling coefficient is high with 6.0%, the quality factor however is somewhat smaller with 210 compared to the 30x30μm^2 resonator.

The measured coupling coefficients compare well with the numerical simulation results presented in paragraph 2.5.4, page 43, which suggest an effective coupling coefficient of around 5.6% using the above stated film thicknesses. The spurious signals are difficult to understand unless one performs 2-dimensional simulations. From what is known from the literature, c.f. paragraph 2.2.4, a width-to-thickness ratio below 100 makes the resonator prone to spurious resonances. The 30x30μm^2 resonator has approximately a width-to-thickness of 80, while the 50x50μm^2 has a width-to-thickness ratio of 130.

The relative dielectric constant measured on the 380nm thick AlN on two series 1x1mm^2 capacitors was ϵ_r =10.45 at 10kHZ with a dielectric loss tangent of 0.1%

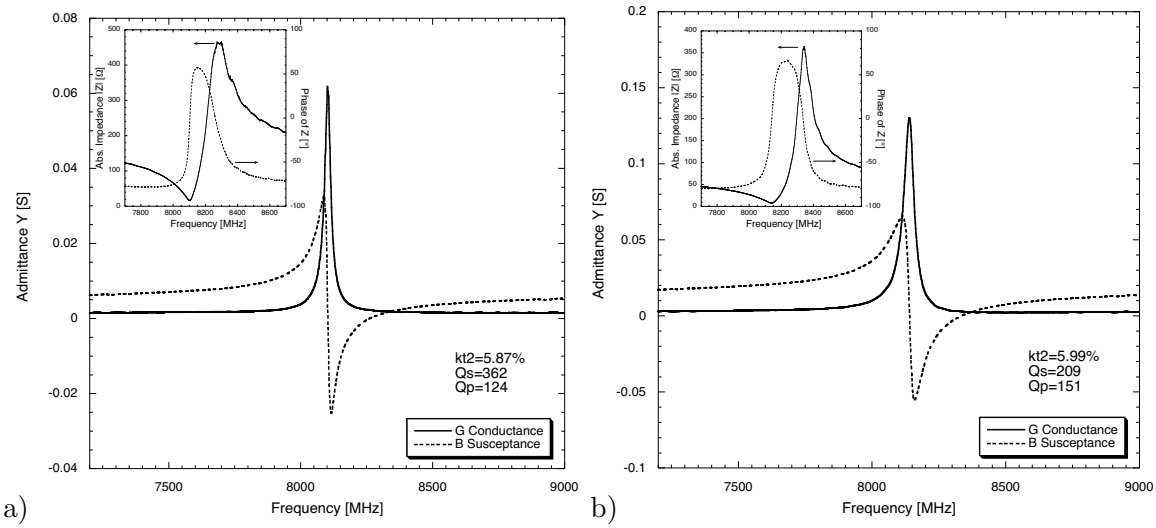

Figure 2.18: (a) Admittance of a double SMR with 30x30 (a), respectively 50x50μm^2 (b) surface area completely fabricated in the Spider tool. The inset shows the absolute impedance along with the phase of the impedance around the resonance. Between the series and parallel resonance, the phase changes from capacitive to inductive. The quality factor derived is Q_s=362 and Q_p=124, with an effective coupling coefficient of 5.87% for (a), respectively Q_s=209 and Q_p=151, and k_t^2=5.99% for (b). The 50x50μm^2 resonator has a better impedance matching, and the ripples at the high frequency side of the resonance in the impedance signal observed in (b) are weaker.

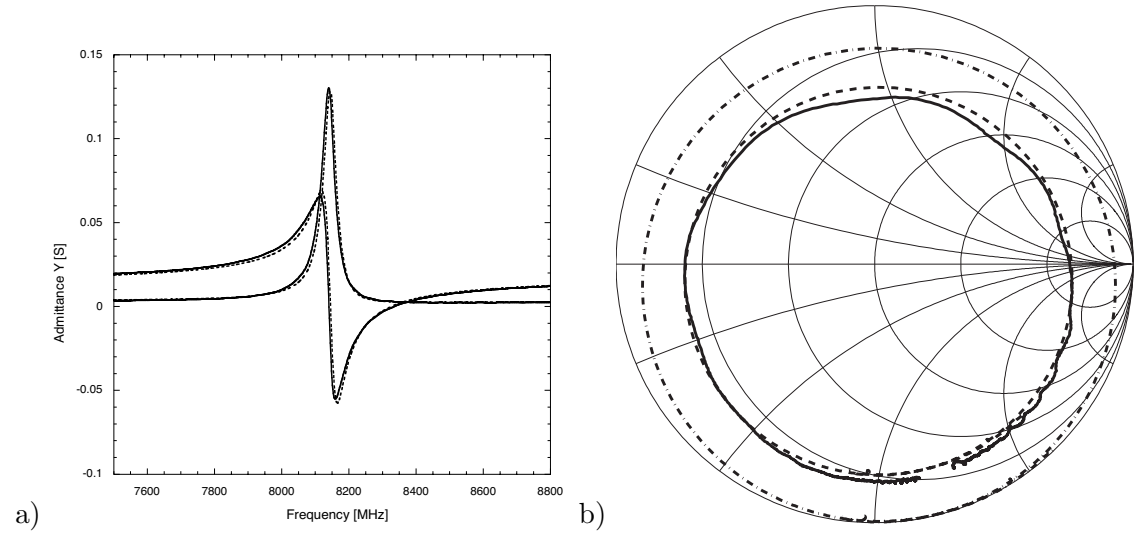

Figure 2.19: Numerical 1-D simulation of a SMR with additional parasitic 5Ω series and 500Ω parallel resistance compared to the measured admittance curve (solid line) from figure 2.18 (b). The left image shows the real and imaginary part of the admittance, and the right image the numerical simulation (dashed line) on a Smith chart before and after applying the parasitic resistances.

2.7.5 Comparison of measured resonator admittance vs. numerical model simulations

To validate the numerical model and verify the assumed material properties the simulation results are compared to the measured resonator admittance.

The numerical simulations are based on the material properties from paragraph 2.5.1. To obtain a good accordance between the measured and simulated f_r and f_a, the AlN material coupling coefficient is chosen as 5.8%. The result of this comparison is shown figure 2.19. The solid line represents the measurement and the dashed line the simulation with parasitic elements. The real and imaginary admittance are compared in (a), and the admittance represented on a Smith chart is given in (b). The outer dashed circle in (b) represents the numerical simulation without parasitic elements. To obtain a good fit, a parasitic series resistance of 5Ω and a parasitic parallel resistance of 500Ω has to be added to the physical model (c.f. loss model in fig. 3.13 on page 114). The result with these parasitics is shown in the same plot as the smaller dashed circle and also in (a) as admittance.

The good accordance between simulation and measurement confirms the validity of the numerical model and assumed materials parameters. This model is very appropriate to investigate geometry and material influences on the resonance. The obvious lack of parasitic capacitance or inductance are the result of our optimized SMR design. The high series resistivity, which causes principally a large reduction in the electrical quality factor of the resonator, is due to i) relatively long top electrode conductor lines, ii) thin top

electrode conductor leads with an electrical resistance of 2-3Ω, and iii) the use of Pt as bottom electrode which by itself has an approximate resistance of 3Ω. Point i) is imposed by the requirement for coplanar probing and will be reduced in filters where the distance between SMR elements is minimized to a few micrometers, ii) could easily be improved by applying an additional thick metallization layer on top of the existing top electrode on the piezoelectric inactive areas, but this requires an additional process step, and iii) may only be improved by using a high conductivity and high acoustic impedance material like Mo because the electrode thickness is imposed and fixed by the SMR working frequency. The low parallel resistance is equivalent to electrical leakage across the film. The parallel conduction is well explained by a loss tangent of AlN that amounts to about 15% at 8 GHz (measured as 0.2% at 1 kHz and being used for the numerical simulation), or alternatively to surface conduction between neighboring electrodes in multi-resonator structures. This could be a result of etching residues.

As evoked just above, the need for high conductivity bottom electrodes is of high importance at microwave frequencies as considered in this work. This was the principal motivation for the development of the Mo electrodes discussed earlier. Unfortunately, as we have seen, the growth of AlN on these electrodes was not as good as on platinum electrodes, and the piezoelectric coefficient was lower. Nevertheless, we fabricated 8GHz SMR using 60nm thick Mo bottom electrodes, 60nm Al top electrodes and 470nm thick AlN film. As expected from the $d_{33,f}$ measurements and the rocking curve FWHM, smaller coupling coefficients of only 3.9-4.6% were obtained. The quality factor Q_s of 210-360 was however high and comparable to the SMR with a platinum electrode.

2.7.6 Frequency dependency on temperature and applied dc-field.

Temperature coefficient of frequency TCF

The requirement of frequency stability in real life environments with changing temperature is important, even more so because the achievable filter bandwidth demanded today are already limited with the available AlN coupling coefficient. If the filter center frequency shifts too much during temperature variations, then precious bandwidth has to be set aside for temperature compensation. Each layer in the SMR has its own thermal coefficient of stiffness resulting in a change of the individual layer velocity, and thus anti-resonance frequency when the temperature changes. Figure 2.20 (a) shows the dependency of the anti-resonance frequency f_a on temperature change between 20 and 90°C as measured on a double SMR. The wafer is heated on the chuck which holds the wafer in the probing station. Due to the bad contact between chuck and wafer, the indicated temperature is afflicted with an estimated error of ±6°C.

The temperature coefficient of frequency (TCF) is linear in the temperature range investigated and amounts to -18ppm/K. The TCF of an ideal AlN resonator with infinitely thin electrodes is theoretically -25ppm/K [141, 50]. The positive temperature coefficient of SiO_2 in the SiO_2/AlN reflector compensates the negative TCF of AlN which result in the observed value of -18ppm/K [101].

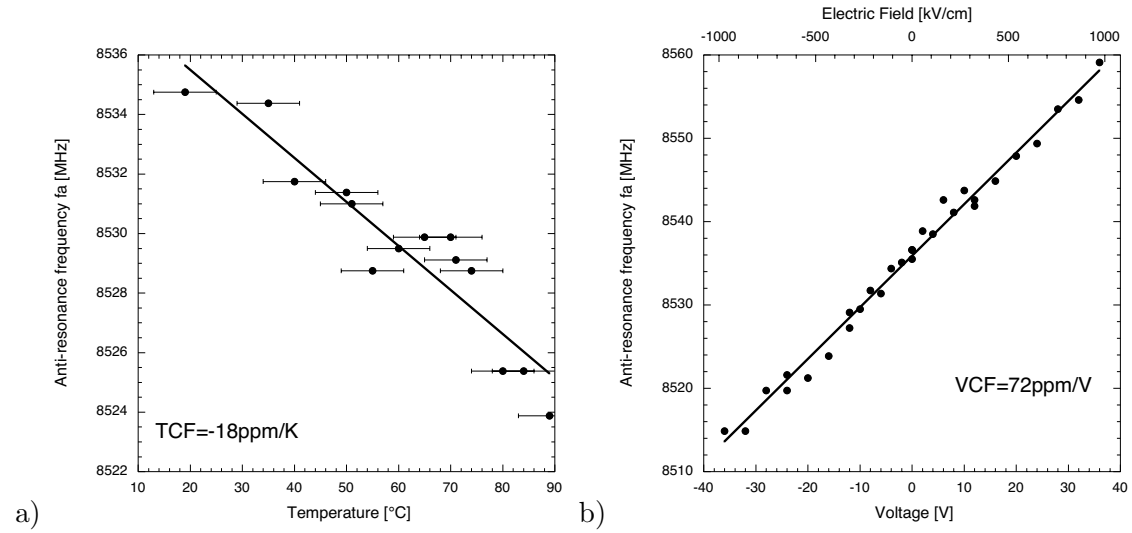

Figure 2.20: Dependency of the anti-resonance frequency on temperature, TCF (a), and on voltage, VCF (b).

Voltage coefficient of frequency VCF

We were interested in the possibilities of voltage tuning of SMR for channel selection or TCF compensation. A dc voltage applied to the SMR should result in some thickness change through the inverse piezoelectric effect and the electrostrictive effect. Assuming only the piezoelectric contribution, a $d_{33,f}$ value of 5pm/V, an AlN film thickness of 380nm at a center frequency of 8GHz, and a sensitivity of the AlN film of -12MHz/nm$_{\mathrm{AlN}}$ (value obtained with numerical simulations) should theoretically result in a voltage coefficient of frequency VCF of approximately 7.5ppm/V.

Figure 2.20 (b) shows the response of the anti-resonance frequency for an applied dc bias on the top electrodes of a single SMR. The anti-resonance frequency increases linearly in the interval from -1 to +1MV/cm for the applied field. The measured VCF is 72ppm/V on the 8GHz SMR with 380nm thick AlN.

The value of 72ppm/V is an order of magnitude larger than what can be expected from the inverse piezoelectric effect alone. The change in anti-resonance frequency is therefore mostly due to a change in sound velocity or elastic stiffness constant. This so-called elasto-electric or electroacoustic effect has been observed on a number of materials, e.g. $LiNbO_3$, $LiTaO_3$ or SiO_2 [6]. The change in the elastic stiffness constant by an applied electric field are described by a fifth rank tensor, called elastoelectric coefficient g_{ijklm}

$$C^*_{ijkl} = C^0_{ijkl} + g_{ijklm}E_m \tag{2.33}$$

where C^0, C^* are the modulus of elasticity and E_m the electric field. The effective elastoelectric coefficient g_{eff} [1] is determined from the change of anti-resonance for an applied

electric field on a thickness-extensional resonator as in figure 2.20 (b)

$$\frac{\Delta v}{v} = \frac{\Delta f_a}{f_a} = \frac{1}{2\rho v^2} g_{\text{eff}} E = \frac{1}{2c^D} g_{\text{eff}} E \tag{2.34}$$

where the relative frequency measurement $\Delta f_a / f_a$ corresponds to the relative elastic wave velocity $\Delta v^D / v^D$. The effective elastoelectric coefficient g_{eff}

$$g_{\text{eff}} = g + \frac{2e}{\epsilon} \cdot Q - \frac{e^2}{\epsilon^2} \chi \tag{2.35}$$

contains contributions of the e piezoelectric and Q electrostrictive coefficients, as well as ϵ dielectric and χ non-linear dielectric coefficients. From the measured VCF we can calculate g_{eff} as 23.0 N/mV

Voltage tuning of FBARs resonance frequency was mentioned by Ruby and Merchant [111]. The VCF of a 3.5GHz FBAR was approximately 10ppm/V for the second harmonic with a slight non-linearity, and significantly smaller for the 1st harmonic. The smaller value of the VCF is due to the thicker AlN film and therefore lower field for the same applied voltage. We can conclude that the VCF increases with increasing frequency and might be exploitable for BAW resonators, filters or VCO's at frequencies above 5GHz.

2.8 Film bulk acoustic resonators obtained by surface micromachining

The fabrication of surface micromachined FBARs differs from SMR fabrication in the following way: a) the resonator has to be deposited on a sacrificial layer, b) VIAs have to be etched across the upperlying films to access the sacrificial layer, c) the sacrificial layer has to be removed completely, without affecting the resonator materials, and d) the released membrane constituting the FBAR and the edge line around the sacrificial area has to be mechanically stable, flat (stress-free) and not sticking to the substrate. Sticking of the membrane can be avoided after wet etching either by freezing the rinsing agent and then sublimating it in a vacuum, thus avoiding capillary forces which arise during normal drying, or by using pillars which prevent the membrane from bending. Another alternative would be dry etching of the sacrificial layer.

2.8.1 Sacrificial layer fabrication

Among various surface micromachining techniques developed and reported in recent years, the polysilicion process, which involves silicon dioxide sacrificial layer wet etching with HF or BHF followed by supercritical carbon dioxide drying process [9] or rinsing in alcohol, to avoid stiction, can be considered as standard. The use of organic sacrificial layers released in oxygen plasma have also been successfully employed and are compatible with aluminum electrodes [128]. However these processes suffer from some inherent problems like stiction related to wet etching, or low etch rates (largely under 1μm/min for organic layers), that make the process not very efficient. FBAR require the release of relatively large membranes with under-etch distances of over 30μm. Lately a new method for surface micromachining with silicon sacrificial layer dry etching with lateral etch rates of up to 15μm/min has been developed by Frédérico et al. [22]. This process was not yet available though at the time of doing the present work.

We chose to deposit the BAW resonators on top of a patterned silicon dioxide layer which acts as sacrificial layer. The SiO_2 is thermally stable and compatible with the following resonator fabrication at temperatures of up to 350°C. It is common to use silicon dioxide as sacrificial layer in conjunction with polysilicon for MEMS fabrication and diluted or buffed HF as etchant. Access VIAs across the continuous AlN film to the sacrificial layer are opened once the resonators were completely finished and the sacrificial layer is etched isotropically to release the membranes. The AlN film, on which the resonators are defined, constitutes the self-supporting membrane itself, there is no additional supporting membrane layer needed.

Positive vs negative sacrificial layer

Two different approaches for the sacrificial layer placement were persued: a) depositing the sacrificial layer on top of the substrate and pattern it (Satoh et al. [115]), and b) etch 'pools' into the substrate, cover the wafer with low pressure low temperature chemical vapor

deposition (LPCVD) doped SiO_2 in a Centroterm oven to fill the pools and then planarize and remove the SiO_2 down to the substrate level (Ruby et al. [112]). Figure 2.21 compares the two approaches schematically. Method a) is faster to be realized and uses standard deposition and patterning techniques. It's obvious disadvantages are the border area over the edge of the sacrificial layer which is the most fragile part in the membrane. It also presents problems with the top electrode coverage over the step which is thin and therefore introduces high ohmic losses. To overcome this an additional second top electrode applied just over the border, outside the active resonator area should be applied which necessitates another process step. Method b) results in almost flat membranes which are very rugged because of the lack of a step. To obtain pools filled with the sacrificial layer the SiO_2 layer outside of the pools has to be removed and planarized down to the substrate level using chemical mechanical polishing (CMP). This represents one more process step when compared to approach a). CMP is quite a new process and some development work had to be done to find optimized parameters. CMP is a method commonly used in the semiconductor industry for the planarization of interlayer dielectric insultators. The polishing combines mechanical action with chemical etching using an abrasive slurry dispersed in an alkaline solution (pH>10). The rate of material removed is controlled by the slurry flow and pH, applied pressure on the polishing head, rotation speed and operating temperature. CMP is an excellent planarization method yielding a surface roughness of less than 1nm over large dimensions, but it is slow, with removal rates in the range of 100nm/min, compared to 1μm/min for standard polishing. The details of the employed CMP process are 40rpm head speed, 30rpm plate speed, 0.5bar working pressure, respectively 0.2bar backside pressure. The removal rate of the 1600μm thick PSG layer was 330nm/min and a dishing of the individual pools of 80-200nm from center to the border of the wafer was observed. Optical microscope inspections also revealed particles incorporated in the pool area which could not be removed with ultrasonic cleaning.

Figure 2.22 (b) shows the good step coverage of sputter deposited AlN over a patterned SiO_2 structure. Figure (a) shows the step coverage of AlN over patterned SiO_2 and the patterned Pt/Ta bottom electrode. The electrode shows a nice tapered angle which results in a good step coverage. The SiO_2 on the other hand was over-etched during the patterning process and hence the membrane step is large and the border gets unnecessary weakened. This was avoided thereafter by using a more appropriate dry-etch process of the SiO_2 with a higher selectivity towards Si and better etch-time control.

Choice of sacrificial layer

Non-doped, boron (BSG) and phosphor (PSG) doped silicon dioxide glasses are deposited with PECVD, PCD and LPCVD methods. These amorphous films will be etched isotropically. The doping of the oxide is especially recommended when fast etch rates are of major concern. The main effect of doping is basically to create a less dense silicon dioxide network. Since the etching process takes place at the interface etchant-SiO_2, surface chemistry of silicon dioxide must be considered: Silanol (SiOH) groups are present on the surface of silicon dioxide. The silicon-oxygen network must be opened to facilitate the nucleophilic attack

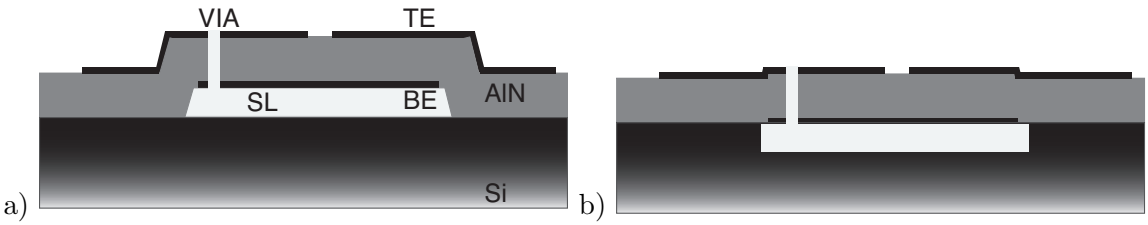

Figure 2.21: Schematic drawing of FBAR with positive (a) and negative (b) sacrificial layer (SL). Top electrode (TE), bottom electrode (BE).

of the fluorine onto the silicon. Opening of the silicon-oxygen network is done in solution by an acidic or basic species that interrupts the network and forms a silanol group on the surface. This provides the fluorine with enough room to attack the silicon. Any florinated species in the hydrofluoric acid solution may supply the fluorine for this reaction.

Phosphor Silicate Glass is deposited for the positive sacrificial layer in a Plasma Enhanced Chemical Vapor Deposition PECVD Alcatel 601-D reactor ($\pm 5\%$ wafer uniformity). The oxygen plasma is generated using the inductively coupled plasma (ICP) method. The gases used are silane (SiH_4) and trimethylphosphite TMPI ($P(OCH_3)_3$). A doping of 5% percent is achieved. The thickness of sacrificial layer relative to the AlN resonator thickness is chosen to be 1, which translate to a thickness of 300nm for 8GHz resonators. This implies that the desired air-gap has an aspect ratio width-to-thickness ratio of more than 100 considering 50Ω matched resonators that have diameters $>30\mu$m. The PSG is anisotropically patterned using a STS Multiplex ICP dry etcher and CF_4, respectively C_4F_8-H_2 chemistry for higher selectivity towards the photoresist.

For the negative sacrificial layer approach pools were dry etched into the Si substrates using the STS etcher with a Cl_2 chemistry. These pools and the rest of the substrate were covered with LPCVD PSG. The atmosphere for LPCVD was a mixture of silan (SiH_4), phosphin (PH_3) and oxygen. The doping with phosphor in the PSG layer is estimated at 6%. The wafer uniformity is $\pm 1.2\%$ which is sufficient for planarization by means of CMP.

Wet etchant, etch rate and selectivity for sacrificial layer

Two different wet etchants were tested as candidates for the silicon oxide sacrificial layer removal and compatibility, respectively high selectivity, with respect to the resonator materials Al, AlN, Pt and Mo. The etchant must posses a sufficiently high lateral etching rate. The first is buffered hydrofluoric acid BHF (NH_4F 40% + HF 50% 7:1 volume ratio), the second is SILOX etch (NH_4F 40% + CH_3COOH 100% + H_2O 4:4:2 volume ratio). The etch rate of each sacrificial layer is determined for both etch solutions using a standard photoresist (PR Shipley 1813, 1.5μm thick) containing vias. This PR is deposited onto a continuous SiO_2 layer deposited on a 4" Si substrate ($PR/SiO_2/Si$). The wafers are dipped into the etch solution for a determined time, rinsed in deionized water and then spin dried under flowing N_2 gas. The etch front progression can be measured with an optical micro-

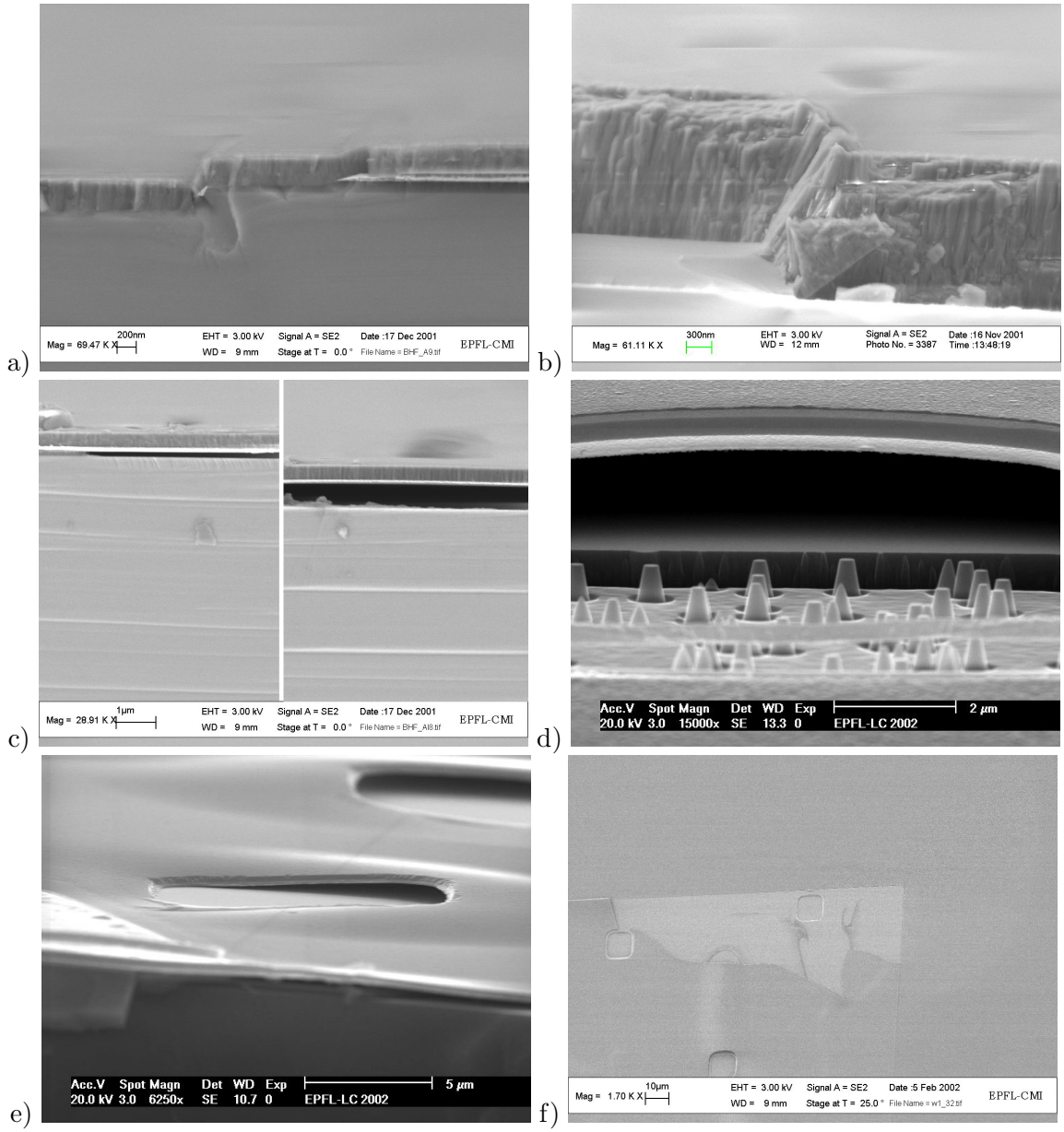

Figure 2.22: (a) Step coverage of AlN over patterned Pt/SiO_2 and (b) over SiO_2. (c) released membranes showing non-complet etching and etch residues. (d,e) Warping and twisting of released membranes around VIAs due to compressive film stresses. (f): Released and fractured test membrane ($AlN/SiO_2/Si$) showing VIAs and exposing part of the etched sacrificial layer where the membrane is missing. Etch residues are visible indicating a non-complete sacrificial layer removal.

Table 2.7: Lateral under-etch rates for different doped and non-doped silicon dioxides obtained with 2 wet etch agents BHF and SILOX. The lower part of the table shows the etch rates for the resonator materials which determines the selectivity.

Sacrificial layer	BHF 7:1		Silox 4:4:2	
	Thickness [nm]	Lat. etch rate [μm/min]	Thickness [nm]	Lat. etch rate [μm/min]
PECVD SiO_2	200nm	0.5±0.3	600nm	1.0±0.1
PECVD PSG	465nm	2.4±0.6	480nm	0.9±0.1
PECVD BSG	260nm	1.3±0.4	470nm	1.0±0.1
PVD SiO_2	270nm	0.8±0.2	-	-
LPCVD PSG	-	-	1600nm	0.85±0.05
AlN	not measurable			not measurable
Al	high and irregular			0.1±0.1
Pt	not measurable			not measurable
Mo	not measurable			not measurable

scope. Table 2.7 summarizes the results of these tests. The thickness of each sacrificial layer is indicated as well as the measured etch rate.

The tested SiO_2 films laterally under-etch with 0.5-2.4μm/min. BHF attains the highest rate of 2.4μm/min for the phosphorous doped SiO_2. But the drawback of BHF is that it also attacks the Al used as top electrode in the resonators. BHF further exhibited sometimes an irregular etch front or occasionally a complete stopping of the etch process if the wafer was dried and re-etched. This is the reason for the higher standard deviation reported for BHF in table 2.7. Silox on the other hand has an almost identical etch rate for all tested silicon oxides (1μm/min), shows an uniform etch front progression and has a high selectivity towards all tested resonator materials.

Based on these results we decided to use Silox for all subsequent etching processes on resonators and PSG as sacrificial layer. As we also decided to use Al top electrodes and aluminum is attacked by Silox with a modest etch rate, we must leave the photoresist used for VIA dry etching as protection during the Silox etch. This introduces the problem of aluminum corrosion caused by absorbed chlorine in the photoresist during the dry etching process. The choice of the Al top electrode is imposed by the high operating frequency of 8GHz. Pt would be the better choice from the wet etch point of view but it reduces k_t^2 too much at 8GHz (c.f. fig 2.7).

Figure 2.23 shows test membranes (AlN/PSG/Si) which are integrated onto the final FBAR wafer batch after a partially accomplished sacrificial layer etch (a,b) and complete release (c) after 20min. The difference in (a) and (b) is the VIA size, 5x5μm^2 vs. 10x10μm^2. Both have a VIA spacing of 50μm. The film thicknesses are 300nm for the sacrificial layer and the AlN film respectively. Both designs show a uniform and regular etch front progression. The design with larger VIA shows a slightly higher etch rate. Thus the membrane is more released and the effects of compressive film stress (-100MPa compressive)

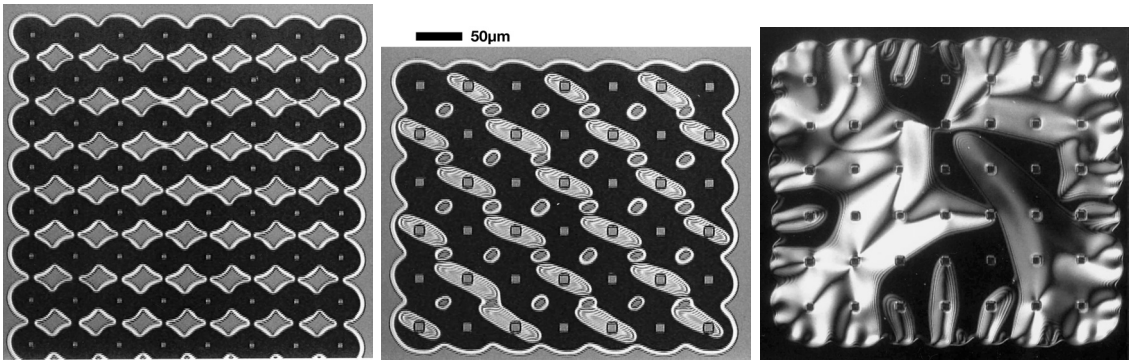

a) b) c)

Figure 2.23: Etch front progression seen through the transparent AlN membrane after partial etch for 20min in Silox (a: 5x5μm VIA 50μm apart, b: 10x10μm VIA 50μm apart, AlN stress -100MPa compressive) and fully released membrane also after 20min Silox etch (c) on another wafer exhibiting a compressive stress of -550MPa which is evidenced through film warping and twisting. The AlN/SiO_2 film thickness is 300/300nm.

start to show as film bending (diagonal ellipses). Picture (c) shows a fully released AlN membrane on another wafer with -550MPa compressive film stress, which deforms and warps the membrane.

In summary, only a weak influence on the under-etch rate is seen for VIA diameters ranging from 5 to 100μm, and no significant influence was noticed for the different sacrificial layer thicknesses. This suggests that the convection and/or diffusion of the etching solution inside the sacrificial layer cavity is high enough and the mass transport is not limiting the etch progression. Satoh et al. only used 100nm thick sacrificial layers and did not report on etch limitations [115, 116].

Design of resonators and sacrificial layer

An *apodized* shape (no two sides of a resonator are parallel) of TFBARs should suppress spurious resonances from trapped lateral modes [110, 112]. These spurious resonances cause ripple in the passband of filters. We chose square and polygonal shaped resonators to investigate the effect of shape on the ripples. The VIAs are square with a sidelength between 3-10μm. VIAs were placed outside and also inside the active resonator area, to study their influence on spurious resonances. The number and distance between VIAs was varied as to have an inter-VIA distance of approximately 30-50μm. This allows the release of the membranes in less than 1h. The active area of resonators was chosen between 500 and 45'000μm^2 which allows for the fabrication of 50Ω matched resonators in the frequency range of 2-10GHz. Because the aspect ratio of the air gap exceeds 100, some designs incorporated membrane supporting points underneath the membrane (in inactive resonator area) which should help avoid stiction and film bending problems.The length of the electrode conductor

lines was reduced to a minimum to avoid ohmic losses. Double series resonators were used to avoid AlN layer etching.

Fabrication of resonators

Out of the two approaches (positive/negative sacrificial layer) only the positive method yielded resonators with acceptable performances. As previously described, particles which are used for CMP planarization were incorporated into the sacrificial layer and lead to very high roughness, and moreover, the pools filled with PSG cold only be etched partially with Silox: An explanation is that the chemical solution used for CMP modified the PSG and made it more resistant towards Silox. Thus we describe here only the positive approach: A 300nm thick PSG film was deposited using a PECVD process in an Alcatel 601-D tool. The film was patterned by dry etching in a STS Multiplex ICP with a CF_4 chemistry. The selectivity towards the underlying Si is not too high which can lead to unwanted over-etches and hence a higher step for the membrane edge.

The resonators themselves (Al/AlN/Pt/Ta 100/290/100/10nm centered for 8GHz resonance frequency) are fabricated analogous as described in paragraph 2.7.3, page 57, for the SMR *Nordico* fabrication, i.e. the bottom electrode was sputter deposited in the BAS450 tool, the AlN film was sputter deposited in the AlN-LC sputter tool (4-5mT N_2, 500W, 400°C) and the top electrode was applied using e-beam evaporation in an Alcatel EVA600. The bottom electrode showed a tensile stress of +300MPa and an electrical film resistivity of 15.9$\mu\Omega$cm (bulk: 10.6$\mu\Omega$cm) measured with the 4-point method. The AlN film showed -100/-550MPa compressive stresses for the 5/4mT depositions and a relative dielectric constant of ϵ_r=10.5. The piezoelectric constant $d_{33,f}$ is 4.1pm/V. The electric resistivity of the Al electrode was measured as 3.6$\mu\Omega$cm (bulk: 2.65$\mu\Omega$cm) and it exhibited a +50MPa tensile stress. Figure 2.24 (a) and (b) show 2 different designs with double series resonators, one with a membrane per resonator the other one single membrane before the VIA opening. The VIAs which access the sacrificial layer were opened with the STS dry etcher using Pt and Al etch as described previously. The AlN was also opened during the dry etching using a Cl_2-Ar chemistry. Because some VIAs are located within the metallized resonator area for test purposes, this 3 step etch Al-AlN-Pt had to be chosen. This did not complicate the process much, it implied only a slightly longer etch time and the masking photoresist had to be spun somewhat thicker.

The release of the membranes was accomplished during 20min in the Silox etch bath. The complete removal of the oxide was confirmed by optical microscope and the resin was then removed with a Shipley 1165 strip resin remover followed by an oxygen plasma. Finished and released FBAR with 2 different designs are shown in figure 2.24 (c: square) and (d: apodized). Close-up views of the corresponding VIAs (e) and (f) show the free standing membrane built up of the Pt bottom electrode (white) and the above AlN and Al films which are each etched laterally about 1μm. The white spots in (f) represent residues of overetching into the silicon substrate, also seen in figure 2.22 (d).

We did not have the necessary means for characterizing the extend of the sacrificial layer removal: The etch front progression was observed by optical light microscopy and cross

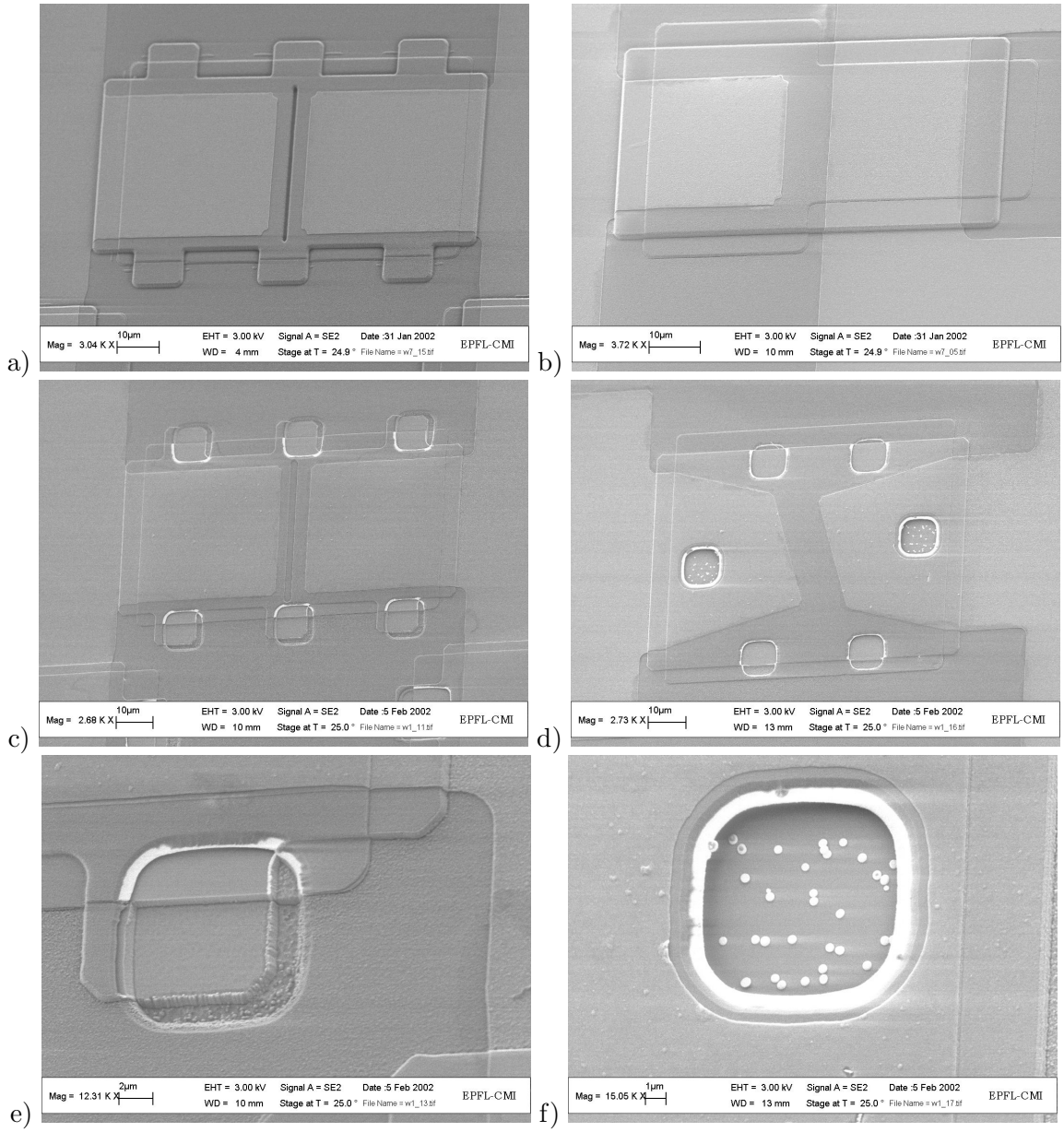

Figure 2.24: FBAR before (a) and after VIA opening and membrane release (c). The detailed view (e) shows the Al/AlN/Pt stack with the underlying air gap and the etched Si substrate. (b,d,e) same sequence on different FBARs, showing an apodized design on a single membrane.

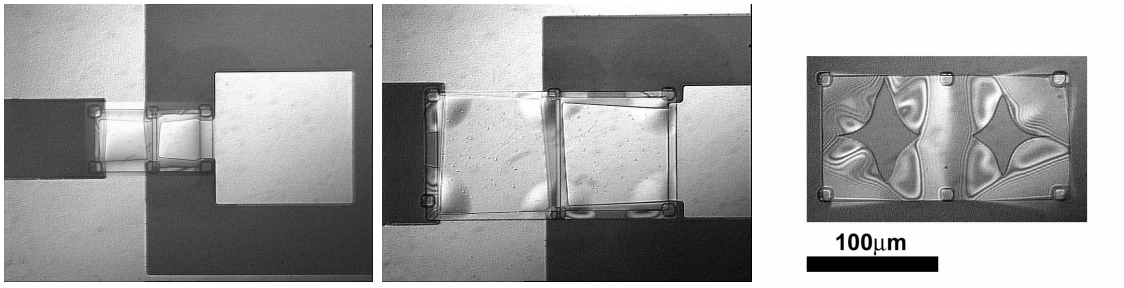

a) b) c)

Figure 2.25: Released apodized double FBARs with sizes of 30x30μm^2 (a), respectively 75x75μm^2 (b) and the corresponding etch test structure (c) showing partial etching of the sacrificial layer for the 75x75μm^2 membrane.

sections of released membranes were observed with SEM. The cross section observation required the breaking of the membrane structures that might damage the membrane (figure 2.22 (c)). This made the characterization of the etch progression difficult. But from fig. 2.22 (c) it is obvious that not all the sacrificial PSG was removed and residual PSG sticking to the substrate or the membrane was also observed. It would be helpful to have access to a Focus Ion Beam FIB microscope to cut the membranes in-situ and control the quality of the etches and look for possible etch residues. Figure 2.22 (f) reveals the quality of the sacrificial layer removal. The membrane cracked and exposes the underlying air gap. Etch residues are clearly visible indicating an uncomplete removal of the sacrificial layer.

2.8.2 Characterization of FBAR microwave properties

A complete membrane release was obtained on the wafer with -550MPa AlN film stress, but only partial release of membranes for the wafer with -100MPa compressive stress after an etch time of 20min. The latter wafer exhibited the sometimes observed etch discontinuity and was thus not used for electrical characterization. A picture of a released test membrane is shown in figure 2.23 (c). It exhibits film warping and twisting due to the high compressive stresses. Figure 2.25 shows pictures of fully released 30x30μm^2 (a) respectively only partially released 75x75μm^2 (b) FBARs. The corresponding etch test structure (c) confirms the partial etching of the larger membranes. Film bending is also clearly observed due to high compressive stresses in the AlN layer. Figure 2.22 (d) and (e) both show the bending of the membrane. This bending may even lead locally to a contact between the membrane and the substrate. Some of the observed membranes were broken, mostly on the edge, indicating not sufficient edge strength due to too high a step from the substrate to the sacrificial layer. The step was larger than needed because of excessive over-etching during the sacrificial layer patterning. During this process step, it was important to remove completely the SiO_2 down to the substrate level to avoid under-etching during the membrane release process.

$\Theta-2\Theta$ XRD measurements on the wafer with fully released membranes showed an almost

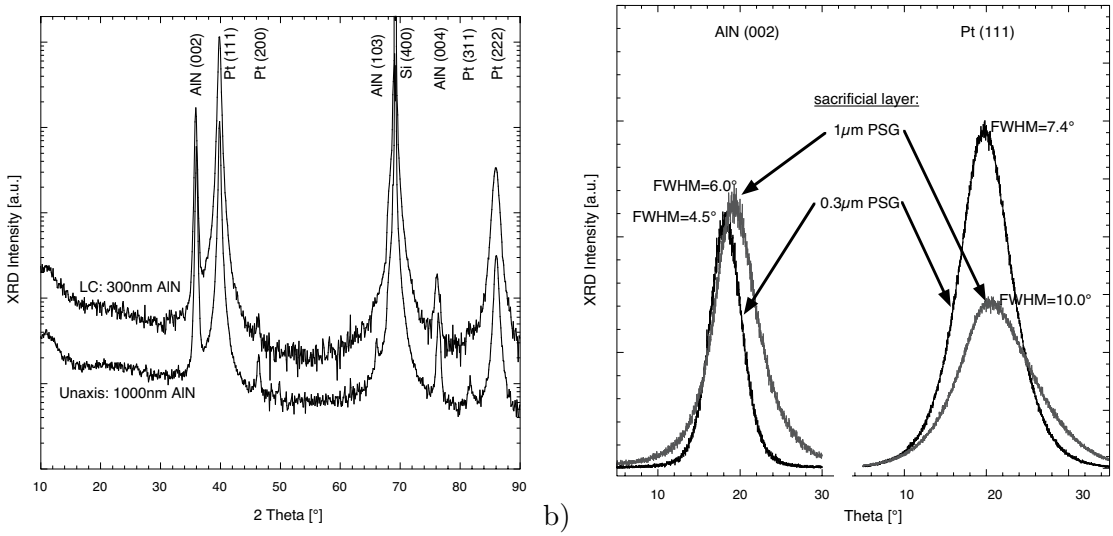

Figure 2.26: (a) $\Theta-2\Theta$ XRD of AlN/Pt/Ta/PSG/Si films deposited in AlN-LC tool (300nm AlN) and Clusterline200 at Unaxis (1μm AlN). The PSG layer thickness is identical with the AlN film thickness. (b) Rocking curve of corresponding AlN (002) and Pt (111) peaks.

perfectly textured (002) AlN film on a non-released test structure with AlN/Pt/Ta/PSG/Si (fig. 2.26). The rocking curve FWHM of the (002) AlN peak was 4.5°, respectively 7.4° for the (111) Pt peak. Another wafer also for FBAR fabrication was processed in parallel to the one mentioned above, but it was designed for a center frequency of 3GHz. The PSG layer was 1μm thick and the 1μm thick AlN was processed at UNAXIS in a Clusterline200 single module with load lock. Film stresses were optimized by adjusting the applied substrate bias. A tensile film with +210MPa stress was obtained with the following process conditions: 7.5kW$_{\text{pulsed dc}}$, 450°C, N_2/Ar=50/30sccm, 6mT, 45W$_{\text{substr. bias}}$ →-80V. A wafer uniformity of ±1% is achieved over a 6" wafer with a deposition rate of 90nm/min. Comparing this with the deposition in the AlN-LC tool where a wafer uniformity of ±13% over a 4" wafer and a deposition rate of 21nm/min was achieved. The XRD results for the AlN film from Unaxis are also shown in figure 2.26. The AlN film is almost perfectly (002) textured, but the rocking curve FWHM for this peak is 5.99° which is very large. It can be explained with the already large rocking curve of the underlaying Pt, which shows a (111) rocking curve FWHM of 10.01°. This high value of the rocking curve can only be explained with the different thickness of the PSG layer. The Unaxis processed wafer has a PSG thickness which is more than 3 times larger than the wafer processed in our laboratory. This resulted in a larger tilting distribution of the (111) oriented Pt lattice planes and hence also influenced the growth of the AlN film. These large values for the AlN rocking curve are expected to reduce considerable the coupling coefficient of realized FBARs. The relative dielectric constant and losses for the AlN film are ϵ_r=10.5 and 3% for the 300nm thick film, respectively ϵ_r=7.1 and 0.6% for the 1μm thick film at 10kHz.

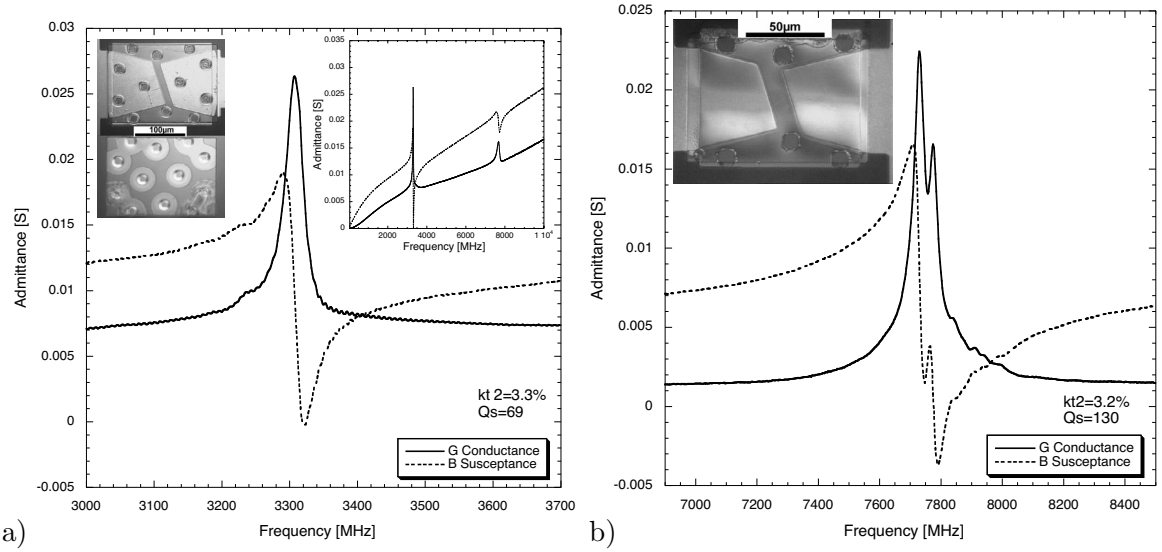

Figure 2.27: (a) Admittance of a surface micromachined FBAR with 1μm thickness for both the sacrificial PSG layer and the AlN membrane. The insets show the broad band impedance response with the overtone around 7.6GHz and an optical microscope image of the FBAR and the corresponding partial released test membrane. (b) Admittance of a FBAR designed for 8GHz with 300nm thickness for both the sacrificial PSG layer and the fully released AlN membrane.

The one-port scattering parameter S_{11} of the fabricated FBARs was measured with a HP Network Analyzer HP8722 D. The calibration of the measurement connections and the Air coplanar probes from Cascade Microtech were done using a impedance standard substrate from Cascade Microtech Inc. 101-190B with open/short/50Ω lines. The complex admittance Y is then calculated from S_{11} using equation 2.32 on page 58. The admittance of a FBAR designed for 3GHz (a), and 8GHz (b) is represented in figure 2.27. The individual resonator size is 9900μm^2 for (a), respectively 970μm^2 for (b). The inserts display the broad band impedance response and optical microscope images of the corresponding resonators.

The 3GHz FBAR (a) presents a fundamental mode resonance at 3.3GHz and a third order mode at 7.6GHz (no even-order resonances exist in simple thickness-mode resonators because of symmetry considerations [59]). The fundamental mode resonance exhibits a quality factor Q of 69 and a coupling coefficient k_t^2 of 3.3%. The low value of the coupling coefficient may be explained with the large rocking curve of the AlN film and hence low piezoelectric coefficient. A spurious resonance appears at the low frequency side of the resonance frequency, and ripples with a Δf of 7.9MHz overlie the admittance curve. This value corresponds to a thickness t of 536μm ($t = \frac{v}{2f_0}$ with v: sound velocity, f_0 fundamental mode resonance) assuming a sound velocity of the Si substrate of v_{Si}=8433m/s. The Si substrate thickness is 525μm which corresponds to the calculated value. This means that a standing acoustic wave is created across the substrate due to insufficient acoustic isolation. In fact it can be noticed that the membrane is only partially released (c.f. inset in figure

2.27 (a)) and even after prolonged time in the wet etchant no change in the etch front was observed. This implies that the released part of the FBAR is electrically parallel coupled with the non-released FBAR which radiates acoustic energy into the substrate. The unreleased resonator area is equally responsible for the lowering of the quality factor because the resonance gets damped. The damping of the resonance with consequences for the quality factor in case of non-released membranes was confirmed with the numerical 1-D model, and also by measurements performed on resonators before they were released. The high value of the conductance G of 7mS around the fundamental resonance and which increases linearly with frequency may be explained either with a high dielectric loss or some electric conduction across the resonator in the area of the step or the VIAs. The measured dielectric losses of the 1μm thick AlN film are $\tan\delta$=0.6% (10kHz) which is not sufficient to explain the high conduction.

The FBAR with the 300nm thick AlN film exhibits the fundamental mode resonance frequency at 7.8GHz. The resonator size is only 970μm^2, which is not impedance matched to 50Ω. The series quality factor is measured as 130 and the coupling coefficient is estimated as 3.2%. The main resonance is showing parasitic resonances on the high frequency side which make the Q_s and k_t^2 determination inaccurate. According to the optical image of the FBAR, the membrane is fully released. The high overtone ripples of 7.9MHz seen in the larger 3GHz resonator are not present, which confirms the separation of the membrane from the substrate. The low resonance quality factor may be explained with i) high series losses from bad step coverage of the top electrode, or ii) residual SiO_2 sticking on the membrane which damps the acoustic vibration.

2.9 Summary and Conclusions

Solidly mounted resonators were analyzed with numerical simulations based on a 1-dimensional physical model. The influence of different electrode materials and thickness variations of the individual layers in the solidly mounted resonator have been studied with regard to resonator coupling coefficient and film frequency sensitivity. It was found that in the frequency range above 5GHz, which is currently the upper limit of commercial applications, materials issues become accentuated and the choice of the right electrode materials is very important. Both Mo and Pt electrodes allow a high effective coupling for electrode thicknesses of 60nm at 8GHz.

Solidly mounted resonators (SMR) were successfully fabricated with sputter deposited piezoelectric AlN, platinum bottom electrodes and aluminum top electrodes. These SMR exhibit a strong and spurious-free resonance at 8GHz. The coupling coefficient was 6% and the series quality factor was 360. The figure of merit of the SMR, i.e. the product of $k_t^2 Q_s$, is therefore 22. If we neglect the ohmic losses in the electrodes of the fabricated SMR, the quality factor and hence the figure of merit should at least be twice as large. Agilent and Infinieon both report on figure of merits of 50 to 100 for BAW resonators in the frequency range of 1 to 5GHz. The temperature coefficient of frequency was -18ppm/K. The voltage coefficient of frequency measured on a SMR was 72ppm/V. This value is too small to be

exploited in microwave technology, for instance for channel selection.

Methods of reducing the electrical resistance in the electrodes have been proposed: Electrodes outside the active resonator area should be covered with a thick metal film to increase the electrical conduction. However, the electrodes defining the resonator may not be changed in thickness as their geometrical dimensions are fixed by acoustic constraints and resonance frequency. Several possible alternative metals have been discussed, and also been compared using numerical simulations, with regard to electric conductivity, acoustic velocity and influence on the effective coupling coefficient of resonators.

Molybdenum is a promising alternative to our currently used platinum electrodes because of its higher conductivity and better acoustic properties. We developed a process for the sputter deposition of molybdenum electrodes. On a Ti seed layer, a pure (110) texture was achieved. The electric resistivity of 7.7$\mu\Omega$cm was less than half the one of Pt films. For achieving c-axis oriented AlN films a larger bias potential during sputtering was necessary. The rocking curve FWHM turned out to be still larger than on Pt electrodes, resulting in a lower $d_{33,f}$ and k_t^2 as was shown in the literature. Two effects are responsible for the higher FWHM values: i) Mo provokes the nucleation of (100), (101), (102) and (103) oriented AlN films because of epitaxial effects, ii) The surface roughness of the Mo films, which is significantly larger than the one of Pt, leads to an increased amplitude of lattice plane tilt, as manifested by the larger width of the X-ray rocking curve. A larger rocking curve width is known to be correlated with a lower $d_{33,f}$. The Mo electrode lattice plane tilt distribution, equivalent to the FWHM of rocking curve needs to be reduced to obtain improved AlN piezoelectric properties. Nevertheless, SMR with Mo electrodes exhibited a coupling coefficient of 4.6% and quality factors of 360.

The numerical 1-dimensional simulation results compared well with the measured resonator admittance using a material coupling coefficient of 5.8% for the Al/AlN/Pt SMR. A parasitic series resistance of 5Ω, as well as a parasitic parallel resistance of 500Ω had to be added to the resonator model to achieve a good match with the measurement. The series resistance corresponds well to the calculated resistance of 3Ω for the top and bottom electrodes of the resonator. The parallel conduction is well explained by a loss tangent of AlN that amounts to about 15% at 8 GHz (0.2% at 1 kHz), or alternatively to surface conduction between neighboring electrodes in multi-resonator structures. This could be a result of etching residues.

We have also demonstrated a possible way of fabricating surface micromachined edge-supported thin film resonators with a very thin air-gap between the semiconductor surface and the diaphragm bottom surface: A P-doped sacrificial SiO_2 layer can be removed uniformly with a lateral under-etch rate of approximately 1μm/min using a wet Silox etch. This rate and the quite high selectivity relative to the used resonator materials Al, AlN and Pt allows for the release of free standing membranes. The VIA size or diameter for the wet etch access to the sacrifical layer can be chooses as small as 5μm, and the sacrificial layer is removed for thicknesses as thin as 250nm. The fabricated Al/AlN/Pt membranes do not need any supporting material. The membranes are mechanically robust and flat if the level of internal stress is limited to a couple of hundred megapascals. We fabricated apodized FBARs with a fundamental mode resonance at 3.3GHz and as high as 8.1GHz which cor-

responds to AlN film thicknesses of 1μm, respectively 300nm with electrode thicknesses of 100nm. The lateral dimensions of these resonators were 100x100μm^2 and 30x30μm^2. These resonators exhibited maximum quality factors of 130 and a coupling coefficient of 3.2%.

A smoother sacrificial layer exhibiting also a larger removal rate is necessary to improve the reliability of fabrication and performance of our free-standing resonators without supporting membrane. A possible solution could be the use of Si film as sacrificial layer and a dry etch proposed in [22]. A further improvement could be achieved by the use of passivated high-resistive Si wafers to avoid microwave losses into the substrate. In order to reduce the electric resistance of the top electrode over the step on the border of the membrane, the thickness of the top electrode aluminum layer should be increased outside the active resonator area as a last process step.

Bibliography

[1] B. A. Agishev, V. V. Lemanov, and N. K. Yushin. Electroacoustic coefficients of lithium tantalate and niobate crystals. *Sov. Phys. Solid State*, 20(9):1629–1630, 1978.

[2] C.R. Aita and C.J. Gawlak. The dependence of aluminum nitride film crystallography on sputtering plasma composition. *Journal of vacuum science & technology A*, 1(2):403–406, 1983.

[3] B. A. Auld. Properties of materials. In *Acoustic Fields and Waves in Solids*, volume 1, pages 122,131,247,357. John Wiley & Sons, New York, 1973.

[4] G. Carlotti, G. Gubbiotti, F. S. Hickernell, H. M. Liaw, and G. Socino. Comparative study of the elastic properties of polycrystalline aluminum nitride films on silicon by brillouin light scattering. *Thin Solid Films*, 310:34–38, 1997.

[5] G. Carlotti, F. S. Hickernell, H. M. Liaw, L. Palmieri, G. Socino, and E. Verona. The elastic constants of sputtered aluminum nitride films. In M. Levy, S. C. Schneider, and B. R. McAvoy, editors, *IEEE Ultrasonics Symposium*, volume 1, pages 353–356, Seattle, WA, 1995. IEEE.

[6] S. I. Chizhikov, N. G. Sorokin, and V. S. Petrakov. The elasto-electric effect in the non-centrosymmetric crystals. *Ferroelectrics*, 41(1-4):143–159, 1982.

[7] N. Chubachi. ZnO films for surface acoustooptical devices on nonpiezoelectric substrates. *Proceedings of the IEEE*, 64(5), 1976.

[8] D. Cushman, K.F. Lau, E. M. Garber, K.A. Mai, A.K. Oki, and K.W. Kobayashi. SBAR filter monolithically integrated with HBT amplifier. In *Ultrasonics symposium*, 1990.

[9] A. Dec and K. Suyama. Micromachined electro-mechanical tunable capacitors and their applications to rf ic's. In IEEE, editor, *IEEE transactions on microwave theory and techniques*, volume 46, pages 2587–2596, 1998.

[10] D. L. Denburg. Wide-bandwidth high-coupling sputtered ZnO transducers on sapphire. *IEEE Transaction on Sonics and Ultrasonics*, SU-18(1):31–35, 1971.

[11] T.P. Drüsedau, K. Koppenhagen, J. Bläsing, and T.-M. John. Texturing effects in molybdenum and aluminum nitride films correlated to energetic bombardment during sputter deposition. *Applied Physics A Materials Science & Processing*, 72(5):541–550, 2001.

[12] M.-A. Dubois. *Aluminum nitride and lead zirconate-titanate thin films for ultrasonic applications: integration, properties and devices*. Ph.D., EPFL, 1999.

[13] M.-A. Dubois and P. Muralt. Properties of aluminum nitride thin films for piezoelectric transducers and microwave filter applications. *Applied Physics Letters*, 74(20):3032–3034, 1999.

[14] M.-A. Dubois and P. Muralt. Stress and piezoelectric properties of aluminum nitride thin films deposited onto metal electrodes by pulsed direct current reactive sputtering. *Appl. Phys. Lett.*, 89(11):6389–6395, 2001.

[15] M.-A. Dubois, P. Muralt, H. Matsumoto, and V. Plessky. Solidly mounted resonator based on aluminum nitride thin film. In *IEEE Ultrasonics Symposium*, volume 1, pages 909–912, Sendai, Japan, 1998.

[16] M.-A. Dubois, P. Muralt, and L Sagalowicz. Aluminum nitride thin films for high frequency applications. *Ferroelectrics*, 224:243–250, 1999.

[17] L. N. Dworsky and L. C. B. Mang. Thin film resonator having stacked acoustic reflecting impedance matching layers and method, Dec. 13 1994.

[18] G. Este and W. D. Westwood. Stress control in reactively sputtered AlN and tin films. *Journal of Vacuum Science & Technology A (Vacuum, Surfaces, and Films)*, 5(4):1892–7, 1987. English 3041713.

[19] G.G. Fattinger, J. Kaitila, R. Aigner, and W. Nessler. Thin film bulk acoustic wave devices for applications at 5.2GHz. In *Ultrasonics symposium Proceedings*, Hawaii, USA, 2003. IEEE.

[20] N.F. Foster and G.A. Rozgonyi. Zinc oxide film transducers. *Appl. Phys. Lett.*, 8(9):221–223, 1966.

[21] M. H. Francombe and S. V. Krishnaswamy. Growth and properties of piezoelectric and ferroelectric films. *Journal of vacuum science & technology A*, 8:1382–1390, 1990.

[22] S. Frédérico, C. Hibert, R. Fritschi, Ph. Flückiger, Ph. Renaud, and A.M. Ionescu. Silicon sacrificial layer dry etching (SSLDE) for free-standing RF MEMS architecture. pages 570–573, 2003.

[23] T. W. Grudkowski, J. F. Black, T. M. Reeder, D. E. Cullen, and R. A. Wagner. Fundamental-mode VHF-UHF miniature acoustic resonators and filters on silicon. *Appl. Phys. Lett.*, 37(11):993–995, 1980.

[24] T. W. Grudkowski, J. F. Black, T. M. Reeder, D. E. Cullen, and R. A. Wagner. Fundamental mode VHF/UHF bulk acoustic wave resonator and filters on silicon. *Ultrasonics symposium proceedings IEEE*, pages 829–833, 1980.

[25] I.L. Guy, S. Muensit, and E.M. Goldys. Extensional piezoelectric coefficients of gallium nitride and aluminum nitride. *Appl. Phys. Lett.*, 75(26):4133–4135, 1999.

[26] J.M.E. Harper, J. J. Cuomo, and H.T.G. Hentzell. Quantitative ion beam process for the deposition of compound thin films. *Appl. Phys. Lett.*, 43(6):1983, 1983.

[27] J.H. Harris, R.A. Youngman, and R.G. Teller. On the nature of the oxygen-related defect in aluminum nitride. *Journal of Materials Research*, 5(8):1763–1773, 1990.

[28] Tomonobu Hata, Fumio Takeda, Osamu Morimoto, Etsuji Noda, and Toshio Hada. High rate deposition of thick piezoelectric ZnO and AlN films using a new magnetron sputtering technique. *Japanese Journal of Applied Physics*, 20:145–148, 1981.

[29] J. R. Heffelfinger, D. L. Medlin, and K. F. McCarty. On the initial stages of AlN thin-film growth onto (0001) oriented Al_2O_3 substrates by molecular beam epitaxy. *Journal of Applied Physics*, 85(1):466–472, 1999.

[30] E.S. Hellmann. The polarity of gan: a critical review. *MRS Internet Journal of Nitride Semiconductor Research*, 3(11):1–11, 1998.

[31] H.T.G. Hentzell, J.M.E. Harper, and J.J. Cuomo. Structure of al-n films deposited by a quantitative dual ion beam process. In *Ion Implantation and Ion Beam Processing of Materials Symposium*, volume 27, pages 519–524, North-Holland, New Work, NY, USA, 1984.

[32] F.J. Hickernell, R.-X. Yue, and F.S. Hickernell. Statistical modeling for the optimal deposition of sputtered piezoelectric films. *IEEE Transactions on Ultrasonics, Ferroelectrics and Frequency Control*, 44(3):615 –623, 1997.

[33] P. Hsieh, R. Reif, and B. Cunningham. Dc magnetron reactive sputtering of low stress AlN piezoelectric thin films for MEMS application. In *Materials Science of Microelectromechanical Systems (MEMS) Devices*, pages 165–170. Mater. Res. Soc., Warrendale, PA, USA, 1999.

[34] H. Jaffe. IRE standards on piezoelectric crystals - the piezoelectric vibrator: Definitions and methods of measurements, 1957. In *Proceedings of the IRE*, pages 353–358, 1957.

[35] K. Jagannadham, A. K. Sharma, Q. Wei, R. Kalyanraman, and J. Narayan. Structural characteristics of ain films deposited by pulsed laser deposition and reactive magnetron sputtering: A comparative study. *Journal of Vacuum Science & Technology A-Vacuum Surfaces and Films*, 16(5):2804–2815, 1998.

[36] J. Kaitila, M. Ylilammi, J. Molarius, J. Ella, and T. Makkonen. ZnO based thin film bulk acoustic wave filters for EGSM band. In *Ultrasonics Symposium*, pages 803–806. IEEE, 2001.

[37] T. Kamiya. Calculation of crystal structures, dielectric constants and piezoelectric properties of wurtzite-type crystals using ab-initio periodic hartree-fock method. *Japanese Journal of Applied Physics*, 35:4421–4426, 1996.

[38] R.S. Ketcham, G.R. Kline, and K.M. Lakin. Performance of TFR filters under elevated power conditions. In *Frequency Control Symposium, 1988., Proceedings of the 42nd Annual*, pages 106 – 111, 1988.

[39] A.L. Kholkin, C. Wutchrich, D.V. Taylor, and N. Setter. Interferometric measurements of electric field-induced displacements in piezoelectric thin films. *Review of scientific instruments*, 67(5):1935–1941, 1996.

[40] H.K. Kim, B.K Ju, Y.H. Lee, S.H Lee, J.K. Lee, and S.W. Kim. a noble suspended type thin film resonator (stfr) using the soi technology. *Sensors and Actuators A: Physical*, A 89:255–258, 2001.

[41] M. Kitayama, T. Fukuichi, T. Shiosaki, and A. Kawabata. VHF/UHF composite resonator on a silicon substrate. *Japanese Journal of Applied Physics*, 22(22-3):139–141, 1982.

[42] G. R. Kline and K. M. Lakin. 1.0-GHz thin-film bulk acoustic wave resonators on GaAs. *Appl. Phys. Lett.*, 43(8):750–751, 1983.

[43] G.R. Kline, K.M. Lakin, and K.T. McCarron. Overmoded high Q resonators for microwave oscillators. In *Frequency Control Symposium*, volume 1, pages 718 – 721. IEEE, 1993.

[44] L.S. Klingbeil and M.R. Wilson. Manufacturing concerns of reactively sputtered aluminum nitride. In *International conference on GaAs Manufacturing Technology.*, pages 195–198, St. Louis, MO, USA, 1996.

[45] D.J. Koneval, W.J. Gerber, and D.R. Curran. Improved vhf filter crystals using insulating film techniques. In *20th Annual frequency control symposium*, volume 20, pages 103–105, 1966.

[46] S.B: Krupanidhi. Rf magnetron sputter depostion and characterization of aluminum nitride thin films. In *Materials Research Society Symposium*, volume 77, pages 399–404, 1987.

[47] K. Kusaka, T. Hanabusa, and K. Tominaga. Effect of nitrogen gas pressure on residual stress in AlN films deposited by the planar magnetron sputtering system. *Thin Solid Films*, 281-282:340–343, 1996.

[48] K. M. Lakin. Analysis of composite resonator geometries. In *Annual symposium on frequency control*, volume 37, pages 320–324, 1983.

[49] K. M. Lakin. Thin film resonators and high frequency filters. *?*, 2001.

[50] K. M. Lakin, J. Belsick, J.F. McDonald, and K. T. McCarron. Improved bulk wave resonator coupling coefficient for wide bandwidth filters. In *Ultrasonics Symposium*, pages 827–831, Atlanta, USA, 2001. IEEE.

[51] K. M. Lakin, G. R. Kline, R. S. Ketcham, Martin. J. T., and K. T. McCarron. Stacked crystal filters implemented with thin films. In *Proceedings of the 43rd Annual Symposium on Frequency Control 1989*, pages 536–543, Denver, CO, USA, 1989.

[52] K. M. Lakin, G. R. Kline, and K. T. McCarron. Thin film bulk acoustic wave filters for GPS. In *IEEE Ultrasonics Symposium*, pages 471–476, Tucson, AZ, 1992.

[53] K. M. Lakin, G. R. Kline, and K. T. McCarron. High-q microwave acoustic resonators and filters. *IEEE Trans. Microwave Theory Tech.*, 41(12):2139–2146, 1993.

[54] K. M. Lakin, G. R. Kline, and K. T. McCarron. Development of miniature filters for wireless applications. *IEEE Transactions on Microwave Theory and Techniques.*, 43(12):2933–2939, 1995.

[55] K. M. Lakin and K. G. Lakin. Numerical analysis of thin films BAW resonator. In *IEEE International Ultrasonics Symposium*, Honolulu, Hawaii, USA, 2003.

[56] K. M. Lakin, J. Liu, and K. Wang. Aluminum nitride on sapphire. *Ultrasonics symposium proceedings IEEE*, pages 302–306, 1974.

[57] K. M. Lakin, K. T. McCarron, and R. E. Rose. Solidly mounted resonators and filters. In Levy-M; Schneider-SC; McAvoy-BR, editor, *IEEE Ultrasonics Symposium*, volume 2, pages 905–908, Seattle, WA, USA, 1995.

[58] K. M. Lakin and J. S. Wang. UHF composite bulk wave resonators. In *Ultrasonics symposium proceedings*, pages 834–837. IEEE, 1980.

[59] K. M. Lakin and J. S. Wang. Acoustic bulk wave composite resonators. *Applied Physics Letters*, 38(3):125–127, 1981.

[60] K. M. Lakin and J.S. Wang. Aluminum nitride thin film and composite bulk wave resonators. In *36th annual frequency control symposium*, pages 517–524, 1982.

[61] K.M. Lakin. Fundamental properties of thin film resonators. In *Frequency Control, 1991., Proceedings of the 45th Annual Symposium on*, volume 1, pages 201 – 206, 1991.

[62] K.M. Lakin. Modeling of thin film resonators and filters. In *Microwave Symposium Digest, 1992., IEEE MTT-S International*, pages 149–152, 1992.

[63] K.M. Lakin. Numerical analysis of two dimensional thin film resonators. In *Frequency Control Symposium, 1993. 47th., Proceedings of the 1993 IEEE International*, volume 1, pages 502 – 508, 1993.

[64] K.M. Lakin, G.R. Kline, R.S. Ketcham, A.R. Landin, W.A. Burkland, K.T. McCarron, S.D. Braymen, and S.G. Burns. Thin film resonator technology. In *Proceedings of the 41st Annual Frequency Symposium 1987*, pages 371–381, 1987.

[65] K.M. Lakin, G.R. Kline, and K.T. McCarron. Self limiting etching of piezoelectric crystals. In *Frequency Control Symposium, 1995. 49th., Proceedings of the 1995 IEEE International*, volume 1, pages 827 – 831, 1995.

[66] K.M. Lakin, J.S. Wang, G.R. Kline, A.R. Landin, Y. Y. Chen, and J. D. Hunt. Thin film resonators and filters. *Ultrasonics symposium*, pages 466–475, 1982.

[67] R. Lanz and P. Muralt. Solidly mounted BAW filters for 8GHz based on AlN thin films. In *IEEE International Ultrasonics Symposium*, page ?, Honolulu, Hawaii, USA, 2003.

[68] III Larson, J., P. Bradley, S. Wartenberg, and R. Ruby. Modified butterworth-van dyke circuit for FBAR resonators and automated measurement system. In *IEEE Ultrasonics symposium*, volume 1, pages 863–868, 2000.

[69] J. III. Larson, R. Ruby, P. Bradley, J. Wen, S.-L. Kok, and A.l. Chien. Power handling and temperature coefficient studies in FBAR duplexers for the 1900 MHz PCS band. In *IEEE Ultrasonics symposium*, volume 1, pages 869–874, 2000.

[70] H.C. Lee and J.Y. Lee. Effects of sputtering pressure and nitrogen concentration on the prefered orientation of AlN thin films. *Journal of Materials Science*, 5:221–225, 1994.

[71] S.H. Lee, J.K. Lee, and K.H. Yoon. Growth of highly c-axis textured AlN films on Mo electrodes for film bulk acoustic wave resonators. *Journal of Vacuum Science & Technology A*, 21(1):1–5, 2003.

[72] H.M. Liaw and F.S. Hickernell. The characterization of sputtered polycrystalline aluminum nitride on silicon by surface acoustic wave measurements. *IEEE Transactions on Ultrasonics, Ferroelectrics and Frequency Control*, 42(3):404–409, 1995.

[73] D. R. Lide. *Handbook of Chemistry and Physics*, volume 75th edition. CRC Press, 1995.

[74] W.T. Lin, L.C. Meng, and G.J. Chen. Epitaxial growth of cubic AlN films on (100) and (111) silicon by pulsed laser ablation. *Appl. Phys. Lett.*, 66(16):2066–2071, 1995.

[75] H. P. Löbl, M. Klee, C. Metzmacher, W. Brand, R. Milsom, and P. Lok. Piezoelectric thin AlN films for bulk acoustic wave (BAW) resonators. *Materials Chemistry and Physics*, 79:143–146, 2003.

[76] H. P. Löbl, M. Klee, C. Metzmacher, W. Brand, R. Milsom, P. Lok, and F. van Straten. Piezoelectric materials for BAW resonators and filters. In *Ultrasonics Symposium*, pages 807–811. IEEE, 2001.

[77] H. P. Löbl, C. Metzmacher, D. N. Peligrad, R. Mauczok, M. Klee, W. Brand, R. Milsom, P. Lok, F. van Straten, A. Tuihout, and J. W. Lobeck. Solidly mounted bulk

acoustic wave filters for the GHz frequency range. In *Ultrasonics Symposium*, pages 919–923. IEEE, 2002.

[78] J. J. Lutsky, R. J. Naik, R. Reif, and C. G. Sodini. A sealed cavity TFR process for RF bandpass filters. In *IEEE International Electron Devices Meeting*, pages 95–98, San Francisco, CA, 1996.

[79] G. D. Mansfeld and S. G. Alekseev. Theory and numerical analysis of bulk acoustic wave multilayer composite resonator structure. In Schneider-SC; Levy-M; McAvoy-BR, editor, *IEEE Ultrasonics Symposium Proceedings*, volume 2, pages 891–894, Toronto, Ont., Canada., 1997.

[80] G. D. Mansfeld, S. G. Alekseev, and I. M. Kotelyanskii. Bulk acoustic wave microwave composite resonators and filters with acoustic isolation of resonating layers. In *IEEE Ultrasonics Symposium*, volume 1, pages 963–966, Sendai, Japan, 1998.

[81] G.D. Mansfeld, M. Levy, S.C. Schneider, and B.R. McAvoy. New types of BAW composite resonators and their properties. In *IEEE Ultrasonics Symposium*, volume 2, pages 913–916, 1995.

[82] F. Martin, P. Muralt, M.-A. Dubois, and A. Pezous. Thickness dependence of the properties of highly c-axis textured AlN thin films. *Journal of Vacuum Science & Technology A: Vacuum, Surfaces, and Films*, 22(1):361–365, 2004.

[83] W.P. Mason. *Physical Acoustics: Principles and Methods*, volume 1-A. Academic Press, New York and London, 1964.

[84] B. Matthes, E. Broszeit, O. Zucker, and P. Gauer. Investigation of thin AlN films for piezolayer-field effect transistor applications. *Thin Solid Films*, 226:178–184, 1993.

[85] K. T. McCarron, G. R. Kline, J. T. Martin, and K. M. Lakin. Growth and characterization of aluminum nitride thin films for piezoelectric devices. In IEEE, editor, *IEEE Ultrasonics Symposium*, 1988.

[86] L. McNeil, M. Grimsditch, and R.H. French. Vibrational spectroscopy of aluminum nitride. *J. Am. Ceram. Soc.*, 76(5):1132–1136, 1993.

[87] W. J. Meng, J. A. Sell, G. L. Eesley, and T. A. Perry. Measurement of intrinsic stresses during growth of aluminum nitride thin films by reactive sputter deposition. *J. Appl. Phys.*, 74(4):2411–2414, 1993.

[88] R. Messier, A.P. Giri, and R.A. Roy. Revised structure zone model for thin film physical structure. *Journal of Vacuum science & technology A*, 2:500–503, 1984.

[89] Y. Miyasaka, S. Hoshino, and S. Takahashi. ZnO/sio2/si diaphragm bulk acoustic wave composite resonators. *Japanese Journal of Applied Physics, Supplement*, 23(1):119–121, 1983.

[90] Y. Miyasaka, S. Hoshino, and S. Takahashi. Advances in structure and fabrication process for thin film acoustic resonators. In *Ultrasonic Symposium*, pages 385–393, 1987.

[91] S. Muhl, J. A. Zapien, J. M. Mendez, and E. Andrade. Aluminium nitride films prepared by reactive magnetron sputtering. *Journal of Applied Physics*, 30:2147–2155, 1997.

[92] R. J. Naik. *Sputter deposition of aluminum nitride for applications in thin-film resonators.* PhD thesis, MIT, 1996.

[93] R.S. Naik, J.J. Lutsky, R. Reif, and C.G. Sodini. Electromechanical coupling constant extraction of thin-film piezoelectric materials using a bulk acoustic wave resonator. *IEEE Transactions on Ultrasonics, Ferroelectrics and Frequency Control*, 45(1):257–263, 1998.

[94] R.S. Naik, J.J. Lutsky, R. Reif, C.G. Sodini, A. Becker, L. Fetter, H. Huggins, R. Miller, J. Pastalan, G. Rittenhouse, and Y.-H. Wong. Measurements of the bulk, c-axis electromechanical coupling constant as a function of AlN film quality. *Transactions on Ultrasonics, Ferroelectrics and Frequency Control, IEEE*, 47(1):292–296, 2000.

[95] R.S. Naik, R. Reif, J.J. Lutsky, and C.G. Sodini. Low-temperature deposition of highly textured aluminum nitride by direct current magnetron sputtering for applications in thin-film resonators. *Journal of the Electrochemical Society*, 146(2):691–696, 1999.

[96] K. Nakamura and H. Kanbara. Theoretical analysis of a piezoelectric thin film resonator with acoustic quarter-wave multilayers. In *IEEE Ultrasonics Symposium*, volume 1, pages 876–881, Sendai, Japan, 1998.

[97] K. Nakamura, H. Sasaki, and H. Shimizu. ZnO/SiO_2-diaphragm composite resonator on a silicon wafer. *Electronics Letters*, 17(14):507–509, 1981.

[98] W.E. Newell. Face-mounted piezoelectric resonators. *Proceedings of the IEEE*, 53:575–581, 1965.

[99] A.J. Noreika, M.H. Francombe, and S.A. Zeitman. Dielectric properties of reactively sputtered films of aluminum nitride. *Journal of Vacuum Science & Technology A*, 6:194–197, 1969.

[100] H. Nowotny and E. Benes. General one-dimensional treatment of the layered piezoelectric resonator with two electrodes. *J. Acoust. Soc. Am.*, 82(2):513–521, 1987.

[101] S. Ohta, K. Nakamura, A. Doi, and Y. Ishida. Temperature characteristics of solidly mounted piezoelectric thin film resonators. In *Ultrasonics Symposium*, Hawaii, USA, 2003. IEEE.

[102] F.S. Ohuchi and P.E. Russell. AlN thin films with controlled crystallogrpahic orientations and their microstructure. *Journal of vacuum science & technology A*, 5(4):1630–1634, 1987.

[103] H. Okano, N. Tanaka, Y. Hirao, M. Kobayashi, K. Shibata, and S. Nakano. Characteristics of AlN thin films deposited by electron cyclotron resonance dual-ion-beam sputtering and their application to GHz-band surface acoustic wave devices. *Jpn. J. Appl. Phys., Part 1*, 33(5B):2957–2961, 1994.

[104] Bolaji L. Olutade and William D. Hunt. Sensitivity analysis of a thin film bulk acoustic resonator ladder filter. In *Proceedings of the 1997 IEEE International Frequency Control Symposium.*, pages 737–742, Orlando, FL, USA, 1997.

[105] D.J. Page. A cadmium sulfide-silicon composite resonator. In *Proceedings of the IEEE*, pages 1748–1749. IEEE, 1968.

[106] S. Pinkett, W. Hunt, B. Barber, and P. Gammel. Broadband characterization of zinc oxide-based sollidly mounted resonators. In *International Frequency Control Symposium*, pages 15–19. IEEE, 2002.

[107] A. Rodrguez-Navarro, W. Otao-Rivera, J. M. Garca-Ruiz, and R. Messier. Development of preferred orientation in polycrystalline AlN thin films deposited by rf sputtering system at low temperature. *J. Mater. Res.*, 12(7):1850–1855, 1997.

[108] D. Royer and V. Kmetik. Measurement of piezoelectric constants using an optical heterodyne interferometer. *Electronics Letters*, 28(19):1828–1830, 1992.

[109] R. Ruby. Micromachined cellular filters. *IEEE international microwave symposium digest*, pages 1149–1152, 1996.

[110] R. Ruby, P. Bradley, III Larson, J., Y. Oshmyansky, and D. Figueredo. Ultraminiature high-Q filters and duplexers using FBAR technology. In *Solid-State Circuits Conference*, pages 120 –121, 2001.

[111] R. Ruby and P. Merchant. Micromachined thin film bulk acoustic resonators. In *Proceedings of the 1994 IEEE International Frequency Control Symposium*, pages 135–138, 1994.

[112] R.C. Ruby, P. Bradley, Y. Oshmyansky, Al. Chien, and III Larson, J. Thin film bulk wave acoustic resonators (FBAR) for wireless applications. In *Ultrasonics Symposium*, Atlanta, USA, 2001. IEEE.

[113] J. A. Ruffner, P. G. Clem, B. A. Tuttle, D. Dimos, and D. M. Gonzales. Effect of substrate composition on the piezoelectric response of reactively sputtered AlN thin films,. *Thin Solid Films*, 354(1-2):100–105, 1999.

[114] R.F. Rutz. Ultraviolet electroluminescence in AlN. *Appl. Phys. Lett.*, 28(7):379–381, 1976.

[115] H. Satoh, Y. Ebata, H. Suzuki, and C. Narahara. An air-gap type piezoelectric composite thin film resonator. In IEEE, editor, *Proceedings of the Annual symposium on frequency control*, volume 39, 1985.

[116] H. Satoh, H. Suzuki, C. Takahashi, C. Narahara, and Y. Ebata. A 400MHz one-chip oscillator using an air-gap type thin film resonator. In *Ultrasonics symposium*, 1987.

[117] C. W. Seabury, J.T. Cheung, P.H. Kobrin, R. Addison, and D. P. Havens. High performance microwave air-bridge resonators. In *Ultrasonics Symposium*, pages 909–911. IEEE, 1995.

[118] C. W. Seabury, P. H. Kobrin, R. Addison, and D. P. Havens. Thin film ZnO bulk acoustic mode filters. In *IEEE MTT-S Symposium*, pages 181–184, Denver, CO, 1997.

[119] T.Y. Sheng, Z.Q. Yu, and G.J. Collins. Disk hydrogen plasma asisted chemical vapor deposition of aluminum nitride. *Applied Physics Letters*, 52(7):576–578, 1988.

[120] T. Shiosaki, T. Fukuichi, M. Tokuda, and A. Kawabata. Temperature compensated high coupling and high quality factor ZnO/sio2 bulk wave resonators on high resistance substrates. In *IEEE Ultrasonics Symposium*, pages 405–410, 1984.

[121] T. Shiosaki, T. Yamamoto, T. Oda, K. Harada, and A. Kawabata. Low temperature growth of piezoelectric AlN film for surface and bulk wave transducers by rf reactive planar magnetron sputtering. In *Ultrasonics Symposium*, volume 1, pages 451–454, 1980.

[122] T. Shiosaki, T. Yamamoto, T. Oda, and A. Kawabata. Low-temperature growth of piezoelectric AlN film by rf reactive planar magnetron sputtering. *Appl. Phys. Lett.*, 36(8):643–645, 1980.

[123] Tadashi Shiosaki and Akira Kawabata. Piezoelectric thin films for SAW applications. *Ferroelectrics*, 42:219–232, 1982.

[124] A.J. Shuskus, T.M. Reeder, and E.L. Paradis. Rf-sputtered aluminum nitride films on sapphire. *Appl. Phys. Lett.*, 24(4):155–156, 1974.

[125] T. R. Sliker and D. A. Roberts. A thin-film CdS-quartz composite resonator. *J. Appl. Phys.*, 38(5):2350–2358, 1967.

[126] R. B. Stokes and J. D. Crawford. X-band thin film acoustic filters on GaAs. *IEEE Trans. Microwave Theory Tech.*, 41(6/7):1075–1080, 1993.

[127] G.G. Stoney. The tension of metallic films deposited by electrolysis. In *Royal Society of London*, volume A82, pages 172–175, 1909.

[128] C.W. Storment, D.A. Borkholder, V. Westerlind, J.W. Suh, N.I. Maluf, and G.T.A. Kovacs. Flexible, dry-released process for aluminum electrostatic actuators. *Journal of Microelectromechanical Systems*, 3(3):90–96, 1994.

[129] S. Strite and H. Morko. Gan, AlN, and inn: A review. *Journal of Vacuum Science & Technology B: Microelectronics and Nanometer Structures*, 10(4):1237–1266, 1992.

[130] J. A. Thornton. Influence of apparatus geometry and deposition conditions on the structure and topgraphy on thick sputtered coatings. *J. Vac. Sci Technol.*, 11(4):666–670, 1974.

[131] J. A. Thornton. The microstructure of sputter-deposited coatings. *J. Vac. Sci Technol. A*, 4(6):3059–3065, 1986.

[132] P.T. Tikka, J. Kaitila, J. Ella, T. Makkonen, J.V. Knuuttila, J. Westerholm, and M.M. Salomaa. Laser probing and fem modeling of solidly mounted resonators. *1999 IEEE MTT-S International Microwave Symposium Digest*, 3:1373–1376, 1999.

[133] P.T. Tikka, J. Kaitila, M. Ylilammi, T. Makkonen, J.V. Knuuttila, K. Hashimoto, and M. M. Salomaa. Laser probing and fem modeling of ultrasonically vibrating surfaces. *Ultrasonics symposium*, pages 1143–1146, 1998.

[134] K. Tsobouchi and N. Mikoshiba. Zero temperature coefficient SAW delay line. In *Ultrasonics symposium*, pages 299–310. IEEE, 1983.

[135] K. Tsubouchi and N. Mikoshiba. Zero-temperature-coefficient SAW devices on AlN epitaxial films. *IEEE Trans. on Sonics and Ultrasonics*, SU-32(5):634–644, 1985.

[136] K. Tsubouchi, K. Sugai, and N. Mikoshiba. AlN material constants evaluation and SAW properties on AlN/al2o3 and AlN/si. In *Ultrasonics Symposium*, pages 375–380, 1981.

[137] C. Vale, J. Rosenbaum, S. Horwitz, S. V. Krishnaswamy, and R. Moore. FBAR filters at GHz frequencies. In *44t annual symposium on frequency control*, pages 332–336, 1990.

[138] C.B. Vartuli, S.J. Pearton, C.R. Abernathy, J.D. MacKenzie, F. Ren, J.C. Zolper, and R.J. Shul. Wet chemical etching survey of III-nitrides. *Solid-State-Electronics. vol.41, no.12; Dec. 1997; p.1947-51*, 41(12):1947–1951, 1997.

[139] R.D. Vispute, H. Wu, and J. Narayan. High quality epitaxial aluminum nitride layers on sapphire by pulsed laser deposition. *Appl. Phys. Lett.*, 67(11):1549–1551, 1995.

[140] J. S. Wang and K. M. Lakin. Sputtered AlN films for bulk acoustic wave devices. In *IEEE Ultrasonics Symposium*, volume 1, pages 502–505, Chicago, IL, 1981.

[141] J. S. Wang, A. R. Landin, and M. M. Lakin. Low temperature coefficient shear wave thin films for composite resonators and filters. In *Ultrasonics Symposium*, pages 491–494, 1983.

[142] K. L. Wang, K. M. Lakin, and J. K. Liu. Growth and properties of silicon films on aluminum-nitride films on sapphire. *J. Appl. Phys.*, 47(4):1580–1582, 1976.

[143] T. Yamada and N. Niizeki. A new formulation of piezoelectric plate thickness vibration. *Review of the electrical communication laboratoires*, 19(5-6):705–713, 1971.

[144] K. Yamanouchi and M. Oba. New air gap type piezoelectric composite thin film resonators. In *Ultrasonics Symposium*, pages 415–418. IEEE, 1987.

[145] W. Zhang, R. Vargas, T. Goto, Y. Someno, and T. Hirai. Preparation of epitaxial AlN films by electron cyclotron resonance plasma-assisted chemical vapor deposition on Ir- and Pt-coated sapphire substrates. *Appl. Phys. Lett.*, 64(11):1359–1361, 1994.

[146] L. Zheng, S. Ramalingam, T. Shi, and R.L. Peterson. Aluminum nitride thin film sensor for force, acceleration, and acoustic emission sensing. *Journal of vacuum science & technology A*, 11(5):2437–2446, 1993.

Chapter 3

Ladder Filters based on BAW resonators

3.1 Introduction

The thin film BAW resonator technology yields filters with insertion losses of less than 3dB whereas only complicated SAW implementations have been able to approach low insertion losses. In multi-channel filter banks SAW implementations require tuning networks and amplifier stages to offset higher insertion losses. Tuning would not be required in FBAR[1] filters and the low insertion loss should eliminate many amplifier requirements. The physical size of FBAR devices are from ten to one hundred times smaller than SAW devices performing the same function. A FBAR is one half wavelength long in its propagation direction whereas a SAW resonator may be up to 1000 wavelength in one dimension in order to synthesize a reflecting plane in the grating. Contrary to FBAR, SAW are generally not integrable due to materials compatibility constraints. For band-pass or band-rejection filters with bandwidth less than several percent, the loss associated with inductors and tolerances of capacitors and inductors make it difficult or impossible to develop passive lumped filters above 1GHz.

One application for FBAR filters are duplexers: The duplexer is the first component following the antenna in wireless phones using code domain multiple access (CDMA) architecture. A half-duplexer system uses a switch to separate the receive (Rx) signals from the transmit (Tx) signals on a time division basis. For a full duplexer solution (i.e. no switch), the signals are separated on a frequency basis. The function of the full duplexer is to allow both receive and transmit chains simultaneous access to the antenna, but with high rejection out-of-band, low insertion in-band, and tremendous isolation (50dB) between the Rx and Tx chains to prevent the low noise amplifier from overloading. Since these wireless bands (each ∼3% of the carrier frequency) are very closely spaced (∼1% of the carrier frequency of 1.9GHz) the narrow band-pass filters must posses a fast filter roll-off [24].

[1]The term FBAR will be used here for both film bulk acoustic resonator FBAR and solidly mounted resonator SMR

Duplexers require high-Q filters for steep roll-off, or alternatively the addition of a series inductor to the shunt FBAR helps increase roll-off [2]. Further requirements on the duplexer are good power-handling capabilities: FBAR withstand high power levels, e.g. a maximum attainable power of +36dBm (corresponds to 4Watts or $\sim$1MW/cm^2) for a 1.9GHz transmit device [24]. FBAR duplexers offer power-handling capabilitites exceeding those of SAW duplexers at 2GHz and they offer the possibility for module integration of both active and filter components. Realized FBAR duplexer meet or exceed many of the specifications for a CDMA PCS 1900MHz ceramic resonator duplexer, which are currently being used in mobile phones. These ceramic resonator duplexers have $\sim$14 times the volume of the FBAR duplexer [32].

Other systems, such as GPS, require front-end filters centered at 1575 ± 5MHz with an insertion loss of less than 1.5dB and a rejection of 30dB in order to achieve a high signal-to-noise ratio.

There has been a tremendous interest in thin-film resonator filters because of their small size and light weight, potential good performance, and integration into monolithic integrated circuits. FBAR or SMR filters can take two forms, represented in figure 3.1: Firstly, individual resonators (c) can be electrically interconnected to form classic filters of the ladder (a) and lattice type (b) [17, 4]. Second, resonators can be closely spaced in a way that the evanescent field overlaps and an transverse acoustic coupling (both shear and longitudinal mode) between the two resonator is established (e). This type is called thin film monolithic crystal filter (MCF). An equivalent circuit approach for monolithic crystal filters was proposed by Rennick [30] in 1973. Ballato and Lukaszek [1] proposed the stacked crystal filter SCF (d) in 1973 using two piezoelectric crystal plates bonded together into a sandwich-type structure. The two stacked resonators radiate directly into each other and are separated by a common ground plane which provides high rejection/isolation between the two ports. The SCF has low insertion loss, but the bandwidth is limited compared with other devices. The SCF was re-introduced using thin films by Kline et al. [10].

In recent years there have been numerous publications that discuss the before-mentioned filter implementations. The monolithic filters require very precise spacing to control the acoustic coupling of the resonators. Moreover, the coupling might not be enough to realize filters with sufficient bandwidth for general wireless communication applications. In a conventional MCF the width of the metal electrode is approximately the same as the plate thickness. At microwave frequencies the metal thickness must be thin to reduce acoustic losses and the electrode long in order to realize a low impedance filter. Consequently, an increase in electrode thickness to reduce electrical losses results in increased mechanical losses. Kline et al. [9] report nevertheless thin film MCF with only 2.9dB insertion loss at 1.4GHz with 15MHz bandwidth, but these devices exhibited a lot of spurious resonances. Filter impedance is more easily matched by thin film SCF because the area can be chosen as large as needed and because of the large width-to-thickness ratio the transverse plate wave propagation is minimized. However, the SCF are difficult to process because they require two layers of superposed piezoelectric films with identical thickness.

Ladder filters offer more flexibility in engineering filter characteristics. The number of resonators determines the steepness of the skirt selectivity and, to a certain extent, filter

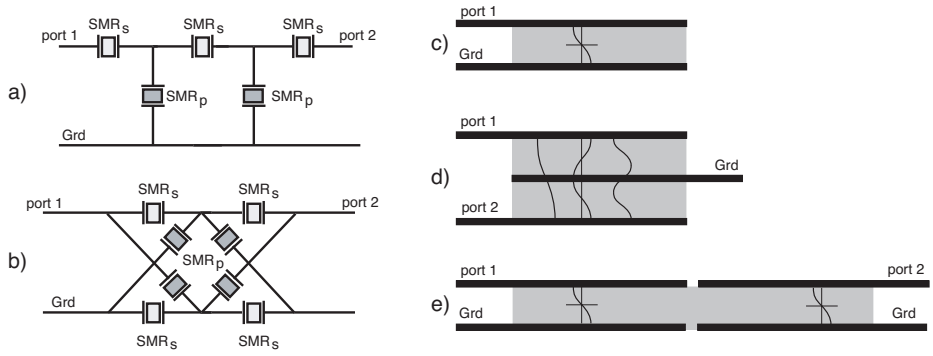

Figure 3.1: Different types of electrically and acoustically coupled passband filters: (a) ladder filter, (b) lattice filter, (c) simple resonator, (d) thin film stacked crystal filter, and (e) thin film monolithic crystal filter.

bandwidth. The ratio of shunt/parallel-to-series capacitance of the resonator (PS-ratio) determines the out-of-band rejection for a given number of resonators. The ladder filter design is advantageous because all resonators can be made identically to one another. Non-harmonic spurious responses are rejected by the cascade of resonators. The very short cutoff is due to the transmission zeros inherent in this structure. The lattice filter topology on the other hand offers wider bandwidth compared to the ladder design [27].

For ladder, lattice and stacked crystal filters the piezoelectric coupling coefficient has a direct effect on filter bandwidth. As a rough rule the ladder filter percentage bandwidth is about half that of the effective k_t^2 of the resonator. Thus a resonator having 5% effective k_t^2 can be used to make a 2.5% bandwidth filter. The insertion loss depends on the figure of merit k^2Q of the individual resonators [16].

3.1.1 State of the art of FBAR ladder filters

At the same time as the FBAR technology emerged in the beginning of the 1980's, filters using FBARs were presented:

The first thin film composite MCF had an insertion loss of 8.5dB, a bandwidth of 0.7MHz at 425MHz, and a rejection of 40dB [6, 7, 20].

AlN based FBAR SCF filters working above 1GHz for GPS, with insertion loss of 1.6dB were presented in 1986-89 [20, 9, 11, 15]. This was probably the first military/commercial applications based on the FBAR technology. A small amount of plate wave spurious response was observed in the passband. SCF on GaAs integrated circuits for filter-amplifier (HBT amplifier) were presented working at 1.0GHz with a 5MHz 3dB bandwidth in 1990 [3]. A SCF filter, with the second harmonic at 7.8GHz had 6.1dB insertion loss and less than 1% bandwidth [35]. Those first SCF had high Q in excess of 1500 resulting in small insertion losses below 2dB. The piezoelectric coupling was however weak resulting in a small bandwidth of maximum 1.5% [21, 19, 12].

Publications on ZnO and later also AlN FBAR ladder filters followed in the beginning of the 1990's [37, 28]. Ladder filters working above 1GHz with insertion losses below 2dB and 3% bandwidth were achieved [13]. Fabricated filters compromise T and L FBAR ladder filters with up to 6 sections [16]. Spurious resonances are observed due to plate mode reflections.

Lakin et al. [17, 18], 1995, showed the feasibility and lack of spuriouses in AlN SMR based 3/2 ladder filters working at 1.6-2.4GHz with an insertion loss of 3dB and rejection of 30-70dB. The materials used as the $\lambda/4$ layers were AlN and SiO_2. To achive such good performances, the SMRs had a very high figure of merit. These SMR filter structures are generally very rugged with regard to vibration and shock. In 1996, TFR Technologies, USA started volume production of SMR filters [18]. At the end of the 1990's and start of 2000's, several other companies reported starting of volume production of FBAR or SMR derived filters for mobile telecommunication applications in the range 0.5-5.5GHz [32, 24, 31, 2, 33, 14, 26, 27, 25]. Recent ZnO based SMR ladder filters working at 0.95GHz have for example an insertion loss of 1.3dB, 22dB rejection, 3.5dB bandwidth of 39MHz (4.1%) which is slightly inferior to the lattice filter which shows a bandwidth of 46MHz (4.9%) [8]. Commercial 5.2GHz AlN SMR ladder filters exhibit for example the following properties: an insertion loss of 2.5dB, a rejection better than 24dB, and a 4dB bandwidth of 170MHz (3.3%). Simple SMR had 6.3-6.5% effective coupling and a quality factor of 700 [4].

3.2 Theory of passband ladder filters

The admittance magnitude response of a FBAR is characterized by a sharp increase in the admittance at the series resonance, f_s, followed by a sharp decrease in admittance at the parallel resonance, f_p. Two FBAR with different frequencies f_p are needed to form a bandpass filter. Two ladder-type filter designs, employing SMRs of two different frequencies (SMR_p and SMR_s), are shown in figure 3.2 schematically and as fabricated. Considering only symmetrical ladder filters, two different topologies are possible: π-filters where the first resonator is parallel and then successsively a series and a parallel resonator is added. The T-filter starts with a series resonator, followed with parallel and series resonator (fig. 3.2). Filters will be identified in the text as S/P filters, where S stands for the number of series, and P stands for the number of parallel resonators. The admittance magnitude responses of both series and parallel SMRs are represented in figure 3.3. The series resonance of SMR_s and the parallel resonance of SMR_p are placed in the center of the band f_0. At this frequency there is a low resistivity path to the output through SMR_s, and, correspondingly, a low insertion loss. Away from the center of the band toward higher frequencies, the admittance of SMR_s starts to decrease, and the admittance of SMR_p starts to increase. Eventually, at the parallel resonance of SMR_s, the path to the load is blocked, resulting in a large insertion loss (attenuation pole or transmission null). A similar effect occurs at frequencies below the center of the band. At the series resonance of SMR_p, the impedance of the shunt devices drops to a low values, and power from the source is shunted to the ground.

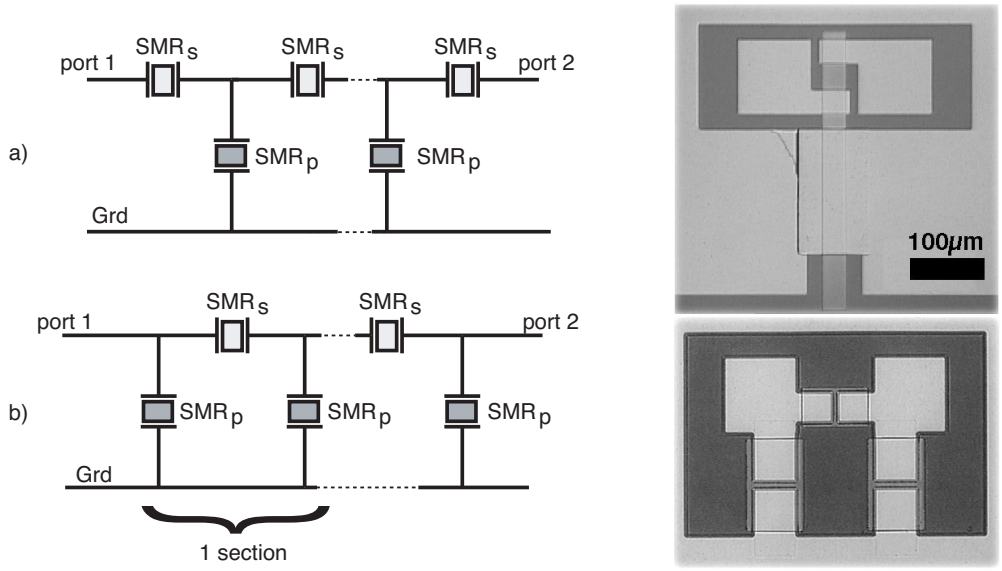

Figure 3.2: Two different symmetric ladder filter types: (a) 1-section T-filter schematic and fabricated, respectively (b) 1-section π-filter schematically and fabricated. Replacing single resonators for each leg by double resonators avoids high resistivity top-bottom electrode interconnects, increases power handling and reduces spuriouses due to the doubled resonator area which is needed to maintain the same impedance.

The two attenuation poles increase the filter skirt selectivity and create a strong filter roll-off. The maximum FBAR filter bandwidth is therefore a fraction of the zeros bandwidth and is determined to first order by the piezoelectric coupling coefficient. The bandwidth is approximately the difference between f_p and f_s, or half of the value of the effective k_t^2. The out-of-band rejection increases with increasing capacitance ratio (PS-ratio), as well as with the number of π or T sections. The insertion loss depends on the figure of merit k^2Q of the individual resonators [16] constituting the filter, and on the relative shifting of parallel and series resonator frequency. The parameters which characterize a passband filter are represented in figure 3.3. The insertion loss (IL) of the filters is taken as the maximum in the passband minus 0.2dB ripple. The 0.2dB channel bandwidth (BW) and the 3dB bandwidth are determined at IL-0.2dB and IL-3dB respectively. The out-of-band rejection is defined as the maximum value of the transmission spectrum outside the passband minus the insertion loss.

The series and the parallel resonators need to have their resonance frequency separated by Δf (fig. 3.3), so that the resonance frequency of the series resonator coincides with the anti-resonance frequency of the parallel resonator. This difference of frequency is of the order of the coupling coefficient, hence of only a few percent for the case of AlN resonators. The precision of this shift is the limiting factor for the good functioning of the ladder filter, i.e. low insertion loss and large bandwidth. Starting with identical resonators, either

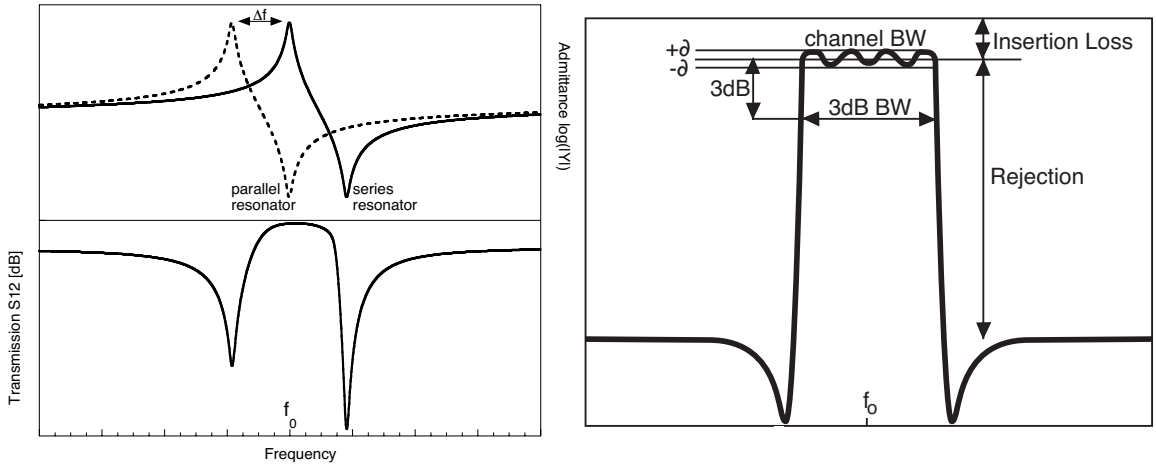

Figure 3.3: The parallel resonance of the shunt resonator is set to the series frequency of the series resonator. The resulting transmission coefficient, or S_{21} parameter, exhibits a passband with low insertion loss at the frequency f_0 where the series resonator has ideally infinite admittance and the shunt resonator infinite impedance. The high frequency transmission zero is due to the ideally infinite impedance of the series resonator. The low frequency transmission zero is due to the ideally infinite admittance of the parallel resonator which shunts the signal to ground. Away from the passband, the rejection is determined by the impedance ratio (PS-ratio) of the resonators. Right: Definition of the main filter characteristics insertion loss, out-of-band rejection, channel (∂=0.2dB) and 3dB bandwidth.

the series or the parallel resonator has to be modified to reflect this shift. Shifting the series resonator to higher frequencies can be accomplished by etching the surface of the top electrode. Shifting the parallel resonator to a lower frequency seems easier from a process technology point of view by adding an additional layer to the top electrode. An alternative method consist of depositing the required thickness on each series and parallel resonator separately with two successive depositions.

3.3 Numerical simulations of ladder filters

The definition of voltage and current becomes difficult at microwave frequencies. In addition, a practical problem exists when trying to measure voltages and currents at microwave frequencies because direct measurements usually involve the magnitude and phase of a wave traveling in a given direction, or of a standing wave. A representation more in accord with direct measurements, and with the ideas of incident, reflected, and transmitted waves, is given by the scattering matrix. Like the impedance or admittance matrix for a N-port network, the scattering matrix provides a complete description of the network as seen at its N ports. While the impedance and admittance matrices relate the total voltages and

currents at the ports, the scattering matrix relates the voltage waves incident on the ports to those reflected from the ports.

$$\begin{bmatrix} V_1^- \\ V_2^- \end{bmatrix} = \begin{bmatrix} S_{11} & S_{12} \\ S_{21} & S_{22} \end{bmatrix} \cdot \begin{bmatrix} V_1^+ \\ V_2^+ \end{bmatrix} \tag{3.1}$$

For ladder filters composed of cascaded sections of T or π-networks, the scattering parameters can be calculated using network analysis techniques.

3.3.1 The transmission (*ABCD*) matrix

The S parameter representation can be used to characterize a microwave network with an arbitrary number of ports, but in practice many microwave networks, e.g. ladder filters, consist of a cascade connection of two or more two-port networks. In this case it is convenient to define a 2x2 transmission, or $ABCD$ matrix, for each two-port network. The $ABCD$ matrix of the cascade connection of two or more two-port networks can easily be found by multiplying the $ABCD$ matrices of the individual two-ports.

The $ABCD$ matrix M_i of a two port circuit, e.g. single shunt or single series resonator, is given by [29], p206

$$M_i = \begin{bmatrix} A & B \\ C & D \end{bmatrix} \tag{3.2}$$

where $A = 1$, $B = Z(f)$, $C = 0$, and $D = 1$ for a series resonator and $A = 1$, $B = 0$, $C = Y(f)$, and $D = 1$ for a parallel resonator. $Y(f)$ and $Z(f)$ are the electrical admittance and impedance of the resonator expressed as a vector of frequency. The scattering parameter S_{21} of a latter filter with a certain number of series and parallel resonators is calculated by multiplying the $ABCD$ matrix of each element in the filter (chain parameters). For a simple 2/1 T-filter the resulting $M_{2/1}$ matrix is obtained with:

$$M_{2/1} = M_s \cdot M_p \cdot M_s \tag{3.3}$$

where M_s is the $ABCD$ matrix of the series resonator which has its series resonance frequency ideally at the passband center frequency, and M_p is the $ABCD$ matrix of the parallel resonator which has its parallel resonance frequency ideally at the passband center frequency f_0. The scattering parameter S_{21}, can then be obtained by conversion from the $ABCD$ or $M_{2/1}$ matrix with

$$S_{21} = \frac{2}{A + B/Z_0 + CZ_0 + D} \tag{3.4}$$

To achieve the passband filter, the series and the parallel resonator have their f_s separated by Δf (figure 3.3). For the simulations below, one input file with the admittance of the series resonator with a resonance frequency f_s was used. To simulate the frequency shift of the parallel resonator, the same data was used, but the admittance data was shifted with respect to frequency. This simplified approach is admissible because the considered shift is only of a few percent of the resonance frequency.

3.3.2 Numerical simulation results

Influence of frequency-shift layer thickness and material

Before doing simulations of ladder filters, it is necessary to understand how individual resonators may be shifted in frequency. This step is usually accomplished by adding an additional layer of material on the shunt resonators (mass-loading).

Numerical simulation results, based on the physical 1-D resonator model (eq. 2.12, page 20), are represented in figure 3.4 (a). The frequencies f_r and f_a are represented as a function the thickness of added material. A perfect match between resonance and anti-resonance frequency is necessary for best insertion loss in the passband filter. This difference corresponds to 187MHz with the simulated resonator (k_t^2=5.8%).

The two mass-loading materials used in this calculation, Al and SiO_2, have a different sensitivity of -13.8MHz/nm for Al and -11.2MHz/nm for SiO_2 when using a 60nm thick Al top electrode and a 70nm thick bottom Pt electrode. The lower sensitivity of SiO_2 is favorable for resonator fabrication because it allows for a higher absolute thickness to be applied for the same frequency shift. The necessary thickness required is 13nm for Al and 17nm for SiO_2. These thicknesses are very small, and to obtain a perfect frequency match it is advisable, from a practical point of view, to choose the material with the larger thickness (=lower sensitivity) because the relative deposition thickness precision is higher. Furthermore, SiO_2 can be sputtered with process conditions that allow a much smaller deposition rate and hence higher absolute thickness control. Figure 3.4 (b) shows the influence of electrode thickness on sensitivity. The sensitivity may be decreased in magnitude for very small electrode thicknesses, but when considering the increasing electrode electrical resistance, it is clear that a compromise has to be made. Furthermore, we have seen in figure 2.7, page 44, that a maximum of the effective coupling coefficient exists at around 60nm electrode thickness.

Influence of resonator size, PS ratio and shunt resonator frequency shift on filter properties

To study realizable theoretical ladder filter performances, simulation calculations with MatLab based on the *ABCD* matrix multiplication were performed. The impedance from a single SMR, either measured on real SMR or numerically simulated, served as input for the *ABCD* matrix (eq. 3.2). To calculate the S_{21} scattering parameter of a specified S/P ladder filter, a minimum of 3 variables have to be chosen in the simplest case, neglecting all parasitics and possible trimming elements. These input variables for the filter calculation are i) the size of the series resonator, ii) the PS ratio (or size of shunt resonator), and iii) the frequency shift applied to the shunt resonator. The first two determine mainly the electrical matching, as well as insertion loss and rejection. These first two are defined by the design of the filters, i.e. lateral dimensions of individual resonators in the filter. The latter plays a major role for the bandwidth adjustment, and is defined during frequency shifting which is a matter of very precise thickness modification of the shunt resonator. In fact, either the PS-ratio or the size of the series resonator could be determined using the so-called image-

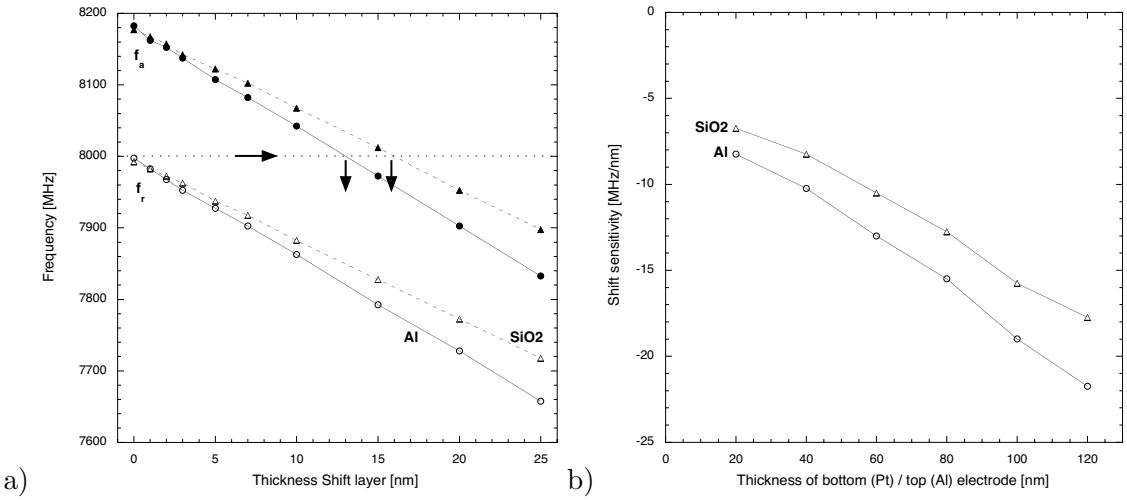

Figure 3.4: (a) Numerical simulation results of the change in frequency of f_r, f_a induced by adding a thin layer of $\circ$ Al or $\triangle$ SiO_2 on top of a 8GHz SMR with 70nm thick Pt bottom and 60nm thick Al top electrodes. Empty symbols represent resonance frequency, solid symbols anti-resonance frequency. The sensitivity is higher for Al (-13.8MHz/nm) than for SiO_2 (-11.2MHz/nm). The necessary thickness needed to match the resonance with the anti-resonance frequency of 187MHz is 13nm for Al and 17nm with SiO_2. (b) Sensitivity of frequency shift when applying an Al or SiO_2 film on a 8GHz SMR with different electrode thicknesses (both top and bottom).

parameter method [29], page 432, simplifying somewhat the numerical simulations: The condition of impedance matching, i.e. the input/output image impedances $Z_{i1/2}$ are both equal to 50Ω and must therefore equal $Z_{i1} * Z_{i2} = 50^2 = \sqrt{AB/CD}\sqrt{DB/AC} = \sqrt{B^2/C^2}$. Using the $ABCD$ parameter defined by a 1/1 L-section with series Z_s and parallel Z_p impedances (using the static capacitance impedances) we find that $50^2 = Z_s Z_p$. Nevertheless, the numerical filter simulations are necessary to predict the exact filter behavior because the image-parameter method does not take into account the frequency dependency of the image parameters which change within the passband.

The numerical filter simulations have to be optimized for certain restraining parameters which we choose to be i) a minimum relative out-of-band rejection of -23dB, and ii) maximization of the 0.2dB channel bandwidth. To determine the optimum input parameters for these requirements, the simulation calculates the S_{21} scattering parameter inside the 3-variable design space {series resonator sidelength, PS-ratio, rel. shift frequency} and extracts the characterizing output parameters 0.2dB channel bandwidth, 3dB bandwidth, insertion loss, and rejection. Only one resonator admittance serves as basis for the simulation and is always adjusted to the 3 input variables.

An example of such an optimization calculation is represented in figure 3.5 a)-c). Figure 3.5 d) shows the resulting S_{21} of this optimization. The input admittance corresponds to a numerical 1-D simulation of a 8GHz SMR with 5.8% material coupling coefficient and assuming zero parasitic losses in the resonator and zero bonding wire inductances. The calculated filter is a 2/3 π-ladder filter. Figures a)-c) represent the orthogonal slices in the 3-variable design space through the point with maximized channel bandwidth and -23dB relative rejection.

Increasing the PS-ratio in a ladder filter, fig. 3.5 (a), primarily enhances the out-of-band rejection. This is simply due to the increase in capacitance ratio. The insertion loss decreases linearly with increasing PS-ratio. The 0.2dB channel bandwidth exhibits a doubling of its value for the PS-ratio interval 1.0-2.6 (due to 50Ω matching), whereas the 3dB bandwidth decreases monotonically over the whole interval studied.

Increasing the series resonator sidelength, fig. 3.5 (b), has only a negligible effect on insertion loss and rejection over the interval studied. However, for resonator sizes comprised between 26 and 30μm, a marked increase in 0.2dB BW is observed, again due to impedance matching. The cause is the same as previously mentioned on the PS-ratio. The 3dB bandwidth increases monotonously.

The shunt and series resonator sizes play an important role in impedance matching of the filter. For a very restricted interval of the geometrical dimensions, good matching results in significantly increased bandwidth. The individual resonator sizes have to be optimized for each ladder filter type (π or T) and for the number of sections, or an insufficient bandwidth will be the result. The simulations results suggest that the possible "design window" is very restricted. If one takes into account likely parasitics like series resistances and inductances, or parallel capacitances or conductors, then this "design window" has to be readapted. Even though parasitics may be extracted from simple resonator measurements, using the resonators in a ladder filter topology introduces additional parasitics (c.f. paragraph 3.6) which are difficult to estimate or forecast. It was thus important to include a large number

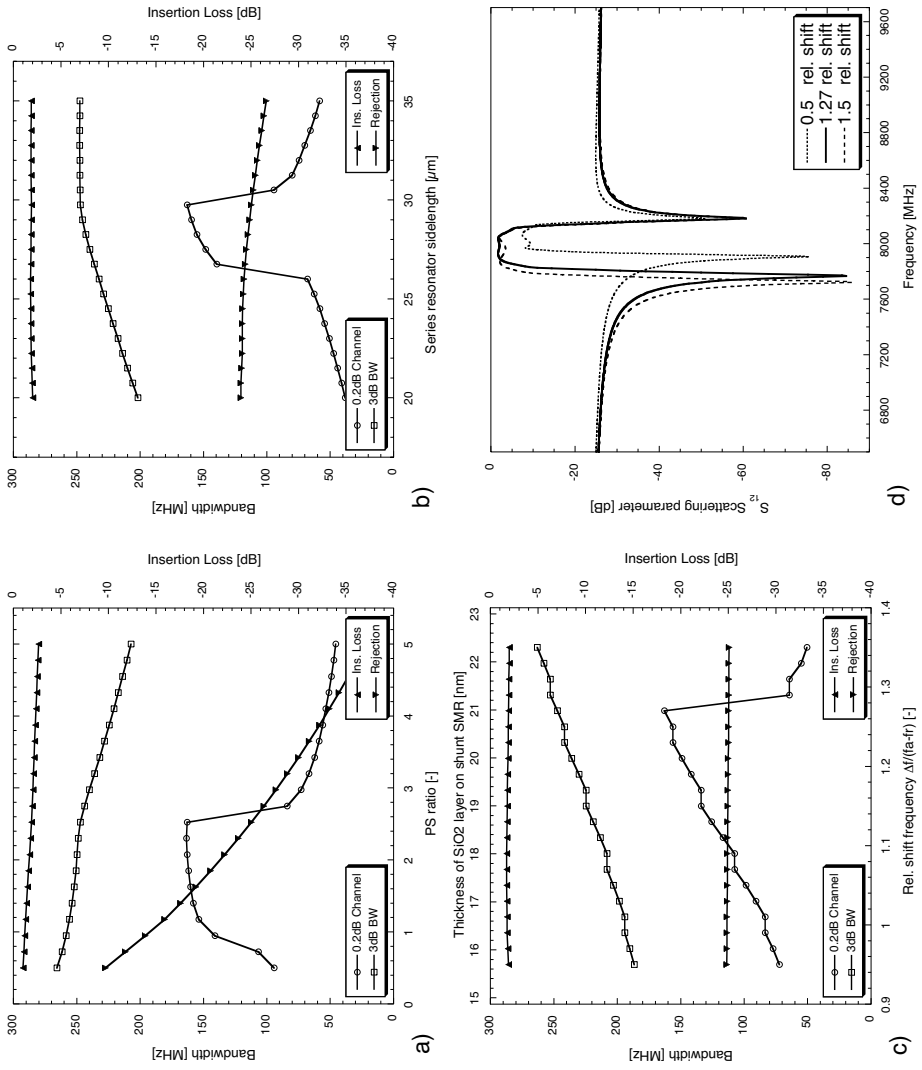

Figure 3.5: Numerical simulations showing the influence of input variables PS-ratio (a), resonator size (sidelength of square resonator) (b), and relative shift of the shunt resonator (f_a-f_r=185MHz) (c) for a 2/3 π-filter. The output parameters studied are ±0.2dB channel BW, 3dB bandwidth, insertion loss and out-of-band rejection. The constraining parameter are a relative rejection of -23dB and the maximum possible channel bandwidth. Figure (d) shows the scattering parameter S_{21} for the optimized variables PS=2.5, sidelength=30μm, and relative shift=127%, as well as under-shifted (0.5) and overshifted (1.5) filters with crippled passbands. For the optimized values, the insertion loss is -1.9dB, the rejection is -25dB, the channel bandwidth is 163MHz (2.0%), and the 3dB bandwidth is 247MHz (3.1%). Figures a)-c) represent the influence of one parameter while keeping two parameters constant at the predetermined optimum conditions.

of different resonator sizes, based on an estimate from numerical simulations, into the mask design.

The third parameter studied in the filter simulations is the frequency shift imposed on the shunt resonators using mass loading, fig. 3.5 (c). This frequency shift is given in relative units of the difference $f_p - f_s$ on the bottom x-axis, and in absolute SiO_2 thickness values on the top x-axis. The shifting has a negligible influence on insertion loss and out-of-band rejection in the interval studied. The 3dB bandwidth increases linearly in the interval of 0.95-1.35 relative frequency shift studied. A significant influence on the 0.2dB bandwidth is observed, which monotonically increases from 0.95 up to 1.27, and then sharply decreases. The largest bandwidth is not observed at a relative shift of 1 but rather at 1.27. This over-shifting or pulling of the shunt resonator frequency by 27% doubles the 0.2dB bandwidth from 80 to 160MHz. This maximum shift corresponds to 21nm of SiO_2(top x-axis). If the maximum thickness of SiO_2 is exceeded during the deposition, the filter becomes unusable. Nanometer precision of the shift layer thickness deposition is thus required!

Figure fig. 3.5 (d) shows the final result of the numerical optimization simulation: The scattering parameter S_{21} of the simulated and optimized 2/3 π-ladder filter (PS=2.5, series resonator sidelength=30μm) is represented as perfectly shifted (rel. shift=1.27), as under-shifted (rel. shift=0.5), and as over-shifted (rel. shift=1.5). The perfectly shifted filter has an insertion loss of -1.9dB, the rejection is -25dB, the channel bandwidth is 163MHz (2.0%), and the 3dB bandwidth is 247MHz (3.1%). The under-shifted resonator has a higher insertion loss and low bandwidth, and the over-shifted filter suffers from a dip or excessive ripple in the passband.

An example of a badly shifted ZnO FBAR ladder filter, which shows a passband with pronounced dip and high insertion loss is given in [36], resembling our simulation results from figure 3.5 (d) with 0.5 or 1.5 relative frequency shift. This is clearly due to under-/over-shifting. Furthermore, the simulated passband characteristics reveal non-optimized resonator sizes (PS-ratio) which result in a "tilted" and therefore very limited passband width. The presented filter also shows pronounced ripples around the high frequency notch which is probably due to plate waves in the FBAR.

Possible means of enhancing the passband bandwidth or flattening the bandpass shape, i.e. over-shifting [23, 24] or by using inductors [5], has been reported.

3.4 Ladder filter fabrication

The main problem in manufacturing FBAR/SMR devices is the deposition of seven or more layers of thin films, such that the final result is a device that is on frequency and is suitable for packaging and operation. Considerable effort has been directed on obtaining ultra-high film thickness wafer uniformity below 1%. Device yield is more a matter of set-on frequency since all devices work but not all are necessarily on frequency depending on tolerances. This is in contrast to integrated circuits where devices yield is often a matter of total device failure that cannot be corrected.

3.4.1 Design of ladder filters

The area of a resonator in a filter is scaled by the source and load impedance, typically 50Ω. The use of double/series resonator in ladder filters at the place of a single resonator has the advantage of doubling the individual resonator sizes. This reduces spurious plate waves due to the larger width-to-thickness ratio, the coupling is enhanced because of less fringing field parasitics due to the lower ratio of resonator circumference to area [4], and the power handling is doubled. Furthermore, there is no need for vias through the AlN film and leads can be kept short which reduces parasitic series resistances.

The major specifications for filters are i) out of band rejection, ii) insertion loss, iii) channel bandwidth, iv) 3dB bandwith and v) in-band ripples. Each filter application has different specifications: We will define below arbitrary rejection levels and in-band ripples to maximize the filter bandwidth and insertion losses. The maximization of the bandwidth is one of the most important goals to be achieved in AlN based ladder filters because the intrinsic material coupling is quite limited with respect to application requirements.

The successful fabrication of ladder filters depends, once the fabrication of SMRs is mastered, on the frequency shifting. As we have seen in the previous numerical simulations, this step requires an addition of approximately 10-20nm of material on the shunt resonator, to set the parallel resonance frequency of the shunt element on the parallel resonance frequency of the series resonator.

The principal problem at higher frequencies is the sensitivity of the resonators to changes in electrode thickness of some nanometers. This precision has to be mastered when shifting resonance frequencies. It is thus important to optimize the electrode thickness and material used for mass-loading/shifting of the resonators (see fig. 3.4) in order to reduce the sensitivity towards a frequency shift. The precision on the thickness of the added shift-layer is crucial and reducing the sensitivity allows for more fault tolerance upon the deposited film thickness. The thinner the top electrode, the less sensitive it is towards added material for shifting. In order not to increase the electrode electrical resistance by making it too thin or influencing the growth of the AlN film due to a bad nucleation surface as a result of a thin bottom electrode, an optimum has to be determined. In summary the electrode thickness should be inferior to 100nm (coupling coefficient, shift sensitivity), but larger than 50nm (film growth, electrode electrical resistance) in order to obtain best filter performances. For 8GHz resonators this is achieved by using 60nm thick electrodes.

3.4.2 Fabrication method

The fabrication process for SMR ladder filters is basically the same as for the SMR (described in paragraph 2.7.3, page 57). Different types of π and T-ladder filters were completely fabricated in the Spider tool. A 3 mask process for the bottom, top electrode and shift layer was necessary, employing standard photolithography and dry etching in the STS tool. Both the series and shunt elements top electrodes were fabricated at the same time. The delicate step of shunt SMR frequency trimming was done at the very end by modifying the shunt top electrode thickness (mass loading). After characterizing the resonator, and

determining the required frequency shift for optimum filter performance, the exact thickness of SiO_2 was sputter deposited and patterned by dry etching.

3.4.3 Frequency shifting

By imprecise trimming of the series/shunt resonators to the required frequency, non-optimum or even unusable filters result [34, 36, 22]. Basically two approaches exist for frequency trimming: The first approach consist in depositing the same top electrode thickness in one run on all filter resonators, and thereafter the shunt elements are mass-loaded for frequency down-shifting, or series resonators are frequency up-shifted by material removal. The second approach consists in depositing the correct electrode thickness on the series and shunt elements in two process steps.

In this thesis I persued two different approaches for frequency shifting:

1. Lift-off process adding aluminum by evaporation on the shunt resonators top electrode only.

2. Sputter depositing SiO_2 over the whole wafer and removing it where not needed using a dry etching process. The added material must be removed without altering the underlying resonator surface. This approach uses a dry etching recipy with CF_4 chemistry which has a high selectivity of SiO_2 to Al. Once the SiO_2 is completely etched, the Al acts as etch stop layer.

Shifting with Al using a lift-off process for patterning

One possibility of adding a certain film thickness, or mass-loading, on top of the shunt resonators for selective frequency shifting is by using a lift-off process: The whole wafer is covered with photoresist and photoresist vias are opened with the photolithographic process only on top of the shunt resonator. The removal of the resin in the vias is done using a developer, either Shipley 351, or Shipley CD26. The latter is not supposed to attack the Al (according to manufacturers specifications), which is used as top electrodes, and which is in direct contact with the developer solution during the developing process.

First prototype filters using this approach suffered from severe insertion losses and a distorted passband. Numerical simulations fitted with the measured filter performances revealed an insufficient thickness that had been deposited. The aluminum deposition process by e-beam evaporation was however calibrated precisely to deposit exactly 13nm of Al. The only possible explanation is that during the developing process, the Al electrode was attacked and its thickness reduced by some nanometers. To avoid this kind of unwanted and uncontrollable frequency shifting, we then tested the CD26 developer. However, the CD26 exhibited the same problems as the 351, i.e. an estimated 10nm thickness is removed during development. By estimating the thickness loss during the photolithography it was possible to deposit the loss-compensated appropriate thickness and passband filters could be produced successfully.

The effect of exposing a finished 8GHz Al/AlN/Pt SMR to the two before-mentioned developers, as required when using a lift-off process for selective frequency shifting, is shown

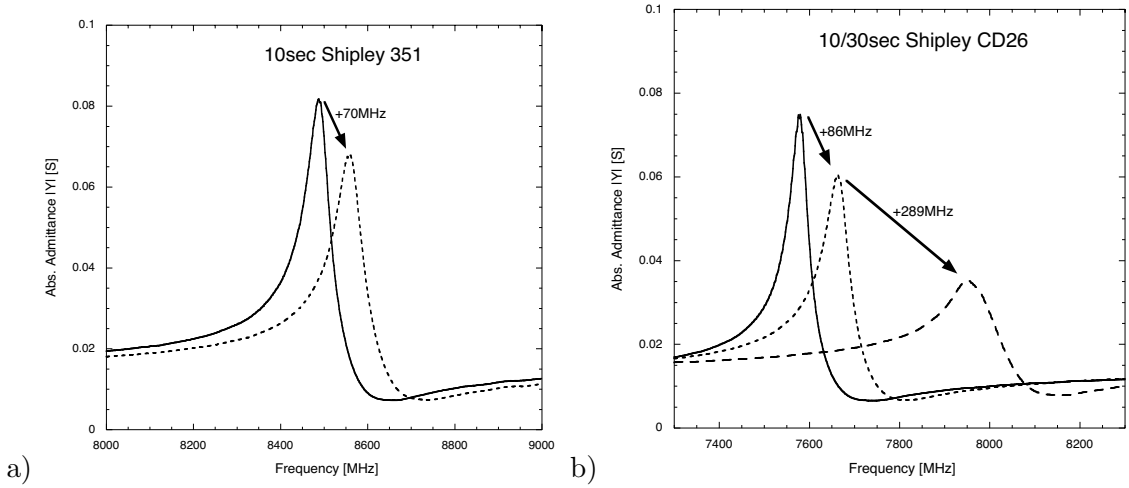

Figure 3.6: Effect of exposing a finished SMR ($1140\mu m^2$) resonator for 10sec to Shipley 351 (a), respectively 10sec plus an addition 20sec to Shipley CD26 developer (b). The corresponding frequency shift is +70MHz, respectively +86 and +289MHz.

in figure 3.6. Both Shipley developers CD26 and 351 attack the surface of the resonators. The resulting frequency shifts are +70MHz (351) and +86MHz (CD26) for a 10 second exposure. This corresponds to 5nm and 6nm removed Al thickness, assuming the sensitivity of -13.8MHz/nm calculated in figure 3.4. This high sensitivity may be exploited in sensors.

Summarizing the above paragraph it becomes evident, that a lift-off process is not appropriate for frequency shifting if the top electrode is susceptible to the slightest attack of the developer solution. Furthermore it must be mentioned that using a metal as shift layer is not appropriate as it has to be deposited exactly on the existing resonator area. Any misalignment results in an increase in the capacity and is accompanied with the creation of a parasitic parallel resonator which has a lower top electrode thickness and hence also lower resonance frequency.

Shifting with SiO_2 using a dry etch process for patterning

The addition of a thin SiO_2 layer, which is then dry etched except on the resine protected parallel resonators, proved to be the better solution for frequency shifting, due to the high selectivity of the dry etch process towards the top electrode (CF_4 process with etch stop on the Al top electrode). The sublimation temperature of AlF_x is 1272°C, which makes the chemical etching highly unlikely. As SiO_2 is an insulator no precision photolithography is required, and it only needs to be removed on and around the series resonator. The contact between developer and Al top electrode is entirely avoided as the wafer is SiO_2 covered.

The SiO_2 was deposited by sputtering. The deposition parameters were optimized for high thickness precision of 21nm SiO_2 with a maximum allowable tolerance of ±0.5nm. The lack of a shutter in the sputter tool exposes the wafer to an increasing sputter rate

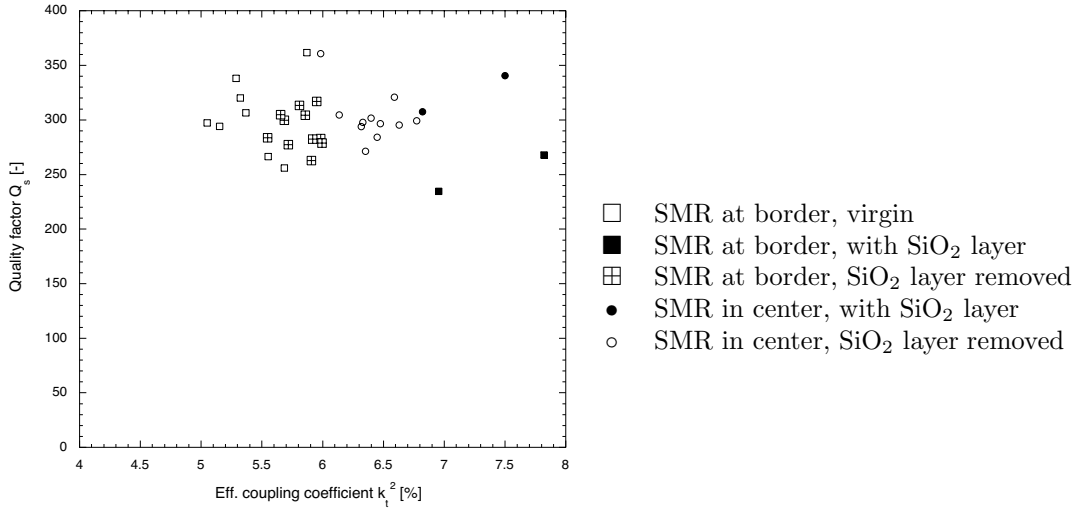

Figure 3.7: Distribution of effective coupling coefficient k_t^2 and quality factor Q_s measured on 30x30 μm^2 sized double SMR. The average quality factor for virgin SMR is Q_s=305±33 and Q_p=143±17. The average quality factor is reduced after the shift process from 305±33 to 292±17, respectively k_t^2 increases from 5.4±0.3 to 5.8±0.2%.

during ramping of the plasma to full power. Occasionally, the plasma on the SiO_2 target cannot be established and successive attempts are taken by the machine. This would have devastating effects on the filter performance because the deposited film thickness would be excessive and out of control. The standard recipe for SiO_2 sputtering in the SPIDER tool was modified: the deposition rate was reduced by using a lower target power. In addition oxygen gas was added reducing the deposition rate by a factor 3 to 0.2nm/sec compared to pure Ar sputtering. The final conditions are 1000W, 30sec ramp, 1sccm O_2, 15sccm Ar and a deposition time of 1:25min.

The SiO_2 film was patterned by using standard photolithography and a dry etch process with a CF_4 chemistry. The plasma in the dry etcher has a power ramp-up time and doesn't always ignite. Over-etching has to be limited to avoid up-shifting of frequencies on the series resonators due to physical etching of the Al electrode. The etching speed is approximately 200nm/min and some extra time has to be allowed to make sure that the SiO_2 is completely removed on the series resonators. The total etch time was a mere 25sec.

The influence of adding and removing SiO_2 was monitored on test SMR integrated on the same wafer as the ladder filter. Figure 3.8 (b) shows an example of a SMR test array, where double resonators with the SiO_2 shift layer, with the removed SiO_2 shift layer, and with mixed resonators are repeated 3 times. The influence of adding and removing the shift layer of 20nm SiO_2 on resonator properties is represented in figure 3.7.

The initial or virgin double 30x30μm^2 SMR on the border of the wafer exhibit a quality factor of Q_s=305±33 and Q_p=143±17, and the coupling coefficient is k_t^2 is 5.4%±0.3. After

the application and removal of the shift layer, as is required for ladder filter fabrication, the $k_t^2 - Q_s$ properties of the SMR are modified. The unshifted resonators quality factor remains constant with 292±17, however the coupling coefficient is increased significantly to 5.8±0.2%. The shifted resonators show an even higher coupling coefficient of more than 7%. This artifact is due to spurious ripples which overlay the admittance signal around the anti-resonance frequency and which make the determination of k_t^2 imprecise. The measured coupling coefficient of 6.4%±0.2 in the center of the wafer on shifted/un-shifted resonators is significantly higher than at the border. This suggests that the AlN film does not have the same quality over the entire wafer.

The proposed frequency shifting process does not significantly reduce the quality factor of the individual resonators, but the coupling coefficient is significantly increased. Unshifted resonators, where the SiO_2 layer is removed, should theoretically exhibit identical properties as the virgin resonators. The modification that affect the unshifted resonators might be i) uncomplete SiO_2 removel, ii) overetch into the Al electrode, or iii) surface roughness modification. Numerical simulations suggest only a slight increase in the effective coupling coefficient from 5.88% to 5.94% when applying the 20nm thick SiO_2 shift layer. The observed increase of the anti-resonance frequency in unshifted resonators of +83MHz corresponds to a thinning of the Al top electrode from 60nm to 54nm, which will also cause an increase in ohmic losses in the electrodes. This is however limited to less than 5% of the total ohmic losses in the resonator electrodes. The roughening of the electrode surface might be an explanation for the increased effective coupling coefficient: Assume two identical parallel resonators with slightly different top electrode thicknesses that lead to a frequency difference between the two resonators equivalent to a fraction of the difference between resonance and anti-resonance frequency. The total admittance of both resonators is the sum of each individual resonator admittance. Because the absolute admittance curve is approximately symmetric about the resonance frequency, f_r of the summed admittance is the average of the two individual resonance frequencies. The admittance curve around the anti-resonance frequency however is dissymmetric and results in f_a of the total admittance to be almost identical to f_a of the higher frequency resonator. Because we use the admittance curve to determine the effective coupling coefficient (eq. 2.11) the effective measured coupling coefficient will be larger. Coming back to the measured differences of k_t^2 for SiO_2 shifted and unshifted resonators, we may conclude that the increase of 0.4% for the unshifted resonator is due to two parallel resonators with a frequency difference of 22MHz that would correspond to a difference in top electrode thickness of 1.6nm due to either roughness or a gradient in electrode thickness. The extremely large effective coupling coefficient 7.4% of the SiO_2 shifted resonator corresponds to a frequency difference of 80MHz. This corresponds to a roughness or thickness gradient of 7nm for the 21nm thick SiO_2 layer. An explanation for this large difference might be that the areas defined for the shift layer are not completely aligned with the top electrode resulting in the border area of the resonators in the creation of two parallel resonators.

The effect of adding and removing the SiO_2 film on resonator admittance is shown in figure 3.8. The initial state of two closely spaced resonators is compared with the state after loading with SiO_2 (frequency downshift) and after loading&unloading (frequency shift

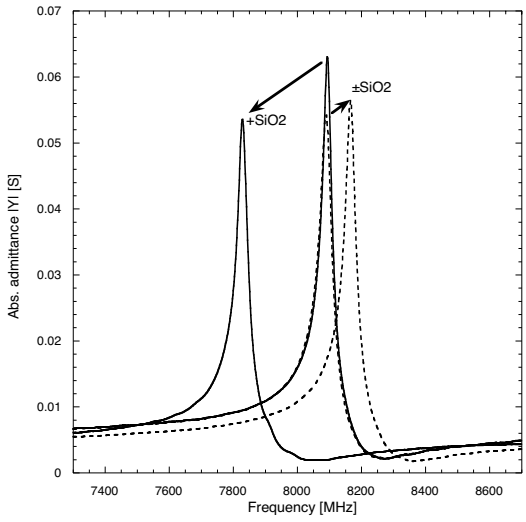

a)

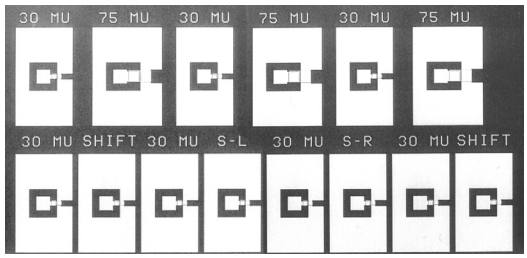

b)

Figure 3.8: (a) Effect of adding 21nm of SiO_2 for shifting and removing it with a CF_4 dry etching process. Whereas the SiO_2 loaded resonator is shifted by -265MHz, the SiO_2 loaded and plasma removed resonator is shifted by an unintended +77MHz. 8 SMR (30x30μ)m^2 closely spaced by 300μm were used to qualify and quantify the effect of adding and removing the SiO_2 layer (b).

upwards) which is achieved in one run, equivalent to filter shifting. Not only the resonance frequency is affected, but also the quality factor and the coupling coefficent are affected (which is also seen in fig. 3.7). The reduction in resonance frequency by -265MHz, which corresponds to 23.7nm SiO_2 according to fig. 3.4, corresponds to a relative frequency shift of 146%. The increase in resonance frequency by +77MHz of the loaded-&-unloaded resonator can only be explained with Al top electrode thinning corresponding to 5.6nm Al. Because the sublimation temperature of the AlF_3 compound is very high (1272°C) chemical etching is very unlikely. The thinning of the Al electrode is therefore due to physical etching. A modification of the etch process with lower platen power (lower substrate bias) might reduce the physical etch contribution.

3.5 Characterization of 8GHz SMR ladder filters

Pictures of finished 8GHz SMR π and T-ladder filters are shown in figure 3.9. (a) is an example of a 2/1 T-ladder filter with a PS-ratio of 6, (b) shows a 3/4 π-ladder filter with PS-ratio of 2.

The transmission spectrum S_{21} was measured with a network analyzer NA HP8722 D with a 2 port setup as described in paragraph 2.7.4 and air coplanar probes with 250μm pitch. The incident power was fixed at -5dBm.

The scattering parameter S_{21} of 1, 2 and 3 sections π-ladder filters centered at 7.85GHz

Table 3.1: Summary of simulated vs. measured filter characteristic on 1, 2 and 3 section π-filters with a PS-ratio of 2, respectively 1 section π-filters with PS-ratio of 2, 3, and 4.

	PS-ratio [-]	Ins. loss [dB]	Rejection [dB]	3dB BW [MHz]	0.2dB BW [MHz]
1-section simulated					
no loss	2	-1.1	-9.9	265	178
with loss	2	-2.6	-12.1	242	134
measured					
1-section	2	-3.2	-13.2	244	111
2-section	2	-5.5	-32.0	224	99
3-section	2	-7.5	-32.6	194	44
1-section	3	-4.6	-19.3	225	107
1-section	4	-4.3	-22.8	208	94

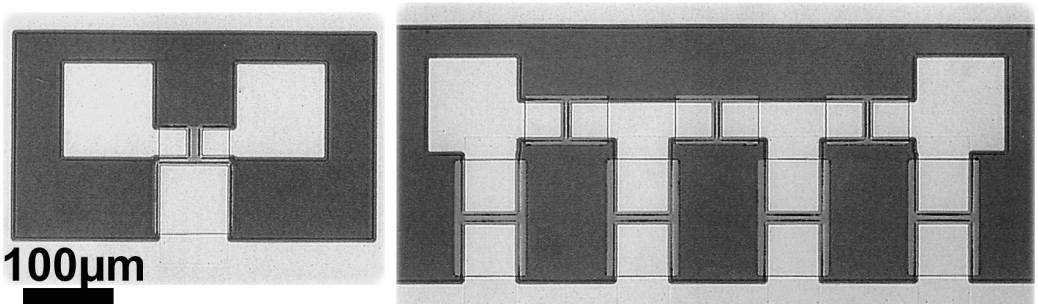

Figure 3.9: Image of 1 section 2/1 T-ladder filter and 3 section 3/4 π-ladder filter. Two series resonators are used for each leg of the π sections. Some of the Al top electrode area covered by the 21nm thick SiO_2 film for the shunt resonator (vertical legs) shifting is visible at the bottom of the image.

with a PS-ratio of 2 are shown in figure 3.10 as wide-band, as well as narrow-band response around the passband. Table 3.1 summarizes the relevant filter properties. The passband is ripple-free which is due to the absence of plate waves in the SMR. Each section contributes with ≈2.2dB to the insertion loss, which leaves a 1dB loss unaccounted for when extrapolating to zero sections. One explanation for these unaccounted losses are series resistances in the connection lines to the *in* and *out* port of the filter. The 0.2dB channel BW and 3dB BW is also reduced for each supplementary section. The largest 0.2dB bandwidth is achieved with the single section filter with 111MHz (1.4%) and the 3dB BW amounts to 244MHz (3.1%). The group delay variations inside a 30MHz channel are 1.8±0.6nsec for a 1/2 ladder filter with a PS-ratio of 3, where the given error represents the standard deviation. Averaging 8 measurements of the group delay variations reduced the standard deviation to ±0.4, which indicated that the variations is due to measurement noise.

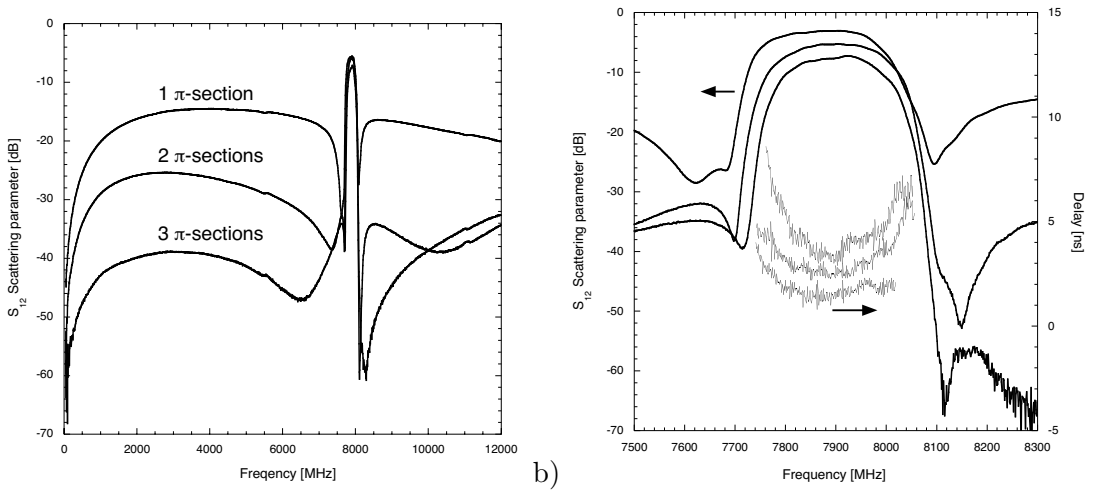

Figure 3.10: S_{21} scattering parameter measurements on π-filters with 1, 2 and 3 sections over broad frequency spectrum (a), and detailed view of passband as well as group delay time (b). The PS-ratio is fixed at 2 and the relative frequency shift is approximately 1.25. The 3-section 3/4 π-filter is represented in the right image of figure 3.9.

Figure 3.11 shows results from a single section π-ladder filter with increasing PS-ratio of 2, 3, and 4. The relevant filter properties are summarized in table 3.1. The increasing PS-ratio leads to an increase in the out-of-band rejection accompanied by an increasing insertion loss. The increase in PS-ratio also reduces the 0.2dB and 3dB bandwidth.

The measured filter performances remained unchanged after dicing of the wafer. The size of a SMR 1/2 ladder filter die is approximately 0.8x0.8x0.5mm^3, figure 3.12.

3.6 Comparison of measured filter characteristics vs. numerical ladder filters simulations

Numerical filter simulation results of a 1/2 π-filter are compared in figure 3.13 with the measured S_{21} scattering parameter. The parasitic elements used for the fit of the simulation are given in table 3.2, and the relevant filter performances obtained with the fit are given in table 3.1. The passband insertion loss and bandwidth, and the out-of-band rejection are different in magnitude, whereas the attenuation poles correspond well assuming a 5.8% material coupling coefficient and 127% relative frequency shifting. The introduction of a 5Ω series resistance $R_{top} + R_{bottom}$ representing electrode losses (loss model of figure 3.13 (b), as already determined for the simple SMR numerical fit (c.f. paragraph 2.7.5, page 62), increases the insertion loss by 0.5dB and reduces the 0.2dB channel BW by 30MHz. This series resistance is due to ohmic losses in the top and bottom electrodes. Introducing a 500Ω parallel resistance $R_{parallel}$, which may be better expressed by a equivalent conduction of 2mS, reduces the insertion loss by another 1dB and the channel bandwidth by 20MHz.

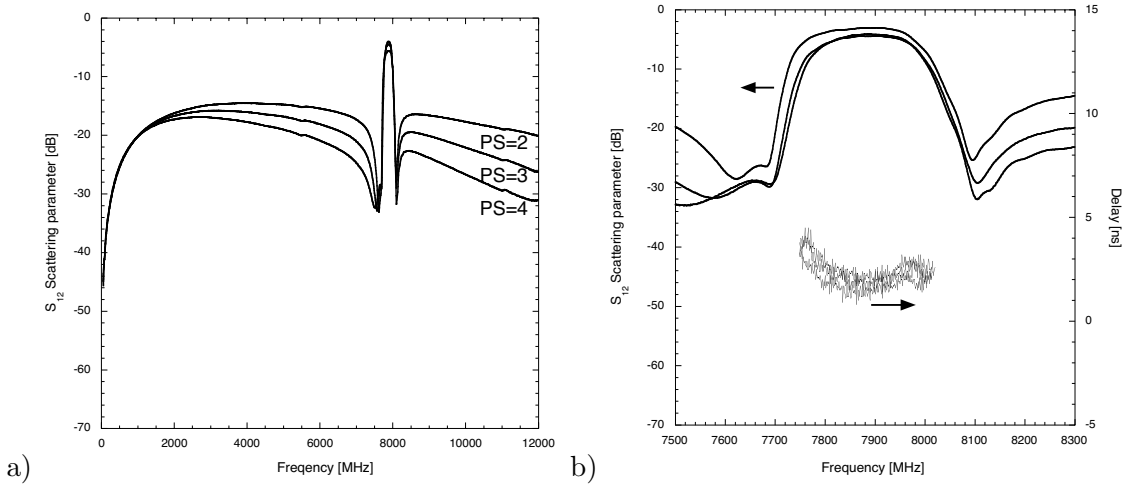

Figure 3.11: S_{21} scattering parameter measurements of 1-section π-filters with a PS ratio of 2, 3 and 4 over broad frequency spectrum (a), and detailed view of passband as well as group delay time (b). The relative frequency shift is approximately 1.25. An image of the corresponding filter is represented in figure 3.2 (b).

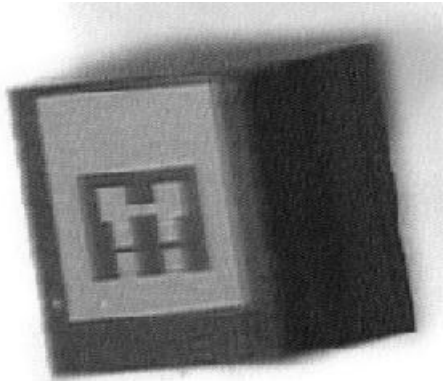

Figure 3.12: Image of finished SMR ladder filter die with dimensions of 0.8x0.8x0.5mm^3 used for sub-system testing.

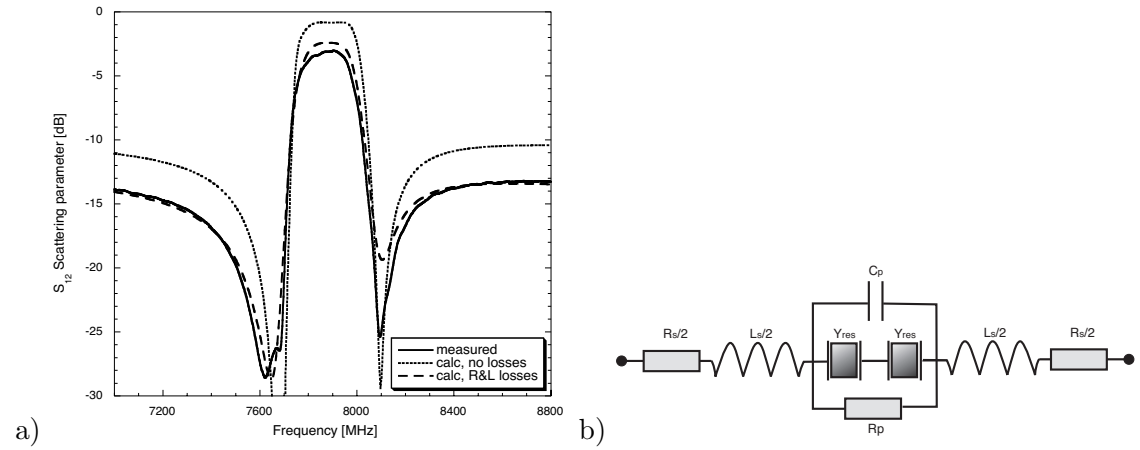

Figure 3.13: (a) Numerical filter simulation using the resonator admittance Y_{res} without, and with parasitic losses compared to the measured 1/2 π-filter. The input admittance Y_{res} corresponds to numerical 1-D simulation using a coupling coefficient k_t^2 of 5.8% for AlN. To improve the fit between simulation and measurement, a model with parasitic series inductance L_{series} and resistance $R_{\text{top}} + R_{\text{bottom}}$, as well as parasitic parallel resistance R_{parallel} and capacity C_{parallel} is proposed (b). The values of the fit are given in table 3.2

Additionally, the zero poles of the filter become less pronounced. This parallel resistance is due, again to conduction between the top electrodes of the double resonator, probably due to an insufficient top electrode dry etch as we have already seen in paragraph 2.7.5, page 62 or dielectric losses.

To adjust the out-of-band rejection levels, a parasitic series inductance L_{series} of 100pH has to be added to each resonator within the ladder filter electrical circuit. This inductance is not present in the measured simple resonator. The parasitic parallel capacity $C_{parallel}$ is zero. The realized fit agrees quite well with the measured filter scattering parameter. Only a small difference of approximately 0.5dB inside the passband is not being accounted for.

The parasitic elements that need to be added to the double SMR and the 1 section 1/2 π-ladder filter are the same with the exception of the series inductance. The cause for the series and parallel resistances, and solutions how the electrode materials, the design and the process flow of fabricated resonators have to be improved to reduce those parasitics has been discussed in paragraph 2.7.5, page 62. The series inductance, which appears only in the filter and enhances the out-of-band rejection by 3dB, is more complicated to understand. A possible explanation might be the electrical resistance of the top electrode between the ground *in* and *out* port which creates non-zero electrical potentials. To reduce this electrical resistance, the top electrode thickness between the individual resonators should be increases and the design of the filter be modified so as to approach all resonators and reduce the distance between *in* and *out* ports.

Table 3.2: Values of parasitic elements added to the simulated admittance of a double SMR to achieve the fit of figure 3.13. The AlN material coupling coefficient and relative frequency shift of ladder filter shunt resonator used in the numerical simulations are given at the bottom.

Loss element	Unit	double SMR	1/2 π-filter
R_{series}	[Ω]	5	5
$R_{parallel}$	[Ω]	500	500
L_{series}	[pH]	0	100
$C_{parallel}$	[F]	0	0
AlN k_t^2	[%]	5.8	5.8
rel. shift	[%]	-	127

3.7 Summary and Conclusions

Numerical filter simulations performed with MatLab programs were used to understand the role of the large number of design variables for SMR bandpass ladder filters. The simulations showed the importance of a precise frequency shift. The additional 20 nm thick SiO_2 thin film used for loading the shunt resonators had to be deposited with nanometer precision, otherwise insertion loss and passband ripple would have been too large for an usable filter. An overshifting of the shunt resonators by 1.3 times the difference of antiresonance and resonance frequency resulted in a doubling of the band width while keeping the ripple below $\pm$0.2dB.

The choice of SiO_2 over Al as frequency shift layer was guided by four considerations. More film thickness is required for a given frequency shift, because of its low specific mass. The sputter process for SiO_2 has a low rate allowing for a good thickness control on the nanometer level. The area covered by the SiO_2 film must not coincide precisely with the top electrode of the shunt resonator since it is an insulator. Finally, SiO_2 can be precisely patterned by dry etching and there is no need to expose the Al top electrode to developer solution that would attack Al. The role of frequency shifting on the figure of merit of individual resonators has been investigated. Two possible ways of frequency shifting have been presented and their advantages and disadvantages have been studied both theoretically and practically.

Passband ladder filters working at 8GHz with different designs were successfully fabricated on 4" silicon wafers. A 2/3 π-filter achieved for example low insertion losses of 5.5dB, a large 0.2dB bandwidth of 99MHz (1.3%), 3dB bandwidth of 244MHz (2.9%), and an out-of-band rejection of 32dB. These characteristics comply fully with the industrial specifications. The group delay variation specification was the hardest to meet. Our measurement set-up was too noisy to evaluate the delay time with one scan below the ns level. We averaged the result over a number of scans and found a decrease to the required level below 0.2ns in 32MHz intervals. Individual filter dies with dimensions of 0.8x0.8x0.5mm^3 were obtained from a ladder filter device wafer and shipped to our industrial partner for

subsystem testing (see figure 3.12).

The filter characteristics were well predicted by simulation calculations. This allowed us to assign deviations to parasitic elements. The major parasitic element in series double resonators was identified as the series resistance given by the bottom electrode path between the resonators. An additional parasitic element was identified in the π-ladder filters. A series inductance is needed to explain the observed filter performance.

Possible improvements for filter design, in addition to the individual resonator improvements that have been discussed in the previous chapter, are twofold: i) the electrode conductivity between resonators has to be increased by increasing the electrode thickness between individual resonators, as well as reducing the distance between the *in* and *out* ports by redesigning the filter topology. ii) the frequency shift process has to be revised so that the over-etching on the series resonators is limited to a strict minimum during the removal of the shift layer.

We have identified in this thesis work the property limitations of FBAR / SMR structures at X-band frequencies. The reduced electrode thickness at frequencies in the range of 5 to 10GHz imposes a very careful selection of the electrode material. The electrical conductivity and acoustic properties have to be balanced to obtain a high figure of merit $k_t^2 Q$ of individual resonators and optimum passband ladder filter performances. A stringent thickness control for depositing and patterning of the frequency shift layer to a few nanometers is necessary to achieve passband filters, which comply with industrial specifications. It can be concluded that it is possible to conceive bandpass filters for industrial applications as far as 10GHz and possibly above.

Bibliography

[1] A. Ballato and T. Lukaszek. A novel frequency selective device: the stacked-crystal filter. In *27th annual frequency control symposium*, volume 27, pages 262–269, 1973.

[2] P. Bradley, R. Ruby, J. Larson, Y. Oshmyansky, and D. Figueredo. A film bulk acoustic resonator (FBAR) duplexer for USPCS handset applications. In *Ultrasonics Symposium*. IEEE, 2001.

[3] D. Cushman, K.F. Lau, E. M. Garber, K.A. Mai, A.K. Oki, and K.W. Kobayashi. SBAR filter monolithically integrated with HBT amplifier. In *Ultrasonics symposium*, 1990.

[4] G.G. Fattinger, J. Kaitila, R. Aigner, and W. Nessler. Thin film bulk acoustic wave devices for applications at 5.2GHz. In *Ultrasonics symposium Proceedings*, Hawaii, USA, 2003. IEEE.

[5] K. Grenier, B. P. Barber, V. Lubecke, M. Zierdt, H. Safar, P. Pons, and P. L. Ammel. Integrated RF MEMS for single chip radio. In *Transducers*, 2001.

[6] T. W. Grudkowski, J. F. Black, T. M. Reeder, D. E. Cullen, and R. A. Wagner. Fundamental-mode VHF-UHF miniature acoustic resonators and filters on silicon. *Appl. Phys. Lett.*, 37(11):993–995, 1980.

[7] T. W. Grudkowski, J. F. Black, T. M. Reeder, D. E. Cullen, and R. A. Wagner. Fundamental mode VHF/UHF bulk acoustic wave resonator and filters on silicon. *Ultrasonics symposium proceedings IEEE*, pages 829–833, 1980.

[8] J. Kaitila, M. Ylilammi, J. Molarius, J. Ella, and T. Makkonen. ZnO based thin film bulk acoustic wave filters for EGSM band. In *Ultrasonics Symposium*, pages 803–806. IEEE, 2001.

[9] G.R. Kline, R.S. Ketcham, and K.M. Lakin. Low insertion loss filters synthesized with thin film resonators. In *IEEE 1987 Ultrasonics Symposium Proceedings*, volume 1, pages 375–380, 1987.

[10] G.R. Kline, R.S. Ketcham, and K.M. Lakin. Thin film microwave acoustic filters on gaas. In *Gallium Arsenide Integrated Circuit (GaAs IC) Symposium, 1988. Technical Digest 1988., 10th Annual IEEE*, volume 1, pages 313 – 316, 1988.

[11] G.R. Kline, K.M. Lakin, and R.S Ketcham. Thin film resonator (TFR) low insertion loss filters. In *Ultrasonics Symposium*, volume 1, pages 339 –342, 1988.

[12] S. V. Krishnaswamy, J. Rosenbaum, S. Horwitz, C. Vale, and R. Moore. Compact FBAR filters offer low-loss performance. *Microwaves & RF*, pages 127–136, 1991.

[13] S. V. Krishnaswamy, J. F. Rosenbaum, S. S. Horwitz, and RA. Moore. Film bulk acoustic wave resonator and filter technology. In *IEEE Microwave Symposium Digest*, volume 1, pages 153–155, 1992.

[14] K. M. Lakin. Thin film resonators and high frequency filters. *?*, 2001.

[15] K. M. Lakin, G. R. Kline, R. S. Ketcham, Martin. J. T., and K. T. McCarron. Stacked crystal filters implemented with thin films. In *Proceedings of the 43rd Annual Symposium on Frequency Control 1989*, pages 536–543, Denver, CO, USA, 1989.

[16] K. M. Lakin, G. R. Kline, and K. T. McCarron. Thin film bulk acoustic wave filters for GPS. In *IEEE Ultrasonics Symposium*, pages 471–476, Tucson, AZ, 1992.

[17] K. M. Lakin, G. R. Kline, and K. T. McCarron. Development of miniature filters for wireless applications. *IEEE Transactions on Microwave Theory and Techniques.*, 43(12):2933–2939, 1995.

[18] K. M. Lakin, K. T. McCarron, and R. E. Rose. Solidly mounted resonators and filters. In Levy-M; Schneider-SC; McAvoy-BR, editor, *IEEE Ultrasonics Symposium*, volume 2, pages 905–908, Seattle, WA, USA, 1995.

[19] K.M. Lakin, R.S. Ketcham, G.R. Kline, and R.J. Weber. Thin film resonator technology. In *Proceedings RF Technology Expo 89*, pages 13–28, 1989.

[20] K.M. Lakin, G.R. Kline, R.S. Ketcham, and S.G. Burns. Thin film resonator based low insertion loss filters. In *IEEE 1986 Ultrasonics Symposium Proceedings*, volume 1, pages 371–375, 1986.

[21] K.M. Lakin, G.R. Kline, R.S. Ketcham, A.R. Landin, W.A. Burkland, K.T. McCarron, S.D. Braymen, and S.G. Burns. Thin film resonator technology. In *Proceedings of the 41st Annual Frequency Symposium 1987*, pages 371–381, 1987.

[22] R. Lanz and P. Muralt. 8 GHz microwave filters based on bulk acoustic waves in piezoelectric AlN thin films. In *13th IEEE International Symposium on Applications of Ferroelectric*, Nara, Japan, 2002. ISAF.

[23] III Larson, J., R. Ruby, P. Bradley, and Y. Oshmyansky. A BAW antenna duplexer for the 1900 MHz PCS band. In *IEEE Ultrasonics symposium*, volume 2, pages 887–890, 1999.

[24] J. III. Larson, R. Ruby, P. Bradley, J. Wen, S.-L. Kok, and A.l. Chien. Power handling and temperature coefficient studies in FBAR duplexers for the 1900 MHz PCS band. In *IEEE Ultrasonics symposium*, volume 1, pages 869–874, 2000.

[25] H. P. Löbl, M. Klee, C. Metzmacher, W. Brand, R. Milsom, and P. Lok. Piezoelectric thin AlN films for bulk acoustic wave (BAW) resonators. *Materials Chemistry and Physics*, 79:143–146, 2003.

[26] H. P. Löbl, M. Klee, C. Metzmacher, W. Brand, R. Milsom, P. Lok, and F. van Straten. Piezoelectric materials for BAW resonators and filters. In *Ultrasonics Symposium*, pages 807–811. IEEE, 2001.

[27] H. P. Löbl, C. Metzmacher, D. N. Peligrad, R. Mauczok, M. Klee, W. Brand, R. Milsom, P. Lok, F. van Straten, A. Tuihout, and J. W. Lobeck. Solidly mounted bulk acoustic wave filters for the GHz frequency range. In *Ultrasonics Symposium*, pages 919–923. IEEE, 2002.

[28] L. Mang, F. Hickernell, R. Pennell, and T. Hickernell. Thin-film resonator ladder filter. In *1995 IEEE MTT-S International microwave symposium*, pages 887–890, 1995.

[29] D.M. Pozar. *Microwave engineering*. Wiley, New York, 2nd edition, 1998.

[30] R. C. Rennick. An equivalent circuit approach to the design and analysis of monolithic crystal filters. *IEEE Transaction on Sonics and Ultrasonics*, SU-20(4):347–354, 1973.

[31] R. Ruby, P. Bradley, III Larson, J., Y. Oshmyansky, and D. Figueredo. Ultra-miniature high-Q filters and duplexers using FBAR technology. In *Solid-State Circuits Conference*, pages 120 –121, 2001.

[32] R. Ruby, P. Bradley, J.D. Larson, and Y. Oshmyansky. PCS 1900 MHz duplexer using thin film bulk acoustic resonators (FBARs). *Electronics Letters*, 35(10):794–795, 1999.

[33] R.C. Ruby, P. Bradley, Y. Oshmyansky, Al. Chien, and III Larson, J. Thin film bulk wave acoustic resonators (FBAR) for wireless applications. In *Ultrasonics Symposium*, Atlanta, USA, 2001. IEEE.

[34] C. W. Seabury, J.T. Cheung, P.H. Kobrin, R. Addison, and D. P. Havens. High performance microwave air-bridge resonators. In *Ultrasonics Symposium*, pages 909–911. IEEE, 1995.

[35] R. B. Stokes and J. D. Crawford. X-band thin film acoustic filters on GaAs. *IEEE Trans. Microwave Theory Tech.*, 41(6/7):1075–1080, 1993.

[36] Q.X. Su, P. Kirby, E. Komuro, M. Imura, Q. Zhang, and R. Whatmore. Thin-film bulk acoustic resonators and filters using ZnO and lead-zirconium-titanate thin films. *IEEE transactions on microwave theory and techniques*, 49(4):769–778, 2001.

[37] C. Vale, J. Rosenbaum, S. Horwitz, S. V. Krishnaswamy, and R. Moore. FBAR filters at GHz frequencies. In *44t annual symposium on frequency control*, pages 332–336, 1990.

Chapter 4

$KNbO_3$ thin films

4.1 Introduction

The available coupling factor of AlN and ZnO is a very limiting factor for the filter bandwidth, which amounts to roughly $k_t^2/2$. AlN and ZnO have an intrinsic thickness-extensional electromechanical coupling k_t^2 limited to 8%. Materials with higher electromechanical coupling could open new possibilities for microwave BAW filters. The exploitation of ferroelectric thin film materials such as PZT results in an increase of k_t^2 compared to AlN and ZnO: Awang et al. [9, 10] and Arscott et al. [7, 8] reported on sol-gel $PbTiO_3$ (PT) and $Pb(Zr_xTi_{1-x})O_3$ (PZT) based composite FBARs. They measured an effective coupling coefficient k_t^2 of approximately 50% and a mechanical quality factor in excess of 500 based on rather precarious, and full of spurious, resonator impedance curves with a fundamental resonance of 0.1GHz. A better defined resonance curve was obtained for the PT/GaAs resonator at 2.3GHz [9]. The high quality factor of 700 is attributable to the high mechanical quality factor of the substrate but the coupling was low. The group of Misu, Yamada et al. [46, 75] reported on PT bulk micromachined membrane type FBARs working at 1.5GHz. The mechanical quality factor was very low with 50-70 and the electromechanical coupling coefficient amounted to k_t^2=10%. Monolithic crystal filters realized with the same technology had an insertion loss of 14dB. Yamagouchi et al. [76] reported on PZT composite FBARs realized with Si substrates. A quality factor of 84 and a k_t^2 of approximately 16% was obtained at the fundamental mode resonance of 1.7GHz. Löbl et al. [43] presented SMR using sol-gel PZT as piezoelectric material. The poled SMR exhibited coupling coefficients of 7.8%-25%, which would allow to conceive ladder filters with a 4 times higher passband when compared with AlN based BAW filters. The drawback is again the low quality factor of 67 at a frequency of 0.9GHz, respectively 18 at 2.3GHz.

The insufficient quality factor of PZT prevents the use of this material for BAW applications at microwave frequencies. Alternative piezoelectric materials with higher coupling coefficients than AlN, but which still exhibit viable mechanical quality factors in the high UHF, and low SHF range would open new possibilites. A potential material candidate is $KNbO_3$. It has recently been reported that $KNbO_3$ single crystal, known as excellent

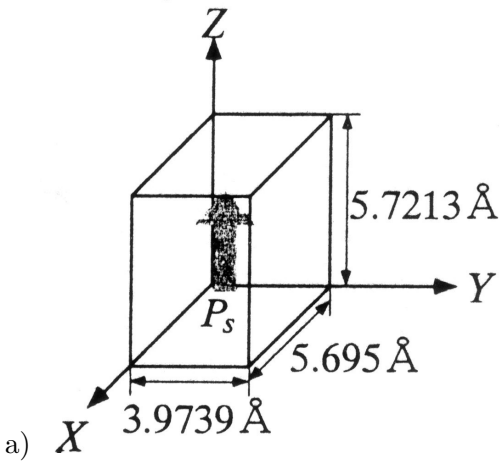

a)

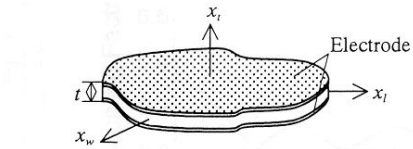

Fig. 5. An infinite plate with electrodes on its major surfaces and its vibrator coordinates.

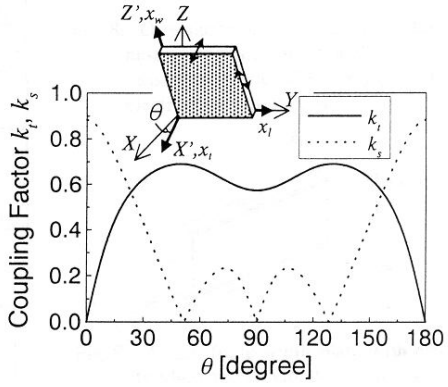

b)

Figure 4.1: Orthorhombic crystallographic axes for $KNbO_3$ (a), and calculated orientation dependence of k_t for the thickness-extensional mode and k_s for the thickness-shear mode in $KNbO_3$ (XYl)θ plate with electrodes on their major faces (b) [47].

nonlinear optic, electrooptic and photorefractive material, has a very high coupling factor for surface acoustic waves [79]. Piezoelectric $KNbO_3$ single crystals have large piezoelectric constants. The SAW propagation properties of KNbO3 single crystals were investigated by Yamanouche et al. [77] and the extremely large electromechanical coupling constant k^2=0.53 of the SAW propagation along the X-axis on the rotated Y-cut plane was obtained theoretically and experimentally. Therefore, $KNbO_3$ films are expected to be materials for high-performance bulk wave transducers and SAW devices. The high coupling is very important for wideband SAW or BAW filters.

Nakamura and Kawamura [47] calculated the electromechanical coupling factors for bulk waves in $KNbO_3$ crystals. It was found that most of these coupling factors are very large along certain crystallographic orientations. The maximum coupling factor of the thickness-extensional mode excited with a longitudinal field, k_t^2, is as high as 48% for the X-cut rotated by 49.5° about the Y-axis (fig. 4.1). This calculation was validated by measurements. The corresponding sound velocity of 8125m/s, lies between PZT (4200m/s) and the one of the c-axis oriented AlN (11350m/s). Considering the high longitudinal wave velocity of $KNbO_3$, the thickness-extensional mode resonator is suitable especially for high-frequency applications.

$KNbO_3$ thin films have several obstacles to overcome before they can be used in a more general fashion: Stoichiometry is far more difficult to control with respect to AlN films because $KNbO_3$ consists of 3 elements, of which potassium is highly volatile. Several groups

reported sodium and potassium losses in Na- and K-based films grown by pulsed laser deposition and sputtering technique. Adding an excess amount of the volatile constituent to the target was used to obtain the correct stoichiometry in the film. However, overcompensated targets often contain other constituents such as carbon, easily crack, absorb water from the atmosphere, and yield irreproducible results because of their inherent instability. The vacancies of monovalent Na and K ions are the main reason of the ionic conductivity in sodium and potassium niobates. Wada et al. [69] claim that the crystals are difficult to grow with sufficient electrical resistance due to the high volatility of potassium during the growth process. Thin film growth of $KNbO_3$, mostly on monocrystalline MgO and $SrTiO_3$ (STO) substrates, has only been reported for the last 10 years, whereas AlN films have already been deposited successfully by MSP on metal substrates in the end of the 1960's. $KNbO_3$ has a cubic-tetragonal phase transition at 435°C which requires deposition temperatures higher than 500°C for crystalline film growth, compared to AlN thin film deposition which is achieved at a minimum temperature of 200°C in magnetron sputtering.

Single crystals of $KNbO_3$ are very difficult to pole. Wada et al. [69] propose a 2 step poling treatment: Non-180° domains were poled at high temperatures under a low dc field, and 180° domains were switched at lower temperatures under a high dc-bias field. The measured dielectric loss was below 10%.

We chose to develop a process for thin film $KNbO_3$ deposition on metallized silicon substrates because of the promising properties for microwave BAW, but also MEMS and other thin film applications. The choice of the deposition method was magnetron sputtering because it allows for deposition on large substrates, which is needed for device processing, gives easy control over the process parameters (pressure, process gases, applied target power, target composition in our case, substrate temperature), it is a technology which our group has strong expertise, and MSP is usually very repeatable. The choice of a MOCVD deposition method might have been better for stoichiometry control but was not possible due to security constraints.

4.2 Properties of $KNbO_3$

4.2.1 Phase diagrams

The binary phase diagram Nb_2O_5-K_2CO_3 in figure 4.2 (a) was determined by Reisman and Holtzberg [54] by differential thermal analysis performed on K_2CO_3 and Nb_2O_5 powders mixed in different ratios. In the region 0-75 mol%, potassium carbonate serves solely as a source of K_2O. In the region 75-100 mol%, K_2CO_3 is actually present as a component of the system. It can be seen from the diagram that there are five compounds corresponding to the compositions: (I) K_3NbO_4, (II) $KNbO_3$, (III) $K_4Nb_6O_{17}$ (hygroscopic), (IV) KNb_3O_8 and (V) $K_6Nb_{44}O_{113}$. Roth [56], and Irle et al. [37] determined 2 more phases between 25 and 40%mol in the Nb_2O_5-K_2CO_3 system: $K_3Nb_7O_{19}$ and the the tetragonal tungsten bronze type $K_{5.75}Nb_{10.85}O_{30}$. The 50-67 mol% region is seen to be the only one suitable for growth of crystals of $KNbO_3$. Reisman and Holtzberg noted that the tendency of $KNbO_3$ to lose oxygen, especially in the vicinity of the peritectic, was quite marked.

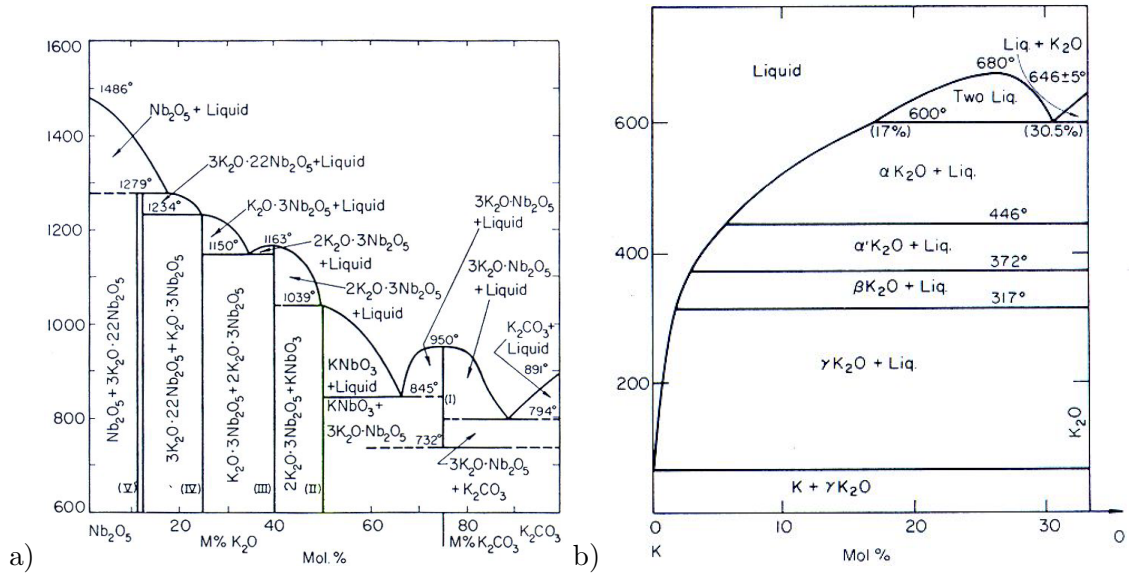

Figure 4.2: Phase diagram of NbO-KO (a) and K-KO (b).

When using ceramic targets with an excess of potassium in the form of K_2O or K_2CO_3, one must also consider the phase diagram O-K_2O [49] (fig. 4.2 (b)). K_2O has a melting point of 646°C. Loss of oxygen in the oxide results in a strong reduction of the melting point, reaching 63°C for the element K. The vapour pressure of potassium at room temperature is 1.10^{-8}T and reaches 1.10^{-6}T at the melting temperature [41]. Free potassium formed in a ceramic target under high vacuum, as for example in vacuum sputter chamber, could easily evaporate, and hence result in a reduction of the potassium content.

4.2.2 Chemical stability and decomposition

Krylov et al. [40] report that $KNbO_3$ produces no new phases when heated in vacuum of 0.1mT to 400-750°C. It merely looses oxygen. The product has the properties of the niobium bronzes, i.e. good electrical conductivity. Above 750°C sodium and potassium metaniobates decompose increasingly with temperature, to give free alkali metals. Potassium metaniobate decomposes more easily than the sodium salt. Gutman et al. [35] observed with XPS measurements an additional K 2p doublet besides the expected K 2p (3/2, 1/2) peak doublet for $KTa_xNb_{1-x}O_3$ grown by liquid-phase epitaxy. This indicates two different chemical states for the K atoms. After annealing only the expected K 2p doublet remained. A similar chemical shift of the K 2p signals was reported for vacuum-annealed pure $KNbO_3$ by Szot et al. [63]. Their conclusion was that there were two different forms of K present: A more ionic K^+ and a more metallic-like form of K which contributes to the electrical conductivity. They reported later that the existence of extended defects in the surface region, which serves as fast diffusion path for oxygen and K atoms, leads to a segregation

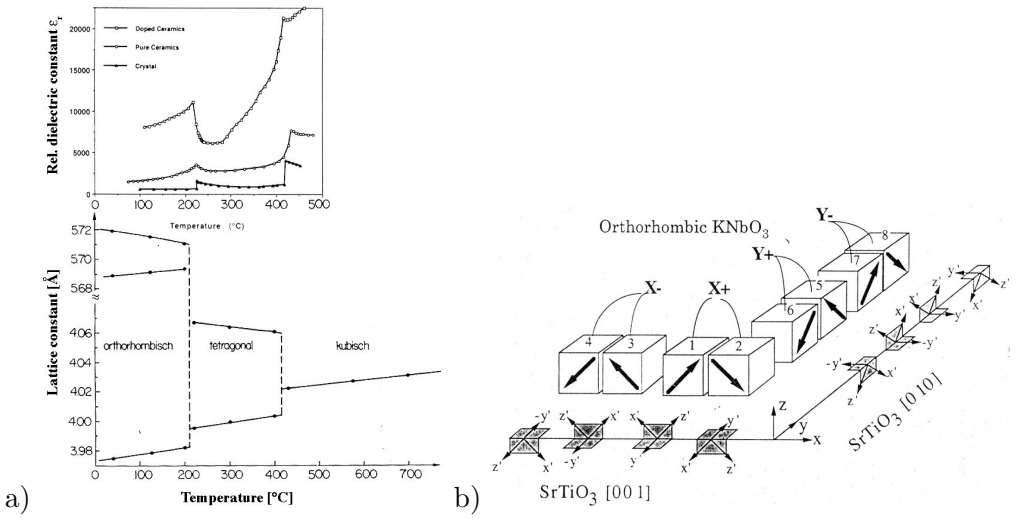

Figure 4.3: (a) Relative dielectric constant of crystal, pure and doped ceramics [28], as well as lattice constants [30] of $KNbO_3$ as functions of temperature. (b) Schematic of the 8 possible domain variants in (101) epitaxial $KNbO_3$ films [32].

of K or KO-complexes already at room temperature [64]. With a rise in temperature, a continuous transition in the surface region between $KNbO_3$ and $KO(KNbO_3)_n$ was found.

4.2.3 Dielectric, elastic and piezoelectric properties

Potassium niobate is a perovskite material like $BaTiO_3$. $KNbO_3$ undergoes phase transitions from the paraelectric cubic high-temperature phase to tetragonal at 435°C, from the tetragonal to the orthorhombic phase at 225°C, and from orthorhombic to rhombohedral at -50°C [31]. Figure 4.3 (a) represents the relative dielectric constant and the lattice parameters as functions of temperature. In the ferroelectric phase, the occurrence of a spontaneous polarization P_s directed along a fourfold, twofold and threefold rotation axis of the oxygen octahedra is associated with a lattice distortion, resulting in a symmetry reduction of the cubic point group m3m to 4mm, m2m and 3m, respectively. In this thesis we will use the orthorhombic phase principal axes a, b, c, which differ from the pseudocubic axes by a $\pi/4$ rotation about the [010] pseudocubic axis. The orthorhombic c axis is parallel to the spontaneous polarization. The orthorhombic and cubic b-axis are identical. The lattice parameters are $a = 5.6950\mathring{A}$, $c = 5.7213\mathring{A}$ and $b = 3.9739\mathring{A}$ (fig. 4.1 (a)).

The film growth takes place in the high-temperature cubic phase. When cooling the substrate to room temperature, a first phase transition to tetragonal and a second phase transition to orthorhombic is expected. A very common film texture of $KNbO_3$ films is the orthorhombic (101), corresponding to (100) pseudecubic, which means that the spontaneous polarization takes an angle of 45° relative to the film normal. An orthorhombic epitaxial (101) $KNbO_3$ film, which is for example deposited on a monocrystalline (100) STO

Table 4.1: Physical properties of potassium niobate [81].

Property		Unit	Value
Density	ρ	kg/m^2	4630
Elastic stiffness	c^D_{1111}	$10^{11}N/m^2$	2.55
	c^D_{1122}	$10^{11}N/m^2$	0.83
	c^D_{1133}	$10^{11}N/m^2$	1.20
	c^D_{2222}	$10^{11}N/m^2$	2.76
	c^D_{2233}	$10^{11}N/m^2$	0.77
	c^D_{3333}	$10^{11}N/m^2$	2.80
	c^D_{1313}	$10^{11}N/m^2$	1.13
	c^D_{2323}	$10^{11}N/m^2$	0.94
	c^D_{1212}	$10^{11}N/m^2$	-
Piezoelectric constant	e_{311}	C/m^2	2.46
	e_{322}	C/m^2	-1.10
	e_{333}	C/m^2	4.40
	e_{131}	C/m^2	5.16
	e_{232}	C/m^2	11.7
Dielectric constant	ϵ^S_{11}	-	34
	ϵ^S_{22}	-	780
	ϵ^S_{33}	-	24

substrate, has 8 different domain variants [32] (c.f. fig 4.3 (b)).

The density, elastic stiffness, piezoelectric constant and dielectric constants of $KNbO_3$ are given in table 4.1 (Zgonik et al. [81]). The important properties for BAW applications are the density ρ, the elastic constants c^D_{ijkl}, the piezoelectric constants e and the clamped dielectric constant ϵ^S_{ij} which can be used to derive the acoustic impedance Z_{ac}, the sound velocity v^D and the electromechanical coupling coefficient k_t^2. The quasi-longitudinal ultrasound velocity v^D in (101) direction for $KNbO_3$ was measured as 8151m/s [81].

In order to calculate the out-of-plane properties of (101)-textured $KNbO_3$ films we define firstly the coordinate system xyz aligned along the orthorhombic crystallographic axes abc (c.f. fig. 4.1). xyz has to be rotated by 45° around the y-axis to be aligned with the [101] orientation. The elastic constants in the [101] direction is

$$c'^D_{3333} = \frac{1}{4}(c^D_{1111} + 2c^D_{1133} + c^D_{3333}) + c^D_{1313} = 3.07\ 10^{11}N/m^2 \quad (4.1)$$

The acoustic impedance Z_{ac} and the acoustic velocity v^D in [101] direction are

$$Z_{ac} = \sqrt{\rho c'^D_{3333}} = \rho v^D = 3.77\ 10^7 kg/m^2s \quad (4.2)$$

$$v^D = \sqrt{\frac{c'^D_{3333}}{\rho}} = 8143m/s \quad (4.3)$$

The piezoelectric coefficient e'_{333} perpendicular to the substrate surface of a (101) oriented

disc is

$$e'_{333} = \frac{1}{2\sqrt{2}}\left(2e_{131} + e_{311} + e_{333}\right) = 6.07\mathrm{C/m}^2 \tag{4.4}$$

The clamped relative dielectric constants is

$$\epsilon'^{S}_{33} = \frac{1}{2}(\epsilon^{S}_{11} + \epsilon^{S}_{33}) = 29 \tag{4.5}$$

The thickness-extensional coupling coefficient can then be derived with equation 2.8, page 19

$$k_t^2 = 46.8\% \tag{4.6}$$

4.2.4 Literature review on $KNbO_3$ thin film synthesis

A summary of reported methods for $KNbO_3$ thin film growth is presented below. Most publications report on sol-gel processing, whereas ion beam sputtering, LPE, MOCVD, PLD and rf diode sputtering is less widely used. The reviewed papers are presented in chronological order.

Sol-Gel The information given in this paragraph is limited to calcination temperature, type of substrate and crystallographic properties, no information about the chemical agents used for sol-gel processing are presented. Most publications report on XRD measurements only. Less frequently, Raman spectroscopy, Rutherford Backscattering (RBS), wave-guiding and ellipsometric measurements were performed. Electrical analysis are rare.

Swartz et al. [62] observed a variety of non-perovskite phases after heat treatment of sol-gel $KNbO_3$ deposited on silicon and alumina, but epitaxial growth of (221) $KNbO_3$ was observed on (210) STO along with other $KNbO_3$ orientations and unidentified phases. Tuttle and al. [68] claim to be the first to report ferroelectric measurements of sol-gel prepared perovskite $KNbO_3$ films on (0001) sapphire and platinized sapphire substrates. The platinized substrate yielded multiple phases of $KNbO_3$ at firing temperature of 800°C. At a firing temperature of 700°C the potassium deficient second phase $K_4Nb_6O_{17}$ was observed. A ferroelectric hysteresis loop measurement on the $KNbO_3$ film yielded a remnant polarization of $4.5\mu\mathrm{C/cm}^2$ and a coercive field of 55kV/cm. The relative dielectric constant was 300, with a loss tangent of 4% at 10kHz. Amini and Sacks [6, 5] obtained single-phase $KNbO_3$ powder after calcination at 700°C, although peak splitting indicative of the orthorhombic phase was not observed. They deposited polycrystalline $KNbO_3$ films on KBr substrates using a calcination temperature of 700°C. Derderian et al. [27] prepared epitaxial (101)/(111) $KNbO_3$ films on (100) MgO with a crystallization temperature of 800°C under flowing O_2. As confirmed by Raman analysis, the film was orthorhombic. Single phase films were produced with stoichiometric sols, while slight variations in stoichiometry (52/48 or 48/52 [K]/[Nb]) of the sols created residual second phases. Xiao et al. [73] prepared amorphous $KNbO_3$ by sol-gel method and anneal below 550°C. A ferroelectric hysteresis loop is shown and the second harmonic generation d_{eff} was measured as 0.52pm/V. Xu [74] reports on

(101) $KNbO_3$ epitaxial growth on STO and MgO substrates using a sol-gel technique and a crystallization temperature of 750°C. Cheng at al. [17] observed (101) epitaxial $KNbO_3$ growth on (100) STO substrates using a sol-gel process and a crystallization temperature of 750°C. Polycrystalline but single-phase $KNbO_3$ films were obtained on MgO and ZrO_2 substrates. Endo and Cima [29] report on epitaxial growth of (101) $KNbO_3$ on (100) MgO and STO substrates by sol-gel after heat treatment above 700°C. Polycrystalline $KNbO_3$ was formed on (111) Si substrates. Suzuki et al. [61] obtained c-axis oriented $KNbO_3$ films on $Pt/Ti/SiO_2/Si$ substrates with a RTA anneal at 750°C.

Liquid phase epitaxy LPE Kakimoto et al. [38] used LPE to grow epitaxial (001) $KNbO_3$ films on (101) STO substrates. The film growth temperature was varied between 900 and 1060°C. The melt composition was K_2CO_3/Nb_2O_3=1.105 and 1.857 (eutectic composition) respectively. For $KNbO_3$ single crystal growth a colorless and transparent crystal is obtained when the K_2O concentration is more than 51 mol% but less than 54 mol%. The only possible process window for film growth (transparent, colorless and smooth) was obtained with the eutectic composition at a growth temperature of 900°C.

Ion beam sputtering IBS Graettinger et al. [4, 33, 34] used ion beam sputtering for the deposition of epitaxial (101) $KNbO_3$ on (100) MgO substrates. Potassium superoxide KO_2 and Nb metal were used as sputtering targets. The deposition rate was 1nm/min. Epitaxial (101) and single crystalline films were grown at 650-700°C and an oxygen background pressure of 0.01-0.1mT. They found that the incorporation of potassium and oxygen is self-limiting. All the films examined showed a potassium deficiency relative to Nb of 5-40% and were smooth and transparent. This K deficiency did not seem to affect the bulk properties of the films. It was mentioned that K sites were substituted by sodium [24] thought to come from contaminations in the KO_2 powder. RBS measurements showed the sodium to be throughout the film. The films become more potassium rich when the temperature was lowered to 550-600°C and often the (111) orientation appears. Pole figure measurements showed an in-plane rotation of the epitaxial film, and also the orthorhombic phase. The optical propagation losses in the film were very high. Later work [25, 24] showed growth on $KTaO_3$ and $MgAl_2O_4$ substrates. It was noted that high quality $KNbO_3$ thin films are difficult to grow due to potassium volatility at the growth temperature. The grain size decreased with higher lattice mismatch and 90° domains were observed in films on $KTaO_3$ substrate which has the best lattice match of all 3 substrates.

Metalorganic chemical vapor deposition MOCVD Nystrom et al. [50, 72] prepared epitaxial potassium niobate thin films on (100) $LaAlO_3$ by MOCVD. The growth temperature was 800°C. Nonlinear optical coefficient as large as 13pm/V were obtained. Onoe et al. [52] deposited single crystal (010) $KNbO_3$ films with smooth surfaces epitaxially on (101) STO substrates at 850°C. The flow of the potassium precursor was chosen 20 times larger than that of the niobium precursor to prevent K deficiency. *Building block-like micro crystals* were observed as microstructure. Some films *deliquesced* (=dissolve by moisture) in

air if they had a [K]/[Nb] ratio equal or larger than 1.5. The [K]/[Nb] ratio decreased below unity when the substrate temperature was raised from 850 to 900°C. Crystalline films were obtained at 650 and 850°C, whereas at 750°C the film became deliquescent. Local micro-crystal growth inside an amorphous matrix was observed for lower potassium contents and a more homogenous nucleation of micro-crystals was obtained for higher K contents. Yamanouchi, Odagawa et al. [78, 51] claim to be the first to measure piezoelectric properties on an as-grown thin $KNbO_3$ film. They deposited $KNbO_3$ on (101) STO substrates using MOCVD (850°C, 5T) and measured the electromechanical coupling coefficient k^2 with SAW as 2.1%. The polarization distribution was measured using a scanning nonlinear dielectric microscope and the polarization could be changed by applying a high electric field. Chattopadhyay et al. [16] used the fabrication process described by Nystrom et al. to fabricate epitaxial $KNbO_3$ films on $MgAl_2O_4$ substrates. The dielectric properties, i.e. frequency, bias and temperature dependency, were studied using interdigital metal electrodes.

Pulsed laser deposition PLD Zaldo et al. [80] were the first to report $KNbO_3$ growth by PLD. The crystalline and stoichiometric $KNbO_3$ films were grown on MgO substrates. To obtain stoichiometric films, the ceramic $KNbO_3$ target had to be enriched with potassium by 185% using K_2CO_3. For crystalline films a substrate temperature of 650°C was necessary and the deposition took place in 15mT of O_2. They observed a reduction of the [K]/[Nb] ratio in the film for increasing substrate-target distances. Gopalan and Raj [32] report on $KNbO_3$ film deposition on STO substrates by PLD using the following deposition conditions: 685°C, 100mT O_2, alternating KNO_3 and $KNbO_3$ targets to provide approximately 65% of K excess during the ablation. The rocking curve FWHM of the (101) $KNbO_3$ reflection was 0.54°. Beckers et al. [11] report on $KNbO_3$ film deposition by PLD on STO and $BaTiO_3$ substrates using single crystal $KNbO_3$ targets. Potassium deficiency in the films could be avoided by increasing the oxygen pressure to 375mT O_2 during deposition. The substrate temperature was higher than 900°C. Christen et al. [26] used PLD to grow $KNbO_3/KTaO_3$ superlattices. A segmented target of $KNbO_3$ and KNO_3 was used to provide approximately 100% excess K. Stoichiometric films were obtained at temperatures of 650-800°C.

Rf sputtering Schwyn et al. [60, 59, 58] were the first and only to publish results on diode sputter deposited $KNbO_3$ films. They used a 200% potassium enriched 150mm powder target of $KNbO_3$. K_2CO_3 was used for potassium enrichment. The target was cold pressed and presputtered for 10h. They obtained stoichiometric (confirmed by RBS) and single crystalline tetragonal films on (100) spinel and (100) MgO substrates. The deposition conditions for the rf diode sputtering were 20sccm Ar, 15mT, 610°C and 50W (6$\mathring{A}$/min). When targets with a lower excess content of K were used, or oxygen was added to the Ar sputtering atmosphere, a K deficient film resulted. The non-linear optical coefficient d_{31} was determined as 5pm/V. Good waveguiding properties were measured. Hashima et al. [36] reported on $KNbO_3$ film deposition by rf magnetron sputtering. The substrates were amorphous SrO-SiO_2 films with different ratios on Si substrates. They report that (101) oriented $KNbO_3$ film could be obtained with a target of 1:1 $KNbO_3$:K_2CO_3 at 500°C substrate temperature, 3mT pressure and a gas mixture of 9:1 Ar:O_2.

Most authors have attributed high importance to the stoichiometry and transparency of films. $KNbO_3$ film synthesis rises much interest because of its very interesting electro-optic properties. Piezoelectric and dielectric properties are only reported for films deposited by MOCVD. Films are most often deposited onto monocrystallin substrates, only few report on using platinized substrates. The deposition of $KNbO_3$ on polycrystalline Pt electrodes is essential for low cost applications and is inevitable for BAW devices. The required substrate temperature for the deposition of crystalline films is higher than 610°C. A potassium excess in the targets of up to 200% was reported using KO_2 or K_2CO_3 power, however the process repeatability or target stability was not discussed. The oxygen or potassium incorporation into the films was described as self-limiting and potassium deficiencies apparently still resulted in the $KNbO_3$ phase. Authors have reported contradictory effects of adding O_2 to the sputtering gas.

4.2.5 Literature review on $Na_{0.5}K_{0.5}NbO_3$ thin film synthesis

Because only one relevant report on $KNbO_3$ sputtering exists, we looked also into the $Na_{0.5}K_{0.5}NbO_3$ (NKN) system where more publications on sputtering exist, and because of similarities with sputtering a close look on PLD for NKN film synthesis is also presented.

$Na_xK_{1-x}NbO_3$ by sputtering Margolin et al. [44] used cathode sputtering to synthesize (Na,K)NbO_3 ferroelectric films. They report that single phase perovskite, polycrstalline films were grown on polykor and stainless steel substrates at temperatures ranging from 250°C to 650°C in 375mT of O_2. The target-substrate distance was 8mm and a discharge power of 16-33W/cm^2 was used. No composition analysis is presented, but a dielectric constant of $\epsilon = 175$ at a field of 1kV/cm and 1kHz was measured on the films.

Wang et al. [70, 71] report on the first epitaxial $Na_{0.5}K_{0.5}NbO_3$ films grown on $LaAlO_3$ and polycristallin $Pt_{80}Ir_{20}$ substrates by rf magnetron sputtering. They used a target composed of Na_2CO_3, K_2CO_3 and Nb_2O_3 powders, which is sintered at 650°C to a density of 2.64g/cm^3. A 50% excess of Na and K was added to the targets to compensate for expected losses during depositions. The process gas was Ar/O_2 30:10sccm at a pressure of 7.5mT. The target diameter, target-substrate distance and applied power were 50mm, 30mm and 50W respectively. The substrate temperature was varied from 500°C to 700°C, best results were obtained at 650°C. The measured on-axis deposition rate was 1.8nm/min, and 3 times lower for off-axis sputtering. The sample was cooled down in 375T O_2. RBS measurements on a film deposited on Si yielded 0.5:0.5:1 ratios for Na:K:Nb within 0.5% accuracy. XRD $\theta - 2\Theta$ measurements showed the (001) c-axis epitaxy of the films on $LaAlO_3$ substrates and (001) orientation on PtIr substrates for on-axis sputtering, and (101) orientation for off-axis respectively. Planar capacitors measurements realized with interdigital electrodes yielded a 35% percent tunability at room temperature and 1MHz, and a dielectric constant of $\epsilon_r = 580$ with a loss tangent of 0.7% on $LaAlO_3$ substrates. Dielectric measurements on the films deposited on PtIr in the on-axis configuration showed an ϵ_r=490-590 and dielectric dissipation factor of 1-14% at 10kHz. C-V curves and P-E hysteresis are presented and a remnant polarization P_r of 6.1μC/cm^2 was measured. The hydrostatic piezoelec-

tric constant was 3.9-14.5pC/N. The same group also presented microwave properties of $Na_{0.5}K_{0.5}NbO_3/SiO_2/Si$ thin films using interdigital and straight gap capacitors [3].

Blomqvist et al. [13, 12] reported recently on the synthesis of $Na_{0.5}K_{0.5}NbO_3$ films grown on $LaAlO_3$ substrates by rf magnetron sputtering from stoichiometric targets. The target was a 25mm diameter high-density and single phase target. Na_2CO_3, K_2CO_3 and Nb_2O_3 powders were mixed and calcinated at 940°C, then cold-pressed and sintered for 4h at 1125°C. The final density was 4.3g/cm^3 (95% of theoretical density). Sputtering conditions were 60W, 650°C, Ar:O2 (3:1), 60mT and the deposition rate was 40nm/min. The films were post-annealed in situ at 540°C in a 700Torr oxygen atmosphere. XRD Θ-2Θ scans indicated only (001) reflections. IDC measurements determined the following electrical characteristics; tanδ=1%, tunability 16.5%, ϵ_r=470 at 1MHz. The electrical resistivity was 2.1 $10^{13}\Omega$cm. The in-plane polarization yielded a saturation polarization of $P_s = 23.5\mu C/cm^2$. Using the same conditions (001) textured films were also synthesized on sapphire substrates to measure optical and waveguiding properties. A rms roughness of 8.2nm was measured by AFM on a 1μm thick film.

$Na_xK_{1-x}NbO_3$ by laser ablation The group of Grishin [18, 22, 19, 1, 20, 23, 2, 21] reported recently on the synthesis of $Na_xK_{1-x}NbO_3$ films deposited by laser ablation on $Pt_{80}Ir_{20}$, SiO_2/Si (001) & (111), Ta_2O_5/Si, Pt/Ti/SiO2/Si, Si (100) and single crystal quartz substrates. The target was stoichiometric to avoid instability (water absorption and cracking). Films were deposited at 635-650°C and 350-450mT of O_2 respectively, followed by an oxygen anneal at the same temperature in 500Torr. An interdiffusion of Na and K into SiO_2 was deduced from C-V loop offset [23]. XRD measurements showed single phase and (001) texture of the deposited films which is attributed to a strong effect of self-assembling. A dielectric constant of ϵ_r=440-480, a loss tangent of 2-5% and a remnant polarization of P_r=12μC/cm^2 was measured with a vertical capacitor on NKN/PtIr [18] which shows dominant (100) texture. Planar capacitor measurements using IDT on NKN films deposited on SiO_2/Si substrates yielded a dielectric permittivity ϵ_r=114-107, a loss <1.5% and ϵ_r=204-193 for films on single crystal quartz respectively, in the frequency range 1kHz-1MHz. They also claim that NKN films deposited on Pt/Ti/SiO2$_2$/Si substrates exhibited a (111) texture, but XRD data was ambiguous [19]. It was noted that the in-plane leakage of the NKN films is very small in contrast to the out-of-plane when measured on a vertical capacitor on a Pt/Si substrate [1].

Table 4.2: Process conditions, targets and substrates for $KNbO_3$ thin film deposition in the Nordico sputtering tool for the preliminary study.

Base Pressure		1.10^{-6}	Torr
Target Power		50-100	W_{rf}
Temperature		440-650	°C
Pressure		8-30	mT
Gas	Ar	0-20	sccm
	O_2	0-2	sccm
Gas mixture	$\frac{Ar}{Ar+O_2}$	0.9-1.0	-
Deposition time		1-6	h
Target composition		200	% K excess
Target-substrate distance		64-84	mm
Substrates		4 variants of: Pt/ adhesion layer /Si	
		adhesion layer: Ta, TaO_x, 2 different TiO_x	
Seed layers on Pt		bare Pt, TaO_x, TiO_2, $PbTiO_3$	

4.3 Substrates, targets and tools used for $KNbO_3$ thin film deposition

4.3.1 Preliminary study

We carried out a feasibility study of $KNbO_3$ film deposition by magnetron sputtering in a single chamber sputter system without load-lock (Nordico). The 4" ceramic target was cold pressed and contained an excess of 200% potassium, in the form of K_2CO_3, in addition to pure $KNbO_3$ powder. This large K excess was chosen based on results from Schwyn, Lehmann and Günter [60] who used a rf-diode sputtering system to deposit stoichiometric $KNbO_3$ films onto (100) MgO and $MgAl_2O_4$ (100)-spinel substrates. The process conditions studied in this preliminary work are detailed in table 4.2. The deposition rate was $4.2\mathring{A}$/min at 75W target power.

The target cracked rapidly due to contact with moisture every time the process chamber was vented for sample exchange. The pump time to base pressure was very slow, indicating out-gasing of the target.

In spite of the instabilities and the degradation of the ceramic target, crystalline and (101) textured $KNbO_3$ films could be grown on platinized Si substrates. These films exhibited no change in the XRD spectrum when aged for 30 days, i.e. the films did not degrade or decompose in ambient atmosphere. One example of a 150nm thick film deposited onto a $Pt/TiO_2/SiO_2/Si$ (Nordico) substrate is shown in figure 4.4 along with the corresponding XRD data. The deposition conditions are 550°C, 20sccm Ar, 15mT, $75W_{rf}$, 6h. The film is piezoelectric when probed under the atomic force microscope (AFM) tip, but shows macroscopically a high electrical conductivity with large area capacitor structures. Based on these encouraging preliminary results we decided to built a new rf magnetron sputter tool, which should remedy the observed problems with the deteriorating target, and avoid contamination of the general purpose sputter system.

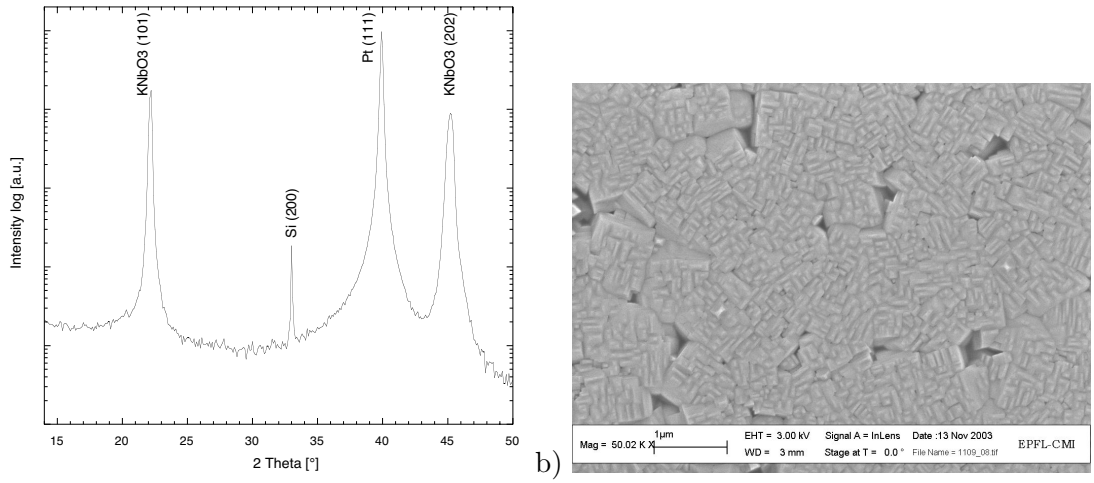

Figure 4.4: (a) $\Theta - 2\Theta$ X-ray diffraction scan of a 150nm thick $KNbO_3$ film deposited in Nordico by rf magnetron sputtering from a ceramic $KNbO_3$ powder target with 200% excess K. (b) The corresponding film microstructure as observed by SEM.

4.3.2 Rf magnetron sputter tool

The new sputter tool was designed to fulfill the following requirements, as derived from our experiences in the preliminary study: i) a sputter-up configuration where mechanically not very stable powder targets could be used, ii) a load-lock to keep the target with the hygroscopic K_2CO_3 powder in vacuum during the whole target usage, iii) a minimum attainable substrate temperature of 600°C in an oxidizing atmosphere, and iv) a substrate holder capable of holding a 4" wafer, necessary for device processing.

Building of sputter tool for $KNbO_3$ thin films

A schematic drawing of the new sputter tool is shown in fig. 4.5. It consists of a main chamber with attached load-lock chamber. Two turbomolecular pumps provide a very high vacuum of 1 10^{-7}T. Ar and O_2 are used as process gases. The substrate holder is introduced across the load-lock to maintain the main chamber under constant vacuum. The non-contact substrate heater may heat the substrate to over 600°C with lamps. The plasma is rf generated.

Chamber, load-lock and substrate holder transfer We reused an existing vacuum chamber with 90cm diameter and 120cm height. A 4-way cross from MECA2000 served as load-lock, along with a magnetic coupled, 610mm long DN40CF Caburn high vacuum transporter used for the substrate holder introduction. The substrate holder is fabricated of INCONEL 600 which resists high temperature oxydation. The connection between SAS and main chamber for the sample transfer is assured with a manual gate valve. The sample

holder is introduction into the SAS through a rapid hinge-open viewport door. A DN160 viewport attached to the main chamber allows for the observation of the plasma during the deposition process. Iso-KF flanges are used throughout the machine with vitton o-rings.

Pumping Chamber pumping is accomplished with a Pfeiffer turbomolecular pump TMH-520C (520l/s), controlled by a TCP380 unit. A Pfeiffer Duo10 rotary-slide-vane pump ($10m^3/h$, T100 oil), with exhaust oil mist filter, serves as primary pump. Venting of the main chamber is either through the turbo pump with a Pfeiffer TSF012 flood valve connected with the N_2 45 gas line, or alternatively with an Edwards PV10 pipeline valve directly attached to the main chamber, and also supplied by the N_2 45 gas line. SAS pumping is accomplished with a Pfeiffer TMH261 (210l/s) turbomolecular pump with a DCU200 unit controller. This turbo pump is connected to the same primary pump as the chamber turbo pump. Venting of the SAS is accomplished trough a TVF005 venting valve connected with a N_2 45 gas line.

The base pressure of the main chamber is 1.10^{-7}T. The pump time of the SAS from atmospheric pressure to 1.10^{-4}T is typically 1:40min, respectively 2h to reach the base pressure. 3 Edwards PV25 pipeline valves (electrovalves) are used to separate chamber turbo, respectively the SAS turbo exhaust, in order to maintain at least 5mBar of backing pressure during pumping-down and venting operations.

Pressure control A VAT PM5 adaptive pressure controller is used for the pressure or position control with a VAT high vacuum (gate) valve. This valve was disassembled, cleaned and remounted with new seals. The process pressure signal is provided by a MKS 120 Baratron with 0.1-100mTorr range. Three Edwards PRM10 Piranis with an Edwards 1101 controller are used to monitor chamber, turbo pump exhaust and primary pump pressure. An Edwards CP25-K Penning with a 1002 controller is used to measure chamber base pressure. The SAS pressure is measured with a Pfeiffer PKR251 Compact Full Range Gauge and monitored with a Pfeiffer TPG261 Single Gauge.

Gas Process gas admission for O_2 and Ar is through 2 Datametrics 825 mass flow meters with a 1605 4-channel controller. One mass flow meter is limited to 10sccm, the other to 50sccm standard N_2 flow. Because sputtering will take place on ceramic targets, Ar was attributed to the 50sccm mass flow meter, reaching effectively 70sccm (ajusted to the Ar gas factor of 1.40). The O_2 flow is regulated with the 10sccm flow meter, reaching a maximum effective flow of 9.9scccm O_2.

Magnetron A 4" AJA340 'push-trough' magnetron sputtering source was disassembled, refited with a 750mm long one-ended DN16CF sliding tube to span the distance from the chamber bottom to 1-12cm distance from the lid-suspended substrate holder. The rf-cable distance from the magnetron to the RFPP AM5 automatic matching network was minimized to approximately 1m. A RFPP RF5S 500W rf-power supply was connected with the matching network via the analog port to allow for automatic load & tune matching. A

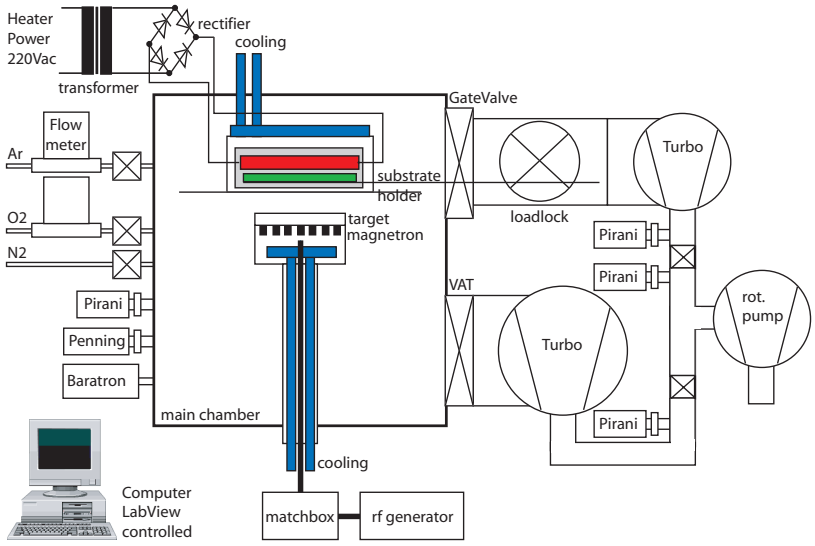

Figure 4.5: Schematic figure of the self-build rf magnetron sputtering tool: The oxygen resistant halogen lamp heater is decoupled from the machine ground with a transformer. The substrate holder is introduced across the load-lock on a rail with a magnetic linear transporter.

sufficient cooling water flow to the magnetron and match box is assured and checked with a Proteus H_2O flow meter electrically acting as control relais. A shutter can be operated using an Edwards 8RK25 rotary feedtrough.

Heater The movable substrate holder and substrate heater were both home made. As a Joule heating did not supply enough radiation to the removable substrate holder, a lamp heating system was designed. Standard 230V-750W halogen lamps from OSRAM (Haloline) with a filament length of 125mm and total lamp length of 186mm were used. The sockets of the lamps, from Roesch Electric AG, Koblenz, use the R7 standard. Because our power source was limited to maximum 2.3kW, 2x750W lamps were used together with 2 series 750W lamps. To further increase the power delivered to the substrate holder, 3 lamps were finally used in parallel. With 3, instead of the alloted 4, the power delivered to the substrate was no more homogeneous over the substrate holder. Nevertheless a homogeneously distributed substrate holder temperature is measured with a Type K (chromel/alumel) thermocouple. A Series 900 Eurotherm reads the temperature of the thermocouple and regulates the power to the lamps with a limitable courant thyristor. Cooling of the substrate holder heat casing, made of copper, and lamp sockets is accomplished using an external water cooling circuit soldered to the upper surface of the copper casing. The filaments of the lamps themself are inside a second stainless steal heat reflector shield inside the copper casing. QF25 1/4" fluid feedtroughs from Lesker were used to deliver the water to the heater encapsulation inside the vacuum chamber. Control of a minimal water flow was assured

with a Proteus flow meter.

When using the lamps simultaneously with a plasma, an electric arc between the magnetron anode and one of the electrical poles of the lamp was generated, making it impossible to have both work simultaneously. Tests showed that at negative lamp potentials the plasma was stable, but for potentials exceeding +80V an electric arc was generated by attracted free electrons of the plasma. This problem was solved by the installation of a 2kW 1:1 transformer from Huber Transformatoren AG between the thyristor and the lamps. This allowed setting of the lamp voltage at arbitrary potentials relative to the ground. An electric circuit is used to set the now floating lamp potential at negative potential when the phase of the lamps turned positive.

Calibrations of the temperature on the surface of a silicium wafer (thermocouple type K bonded with cement onto the Si surface) mounted on the substrate holder showed that the Si temperature is superior to the reference temperature measured on the heater lamp shield. The same measurements in a vacuum of $1x10^{-6}$T showed that the Si surface temperature is lower than the reference temperature due to the lack of heat conduction present in air. A maximum temperature of approx. 630°C can be attained on the substrate surface. The temperature variations over the 4" substrate holder is of a few degrees only at 600°C in air.

Controler and Computer In order to automatically run the sputter tool, and to get a complete monitoring of the deposition parameters, all the controllers are connected to digital and analog National Instruments I/O PCI cards in a Pentium computer (Input: PCI-6033E, Output: PCI-6703). Using LabVIEW 6i, virtual instruments (VI) were written to control each machine parameter. Only the load-lock transfer gate and the transfer of the sample from the SAS into the main chamber was still manual. Another VI using the machine VI as sub-VI was used to run the deposition sequences, e.g. heating the substrate holder, awaiting the base pressure, injecting the process gases and controlling the pressure, presputtering and doing the deposition by controling the rf power generator. During this time all the process parameters were being monitored and stored in a log file.

Figure 4.6 (a) shows a picture of the finished sputter tool, the rack with controllers and the piloting computer. A detailed picture of the 4" substrate holder inside the copper heat shield is shown in (b). The electrical connections to the Halogen lamps can be seen as white cables.

Substrates and process details for rf magnetron sputtering of $KNbO_3$ films

We used 4 different Pt substrates, table 4.3 for $KNbO_3$ film depositions. The study of different Pt substrates was necessary, because we observed a large influence of the type of Pt substrate on the $KNbO_3$ film growth during the preliminary study.

The process parameters studied for $KNbO_3$ film growth are summarized in table 4.4.

For each process run 4 different substrates were introduced. The *reference* substrate is $Pt/TaO_x/SiO_2/Si$ (Spider) which is always introduced, the three others are either different platinum variations, contain a seed layer on the Pt electrode, or are monocrystallin substrates (STO, Quartz). All films were analysis with XRD and SEM. The XPS analysis were

a) b) 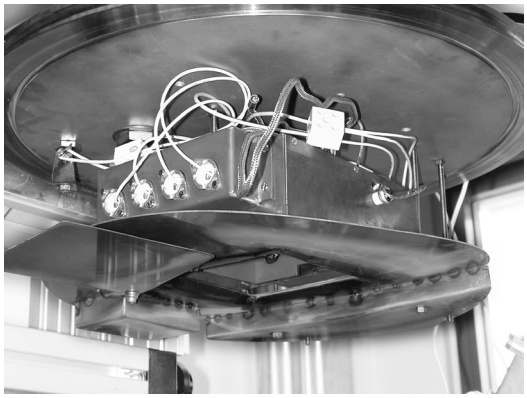

Figure 4.6: (a) In-house built sputter tool used for the thin film fabrication of $KNbO_3$, control tower and labview control. (b) Copper substrate heater casing which engulfs the three 230V-750W halogen lamps inside the stainless steel reflector. Also visible are the 220V lamp cables, a thermocouple to read the inner casing temperature and the mechanical shutter.

Table 4.3: The four different types of polycrystalline (111) Pt substrates, seed layers, and mono-crystalline substrates used for $KNbO_3$ film deposition.

Pt substrates	SPIDER	$Pt/TaO_x/SiO_2/Si$	500°C
	BAS450	$Pt/Ta/SiN/SiO_2/Si$	300°C
	NORDICO 2000	$Pt/TaO_x/SiO_2/Si$	500°C
	NORDICO 2000	$Pt/TiO_x/SiO_2/Si$	500°C
Seed layers on Pt		IrO_2, TaO_x, NbO_x TiO_x, $PbTiO_3$	
Mono-crystalline substrates		(100) $SrTiO_3$ (101) Quartz	

Table 4.4: Range of process conditions for $KNbO_3$ thin film fabrication in the specially dedicated magnetron sputtering tool with 4" target and 4" substrate size.

Base Pressure		1.10^{-7}	W_{rf}
Target Power		50-250	W_{rf}
Temperature		25-600	°C
Pressure		1-16	mT
Gas	Ar	0-70	sccm
	O_2	0-10	sccm
Gas mixture	$\frac{Ar}{Ar+O_2}$	0-1	-
Deposition time		1-6	h
Target composition		0, 10, 25, 40, 100, 200	% K excess
Target-substrate distance		80	mm

only performed on the reference substrate. The obtained results were immediately used to optimize process parameters in the search of a suitable process window.

To ensure a precise process control and to have a follow-up of the process, LabView programs are used to control the sputter process and log all important parameters into a file. The main sequences of the sputter program are the following: After reaching the base pressure of 1.10^{-7}T, the substrate is heated to the required temperature of 0-600°C within 15-20min, then a minimum base pressure of 3.10^{-6}T is awaited before continuing the process. The process gases Ar and O_2 are injected, the sputter pressure is set and regulated, then the target is presputtered for 10min. The shutter is opened to start the deposition and once the deposition end is reached, the rf target power and the heating is turned off and the substrate is cooled in 80mT of O_2 to room temperature. Each step is controlled and continuation delayed if the process parameter is not within a 5% tolerance limit of the set value. Optionally an oxidation step can be introduced before the plasma start to oxidize the substrate and target. The reflected power is generally kept below 5W during the entire deposition process.

The plasma discharge can be started at process pressures superior of 3mT. For depositions which were carried out at a lower process pressure, the plasma was started at 4mT and then the pressure was reduced.

Because oxygen is present during the sputtering process (provided by target or purposely introduced) there could be some influence on the film growth from negative ions. Misium [45] showed however, that for pressures of less than 10mT the negative ions make up less than 5% of the ion density. Because the sputtering pressure used in this work for $KNbO_3$ film deposition is less than 10mT the negative effect of O_2^- bombardment is minimal. We investigated only on-axis sputtering which is used for technical applications for large wafer diameters.

In-house fabricated ceramic powder targets

Potassium niobium oxide $KNbO_3$ 99.999% (Puratronic) from Alfa-Aesar served as starting material for the target fabrication and potassium carbonate K_2CO_3 99.997% (Puratronic) was added in different ratios to provide excess potassium. Targets with 0%, 15%, 25%, 40%, respectively 100% excess potassium were fabricated. The 2 powders are mixed in 99.5% pure acetone and milled for 12h with zirconia balls at 97rpm in a polyethylene bottle (porcelain method). The acetone was evaporated during 3h on a hot-plate with simultaneous stirring and infrared heating. A stainless steel matrix with 97mm inner diameter was machined. It was used to uniaxially cold-press the powder with a pressure of 10.8MPa (80kN) into a mechanically stable, approximately 3-5mm thick target. A green-body density of 2.08g/cm^3, which corresponds to 47% of the theoretical density, was obtained with this method on the +15% excess K target. Some targets were annealed for 1h at 600°C with a heating/cooling rate of 2°C/min. The pressed powder discs were placed onto a copper backing plate and transferred immediately into the vacuum chamber to minimize moisture absorption and subsequent bending and cracking.

UMICORE target

UMICORE, former Unaxis Materials, optimised and fabricated an equimolar K_2CO_3:$KNbO_3$ target based on the results from the preliminary work in our laboratory. The obtained green body density was 1.879g/cm^3, which corresponds to 57% of the theoretical density. After sintering at 650°C for 3h the density increased to 1.976g/cm^3, respectively 60% of the theoretical value. This target was vacuum sealed and shipped to our laboratory. An EPO-TEK K72 two component glue with low outgasing and high thermal conductivity was used to bond the target to a copper backing plate. The target was immediatly transfered into the vacuum chamber.

4.4 Characterization of the sputter process

4.4.1 Effect of process parameters on target voltage

The important parameters from the power generator for magnetron sputtering are the incident and reflected power and the target voltage. Usually the power level is set to a specific value, and the reflected power is minimized with a matchbox in case of rf sputtering. The target voltage is then a function of the pressure and sputtering gas, the target and the magnetron geometry.

The effect of adding O_2 to the Ar sputter gas ($\frac{O_2}{O_2+Ar}$) on the target voltage is represented in figure 4.7 (a). Increasing the oxygen partial pressure reduces the voltage almost linearly from 315V to 225V (process conditions: 150W, 10mT, 200% excess-K target, substrate at room temperature). An almost linear relationship between rf power and target voltage is found, showing a slight hysteresis during the up/down cycling, fig. 4.7 (b).

Figure 4.8 (a) shows the recorded target voltage for a 2h deposition with 200W, 4mT of 50/2sccm Ar/O_2 and a substrate temperature of 560°C. No shutter was used, the target

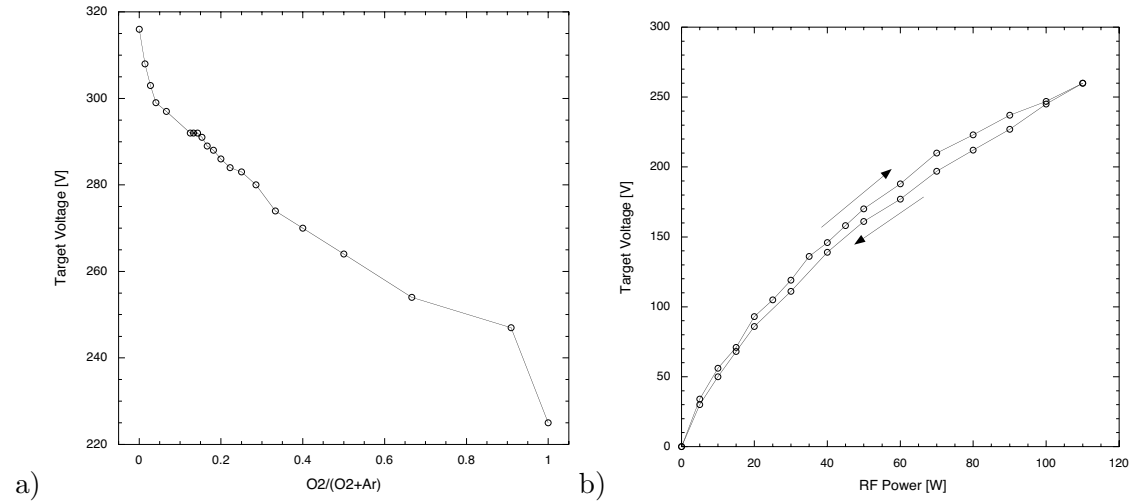

Figure 4.7: Absolute value of dc-voltage of target as (a) a function of O_2-Ar gas mixture for a target with 200% excess K at 150W, 10mT and room temperature, and (b) over applied rf power for the same target at a pressure of 10mT, pure Ar atmosphere and a substrate temperature of 360°C.

was therefore heated by the substrate holder during the heating period. The observed voltage curve is representative for all depositions done with different process parameters and targets, as well as for room temperature depositions.

The target voltage changed with sputter time. During the first few minutes of sputtering, it dropped by approximately 10% and reached a minimum after about 5min. During the subsequent sputtering time, the voltage increased again slowly to reach the original value. For some depositions, this increase was absent. Small changes in the reflected power did not influence the target voltage.

Figure 4.8 (b) shows the evolution of the stabilized target voltage measured at the end of each deposition, for targets containing 0, 10, 25, 40, 100 and 200% excess potassium. Each point represents a deposition process with different process conditions. Target voltage which were obtained from depositions with a rf power different from 100W were scaled and adjusted linearly to 100W. This is admissible as the voltage and rf power have an almost linear relationship. Points market *RT* correspond to room temperature depositions. No correlation was found when plotting the target voltages over the substrate temperature. The voltages measured during room temperature depositions are however higher than voltages obtained with depositions performed between 380 and 610°C.

For increasing K contents in the targets an overall increased target voltage is observed, with the exception of the target with +10% K. A constant or slightly decreasing target voltage over target usage can be observed for all targets. The variations in target voltage may be an indication for changing target properties. The tendency for a decreasing target voltage with increasing target usage may be interpreted as an impoverishment of the target

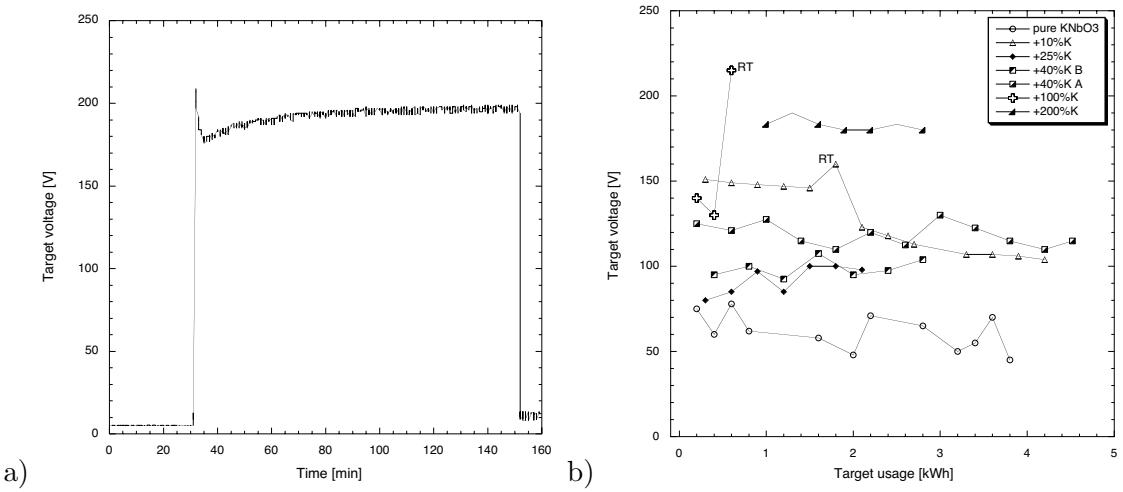

Figure 4.8: (a) Target voltage recorded during the deposition of $KNbO_3$ with 4mT 50/2sccm Ar/O_2, 200W_{rf} and 560°C after a target usage of 2kWh. The target contained a K-excess of +40%. (b) Stabilized target voltage over target usage for targets containing different contents of excess potassium. The process conditions are pure Argon, rf power of 100W (40 & 200%K corrected from 200, respectively 150W to 100W), a pressure between 1-16mT and a temperature of 400-605°C. Points marked *RT* correspond to room temperature depositions. Every point represents a single deposition.

with respect to potassium because the voltage is proportional to the potassium content in the target.

The color of the Ar plasma was observed visually during the deposition processes. The spectrum of colors observed range from white to pink and violet. Qualitative color changes were observed not only between different depositions but also throughout the deposition time. A spectrum analysis could have given additional information relative to the sputtered species present in the plasma. Potassium has weak spectral lines at 404 and 405nm (violet), and stronger spectral lines at 766 and 770nm (red near infrared). Niobium shows weak spectral lines at 295, 335, 371, 375, 410 and 412nm, and stronger lines at 358, 406 and 408nm (violet). The variable colors observed during the sputtering process probably reflected changing concentrations of K and Nb species present in the plasma.

4.4.2 Effect of pressure and substrate temperature on deposition rate

The deposition rate obtained with all targets scaled linearly with applied rf power in the range of 100 to 250W. At a distance of 2cm from the substrate holder center the rate is measured as $0.39\mathring{A}$/Wmin. The uniformity of the deposition thickness is approximately $\pm 50\%$ over a 4" wafer, calibrated with a SiO_2 deposition.

The $KNbO_3$ deposition rate decreased with increasing sputter pressure (fig. 4.9 (a)), whereas the target voltage remained almost constant over the same pressure range. The $KNbO_3$ deposition rate was however almost independent of the substrate temperature (b).

4.5 Film stoichiometry analyzed with XPS

Effect of excess potassium in targets on film stoichiometry

The film stoichiometry of each deposition was measured by X-ray photoelectron spectroscopy (XPS) on the reference substrate (Pt/TaO_x Spider). The peak intensities of the K 2p, respectively Nb 3d line were calibrated on pure $KNbO_3$ powder to obtain a correct quantitative analysis. Figure 4.10 (a) shows the XPS survey on a 1.4μm thick $KNbO_3$ film. Only the elements O, C, Nb and K are present, indicating a pure K-Nb-O film with no contamination. The measured [K]/[Nb] atomic concentration ratio (KN-ratio) of this film was 0.96.

Figure 4.10 (b) shows the KN-ratio vs target usage measured on films obtained from different targets and process conditions. The points marked *RT* and 440°C represent room temperature, respectively a 440°C deposition. These were the depositions with the coldest substrate temperature, all other runs were done at higher substrate temperatures between 480 and 605°C.

There is a clear trend to more potassium incorporation into the film with higher K-excess concentrations in the targets. The KN-ratio is not constant for any particular target over it's lifetime and variations of $\pm 10\%$ between two successive depositions are common. There is no general tendency for an increase or decrease of the KN-ratio over the target usage

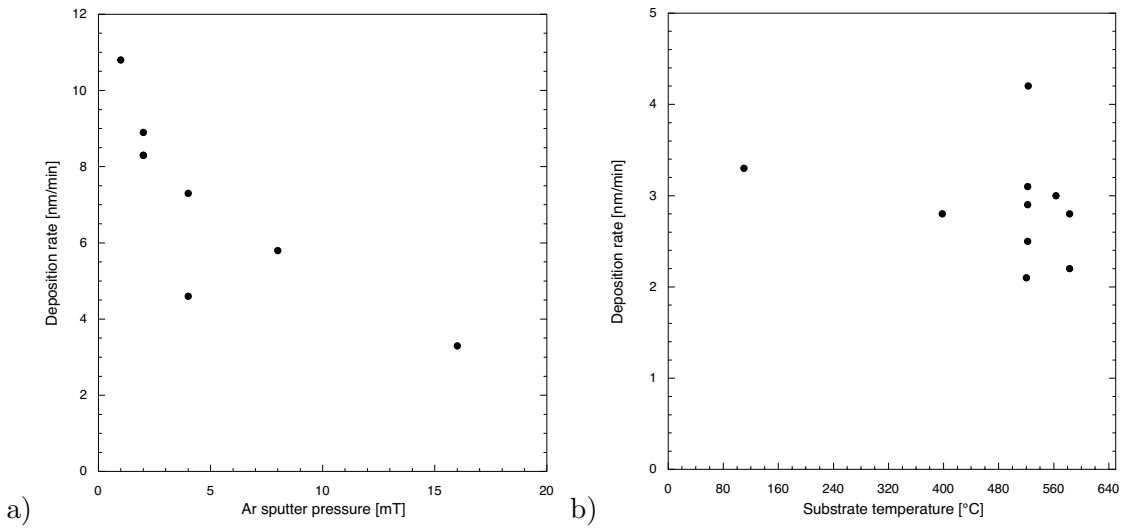

Figure 4.9: (a) The $KNbO_3$ deposition rate decreases with increasing sputter pressure (40% excess K target, 200W_{rf}, pure Ar). Simultaneously, the target voltage was almost constant with 230V from 1 to 2mT sputter pressure, respectively 240-260V from 4 to 16mT. (b) The $KNbO_3$ deposition rate is approximately constant in the temperature interval from room temperature to 600°C at constant process conditions (10% excess K target, 100W_{rf}, pure Ar, 4mT).

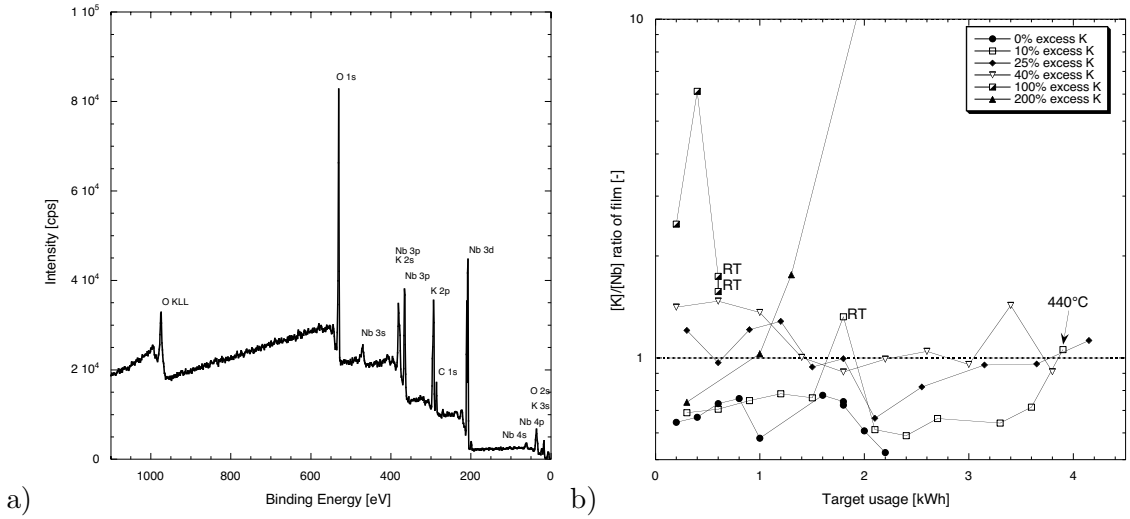

Figure 4.10: (a) XPS survey of a 1.4μm thick $KNbO_3$ film deposited on a Pt/TaO_x (Spider) substrate. (b) [K]/[Nb] atomic ratio measured on $KNbO_3$ films by XPS as a function of target usage for targets containing from 0 to 200% excess K.

except for the +200%K target which shows an exponential increase. Lowering the substrate temperature results in KN-ratios significantly different from the higher temperature depositions.

The films made from the stoichiometric target exhibit a KN-ratio between 0.6 and 0.8. Increasing the K excess in the target to 10% does not significantly increase the KN-ratio. With the +25%K target near stoichiometric films with a KN-ratios in the interval 0.7-1.3 were obtained. A further increase of the K content in the target to +40% resulted in a slightly higher film KN-ratio of 0.9-1.5. Films obtained by sputtering from the +100% or +200% K excess targets yielded KN-ratios of 1.6 to 6.0, respectively the KN-ratio was increasing exponentially with increasing target usage. The target +200%K exhibited a locally yellowish and blueish color on the surface after 2kWh target usage. The yellowish color observed on the target surface can be attributed to potassium superoxide KO_2 accumulation on the target surface which is a decomposition product of K_2CO_3 contained in the target.

We believe that the changing KN-ratio with increasing target usage is not only due to the different process conditions but also varies because of changing potassium concentration inside of, or rather on the target surface.

A cold deposition with a target of +100%K yielded films with a KN-ratio similar to the target stoichiometry, whereas films deposited at a temperature of 560°C yielded more than triple the amount of potassium provided in the target. Generalizing the information obtained from depositions performed at room temperature and up to a temperature of approximately 440°C it can be concluded that a film stoichiometry similar to the target stoichiometry is obtained. At higher substrate temperatures, the final film stoichiometry also depends on process conditions.

Valency state of the potassium ion in $KNbO_3$ films

Most of our $KNbO_3$ films exhibit a high electric conductivity. The dielectric losses are 8% at best. RTA anneals in oxygen did not reduce the electric conduction. To better understand this phenomena, films were analyzed with XPS, concentrating on the K 2p peak doublet at 292.6, respectively 295.3eV (c.f. figure 4.11 (b)). The calibration for the binding energies is correct as can be checked with the peak for niobium Nb $3d_{5/2}$ (Nb_2O_5) which is at the correct binding energy of 207.8eV (c.f. figure 4.11 (a)). According to Szot et al. [68] and Gutmann et al. [35], potassium may be present in two different states: K^+ and a more metallic-like form. This form of K is present if there is a small oxygen deficiency. The more metallic-like form of K is thought to contribute to the electrical conductivity.

Our XPS measurements indicate also clearly that there a 2 peak doublets present. One is K^+ as occurring in $KNbO_3$, the other is closer to a metallic state. It's XPS peaks are shifted towards the one of metallic K. The second peak doublet not corresponding to K^+ is shifted to higher binding energies, where the peaks for the metallic form of K is known (294.4eV). This observation can be interpreted in the same way as already mentioned before by Szot and also Gutmann, that potassium is present in two forms. The metallic-like form may explain the electric conduction.

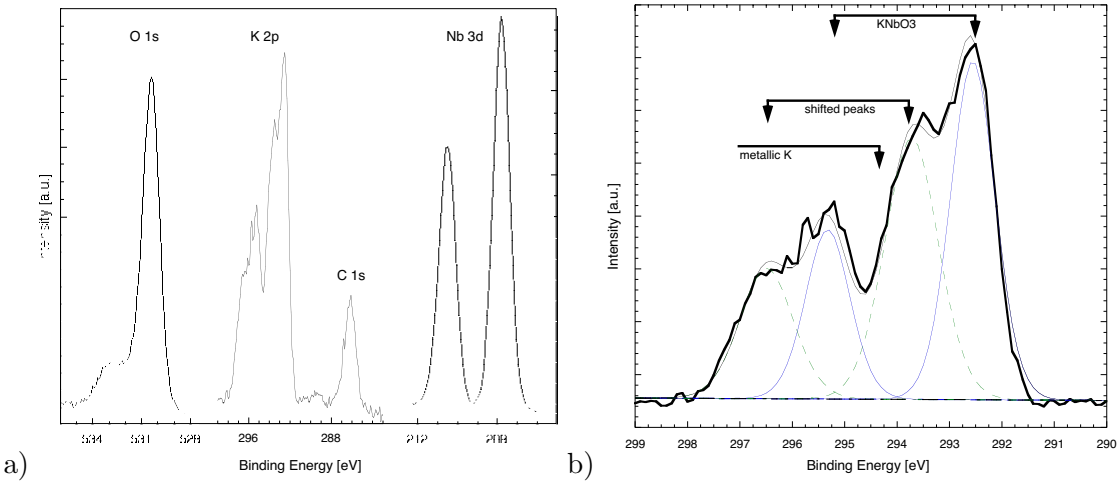

Figure 4.11: (a) XPS spectra of the O 1s, K 2p, C 1s and Nb 3d core levels. (b) XPS curves (measured and fitted) exhibiting the splitting of the K 2p doublet peak with 47.5% of the area intensity shifted by 1.15eV to higher binding energies.

4.6 Film crystallography analyzed with XRD and Micro-Raman measurements

4.6.1 Crystallographic phases and textures observed with XRD

The crystallographic phases and texture of more than 220 films obtained with the different targets, process conditions and on the different substrates, were analyzed with X-ray $\Theta-2\Theta$ measurements. The angle 2Θ was scanned from 10 to 90° with a stepsize of 0.1°. Because of the large number of phases possible in the K-Nb-O system, it was difficult to identify and index the individual x-ray peaks. This difficulty in indexing certain peaks is also reflected in certain publications on $KNbO_3$ films, where peaks could not be indexed. To get a better understanding and to evaluate the large amount of data collected from all samples a statistical approach is chosen: All X-ray data obtained with the different targets, process conditions and on the different Pt substrates (inclusive seed layers) were summed and are represented in figure 4.12 (a). To index the observed peaks, the following International Centre for Diffraction Data ICDD Powder diffraction files (PDF) were taken into consideration: $KNbO_3$ cubic (8-212), tetragonal (71-948), orthorhombic (32-822), rhombohedral (71-947), $K_3Nb_7O_{19}$ (38-1499), $K_4Nb_6O_{17}$ (76-977), K_3NbO_4 (26-1325) and K_3NbO_8 (75-1033). Many more off-stoichiometric phases are possible in the K-Nb-O system according to the PDF database and an exhaustive number of PDF files are available. These were discarded as they did not fit the observed peaks.

The complete range of possible phases observed in the deposited films is, according to figure 4.12 (a): $\mathbf{KNbO_3}$ which may be present as tetragonal or orthorhombic, mostly exhibiting a strong peak at 2Θ=21.9-22.3° that corresponds to the pseudocubic (100) orientation

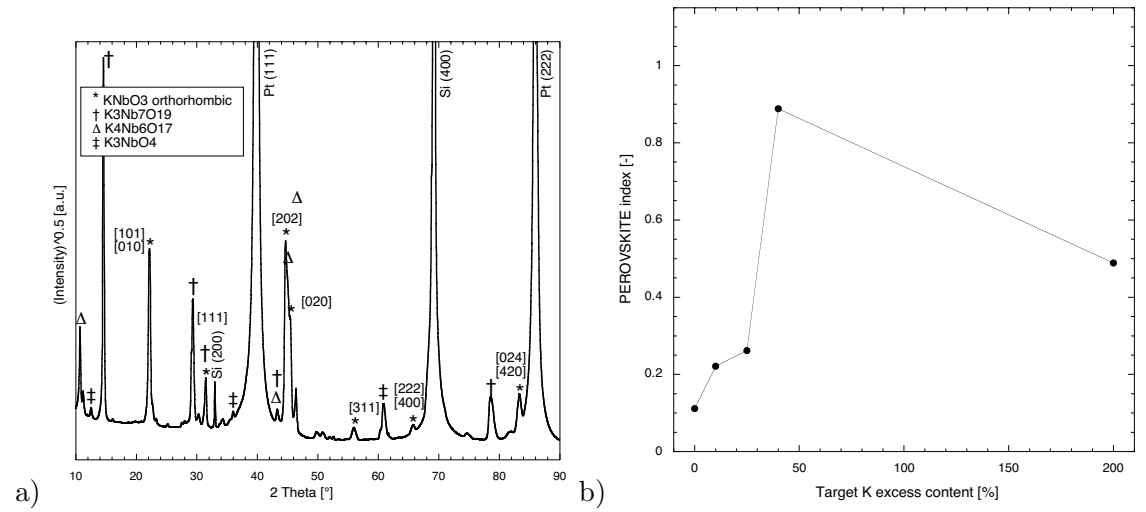

Figure 4.12: (a) Sum of all 221 $\Theta - 2\Theta$ analysis of $KNbO_3$ films which shows all phases observed on the different Pt/Si substrates and for all sputtering conditions. Only $KNbO_3$ peaks are indexed. (b) The perovskite index, *PER* defined in equation 4.7, indicates that the highest fraction of $KNbO_3$ perovskite phase in the films is obtained with the target containing +40% excess K.

which splits into (101)/(010) orthorhombic (difficult to distinguish in XRD), $\mathbf{K_4Nb_6O_{17}}$ orthorhombic, often showing a high intensity at 2θ=10.6°, $\mathbf{K_3Nb_7O_{19}}$ triclinic, often showing a high intensity at 2θ=14.5°, and the potassium rich $\mathbf{K_3NbO_4}$ orthorhombic, showing a high intensity at 2θ=11.2° and 12.35°. It is impossible to make a quantitative estimate on relative amounts of these phases present when compared with $KNbO_3$. The fact that certain (hkl) from the phase $K_4Nb_6O_{17}$ coincide with some of the $KNbO_3$ peaks make the identification the more complicated. To distinguish the two phases, a different method, e.g. Raman measurements, must be taken into consideration (c.f. paragraph 4.6.3). Considering the XRD data from figure 4.12 (a) it is likely that a phase with too high a potassium content is present: K_3NbO_4. This phase is also difficult to distinguish from $K_3Nb_7O_{19}$ and $K_4Nb_6O_{17}$ as some of the 2Θ diffraction angles coincide.

4.6.2 Effect of excess K in targets on film crystallography

The effect of potassium excess concentration in the different targets on the relative amount of the perovskite phase relative to second phases present in the films is plotted in figure 4.12 (b). To statistically estimate the $KNbO_3$ perovskite fraction relative to the second phases $K_3Nb_7O_{19}$ and $K_4Nb_6O_{17}$ a PEROVSKITE index is defined using the XRD peak intensities of all XRD from all samples obtained with the same target, similar to a texture

index.

$$PER = \frac{I^{KNbO_3}_{(101)/(010)} + I^{KNbO_3}_{(111)} + I^{KNbO_3}_{(042)/(402)}}{I^{KNbO_3}_{(101)/(010)} + I^{KNbO_3}_{(111)} + I^{KNbO_3}_{(042)/(402)} + I^{K_3Nb_7O_{19}}_{(\bar{2}10)} + I^{K_4Nb_6O_{17}}_{(040)}} \tag{4.7}$$

A value of $PER = 1$ corresponds to 100% perovskite $KNbO_3$. The evaluated second phases are $(\bar{2}10)$ $K_3Nb_7O_{19}$ at 2Θ=14.5° and (040) $K_4Nb_6O_{17}$ at 2Θ=10.6°.

A clear trend to higher percentage of the perovskite $KNbO_3$ relative to the second phases is observed for targets with increasing potassium content up to 40%. Thereafter a decrease occurs. The increase from 10% $KNbO_3$ obtained with the stoichiometric target to more than 90% for the 40% excess K target is substantial.

In conclusion it can be said that the target with 40% excess potassium favors the nucleation and growth of the $KNbO_3$ phase over the potassium deficient $K_3Nb_7O_{19}$ and $K_4Nb_6O_{17}$ phases. The target with +200% does not seem much more favorable for the nucleation and growth of the $KNbO_3$ phase when compared with the 0 and +10% K targets.

4.6.3 Phase determination by Micro-Raman measurements

The phase determination of $KNbO_3$ films at root temperature has yielded different results: Derderian et al. [27] prepared epitaxial (101)/(111) $KNbO_3$ films on (100) MgO by sol-gel at a crystallization temperature of 800°C. The niobium rich film ([K]/[Nb]=52/48) showed rosettes in a darker matrix, whereas equimolar films were smooth. SEM EDX analysis maps of potassium and niobium in the films with rosettes revealed that the matrix contained little potassium while niobium was spread evenly throughout the film. Raman microprobe spectra of the resettes confirmed that they are orthorhombic $KNbO_3$ while the matrix exhibited no appreciable Raman scattering. Graettinger et al. [34] deposited (101) textured $KNbO_3$ films on MgO substrates by ion beam sputtering and determined the phase of the films as orthorhombic using pole figure measurement. Schwyn et al. [60] on the other hand determined the crystallographic phase of sputter deposited $KNbO_3$ films on MgO substrates as tetragonal using x-ray diffraction measurements. The thermodynamical unstable tetragonal phase might be explained with strain in the film.

We performed Micro-Raman spectroscopy on a selected number of $KNbO_3$ films to gain a better understanding of the phases present. It is impossible to distinguish with certainty between the orthorhombic and tetragonal phase using $\Theta - 2\Theta$ X-ray diffraction: The peak splitting and absolute values of the 2Θ angles corresponding to the (101)/(010) orthorhombic and (100)/(001) tetragonal phase are too similar. Furthermore, the 2Θ angle of the (101) diffraction peak might be shifted due to stresses in the thin film.

The Raman spectroscopy measures inelastically scattered phonons, with an energy of the scattered radiation less than the incident radiation (Stokes lines). The Raman effect comprises a very small fraction, about 1 in 10^7, of the incident photons. The energy increase or decrease from the excitation is related to the vibrational energy spacing in the ground electronic state of the molecule. Therefore the wavenumber of the Stokes and anti-Stokes lines are a direct measure of the vibrational energies of the molecule or crystal. Since the Raman scattering is not very efficient, we need a high power excitation source such

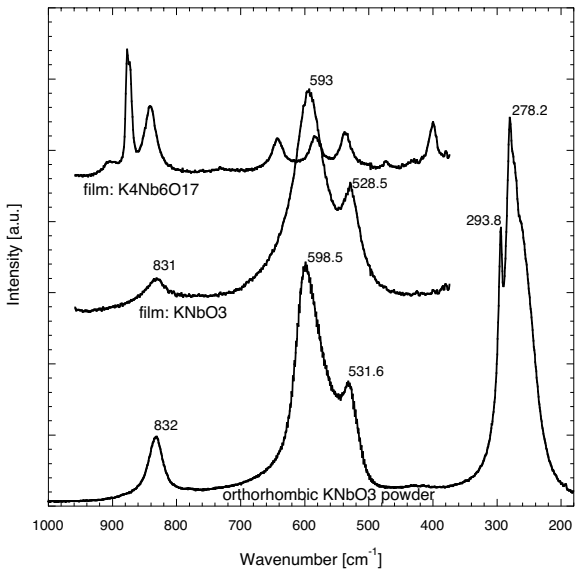

Figure 4.13: Raman spectroscopy of $KNbO_3$ powder showing the orthorhombic phase with the characteristic phonon at 832cm^{-1} for the tetragonal phase, and the peak splitting at 531.6–598.5cm^{-1} for the orthorhombic phase [53]. $KNbO_3$ films as deposited in this work show the same characteristic spectrum. Locally the spectrum corresponding to $K_4Nb_6O_{17}$ [42] was found on samples with a large amount of potassium deficient second phases.

as a laser. Also, since we are interested in the energy (wavenumber) difference between the excitation and the Stokes lines, the excitation source should be monochromatic. A red laser with a wavelength of 633nm with 18mW power was used as monochromatic and coherent light source for the employed Micro-Raman spectroscopy. The beam traverses a beam expander, is reflected on a notch filter and is then focused on the sample using a microscope with 50x objective lens with xy sample displacement support. The spot size of the incident beam is approximately 1μm. The inelastically scattered light, representing vibrations of the crystallographic lattice, travels back along the incident optical path along with the elastically scattered photons (Rayleigh scattering). Only the inelastically scattered light passes the notch filter, which also cuts the spectrum corresponding to Raman shifts between 0-180cm^{-1}. The beam undergoes a refraction on a grating to open the spectrum geometrically. The Raman spectrum is then measured with a CCD.

The Raman shift spectrum of pure and orthorhombic $KNbO_3$ powder is shown in figure 4.13. It is identical to the Raman spectrum measured for orthorhombic $KNbO_3$ by Perry and Tornberg [53]. The phonon at 832cm^{-1} (LO_4 mode) is present in all polymorphs of $KNbO_3$ except the cubic phase. The phonon splitting at 531.6-598.5cm^{-1} (TO_4 and TO_4' mode) appears at the tetragonal-orthorhombic phase transition. The TO_4 and TO_4' modes are the highest transverse optic mode split by anisotropy in the crystal.

Measurements at room temperature on a selected number of films (fig. 4.13: *film:*

Table 4.5: Process conditions for $KNbO_3$ thin film deposition on a (100) $SrTiO_3$ substrate.

Target Composition		5:1 $KNbO_3$:K_2CO_3	mol
Target Power		200	W_{rf}
Temperature		560	°C
Pressure		4	mT
Gas flow	Ar / O_2	50 / 2	sccm

$KNbO_3$), exhibiting a clean (101) $KNbO_3$ texture as confirmed by X-ray measurements, yielded a spectrum identical to the orthorhombic $KNbO_3$ powder spectrum. This confirms the orthorhombic phase of the $KNbO_3$ films, which corresponds to the thermodynamical stable state at room temperature. When focusing the laser on potassium deficient second phases identified by XRD as $K_4Nb_6O_{17}$, a spectrum identified as $K_4Nb_6O_{17}$ by Liu et al. [42] was found (fig. 4.13: *film: $K_4Nb_6O_{17}$*).

4.7 $KNbO_3$ film deposition on (100) $SrTiO_3$ substrates

To validate our sputter process, we deposited a $KNbO_3$ film on a monocrystalline (100) $SrTiO_3$ (STO) substrate. The 500nm thick $KNbO_3$ was deposited from a target containing 40% excess potassium. The sputter conditions are given in table 4.5, and the deposition time was 2h.

The obtained film was only partially crystallized. The crystalline part grows in cubic (100) orientation epitaxially on STO (100) (fig. 4.14 (a)). No second phases were observed. The (202) peak shows peak splitting indicating a partial (200) tetragonal, partial (202) orthorhombic texture of the $KNbO_3$ film. A SEM image at two different magnifications of the film surface is shown in figure 4.14 (b). Isolated islands have a cubic textured morphology, which corresponds to the (101) texture of the film seen in the $\Theta - 2\Theta$ x-ray diagram. The edges of the cube-like morphology of the textured areas (inset) are all aligned, even among the different islands indicating an epitaxial growth on the STO substrate. The grain size is approximately 200nm. The homogeneous phase around the islands might be an amorphous $KNbO_3$ phase, which can be explained with the insufficient thermal energy available for crystallization to occur at the relatively low deposition temperature of 560°C. The $\Theta - 2\Theta$ diagram shows a "bump" between 2Θ=15-20° which could be caused by an amorphous phase in the film. Onoe et al. [52] also observed a *blocklike micro-crystal* film morphology of (010) $KNbO_3$ films deposited on (110) STO substrates at 850°C by MOCVD. The film exhibited a [K]/[Nb] ratio of 1, as measured by XPS. Films which were slightly potassium deficient showed a locally limited crystal growth inside an amorphous matrix, similar to our observations.

A $KNbO_3$ film which we deposited on a (101) quartz substrate during the same deposition run, was transparent and crystalline with a random $KNbO_3$ texture. Schwyn et al. [60] reported that a complete crystalline $KNbO_3$ film deposited on MgO and spinel could only

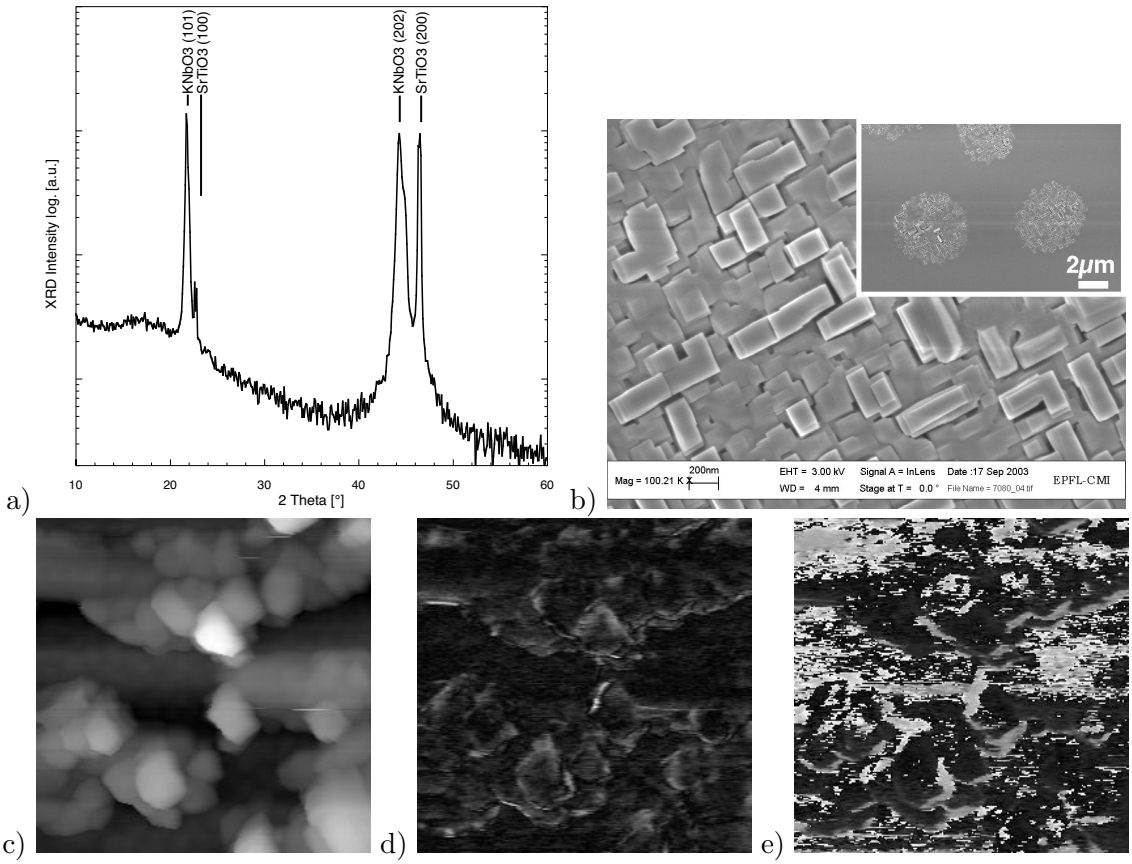

Figure 4.14: $\Theta - 2\Theta$ measurement of a 500nm thick $KNbO_3$ film deposited onto a (100) $SrTiO_3$ substrate with the process condition given in table 4.5 show the orthorhombic (101) as well as the tetragonal (100) texture, but also some contribution of an amorphous phase. The surface morphology (b) observed by SEM shows a crystalline phase with aligned crystallites surrounded by a homogeneous, probably amorphous matrix. AFM topography image with 1.5x1.5μm^2 sidelengths (c), and corresponding piezoelectric amplitude (d) and phase signal (e).

be obtained at a substrate temperature of 610°C, below which only weak (101) reflections of the orthorhombic phase were observed. Their $KNbO_3$ film, deposited at 610°C, had a (001) tetragonal texture.

The $KNbO_3$ film deposited on the STO substrate was analyzed with an AFM equipped for piezoelectric activity measurements. The surface topography (fig. 4.14 (c)) shows a 1.5x1.5μm^2 scan of an area with crystalline features similar to the ones seen in the SEM image. The peak-valley roughness of the 500nm thick film is 200nm, respectively 37nm for the rms roughness. The high peak-valley roughness is due to the outgrows of some of the cubic features. The images of the piezoelectric amplitude (d) and phase signal (e), corresponding to the topography image, confirm the piezoelectric activity of the film. Most of the grains show a top-to-bottom polarization (dark areas in phase image). The areas corresponding to the bottom-to-top polarization (white areas in phase image) show a much higher response.

4.8 $KNbO_3$ film deposition on polycrystalline (111) Pt/Si substrates

The majority of all depositions were performed on polycrystalline (111) Pt/../Si substrates. We have seen before that 3 different off-stoichiometric phases were observed next to the $KNbO_3$ phase.

4.8.1 $KNbO_3$, K_3NbO_4, $K_3Nb_7O_{19}$ and $K_4Nb_6O_{17}$ film microstructure

The XRD results will be correlated with the microstructure observed by SEM. A highly (101)-textured $KNbO_3$ film is compared in figure 4.15 (a) to a preferentially textured $(\bar{2}10)$ $K_3Nb_7O_{19}$ film (b), respectively a (040) textured $K_4Nb_6O_{17}$ film (c). The substrates are Pt/TaO_x (Spider) with a $PbTiO_3/TiO_2$ 10/2nm seed layer for (a), Pt/TaO_x (Spider) with a 1nm thick TaO_x seed layer for (b) and a Pt/TaO_x (Nordico) substrate for (c).

The microstructure of the (101)/(111) textured $KNbO_3$ film is *bi-phased* with a characteristic size of the segregations of 5-20μm diameter. The white areas, which represent a high intensity in backscattered electrons (Inlense mode of SEM), reveals a microstructure composed of cubes and rectangles. This is the characteristic microstructure of orthorhombic $KNbO_3$. The cubes or rectangular prism are locally aligned. This alignment can reach lateral extends of several micrometers, which is more than 10 times larger than the grain-size of the Pt electrode or IrO_2 seed layer which is typically 30-100nm. The local epitaxy on the electrode is therefore weak, compared with the lateral induced growth. The grain boundaries between the individual square grains seem to be quite large, but as we will see later, this depends very much on the substrate temperature. An EDX analysis of the dark areas shows a KN-ratio of 0.39, whereas the microstructure exhibiting the cubes (large picture) on the other hand has a KN-ratio of 0.91. The average KN-ratio of the film measured by XPS is 0.6.

The microstructure of a film exhibiting predominantly the $K_3Nb_7O_{19}$ phase is constituted of darker and almost smooth areas or grains which are very unordered when compared

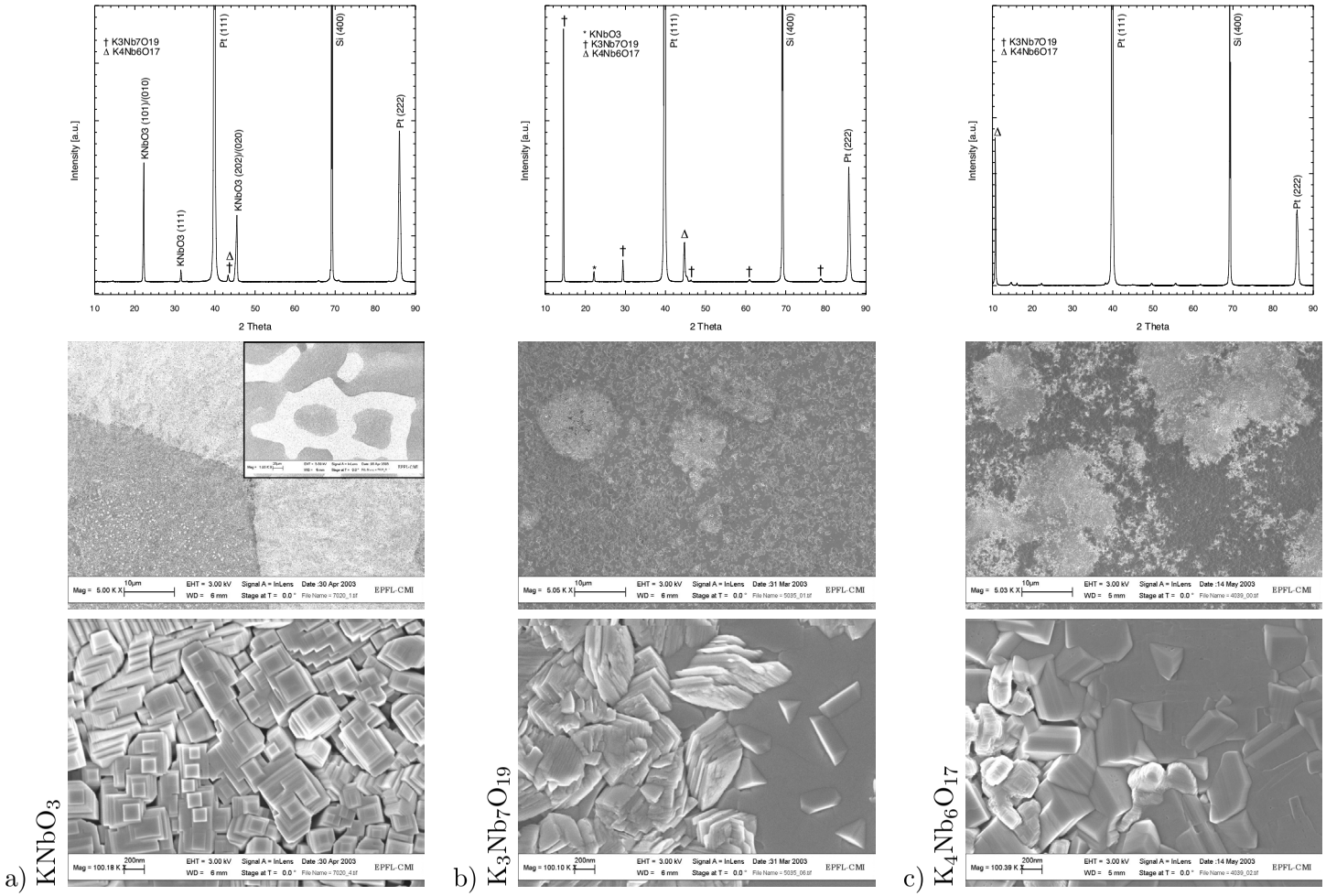

Figure 4.15: Example of microstructure mostly exhibiting the (101)/(111) $KNbO_3$ phase (a), respectively the $K_3Nb_7O_{19}$ phase (b), or the $K_4Nb_6O_{17}$ phase (c). The $KNbO_3$ phase consists mostly of cube-like shapes showing its faces, edges or corners on the surface depending on crystallographic orientation. $K_4Nb_6O_{17}$ is reported to grow in a lamella type of growth, similar to mica.

with the $KNbO_3$ grains. Some of them have a lamellae like appearance. Locally, some whiter areas can be seen in this microstructure of 5 to 10μm diameter, which are $KNbO_3$ phases.

The SEM image of the $K_4Nb_6O_{17}$ phase resembles very much the one of the $K_3Nb_7O_{19}$ phase. Reisman and Holtzberg [54] reported that the $K_4Nb_6O_{17}$ phase has a lamellar type of growth, similar in appearance to mica.

Two more examples of a (101)/(010) $KNbO_3$ microstructure are shown in figure 4.16 (a) and (c). These depositions were obtained with the unstable +200% K target. (a) shows a mostly (101)/(010) textured $KNbO_3$ film on a Pt (Spider) substrate obtained at a substrate temperature of 490°C after 0.7kWh target usage. The 150nm thick film looks dense and has quite a smooth surface. The film is almost stoichiometric with a KN-ratio of 1.03. The film (c) is obtained at a target usage of 1.3kWh. The substrate is Pt/TiO_2 (Nordico) with a 2nm TiO_2 seed layer. The film was deposited at 520°C. The XRD data indicate a (101)/(010)/(111) textured $KNbO_3$ film, even though the KN-ratio is approximately 3. The microstructure is constituted of loosely assembles cubes which are not very dense.

The second film (b) in figure 4.16 was obtained with exactly the same process conditions on the same substrate as film (a), but was deposited after a longer target usage (2.5kWh) and contains a much higher potassium content due to potassium accumulation on the target surface (c.f. paragraph 4.5). The value for the KN-ratio is interpolated from figure 4.10 and is estimated at more than 10. The XRD peaks may be indexed using the 26-1325 PDF file corresponding to K_3NbO_4 which represents the only thermodynamically stable phase in the K-Nb-O system with an excess of K compared to $KNbO_3$. The microstructure of the film is dense and homogeneous.

4.8.2 Phase segregations of $KNbO_3$-$K_3Nb_7O_{19}$-$K_4Nb_6O_{17}$ films

Most of the films show a bi-phased morphology when observed under the optical or scanning electron microscope. The spacing between the centers of these segregations, respectively the wavelength of this perturbation, is between 2 and 10μm. Figure 4.15 (a), 4.17 and 4.19 show examples of such segregations. The $KNbO_3$ phase are the white areas, and the darker areas represent $K_3Nb_7O_{19}$ and $K_4Nb_6O_{17}$ phases. The segregation observed in figure 4.17 is an extreme case which shows in the center of the segregation outgrows of loosely spaced cubic crystals which sometimes reach tower-like height-to-thickness ratios of 10. The area surrounding the center grows in a star-like lateral way with the cubic-shaped crystals radially aligned. This lateral growth is commonly observed in most of our bi-phased films. An EDX analysis performed along the radius of such a circular segregation revealed a significant potassium gradient. In the center a [K]/[Nb] ratio of 0.85 is found which decreases along the radius to 0.65 still in the cubic-crystals zone to reach 0.35 inside the surrounding matrix. The average KN-ratio measured by XPS over a 500x500μm^2 large area on the standard Pt/Si substrate amounts to 0.72. The XRD measurements indicate the presence of $KNbO_3$, $K_3Nb_7O_{19}$ and $K_4Nb_6O_{17}$ phases.

The distance between the white $KNbO_3$ and the darker $K_3Nb_7O_{19}/K_4Nb_6O_{17}$ phase zones of up to 10μm is quite large when compared to the film thickness of less than 1μm. This implies that the adatoms have a very long diffusion path. It can be assumed that the

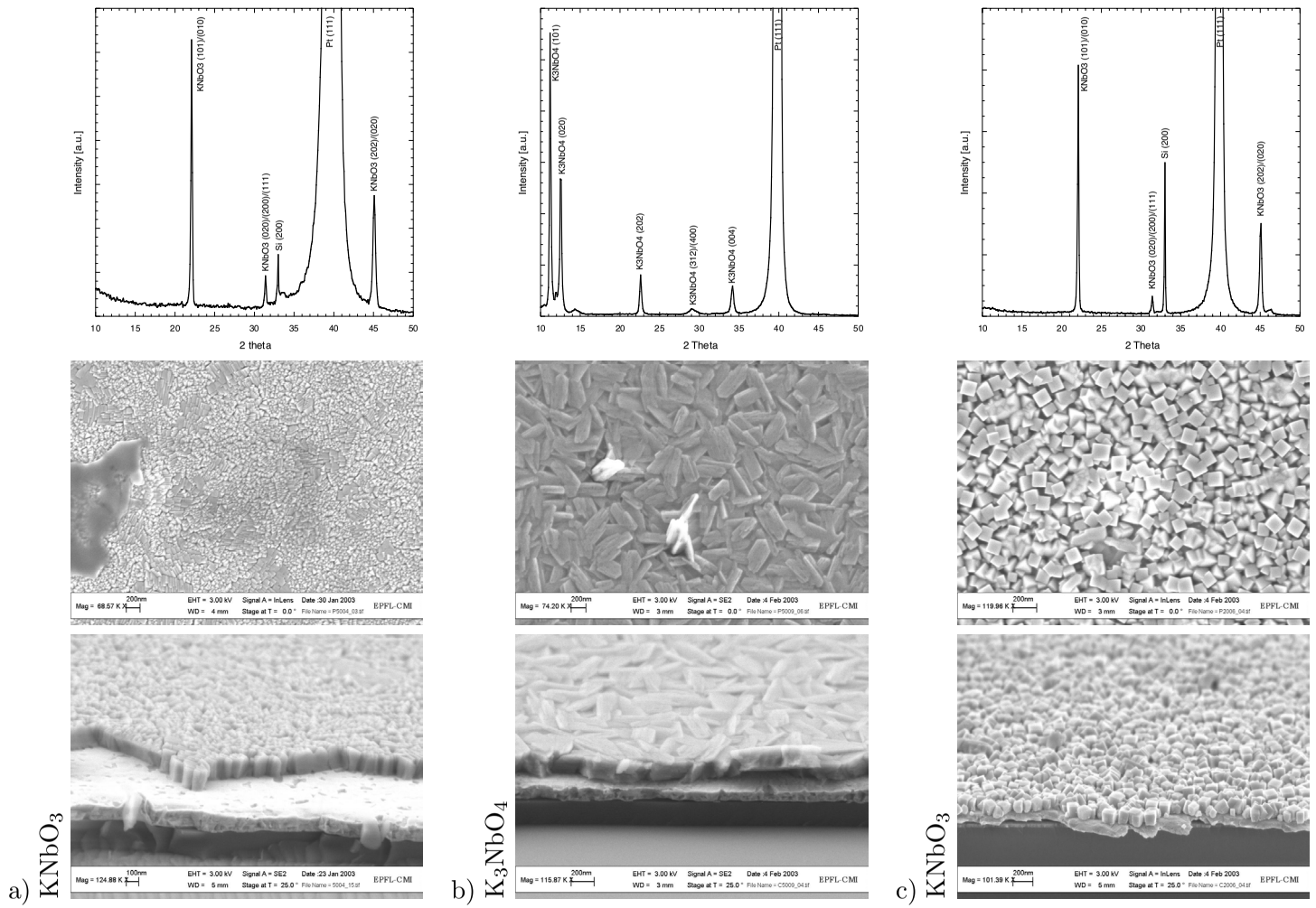

Figure 4.16: Microstructure and XRD of films deposited with the +200%K target, with 10mT of Ar, 150W, 2h at 480°C (a, b) and 522°C (c) on a Pt/TaO_x (Spider) substrate (a, b), and TiO_2/Pt/TiO_2 (Nordico) substrate (c). Film (a) was deposited after 0.7kWh, film (b) after 2.2kWh and film (c) after 1.3kWh respectively.

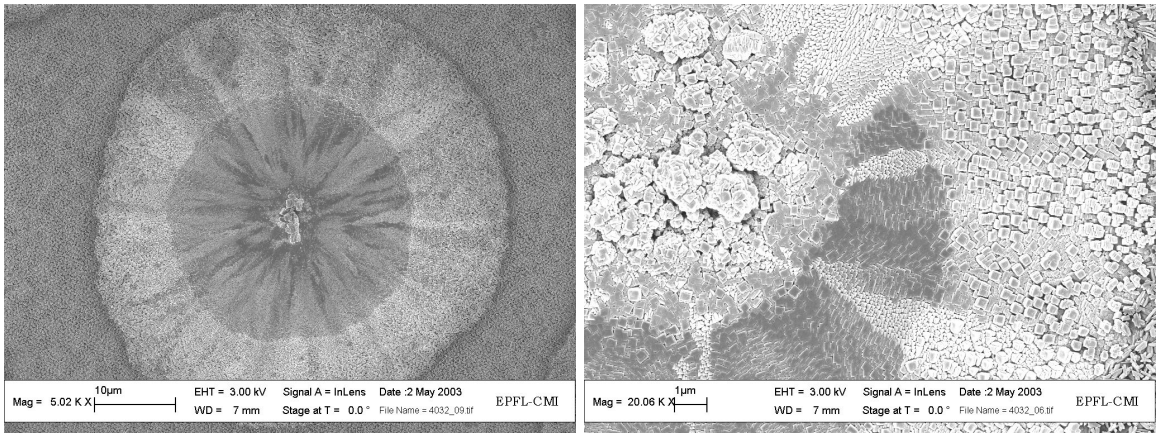

Figure 4.17: Film exhibiting a phase segregation. EDX analysis show a decreasing KN-ratio along the radius starting from the center of the circular segregation. The substrate is Pt/TaO_x (Nordico) and the deposition conditions were 522°C, 4mT Ar and $100W_{rf}$. The XRD analysis shows the presence of $KNbO_3$, $K_3Nb_7O_{19}$ and $K_4Nb_6O_{17}$ phases.

surface diffusion is mainly accomplished by potassium atoms as K has a low melting point of 63°C and the vapor pressure at the deposition temperature of 522°C is 55Torr[1]. Potassium can therefore only exist in bound states to oxygen or niobates, or eventually as adatom on oxides. The vapor pressure of solid Nb at the deposition temperature can be neglected compared with K: 710^{-37}Torr[2]. The vapor pressures of KO_2 and Nb_2O_5, which are relevant for the understanding of nuclei and film stability, could not be found in litterature. The high mobility of potassium atoms leads to a depletion of potassium atoms around stable $KNbO_3$ nuclei. This in return leads to the nucleation of $K_3Nb_7O_{19}$ and $K_4Nb_6O_{17}$ phases in the area surrounding the nuclei.

There are only a few nucleation sites for $KNbO_3$ on some of the substrates. The lateral induced growth of the $KNbO_3$ phase, or the radial growth from a nuclei center might be explained with the model of figure 4.18. Once a (100) $KNbO_3$ grain is nucleated, it grows in thickness direction, but also nucleated new $KNbO_3$ grains in lateral direction, overgrowing the surrounding potassium deficient second phases. This growth method would explain the decreasing KN-ratio observed along the radial direction of circular segregations, due to the decreasing $KNbO_3$ thickness.

4.8.3 Effect of seed layers on $KNbO_3$ film growth

Because the $KNbO_3$ film growth on Pt substrates is nucleation controlled we investigated different seed/nucleation layers. These are TaO_x, NbO_x, TiO_2, IrO_2, $PbTiO_3$ and KO_2. They were tested as seed layers even though some of them might be disadvantageous with

[1] vapor pressure of liquid K: log(p [atm])=4.402-4453/T [K]
[2] log(p [atm])=8.822-37818/T-0.2575logT [K])

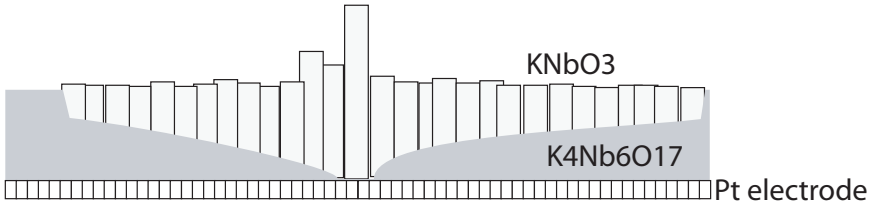

Figure 4.18: Model of possible $KNbO_3$ growth on polycrystalline (111) Pt/Si substrates.

regards to the phase diagrams: TaO_x forms a solid solution with $KNbO_3$ above 1000°C. Below 1000°C a possible sub-solidus composition separation of the K(Nb,Ta)O_3 phase might occur. NbO_x might nucleate an off-stoichiometric $KNbO_3$ phase. IrO_2 is a conductive oxide that exhibits more pronounced grain boundaries than the Pt electrode and might help in providing many defect points which possibly provide nucleation sites. $PbTiO_3$ (PT) is a perovskite, which can easily be deposited in thin film form of 10nm thickness on Pt electrodes. PT would provide a perovskite template for $KNbO_3$ growth very much like a monocrystalline substrate of STO or MgO. All of these nucleation layers were deposited in Nordico, process details will not be given. Potassium superoxide was added in a small quantity in proximity of the Pt substrate during a few depositions with the intention of evaporating it on the hot substrate and forming a potassium oxide rich Pt surface. KO_2 decomposes above 425°C and is dangerous to handle.

Figure 4.19 compares the simultaneous film growth on a plain Pt electrode (Spider) to a 50nm thick IrO_2 seed layer covered Pt electrode. The film was deposited with a +25% excess K target, at 540°C, 200W, 2mT, 50sccm Ar for 3h resulting in a 1.5μm thick film. XRD results indicate that the IrO_2 seed layer promotes the $KNbO_3$ phase whereas the plain Pt surface also promotes non-stoichiometric second phases. The $KNbO_3$ film grown on the IrO_2 seed layers has a (101)/(010), but also a (042)/(402) texture, which correspond to the pseudocubic (100) and (111) orientations. The darker areas, which are plate-like are the (101)/(010) oriented grains, whereas the white areas, with the cubic corners upwards, correspond to the (042)/(402) texture. The lateral growth of the pseudocubic (100) areas is again evident, indicating a laterally nucleation and growth of the $KNbO_3$ phase.

The PT seed layers also promotes the $KNbO_3$ phase with (101)/(010) texture (fig. 4.19 (c)). Simultaneous depositions on bare Pt (Spider) substrates only yielded the $K_3Nb_7O_{19}$ phase.

The use of the TaO_x seed layer clearly promoted the $K_3Nb_7O_{19}$ and $K_4Nb_6O_{17}$ phase, whereas a crystalline $KNbO_3$ phase was observed on the bare Pt substrate in the same deposition run. The NbO_x seed layer promoted second phases, but didn't inhibit the $KNbO_3$ crystalline phases. A mixted (101) and (111) texture was observed. TiO_2 seed layers usually did not help to nucleate the $KNbO_3$ phase. The film shown in figure 4.16 (c) however was obtained with a TiO_2 seed layer and has a strong (101)/(010) $KNbO_3$ texture. The microstructure shows loosely spaced crystallites.

The evaporation of KO_2 powder prior and during the $KNbO_3$ deposition process led to

Figure 4.19: (a) Morphology of a 1.3μm thick $KNbO_3$ film deposited on bare Pt (Spider) substrate The deposition conditions were 25% K excess target, 530°C substrate temperature and 2mT Ar, 200W. The KN-ratio is 0.95 and the x-ray measurements show a equal (101) and (111) texture with second phases. (b) A simultaneous deposition on a 50nm thick IrO_2 seed layer yields a mixed (101)/(010) and (042)/(402) texture. Film (c) is deposited onto a 10nm thick $PbTiO_3$ seed layer on a Pt (Spider) substrate and exhibits a pure (101)/(010) texture. The deposition conditions were 25% K excess target, 560°C substrate temperature and 8mT Ar, 100W.

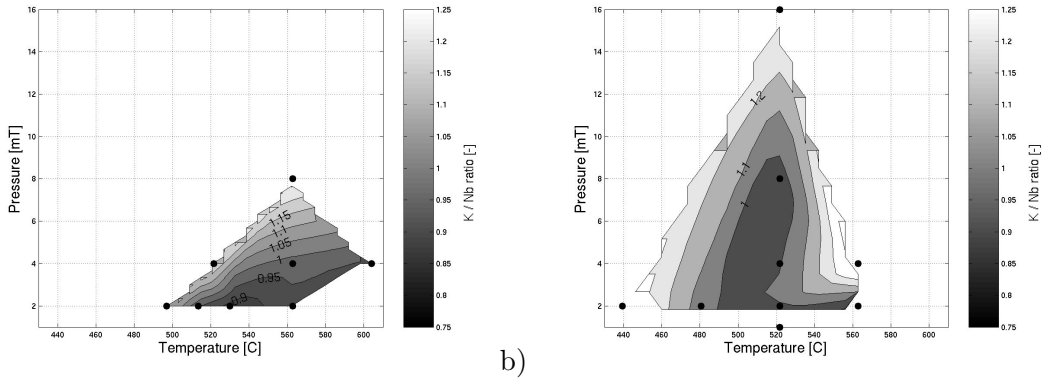

a) b)

Figure 4.20: [K]/[Nb] atomic concentration ratio measured by XPS on $KNbO_3$ films as a function of deposition temperature and process pressure obtained with the target containing 25% (a), respectively 40% (b) excess K.

a strongly (101)/(010) textured $KNbO_3$ film on bare Pt substrates and Pt substrates with IrO_2 seed layer. A multitude of other $KNbO_3$ orientations was also observed, as well as the potassium rich K_3NbO_4 phase.

4.8.4 Effect of sputter pressure and substrate temperature on film stoichiometry

The effect of process parameters on the film stoichiometry, or [K]/[Nb] atomic ratio, is shown in figure 4.20 for the targets yielding near-stoichiometric films. The KN-ratio is plotted as a function of pressure and temperature for targets containing +25% (a), respectively +40% potassium (b). Each black dot in the plot represents one single or several averaged XPS measurements for the given process condition. The contour surface is calculated from the data points using a cubic interpolation. Contour lines of constant KN-ratios are drawn with their corresponding values to facilitate the interpretation.

The results and tendencies for both targets are coherent: Increasing the sputtering pressure leads to an increase in the KN-ratio. Both targets show an increasing potassium content in the film for decreasing temperatures. The threshold temperature for the increasing KN-ratios is 560°C for the +25%K target, respectively 520°C for the +40% K target. In general there is more potassium provided by the target containing 40% excess K. For the +40% K target an increase in the KN-ratio can be observed for substrate temperatures exceeding 520°C. The 40% K target has a minimum of the KN-ratio as a function of temperature which corresponds to stoichiometric $KNbO_3$. This minimum extends from 490 to 520°C and a pressure in the range of 2-8mT. All other process conditions result in too high a KN-ratio.

Lowering the substrate temperature below 560, respectively 520°C, leads to an increasing KN-ratio which approaches the potassium-to-niobium ratio of the targets. The lower

thermal energy of the adatoms probably leads to a desorption rate which becomes equal for both the potassium and niobium atoms. For increasing substrate temperatures, the potassium which is not yet chemically bonded to the substrate as $KNbO_3$, respectively other K-Nb-O phases, will be desorbed more easily. This desorption is proportional to the substrate temperature and leads to an impoverishment of potassium on the film surface.

Increasing the process pressure results in a higher KN-ratio. The atomic mass differences between the sputter gas Ar and the Nb and K atoms are not resulting in a significantly different sputter yield for each species. The mean free path of the sputtered species decreases with increasing pressure. The energy exchange between the argon and potassium atoms is more efficient as both have almost the same atomic mass. The increased collisions prevent desorbed potassium atoms from diffusing far away from the target-substrate volume and therefore provides more potassium, e.g. a higher arrival rate.

At higher temperatures (above 520°C), the heat radiated from the substrate heats the target surface increasingly (the heat radiated scales with $\sim T^4$) and may lead to a thermal decomposition of the K_2CO_3 contained in the target. This leads eventually to a quasi evaporation of potassium from the target in addition to the sputtered K and Nb species, and results finally in higher KN-ratios in the film. The increase in KN-ratio for increasing substrate temperature is only observed on the target with +40% excess K supporting the hypothesis that the additional K originates from the excess K_2CO_3.

Adding oxygen to the Ar sputter gaz, even at concentrations as low as 2%, a net reduction of K in the films results. A $KNbO_3$ film deposited with the pure $KNbO_3$ target (522°C, 100W, 4mT, 2h) yielded a [K]/[Nb] ratio of 0.76 in a pure Ar atmosphere and only 0.58 in the following deposition using 25% of O_2.

4.8.5 Effect of sputter pressure and substrate temperature on film crystallography

Figure 4.21 shows the influence of deposition pressure and temperature on the microstructure of $KNbO_3$ films. The left column shows a pressure series (2-4-8-16mT) for a constant temperature of 520°C, respectively a temperature series (440-480-520-560°C) for a constant pressure of 2mT in the right column. The deposition conditions were pure Ar atmosphere, $200W_{rf}$, +40% excess K, and 2h (sample 440°C only 1h). The substrate is $IrO_2/Pt/TaO_x/SiO_2/Si$ (Spider). The same depositions yielded no particular trend on bare Pt/TaO_x (Spider) substrates. The roughness measured on the pressure series relative to the film thickness increases from 4%, to 27% and finally 43% for the last two samples, which corresponds to 34, 245, 395 and 401nm rms roughness measured with the α-step over 400μm distance on the 900nm thick films.

The corresponding XRD data of these films is given in figure 4.22. When considering the XRD data of the pressure series a tendency for stronger (101)/(010) $KNbO_3$ texture can be seen for decreasing pressures. Second phases are hardly present. The microstructure shows a decrease in roughness at the same time. The films are dense, no voids appear between individual grains. Squares which represent stable facets of the orthorhombic phase appear at a pressure of 2mT on the surface. The films are fibrous in appearance. According to the

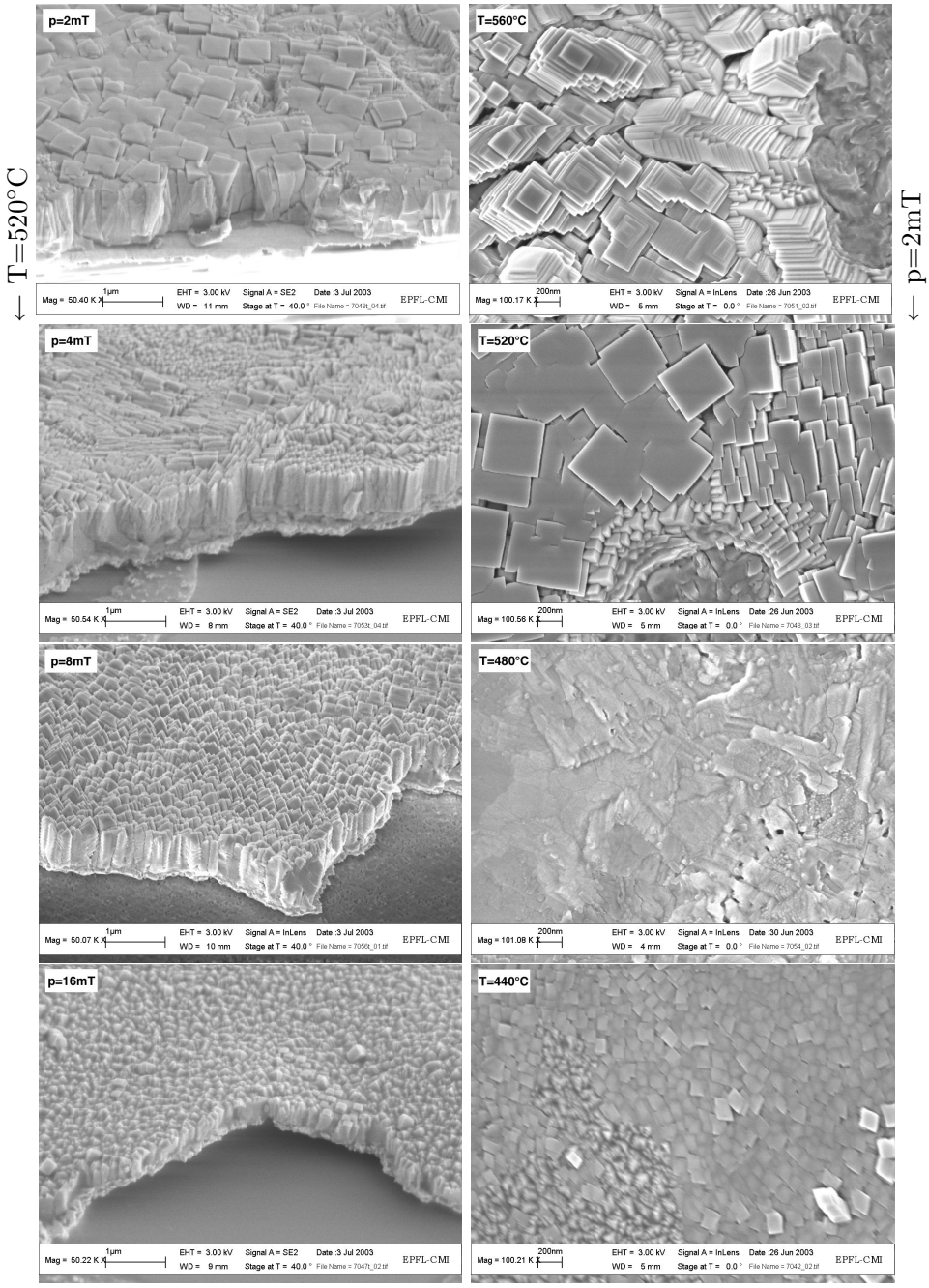

Figure 4.21: Left column showing the influence of sputter pressure on the microstructure of a $KNbO_3$ film obtained at the constant deposition temperature of 520°C. Right column showing the influence of temperature on the microstructure at a constant pressure of p=2mT. The substrates are $IrO_2/Pt/TaO_x/SiO_2/Si$ (Spider), the target contains +40% excess K, the rf power is $200W_{rf}$, and the sputter atmosphere is pure Ar.

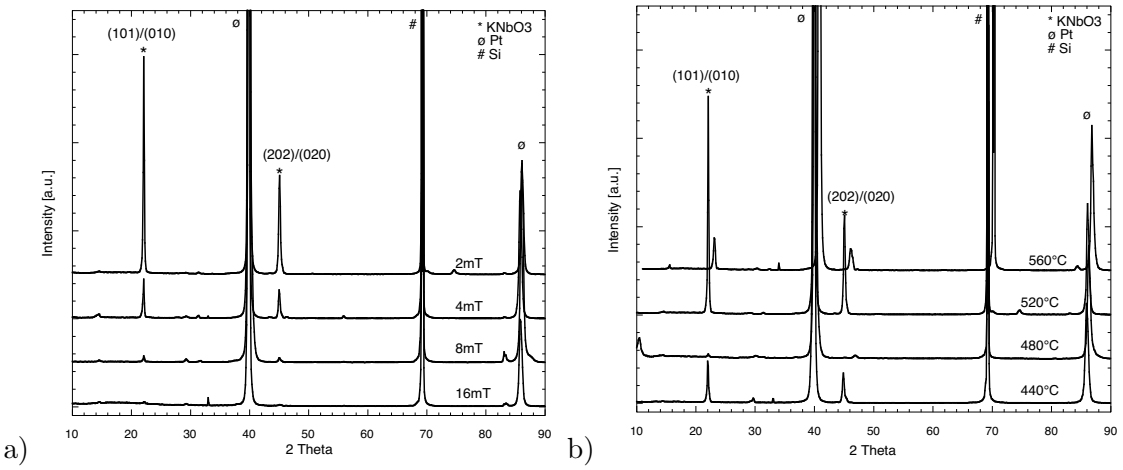

Figure 4.22: XRD $\Theta - 2\Theta$ scans showing the effect of pressure (a) and temperature (b) on film crystallinity. The measurements correspond to the films in figure 4.21. Note: The scan 560°C in (b) is shifted by 1° for clarity.

XPS measurements, fig. 4.20 (b), the films are stoichiometric in the range 2-8mT.

The temperature series shows depositions which were done at 2mT just around the tetragonal-cubic phase transition of 440°C and higher temperatures of up to 560°C. The deposition 520°C-2mT is present in both columns. The presented temperature series does not exhibit any clear tendencies when considering the XRD data of figure 4.22. All except the temperature of 480°C lead to (101)/(010) textured $KNbO_3$ films, with the highest intensity for the film deposited at 520°C. The films are dense up to a deposition temperature of 520°C. At 560°C voids between the individual grains appear, also denoted voided growth structure by Thornton [67]. There is enough thermal energy available for surface diffusion so that the grains minimize surface energy by clustering into small crystallites.

The homologous temperature T/T_m of $KNbO_3$, which has a melting point of T_m=1039°C is 0.61 at 520°C. The homologous temperature range is 0.54-0.64 in the temperature range presented in figure 4.21. According to the structure-zone model as proposed by Thornton [67, 66], the inert working gas pressures of 2-10mT and the homologous temperature define these depositions to be in the Zone 2. It must be taken into consideration that oxygen has been found to reduce adatom mobilities, and therefore can promote Zone 1 structures. At these high homologous temperatures the surface mobility is high and grain boundary migration and recristallization are possible.

4.8.6 TEM plane view bright field and diffraction images

A $KNbO_3$/Pt/Si sample exhibiting strong (101)/(010) texture with small amounts of (002)/-(200)/(111) and (024)/(420) texture was prepared for Transmission Electron Microscope (TEM) analysis, the SEM surface image of which can be found in figure 4.28 (d). The bright

field TEM image in figure 4.23 (a) shows a microstructure with cubic shaped crystallites set on their faces (spot 1), on their edges (spot 2) and on their corners (spot 3). EDX analysis on different grains showed a slightly potassium deficient film. The observed grains/crystallites have the right stoichiometry with a [O]/[Nb]-atomic ratio of 2.96±0.03 and a [K]/[Nb]-atomic ratio of 0.93±0.05.

The diffraction images taken on the three spots are represented in figure c), d) and e). They can be identified in (b) as (101)/(010), in (c) as (002)/(200)/(111) and in (d) as (024)/(420) planes. These correspond to (b) $(100)_{\mathrm{pc}}$, (c) $(110)_{\mathrm{pc}}$, and (d) $(111)_{\mathrm{pc}}$ planes in pseudo-cubic (pc) notation. The different domain variants cannot be distinguished because the inter-lattice plane distances are too similar. It can be concluded from the discrete and clear diffraction spots that each grain or crystallite is single-crystalline. The slightly smeared diffraction spots in image (d) are due to the size of the electron beam which excites several surrounding grains.

4.8.7 Film outgrows-nanorods observed in the Nb_2O_5-K_2O system

One more particularity of the Nb_2O_5-K_2O system is that during film growth, certain grains undergo a faster growth than the sourrounding matrix. This phenomena is shown in figure 4.24 on SEM images of two different films exhibiting different kind of *outgrows*. The left image is deposited on Pt/TaO_x (Nordico) with 10mT Ar, 150W using the +200% K target and a substrate temperature of 480°C. The measured KN-ratio of the same deposition on the Pt/TaO_x (Spider) substrate is 1.03 which indicates a near stoichiometric $KNbO_3$ film. The XRD data shows reflections corresponding to either the potassium rich K_3NbO_4 / K_3NbO_8 phase or the potassium deficient $K_4Nb_6O_{17}$ phase. Fibers grow out of the matrix in an oblique angle and show a length-to-width aspect ratio of at least 10. The total lengths of some fibers is more then 1μm, with a overall film thickness of only 200nm. The same deposition on the Pt/TaO_x (Spider) substrate yielded a homogeneous and (101)/(010) textured $KNbO_3$ film as seen in figure 4.16 (a).

The micrograph in figure 4.24 (b) is taken from a film grown on Pt/TaO_x (Nordico) with 10nm IrO_2 seed layer. The deposition conditions were 560°C, 2mT Ar, $100W_{\mathrm{rf}}$ and the target contained +25% excess K. The KN-ratio is measured as 0.66 on the reference substrate. The XRD data indicated $K_3Nb_7O_{19}$, $K_4Nb_6O_{17}$ and $KNbO_3$ phases in different orientations. It is impossible to identify the stoichiometry of the outgrows using EDX in the SEM as the interaction volume is approximately $1\mu m^3$ and thus larger than the grains.

Similar types of outgrows were already observed on $LiNbO_3$ films deposited onto Al_2O_3 with off-axis sputtering by Kingston et al. [39]. They explain the outgrows of c^- grains inside a matrix of c^+ grains with different growth rates for grains with the c axis perpendicular to the film surface and the polarization directed from the film surface towards the substrate. The higher growth speed of the c^- grains is explained with the higher coulombic forces between the c^- grains and the ionized Li and Nb species in the plasma. The density of outgrows is higher on scratches and areas where the substrate was inadequately cleaned and it is also found that the size and area density of the outgrows is proportional to the film thickness. Because our films were grown in the paraelectric cubic phase, the grains are not

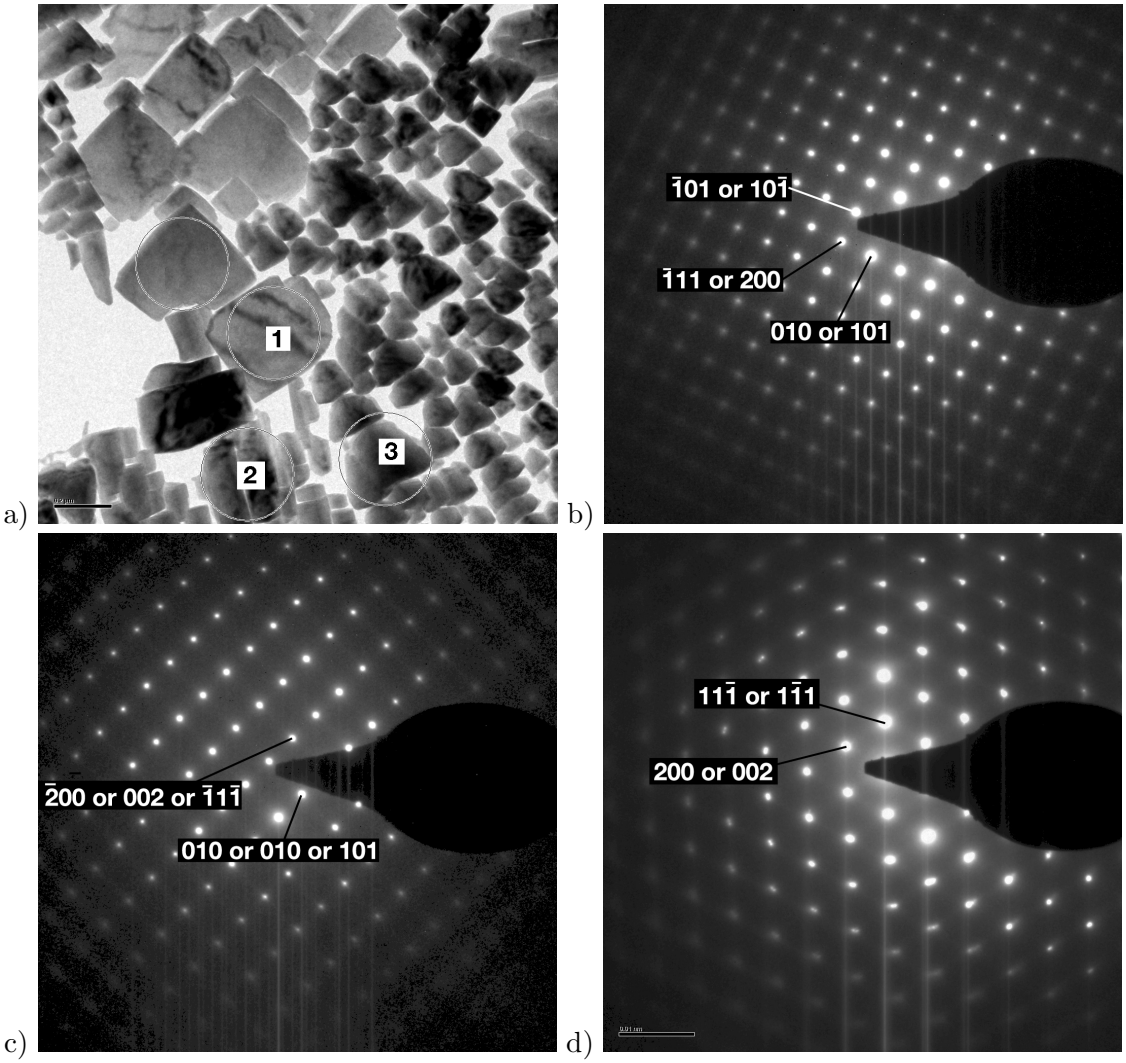

Figure 4.23: (a) TEM plane view bright field image of a $KNbO_3$/Pt/Si sample. (b) Diffraction pattern observed on spot 1 representing a (101) or (010) plane. (c) Diffraction pattern observed on spot 2 representing (001), (100) or (121) planes. (d) Diffraction pattern observed on triangular shaped grains (spot 3) representing (011) or (110) planes. This corresponds to (b) $(100)_{\mathrm{pc}}$, (c) $(110)_{\mathrm{pc}}$, and (d) $(111)_{\mathrm{pc}}$. The domain variants cannot be distinguished. The observed grains are single crystalline.

a) 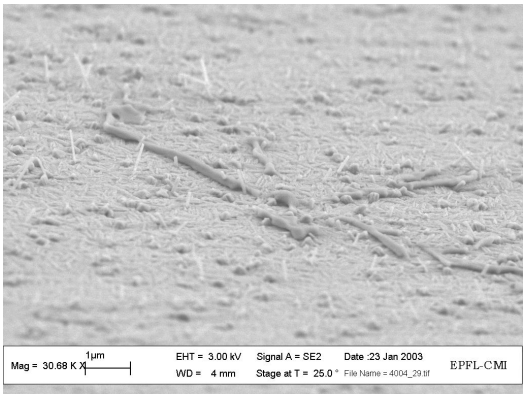

b) 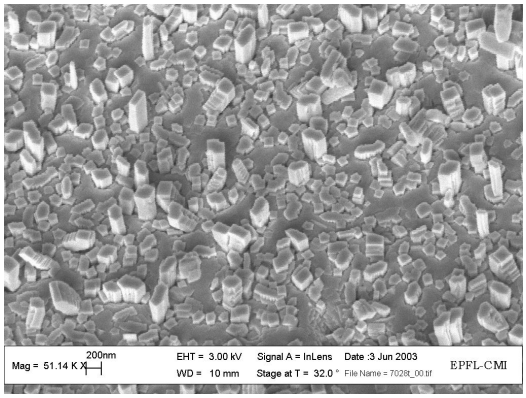

Figure 4.24: Outgrows in $KNbO_3$ films with different morphologies obtained on different substrates with different deposition conditions. (a) shows the (101) perovskite $KNbO_3$ phase as well as potassium excess and deficient second phases, the KN-ratio is 1.03, and it is fabricated from the +200% K target. (b) shows a strong (101)/(010) $KNbO_3$ texture but also various second phases, the KN-ratio is 0.66, and it is fabricated from the +25% K target

polar. We believe that the different phases present have each a different growth rate which results in the observed outgrows. We also find that these outgrows are favorably observed on the Nordico Pt substrates, which probably has a rougher surface with more defects than the Spider Pt substrates.

4.9 Dielectric and piezoelectric characterization of $KNbO_3$ films

Samples that exhibited a strong (101)/(010) $KNbO_3$ texture were coated with platinum top electrodes dots having a surface area of approximately $0.24mm^2$ and a thickness of 100nm. The samples were probed for polarization-electric field and capacity-electric field measurements. Unfortunately, most of these samples exhibited very high dielectric loss tangents of more than 10%, high leakage and low breakdown fields.

The high electric conduction could be due to oxygen deficiency or eventually metallic-like potassium at grain boundaries. Such potassium was observed by XPS on some of the samples. Different Rapid Thermal Anneals between 500 and 650°C in an oxygen atmosphere however did not improve the electric quality of the films.

4.9.1 Macroscopic $d_{33,f}$ measurements with double beam laser interferometer

Piezoelectric and dielectric properties were analyzed on a 1.4μm thick $KNbO_3$ film with strong (101)/(010) and (042)/(402) texture deposited at 515°C, 2mT Ar, 250W with the

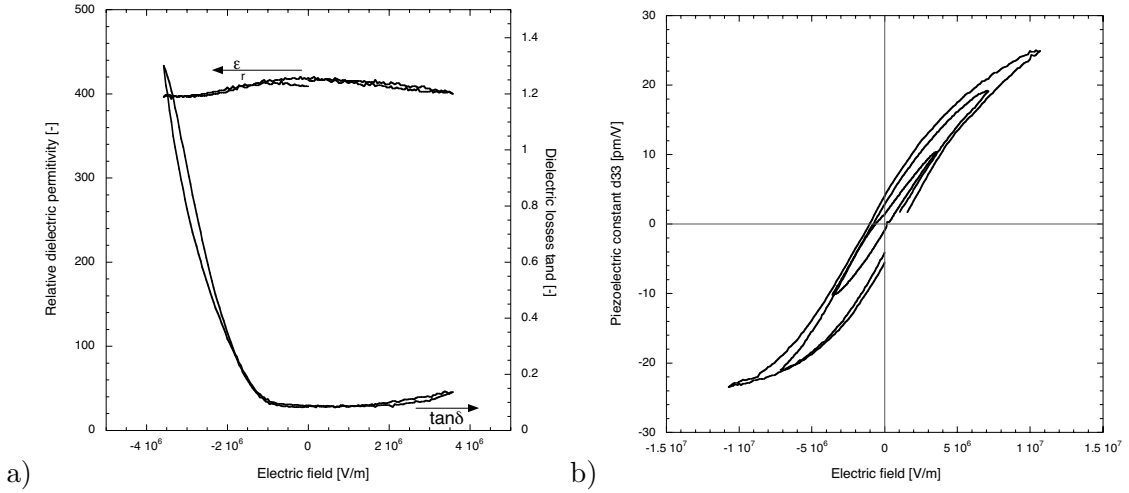

Figure 4.25: Dielectric permittivity and loss tangent vs electric field (a), and piezoelectric hysteresis loop (b) measured on a 1.4μm thick $KNbO_3$ film deposited on a $IrO_2/Pt/TaO_x$ (Nordico) substrate by double beam laser interferometry. The film has a (101)/(010) as well as (024)/(420) texture and a KN-ratio of 0.96.

+25% target on a 10nm IrO_2 seed on Pt/TaO_x (Nordico) substrate and exhibiting a KN-ratio of 0.96 on the reference substrate. Figure 4.25 shows the relative dielectric constant and the dielectric losses (a), respectively the piezoelectric $d_{33,f}$ constant (b), as measured by double beam interferometry. The piezoelectric hysteresis loop was measured counterclockwise, with the field applied on the top electrode. This film has a saturation piezoelectric constant of ±24pm/V, but the remanent piezoelectricity is very small as the remanence of polarisation is very weak. The polarization in the $KNbO_3$ film switches when the electric field is reversed, which shows the ferroelectric nature of the film. The film has an electric break-down field of 13MV/m.

Wada et al. [69] reported recently on a special poling treatment which they used to pole single crystal $KNbO_3$. 4 different kind of domain structures exist in $KNbO_3$: 180°, 90°, 60° and 120°. The difficulty in poling $KNbO_3$ might explain the small hysteresis loop measured on our samples. A certain poling takes place as there is a field dependency seen in our interferometer measurements, but when reducing the applied dc field, the domains return to their initial state, reducing thus the polarization and almost no piezoelectric remanence is observed.

The saturated clamped piezoelectric coefficient $d_{33,f}$ in [101] direction can be calculated using equation 2.30, page 39.

$$d_{33,f} = \frac{e'_{333}}{c^{E}_{3333}{}'} = \frac{6.07}{1.62\ 10^{11}} = 37.5\text{pm/V} \tag{4.8}$$

The magnitude of the clamped piezoelectric coefficient $d_{33,f}$ measured by double beam interferometry is only about half of the calculated value. This reduction may well be

explained with the mixed (101)/(010) but also the (042) texture. The (010) and (042) texture both have their polarization vector at an angle superior to 45° to the substrate normal and have therefore a reduced piezoelectric coefficient, respectively zero for the (010) texture.

The relative dielectric permittivity was measured as $\epsilon_r = 415$ at zero electric field. When increasing the electric field to 3.5MV/m the dielectric permittivity is reduced by 4%. The dielectric losses amount to 9% at zero field and increase to 14% at a positive field of 3.5MV/m. When applying a negative field, the losses exceed 20% at -1.6MV/m already and increase rapidly at higher fields.

The value of 415 for the relative dielectric constant can be interpreted as follows: We calculated the dielectric permittivity for a (101) textured $KNbO_3$ film in paragraph 4.2.3. The clamped and unclamped values are 29 and 99. The much larger measured value results from the considerable contribution of the (010) direction, along which ϵ_r amounts to 780 and 985 for the clamped and unclamped condition respectively. The observed additional (024)/(420) orientation may also contribute to the larger value.

The thickness-extensional coupling coefficient can be calculated with the measured values of $d_{33,f}$ and ϵ_r using equation 2.31, page 39.

$$k_t^2 = \frac{d_{33,f}^2 c_{33}^E}{\epsilon_{33}^{\text{film}}} = \frac{(24.0\ 10^{-12})^2 1.62\ 10^{11}}{415\epsilon_0} = 2.8\% \tag{4.9}$$

This value of k_t^2 is extremely small compared to the calculated value of single crystal data k_t^2=46.8% (eq. 4.6, page 127).

Only few authors have published measurements of piezoelectricity in $KNbO_3$ thin films. Yamanouchi, Odagawa et al. [78, 51] claim to be the first to measure piezoelectric properties on an as-grown $KNbO_3$ thin film. They deposited $KNbO_3$ on monocrystalline (101) STO substrates using MOCVD and measured the electromechanical coupling coefficient with interdigital electrodes (SAW) as 2.1%, which is very high for a SAW resonator.

We can tentatively explain our small coupling coefficient with the amount of (010) texture relative to the (101) texture. Assuming parallel grains of both textures in the film, we can calculate the contribution of each texture to the dielectric constant as $\epsilon_{\text{tot}} = \alpha\epsilon_{(101)} + (1-\alpha)\epsilon_{(010)}$, the stiffness as $c_{\text{tot}}^D = \alpha c_{(101)}^D + (1-\alpha)c_{(010)}^D$ and the piezoelectric constant as $e_{\text{tot}} = \alpha e_{(101)} + (1-\alpha)e_{(010)}$, where $\alpha = \frac{V_{(010)}}{V_{(010)}+V_{(101)}}$ is the volume fraction of (010) textured domains. The coupling coefficient can then be derived as a function of α with equation 2.8, 19 (fig. 4.26 (a)). This result is the worst case scenario. If we assume the grains to be arranged in series instead of parallel direction, then the coupling coefficient will be less strongly reduced.

A small percentage of the (010) texture in a (101) textured film reduces the coupling coefficient significantly, approximately proportional to $1/\alpha$. This is firstly due to the high dielectric constant and secondly to the piezoelectric constant which is zero along the [010] direction. The coupling coefficient k_t^2 is zero along the [010] direction [48]. The calculated value of k_t^2 from the measured piezoelectric and dielectric constant corresponds to roughly

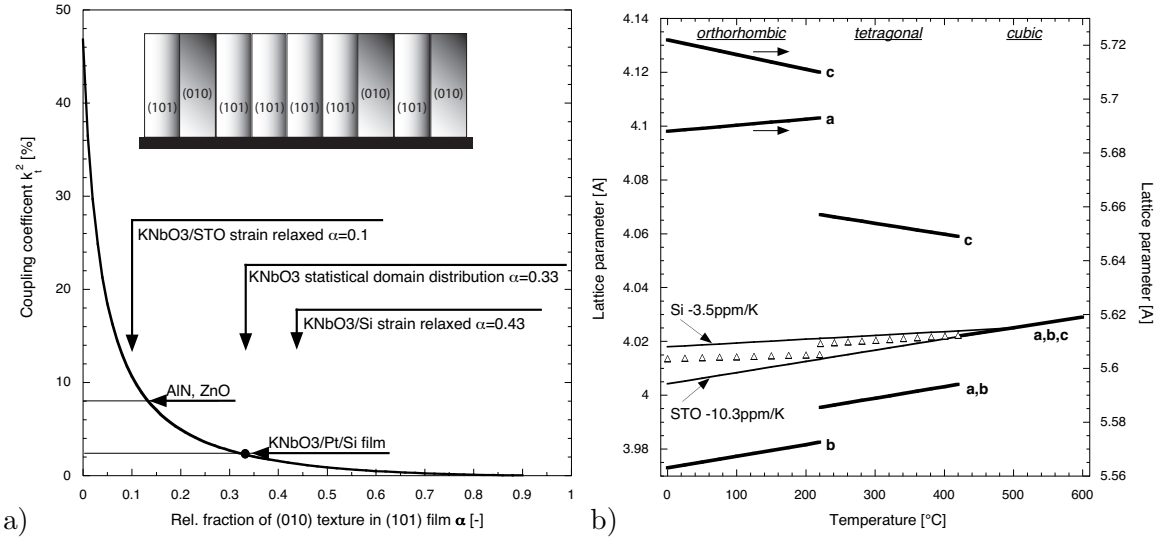

Figure 4.26: (a) Coupling coefficient k_t^2 as a function of the volume fraction α of the film with (010) texture compared to (101) texture for the worst case scenario with vertical domain walls. The value of k_t^2=2.8% determined on our films corresponds to approximately $\alpha = \frac{1}{3}$, i.e. one third of all domains are (010) oriented. To obtain a coupling coefficient higher than AlN or ZnO, these (010) domains have to be reduced to less than 10% with a poling treatment. (b) Lattice parameters of $KNbO_3$ as a function of temperature for the three phases cubic, tetragonal and orthorhombic (c.f. fig. 4.3). The fine lines represent the lattice parameter of Si and STO adjusted to cubic $KNbO_3$ at the growth temperature of 500°C. The △ represent the calculated lattice parameters for $\frac{1}{3}$ volume fraction of b-axis$_{\text{orthorhombic}}$ domains, respectively c-axis$_{\text{tetragonal}}$ domains.

$\alpha = 0.33$ which would indicate a $\frac{2}{3} : \frac{1}{3}$ distribution of (101)/(010) texture. This ratio corresponds to the probability of obtaining the (101) texture when cooling {100} pseudocubic nucleated grains to the orthorhombic phase. To increase the coupling coefficient, a poling treatment is needed which could switch the (010) domains into (101) domains. In order to obtain a higher coupling coefficient than AlN or ZnO, the fraction of (010) domains has to be reduced to less than 10%. From literature it is known that the poling of $KNbO_3$ crystals and ceramic is a difficult task.

We calculated the average lattice parameter a^* of the tetragonal and orthorhombic unit cell as a function of temperature, based on data from figure 4.3, with the hypothesis of having the pure statistical situation with $\frac{1}{3}$ c-axis domains in the tetragonal phase, and $\frac{1}{3}$ [010] domains in the orthorhombic phase, figure 4.26 (b):

$$\text{tetragonal} : a^* = \frac{1}{3}a + \left(1 - \frac{1}{3}\right)\sqrt{ac} \tag{4.10}$$

$$\text{orthorhombic} : a^* = \frac{1}{3}\sqrt{\frac{ac}{2}} + \left(1 - \frac{1}{3}\right)\sqrt{\frac{b\sqrt{a^2 + c^2}}{2}} \tag{4.11}$$

This will result in a lattice mismatch of 0.2% compared with STO, respectively -0.1% compared with Si. It is known that film stress can be partially released by reconfiguring ferroelastic domains [55]. The mismatch could indeed be reduced to zero by assuming a fraction of (010) domains of α=0.1 on STO and 0.43 on Si. This would lead to a much smaller coupling on Si than on STO (see figure 4.26 (a)). Our measurements support the idea that we have rather a statistical distribution between (010) and (101) domains. To achieve a high electromechanical coupling larger than the one obtainable with AlN or ZnO, the film needs to be poled and a domain state with more than 90% of (101) oriented domain is necessary.

4.9.2 Microscopic measurement of piezoelectric activity with AFM

Piezoelectrical and ferroelectrical activity were verified by means of a scanning probe microscope, i.e. piezoelectric sensitive atomic force microscope as an alternative to the macroscopic measurements. This method allows to probe very small areas of a few μm^2 and even individual grains. Figure 4.27 shows such a measurement on a 200nm thick film which is represented in figure 4.16 (a) as SEM image. The film has a strong (101)/(010) texture and a KN-ratio of 1.03.

The entire film exhibits a piezoelectric response when a dc field of +8V is superimposed to the probing ac field. The strongest amplitude response originates from grains which are protruding from the surrounding matrix. It is observed that the highest response is found on the edges of the grains. When changing the sign of the dc field, the phase of the piezoelectric response changes by 180° on the entire area scanned as expected for a ferroelectric film. This is seen in the phase image with the color change from white to black.

Figure 4.28 (a) and (b) show the 2D and 3D topography measured by AFM on another sample. The film was 350nm thick, has a strong (101)/(010) texture and only weak second phases, the KN-ratio was 0.7 as measured on the reference substrate and the process

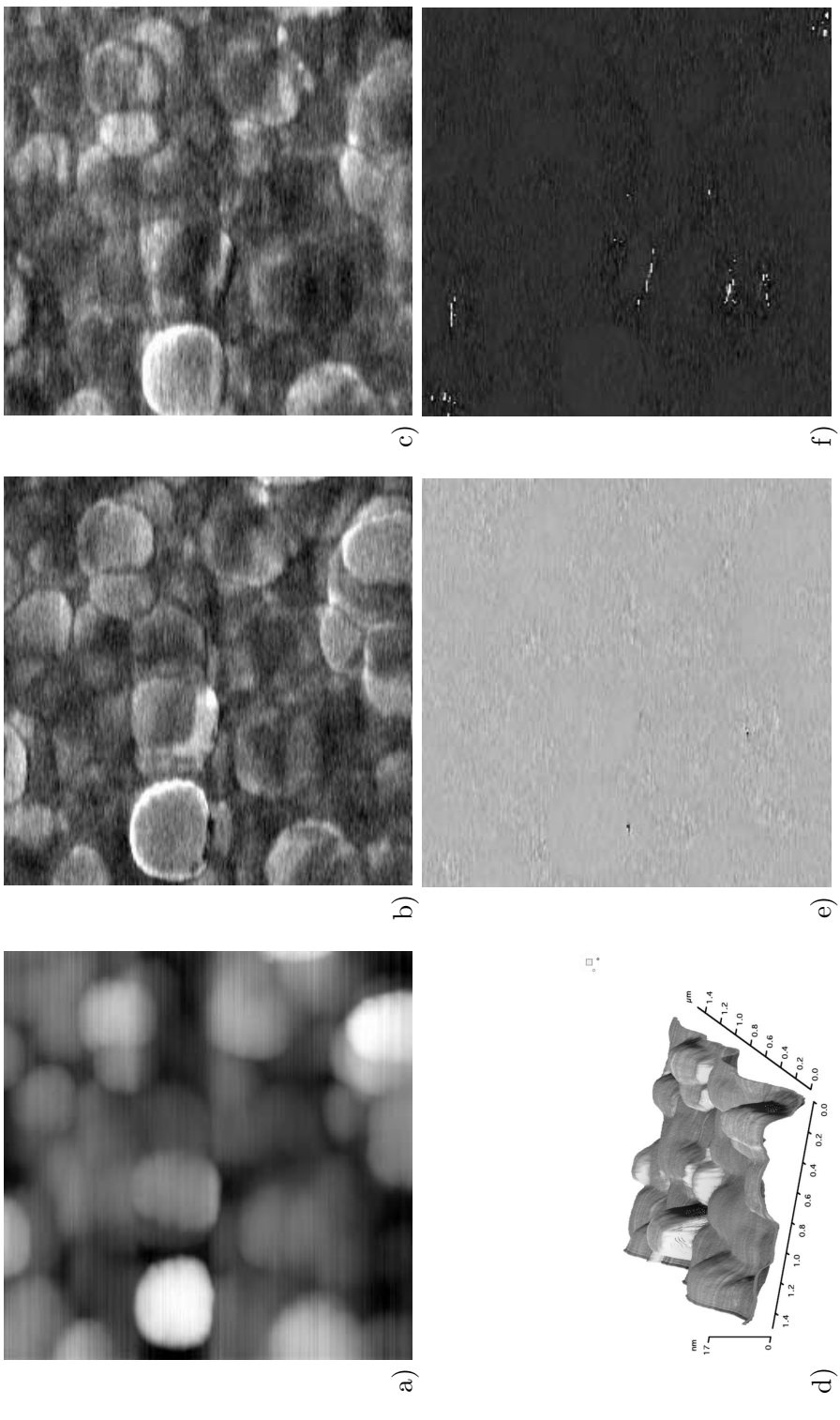

Figure 4.27: AFM measurements 1.5x1.5μm on sample from figure 4.16 a). a) Topography, d) 3D topography, b) Amplitude signal of piezoresponse with an applied +8V dc field, e) corresponding phase signal, c) Amplitude signal of piezoresponse with an applied -8V dc field, f) corresponding phase signal.

conditions were 520°C, 4mT Ar, $100W_{rf}$ and the target had a +10% K excess. The film microstructure is shown in (d). The piezoelectrical activity of the virgin film, measured on a $2x2\mu m^2$ area with zero applied dc-field showed a strong piezoelectric activity on about 10% of the grains, most other grains showed a weaker piezoelectric activity. The area was poled with -10V applied to the AFM tip. The remanent piezoelectric activity was measured after the removal of the dc bias, in as amplitude signal (c), respectively as phase signal (e). After this poling treatment, about 50% of the grains showed a strong piezoelectric activity, indicating a remanent polarization of the grains. Most grains have switched (white area in phase image indicating bottom-to-top polarization). A subsequent poling treatment with +10V reduced the piezoelectric activity on some of the grains, but only 10% of the grains switched their polarization.

Piezoelectric loops measured on grains A and B are represented in figure 4.28 (f). The ac frequency for measuring the piezoelectric response was 17kHz using a $0.5V_{amp}$ signal overlaying the dc-field. The calibration factor to calculate the piezoelectric constant d_{33} reported to the right y-axis from the AFM cantilever A-B signal response reported to the left y-axis is ($1982\mu V_{rms}$ for a PZT sample with d_{33}=45pm/V, using an excitation signal of $1.414V_{amp}$).

Grain A shows a piezoelectric hysteresis loop with its coercitive fields shifted towards the negative field. The grain has a very high maximum piezoelectric signal of more than ±100pm/V and a saturation piezoelectric activity of +40, respectively -60pm/V. This grain can be considered as unclamped as it protrudes by about 100nm out of the surrounding matrix. Domain mobility increases on freestanding high aspect ratio grains [14]. Grain B also shows a piezoelectric hysteresis loop, but the polarization does not switch and the signal phase remains negative. Furthermore B's maximum piezoelectric value is almost 3 times lower, possibly because of film clamping or a domain orientation that has the polarization vector near in-plain. It must be noted that the form of the piezoelectric loop signal changed on subsequent measurement repetitions due to changing domain wall configurations.

The observed loop on A witnesses a strong impact of domain wall motion. The domain pattern - domain walls are pinned by defects which leads to back-switching at 0V. It can be concluded that the single crystal grain A has a strong imprint. The shape of the piezoelectric loop exhibit a 'nose' and a 'hump' at the negative voltage, which are due to significant 180° domain wall contributions to the piezoelectric coefficient [65]. The overshooting at positive voltages can only be explained by ferroelastic domain wall motions.

The lattice contribution of the unclamped piezoelectric coefficient in the [101] direction, d'_{333}, can be calculated using equation 4.4, page 127.

$$d'_{333} = \frac{1}{2\sqrt{2}}\left(2d_{131} + d_{311} + d_{333}\right) = 87.1\text{pC/N} \tag{4.12}$$

The measured values of d_{33} by the AFM on the $KNbO_3$ films are close to the single crystal value of d'_{333}. This value corresponds to the unclamped piezoelectric coefficient because the analyzed grains protrude out of the surrounding matrix by some 20-30nm and can thus be assumed as unclamped.

The piezoelectric constant measured by AFM on the $KNbO_3$ grain A has an extremely

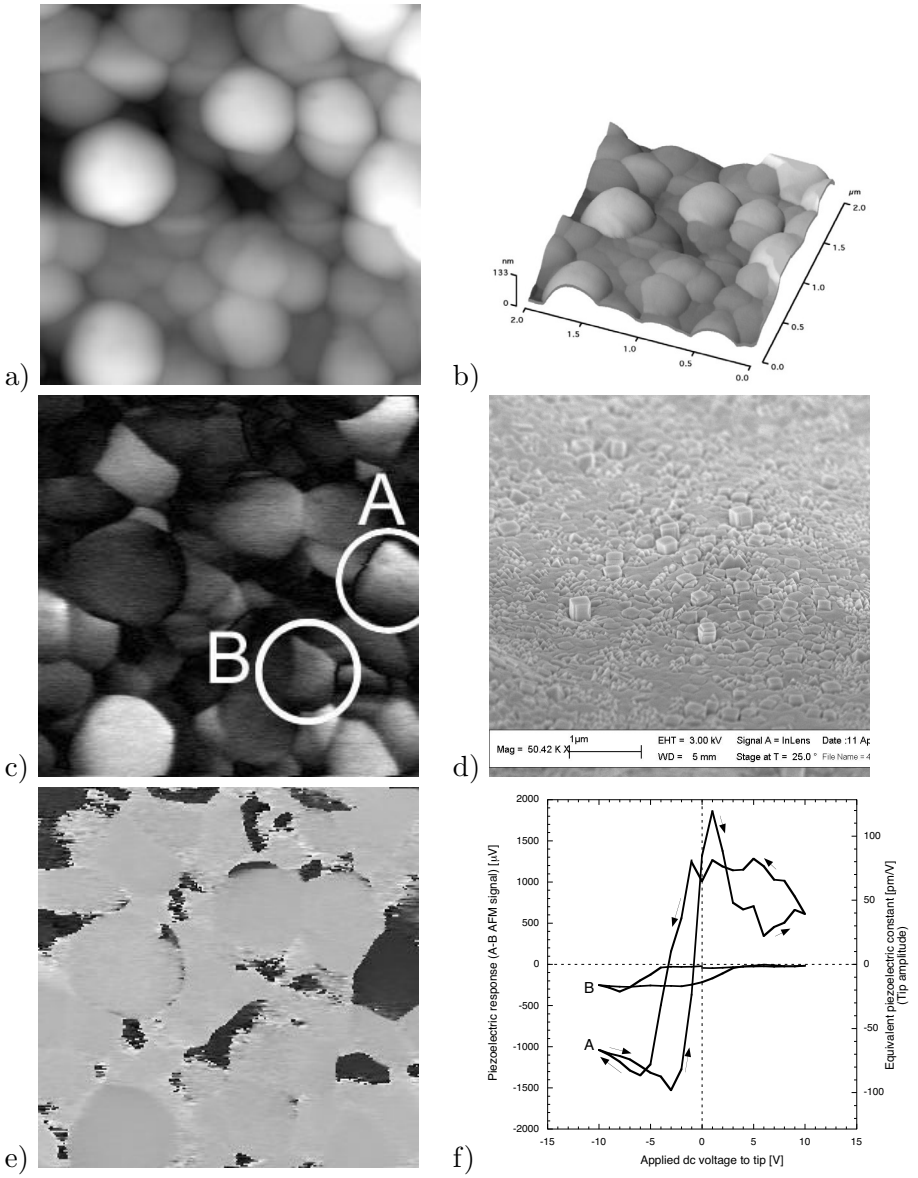

Figure 4.28: 2D (a) and 3D (b) topography measured by AFM on a 350nm thick $KNbO_3$ film over a 2x2μm^2 area, with the piezoelectric amplitude signal (c), and phase signal (e) obtained after poling the area with -10V applied on the AFM tip. (d) shows the microstructure of the predominantly (101)/(010) textured film with few second phases and which has a KN-ratio of 0.7. The piezoelectric loops measured by the AFM tip on the grains A and B (f) show a very strong piezoelectric signal. Grain A shows a sign reversal of the piezoelectric signal due to the ferroelectric nature, whereas B does not switch and has a lower piezo-response magnitude possibly due to film clamping. The AFM tip signal is related on the right x-axis to a pseudo-d_{33} value derived from tip vibration amplitude. This pseudo-d_{33} should be multiplied with a factor 7 to obtain the equivalent $d_{33,f}$ of large capacitance structures as used for double beam interferometer measurements.

high response and exceeds by a factor 10 the values measured on small self-assembled PZT single crystals [15].

4.10 Summary and Conclusions

$KNbO_3$ films were deposited onto platinized silicon substrates as well as on (100) $SrTiO_3$ substrates with an in-house built rf magnetron sputtering system including a load-lock chamber. Several excess concentrations of potassium in the form of K_2CO_3 were added to the $KNbO_3$ ceramic powder targets. The targets enriched with 25 and 40% excess potassium yielded near stoichiometric films, i.e. [K]:[Nb] atomic ratio equals 1. Targets with zero and 10% excess potassium yielded understoichiometric films, whereas 100 and 200% excess K resulted in unstable targets and films with excess potassium.

The potassium-to-niobium ratio in the deposited $KNbO_3$ films does not only depend on the target composition, but also strongly on the sputter parameters such as gas pressure and Ar-O_2 mixture, as well as substrate temperature. An increase in substrate temperatures from room temperature to 520°C and a decrease in sputtering pressure leads to a decrease in the KN-ratio of the films. This can be explained with a higher desorption rate of potassium from the substrate with increasing temperature. An increase of the substrate temperature above 520°C leads again to an increase in potassium incorporation into the films, which might be due to the sublimation of potassium from the target. The K_2CO_3 in the target becomes unstable when heated by radiation from the hot substrate and acts as source of potassium to the plasma.

Both of the targets with +25 and +40% excess K led to the highest volume fraction of the perovskite $KNbO_3$ phase. Second phases could be identified with XRD measurements as $K_3Nb_7O_{19}$ and $K_4Nb_6O_{17}$. The 200% excess K target yielded the potassium rich K_3NbO_4 phase besides $KNbO_3$. Micro-Raman measurements confirmed orthorhombic splitting in $KNbO_3$, and the presence of $K_4Nb_6O_{17}$ in the investigated film.

We have seen that the perovskite $KNbO_3$ phase is complicated to fabricate, more complicated than for example $BaTiO_3$ (BT), $PbTiO_3$ (PT) and $PbZrO_3$ (PZ): All four systems have an extremely limited solubility of the constituents around the correct 1:1 perovskite stoichiometry (c.f. phase diagrams in [57]), except in the PbO-TiO_2 system where the PT phase has a stable solid solution for 38-50mol% TiO_2. This wide range of solid solution makes the PT more tolerable for slight stoichiometry deviations compared to the three other systems. The probability for the nucleation of a second phase depends on its stoichiometry. The closer it is to the one of the target phase, the more likely it nucleates. The stoichiometry of nearest second phases in the BT system are 33 and 75mol% for Ba_2TiO_4 and $BaTi_3O_7$ respectively. In the PZ system these nearest phases are the basic constituents PbO and ZrO_2 at 4 and 100mol%. The Nb_2O_5-K_2CO_3 however has its nearest second phases at 40 and 75mol% which renders it more prone to the nucleation of off-stoichiometric second phases compared to the 3 other systems.

Strongly (101)/(010) textured $KNbO_3$ films were obtained on bare (111) Pt/Si substrates as well as on IrO_2 seed layers at substrate temperatures of 520°C and above in pure Ar at

a sputter pressure of 2-4mT. According to our literature study we believe to be the first to report on the growth of $KNbO_3$ films on platinized silicon substrates with magnetron sputtering. The microstructure of our films is often very facetted, especially at temperatures above 540°C. These so-called building block like micro-crystals were already observed on STO by Onoe et al. [52]. As in our case, the observed local micro-crystals grow inside an amorphous matrix on STO. Onoe et al. attributed it to too a low potassium content in the growing film.

Most of the films exhibited a high electric leakage. The reason could be voids, oxygen vacancies or not-fully oxidized potassium, as we have observed with XPS measurements. RTA anneals in oxygen as high as 650°C on some of the films did not reduce their conductivity. On a good $KNbO_3$ film a relative dielectric constant of ϵ_r=420 and dielectric losses between 5 and 10% were measured. A piezoelectric hysteresis loop could be measured with double beam laser interferometry. The piezoelectric loop, showing the ferroelectric nature of our films, had a saturation value of 24pm/V. This is the first report of piezoelectric properties measured on $KNbO_3$ films deposited onto platinized silicon substrates.

AFM measurements on single grains, which are according to TEM diffraction results single crystalline grains, show that the $KNbO_3$ films are piezo- and ferroelectric with values close to the calculated single crystal value of 87pC/N. The piezoelectric loop showed a strong imprint and large domain contribution. The magnitude of the piezoelectric constant as measured by the AFM tip vibration corresponds to an extremely high response and exceeds by a factor 10 the values measured on small self-assembled PZT single crystals [15].

So far, only a few other authors have published piezoelectric measurements of $KNbO_3$ thin films, deposited onto single crystalline substrates. Yamanouchi, Odagawa et al. [78, 51] claim to be the first to measure piezoelectric properties on an as-grown $KNbO_3$ thin film. They deposited $KNbO_3$ on (101) STO substrates using MOCVD at 850°C and measured the electromechanical coupling coefficient k^2 with SAW as 2.1%. For our films, the thickness-extensional coupling coefficient was calculated based on piezoelectric and dielectric measurements at a film with mixed (101)/(010) and (042) texture. A value of 2.8% was obtained. This value is 17 times lower than the value calculated for a (101) textured film. It can be explained by the presence of non-contributing (010) domains. This domain variant has a zero piezoelectric coefficient, and in addition a very high dielectric constant. Both effects reduce the coupling. The worst situation would be met if (101) and (010) domains would act as parallel elements in the BAW capacitor. A volume fraction of 1/3 of (010) domains reduces the coupling factor to 2.2%. The least effect of (010) domains is expected if separated from (101) domains by horizontal domain walls to obtain a series connection (k_t^2 would be reduced proportionally to (010) volume fraction). However, such domain walls do not exist in theory. Moreover, TEM plane view images suggest that the grains contain mostly only one domain. The parallel arrangement is in this case obtained through the columnar growth of the film. More investigations would be needed to clarify this point. Nevertheless, our study shows that it is important to switch a large fraction of (010) domains to (101) domains in order to achieve a sufficiently large coupling coefficient. In our films, a remanent switching was not observed at room temperature. Possibly one can apply a hot poling procedure.

A further point to be investigated in more detail is film roughness, which leads to acoustic

losses in BAW applications, and to light scattering in electro-optical applications. Many films show different growth rates depending on the individual grains (phase or texture), which leads to outgrows and undesirable film roughness. Some outgrows exhibited an aspect ratio of 10.

Repeatability of $KNbO_3$ film deposition by rf magnetron sputtering using potassium enriched target was found to be the crucial problem. Successive depositions with the same process conditions yielded different film properties. It was therefore extremely difficult to correlate film properties with process parameters. For this reason, some results were presented with a statistical approach. The problem lies in the chemically instable ceramic targets with a fluctuating potassium concentration on the surface. The problem of stoichiometry is aggravated by the highly volatile nature of potassium and its oxides. A possible alternative for sputtering from ceramic targets would be to use co-deposition: reactive sputtering of Nb_2O_5 combined with KO_2 evaporation from an effusion cell. Using this approach, the sputtering process might be more repeatable because a reactive sputter process is easily controlled, and the stoichiometry of the film could be easily adjusted for each deposition. Furthermore a compositional gradient could be incorporated into the film for example for nucleation purposes. Another valid alternative, which provides good homogeneity and high stoichiometry control, would be the use of MOCVD.

Bibliography

[1] S. Abadei, C.R. Cho, A. Grishin, and S. Gevorgian. Low frequency characterisation of laser ablation deposited thin $Na_{0.5}K_{0.5}NbO_3$ (NKN) films for microwave application. *Ferroelectrics*, 263(1-4):1473–1479, 2001.

[2] S. Abadei, S. Gevorgian, C.R. Cho, and A. Grishin. Low-frequency and microwave performances of laser-ablated epitaxial $Na_{0.5}K_{0.5}NbO_3$ films on high-resistivity SiO_2/Si substrates. *Journal of Applied Physics*, 91(4):2267–2276, 2002.

[3] S. Abadei, S. Gevorgian, V. Kugler, U. Helmersson, and J. Andreasson. Microwave properties of tunable capacitors based on magnetron sputtered ferroelectric $Na_{0.5}K_{0.5}NbO_3$ film on low and high resistivity silicon substrates. *Integrated Ferroelectrics*, 39:359–366, 2001.

[4] M.S. Ameen, T.M. Graettinger, S.H. Rou, H.N. Al-Shareef, K.D. Gifford, O. Auciello, and A.I. Kingon. Processing and structural characterization of ferroelectric thin films deposited by ion beam sputtering. In *Ferroelectric Thin Films Symposium. Mater. Res. Soc*, volume 200, pages 66–76, 1990.

[5] M.M. Amini and M.D. Sacks. Preparation of single phase $KNbO_3$ using bimetallic alkoxides. In *Materials Research Society Symposium Proceedings*, volume 180, pages 675–683, 1990.

[6] M.M Amini and M.D. Sacks. Synthesis of potassium niobate from metal alkoxides. *Journal of the American Ceramic Society*, 74(1):53–59, 1991.

[7] S. Arscott, Z. Awang, Y.L. Tu, S.J. Milne, and R.E. Miles. PZT bulk acoustic wave resonators for MMIC technology. *Ferroelectrics*, 187(1-4):49–56, 1996.

[8] S. Arscott, R.E. Miles, and S.J. Milne. Lead-zirconate-titanate thin-films for microwave device applications. *Circuits devices and systems*, 145(5):373–378, 1998.

[9] Z. Awang and R.E. Miles. Gallium arsenide bulk acoustic wave resonators fabricated using sol-gel technology. *Electronics Letters*, 7(7):626–627, 1993.

[10] Z. Awang, Y.L. Tu, R.E. Miles, and S.J. Milne. Fabrication of bulk acoustic wave resonators using sol-gel derived lead zirconate titanate thin films. In *25th European Solid State Device Research Conference*, pages 663–666, 1995.

[11] L. Beckers, Ch. Buchal, D. Fluck, T. Pliska, and P. Günter. Potassium niobate waveguides: He+ implantation in bulk single crystals and pulsed laser deposition of thin films. *Materials Science and Engineering A*, 253(1-2):292–295, 1998.

[12] M. Blomqvist, S. Khartsev, A. Grishin, A. Petraru, and Ch. Buchal. Optical waveguiding in magnetron-sputtered $Na_{0.5}K_{0.5}NbO_3$ thin films on sapphire substrates. *Applied Physics Letters*, 82(3):439–441, 2003.

[13] M. Blomqvist, J.-H. Koh, S. Khartsev, A. Grishin, and J. Andrasson. High-performance epitaxial $Na_{0.5}K_{0.5}NbO_3$ thin films by magnetron sputtering. *Applied Physics Letters*, 81(2):337–339, 2002.

[14] S. Bühlmann, J. Baborovski, B. Dwir, and P. Muralt. Size-effect in mesoscopic epitaxial ferroelectric structures: Increase of piezoelectric response with decreasing feature-size. *Appl. Phys. Lett.*, 80(17):3195, 2002.

[15] S. Bühlmann, P. Muralt, and S. Von Allmen. Lithography-modulated self-assembly of small ferroelectric $Pb(Zr,Ti)O_3$ single crystals. *Appl. Phys. Lett.*, 84(14):2614–2616, 2004.

[16] S. Chattopadhyay, B.M. Nichols, J.H. Hwang, T.O. Mason, and B.W. Wessels. Dielectric properties of epitaxial $KNbO_3$ ferroelectric thin films. *Journal of Materials Research*, 17(2):275–278, 2002.

[17] C.-H. Cheng, Y. Xu, and J. D. Makcenzie. The growth of single crystal-like and polycrystal $KNbO_3$ films via sol-gel process. In *Mat. Res. Soc. Proc.*, volume 271, pages 383–388, 1992.

[18] C.R. Cho and A. Grishin. Self-assembling ferroelectric $Na_{0.5}K_{0.5}NbO_3$ thin films by pulsed-laser deposition. *Applied Physics Letters*, 75(2):268–270, 1999.

[19] C.R. Cho and A.-M. Grishin. Ferroelectric $Na_{0.5}K_{0.5}NbO_3//SiO_2$/si thin film structures for nonvolatile memory. In *Materials Science of Novel Oxide Based Electronics Symposium*, volume 623, pages 155–160. Mater. Res. Soc, 2000.

[20] C.R. Cho and A.-M. Grishin. Thickness dependent performance of $Na_{0.5}K_{0.5}NbO_3$/sapphire thin film varactors. *Integrated Ferroelectrics*, 39(1-4):403–410, 2001.

[21] C.R. Cho, I. Katardjiev, M. Grishin, and A. Grishin. $Na_{0.5}K_{0.5}NbO_3$ thin films for voltage controlled acoustoelectric device applications. *Applied Physics Letters*, 80(17):3171–3173, 2002.

[22] C.R. Cho, J.-H. Koh, and A. Grishin. $Na_{0.5}K_{0.5}NbO_3/SiO_2$/Si thin film varactor. *Applied Physics Letters*, 76(13):1761–1763, 2000.

[23] C.R. Cho, S.H. Park, B.M. Moon, J. Sundqvist, A. Harsta, and A. Grishin. $Na_{0.5}K_{0.5}NbO_3$ thin films for MFIS FET type non-volatile memory applications. *Integrated Ferroelectrics*, 49:21–30, 2002.

[24] A. F. Chow, D. J. Lichtenwalner, and T. M. Graettinger. Microstructural and optical properties of potassium niobate thin films. In *ISAF '94, Application of Ferroelectronics*, pages 794–796, 1994.

[25] A. F. Chow, D. J. Lichtenwalner, R.R. Woolcott, T. M. Graettinger, O Auciello, A.I. Kingon, L.A. Boatner, and N.R. Parikh. Epitaxial $KNbO_3$ thin films on $KTaO_3$, $MgAl_2O_4$ and MgO substrates. *Appl. Phys. Lett.*, 65(9):1073–1075, 1994.

[26] H.-M. Christen, L. A. Boatner, J. D. Budai, M. F. Chisholm, L. A. Ga, P. J. Marrero, and D. P. Norton. The growth and properties of epitaxial $KNbO_3$ thin films and $KNbO_3/KTaO_3$ superlattices. *Applied Physics Letters*, 68(11):1488–1490, 1996.

[27] G.J. Derderian, J.D. Barrie, K.A. Aitchison, P.M. Adams, and M.L. Mecartney. Microstructure/process relations in sol-gel-prepared $KNbO_3$ thin films on (100) MgO. *J. Am. Ceram. Soc.*, 77(3):820–828, 1994.

[28] S. Ding and J. Shen. Microstructure and dielectric properties of pure and doped $KNbO_3$ ceramics. *Journal of the American Ceramic Society*, 73(5):1449–50, 1990.

[29] H. Endo and M.J. Cima. Preparation and characterization of epitaxial $KNbO_3$ thin films by a sol-gel method. In *Ferroelectric thin films III*, volume 310, pages 325–330, 1993.

[30] U. J. Flueckiger. *Darstellung und Eigenschaften von reinen und dotierten, eindomaenigen $KNbO_3$ Kristallen.* PhD thesis, Universitt Zrich, 1976.

[31] M. Fontana, C. Carabatos, G. Mtrat, and G. Dolling. Temperature dependence of acoustic modes in $KNbO_3$ near the orthorhombic-tetragonal phase transition. *Solid state comunications*, 28:887–890, 1978.

[32] V. Gopalan and R. Raj. Domain structure - second harmonic generation correlation in potassium niobate thin films deposited on a strontium titanate substrate. *Journal of the American Ceramic Society*, 79(12):3289–3296, 1996.

[33] T.M. Graettinger and A.I. Kingon. Optical characterization of potassium niobate thin film planar waveguides. *Ferroelectric Thin Films II Symposium.*, 243:557–563, 1992.

[34] T.M. Graettinger, P. A. Morris, R. R. Woolcott, F. C. Zumsteg, A. F. Chow, and A.I. Kingon. Growth, microstructures and optical properties of $KNbO_3$ thin films. In *Mat. Res. Soc. Symp. Proc.*, volume 310, pages 301–311, 1993.

[35] R. Gutmann, J. Hulliger, R. Hauert, and E.M. Moser. Auger-electron and x-ray photoelectron-spectroscopy of monocrystalline layers of $KTa_{1-x}Nb_xO_3$ grown by liquid-phase epitaxy. *Journal of Applied Physics*, 70(5):2648–2653, 1991.

[36] H. Hashima, A. Konishi, H. Wakabayashi, and Y. Kawamoto. Orientation control of potassium niobate thin film prepared by sputtering. *Journal of the Vacuum Society of Japan*, 42(5):581–584, 1999.

[37] E. Irle, R. Blachnik, and B. Gather. The phase diagrams of Na_2O and K_2O with Nb_2O_5 and the ternary system Nb_2O_5-Na_2O-Yb_2O_3. *Thermochimica Acta*, 179:157–169, 1991.

[38] K.-I. Kakimoto, S. Ito, I. Masuda, and H. Ohsato. Growth morphology and crystal orientation of $KNbO_3$ film on $SrTiO_3$ by liquid phase epitaxy. *Japanese Journal of Applied Physics*, 41(11B):6908–6911, 2002.

[39] J.J. Kingston, D.K. Fork, F. Leplingard, and F.A. Pence. C^- outgrowths in C^+ thin films of $LiNbO_3$ on Al_2O_3-c. In *Epitaxial Oxide Thin Films and Heterostructures. Mater. Res. Soc.*, pages 289–294, San Francisco, CA, USA, 1994.

[40] E. I Krylov, I. A. Dmitriev, and M. M. Strelina. Thermal decomposition of potassium and sodium metaniobates. *Russian Journal of Inorganic Chemistry*, 7(4):415–420, 1962.

[41] D. R. Lide. *Handbook of Chemistry and Physics*, volume 75th edition. CRC Press, 1995.

[42] J.-F. Liu, X.-L. Li, and Y.-D. Li. Synthesis and characterisation of nanocrystalline niobates. *Journal of Crystal Growth*, 247:419–424, 2003.

[43] H. P. Löbl, M. Klee, C. Metzmacher, W. Brand, R. Milsom, P. Lok, and F. van Straten. Piezoelectric materials for BAW resonators and filters. In *Ultrasonics Symposium*, pages 807–811. IEEE, 2001.

[44] A.M. Margolin, Z. S. Surovyak, I. N. Zakharchenko, V. A. Aleshin, L. K. Chernysheva, M. G. Radchenko, and V. P. Dudkevich. (k,na)nbo3 ferroelectric films synthesized by cathode sputtering. *Sov. Phys. Tech. Phys.*, 33(12):1435–1438, 1988.

[45] G. R. Misium. Macroscopic modeling of oxygen plasmas. *Journal of Vacuum Science & Technology A: Vacuum, Surfaces, and Film*, 8(3):1642–1647, 1990.

[46] K. Misu, T. Nagatsuka, S. Wadaka, C. Maeda, and A. Yamada. Film bulk acoustic wave filters using lead titanate on silicon substrate. In *IEEE Ultrasonics Symposium*, Sendai, Japan, 1998.

[47] K. Nakamura and Y. Kawamura. Electromechanical coupling factor of $KNbO_3$ single crystal. In *IEEE Ultrasonics Symposium*, volume 2, pages 1013 –1018, 1999.

[48] K. Nakamura and Y. Kawamura. Orientation dependence of electromechanical coupling factors in $KNbO_3$. *Transactions on Ultrasonics, Ferroelectrics and Frequency Control, IEEE*, 47(3):750–755, 2000.

[49] F. Natola and Ph. Touzain. Diagram of phases of system K-K_2O and potassium monoxide K_2O. *Canadian Journal of Chemistry*, 48(13):1955, 1970.

[50] M. J. Nystrom, B. W. Wessels, J. Chen, and T. J. Marks. Microstructure of epitaxial niobate thin films prepared by metalorganic chemical vapor deposition. *Appl. Phys. Lett.*, 68(6):761–763, 1996.

[51] H. Odagawa, K. Kotani, Y. Cho, and K. Yamanouchi. Observation of ferroelectric polarization in $KNbO_3$ thin films and surface acoustic wave properties. *Japanese Journal of Applied Physics*, 38(Part 1, No 5B):3275–3278, 1999.

[52] A. Onoe, A. Yoshida, and K. Chikuma. Heteroepitaxial growth of $KNbO_3$ single-crystal films on $SrTiO_3$ by metalorganic chemical vapor deposition. *Applied Physics Letters*, 69(2):167–169, 1996.

[53] C. H. Perry and N. E. Tornberg. The raman spectra of $PbTiO_3$ and solid solutions of $NaTaO_3$-$KTaO_3$ and $KTaO_3$-$KNbO_3$. In *International Conference on Light Scattering Spectra of Solids*, pages 467–476, 1968.

[54] A. Reisman and F. Holtzberg. Phase equilibria in the system K_2CO_3-Nb_2O_5 by the method of differential thermal analysis. *Journal of the American Chemical Society*, 1:2115–2119, 1955.

[55] A. L. Roitburd. Equilibrium structure of epitaxial layers. *Phys. Stat. Sol. (a)*, 37:329, 1976.

[56] R.S. Roth. Thermal stability of long range order in oxides. *Progress in Solid State Chemistry*, 13(2):159–192, 1980.

[57] R.S. Roth, M.A. Clevinger, and D. McKenna. *Phase diagrams for ceramists.* The American Ceramic Society, Inc., 1984.

[58] S. Schwyn Thöny. *RF sputter deposition of waveguiding epitaxial $LiNb_O3$ and $KNbO_3$ thin films.* Ph.d., ETHZ, 1992.

[59] S. Schwyn Thöny. Epitaxial waveguiding KNbO3 thin films grown by RF-sputter deposition. In Mater. Res. Soc, editor, *Epitaxial Oxide Thin Films and Heterostructures*, volume 341, pages 253–264, Pittsburgh, PA, 1994. Mater. Res. Soc.

[60] S. Schwyn Thöny, H. W. Lehmann, and P. Günter. Sputter deposition of epitaxial waveguiding $KNbO_3$ thin films. *Applied Physics Letters*, 61(4):373–375, 1992.

[61] H. Suzuki, T. Ohno, H. Miyasaka, D.S. Fu, K. Ishikawa, and K. Kodaira. Orientation control of $KNbO_3$ thin film on silicon wafer with chemical solution deposition. *Key engineering materials*, 206-213:1493–1496, 2002.

[62] S.L. Swartz, P.J. Melling, and C.S. Grant. Ferroelectric thin films by sol-gel processing. In *Materials Research Society Symposium Proceedings*, volume 152, pages 227–232, 1989.

[63] K. Szot, F. U. Hillebrecht, D. D. Sarma, M. Campagna, and H. Arend. Surface defect segregation in the perovskite-type ferroelectric $KNbO_3$. *Applied Physics Letters*, 48:490, 1986.

[64] K. Szot, W. Speier, S. Cramm, J. Herion, C. Freiburg, R. Waser, M. Pawelczyk, and W. Eberhart. Surface layer on $KNbO_3$ and the hysteresis loop anomaly. *Journal of Physics and Chemistry of Solids*, 57(11):1765–1775, 1996.

[65] A.K. Tagantsev, P. Muralt, and J. Fousek. Shape of piezoelectric hysteresis loop for non-ferroelastic switching. In *Mat. Res. Soc. Symp.*, volume 784, pages C10.6.1–C10.6.6, 2004.

[66] J. A. Thornton. Influence of apparatus geometry and deposition conditions on the structure and topgraphy on thick sputtered coatings. *J. Vac. Sci Technol.*, 11(4):666–670, 1974.

[67] J. A. Thornton. The microstructure of sputter-deposited coatings. *J. Vac. Sci Technol. A*, 4(6):3059–3065, 1986.

[68] B.A. Tuttle, B.C. Bunker, D.L. Lamppa, R.G. Tissot, and J.L. Yio. Ferroelectric potassium niobate thin films. In *Proceedings of the Symposium on Ceramic Thin and Thick Films held during the 91st Annual Meeting of the American Ceramic Society, Inc.*, volume 9, pages 329–341, Indianapolis, 1990. The American Ceramic Society.

[69] S. Wada, A. Seike, and T. Tsurumi. Poling treatment and piezoelectric properties of potassium niobate ferroelectric single crystals. *Japanese Journal of Applied Physics - part1 regular papers, short notes & review papers*, 40(9B):690–5697, 2001.

[70] X. Wang, U. Helmersson, S. Olafsson, S. Rudner, and L.-D. Wernlund. Growth and field dependent dielectric properties of epitaxial $Na_{0.5}K_{0.5}NbO_3$ thin films. *Applied Physics Letters*, 73(7):927–929, 1998.

[71] X. Wang, S. Olafsson, L.D. Madsen, S. Rudner, I.P. Ivanov, A. Grishin, and U. Helmersson. Growth and characterization of $Na_{0.5}K_{0.5}NbO_3$ thin films on polycrystalline $Pt_{80}Ir_{20}$ substrates. *Journal of Materials Research*, 17(5):1183–1191, 2002.

[72] B. W. Wessels, M. J. Nystrom, J. Chen, D. Studebaker, and T. J. Marks. Epitaxial niobate thin films and their nonlinear optical properties. In *Mat. Res. Soc. Proc.*, volume 401, pages 211–218, 1996.

[73] R.F. Xiao, H. D. Sun, H. S. Siu, Y. Y. Zhu, P. Yu, and G.K.L. Wong. Amorphous $KNbO_3$ thin films with ferroelectriclike properties. *Appl. Phys. Lett.*, 70(2):164–166, 1997.

[74] Yuhuan Xu. Ferroelectric thin films fabricated by sol-gel technique. In *6th international conference on solid-state and integrated-circuit technology*, pages 696–701. IEEE, 2001.

[75] A. Yamada, C. Maeda, T. Sato, T. Umemura, F. Uchikawa, K. Misu, and S. Wadaka. Piezoelectric properties and microstructures of lead titanate thin films for GHz-band bulk acoustic wave filters. *Integrated Ferroelectrics*, 22:353–361, 1998.

[76] M. Yamaguchi, K. Hashimoto, R. Nanjo, N. Hanazawa, S. Ttsutsumi, and T. Yonezawa. Ultrasonic properties of PZT thin films in UHF-SHF ranges prepared by sol-gel method. In *1997 IEEE International Frequency Control Symposium*, volume 51, pages 544–551, 1997.

[77] K. Yamanouchi, H. Odagawa, T. Kojima, and T. Matsumura. Super high electromechanical coupling and zero-temperature coefficient surface acoustic wave substrates in $KNbO_3$/ single crystal. In *IEEE International Frequency Control Symposium*, pages 540 –543, 1997.

[78] K. Yamanouchi, H. Odegawa, T. Kojima, and Y. Cho. New piezoelectric $KNbO_3$ films for SAW device applications. In *Eleventh IEEE International Symposium on Applications of Ferroelectrics, ISAF 98.*, pages 385–388, 1998.

[79] K. Yamanouchi, H. Odegawa, T. Kojima, and T. Matsumara. Theoretical and experimental study of superhigh electromechanical coupling surface acoustic wave propagation in $KNbO_3$ single crystal. *Electronics Letters*, 33(3):193–194, 1997.

[80] C. Zaldo, D.S. Gill, R.W. Eason, J. Mendiola, and P.J. Chandler. Growth of $KNbO_3$ thin films on MgO by pulsed laser deposition. *Appl. Phys. Lett.*, 65(4):502–504, 1994.

[81] M. Zgonik, R. Schlesser, I. Biaggio, E. Voit, J. Tscherry, and P. Günter. Materials constants of $KNbO_3$ relevant for electro- and acousto-optics. *J. Appl. Phys.*, 74(2):1287–1297, 1993.

Conclusions and outlook

Appreciating the market chances of thin film BAW (FBAR) filters today in this year 2004, one must come to the conclusion that FBAR filters are about to replace SAW filters in important segments of mobile telecommunication. This was very much different in 1999, when the project for this thesis was planned. Still in 1998, the idea of making RF filters with bulk acoustic waves was considered as rather exotic and attracted in the best case the curiosity of SAW manufacturers - with the exception of two companies developing secretly thin film BAW filters - and one US company reporting in 1995 on well performing SMR passband filters with a frequency distribution below 1% over 100mm wafers. Generally it was very much doubted whether the film uniformity and reproducibility would ever meet the tough requirements. The good reproducibility of AlN film quality as obtained by reactive sputter deposition, combined with efforts of the sputter tool industry, show today that uniformity and thickness control is just a matter of industrial effort. At present, at least two companies are selling BAW RF filters for the 2 GHz bands. It is of interest to note that these companies are not SAW filter producers, but microwave sub-system and semiconductor providers. They identified new products consisting of modules with integrated BAW filters. These modules offer more performance in a smaller volume with lesser components. The engagement of semiconductor industry highlights the prospects to integrate AlN FBAR filters on chip, and thus to offer chips for complete RF signal treatment. Finally it is also clear that the RF filters for the 5GHz bands - as reserved for local area networks - are much easier realized by bulk acoustic wave devices than by surface acoustic wave devices.

The AlN part of this work has to be seen in the light of the year 2000, when we wanted to show that BAW filters can be realized at very high frequencies and meet industrial specifications for a microwave phone link. We were able to prove the feasibility both theoretically and practically, by fabricating industrially viable FBAR filters for 8GHz using piezoelectric AlN. They complied fully with stringent industrial specifications, and diced prototype filters were used for subsystem testing. The theoretical investigation showed in addition that with suitable electrode choice BAW resonators can be scaled to 10GHz and possibly beyond without loosing much coupling or quality factor.

Given the coupling factor provided by AlN, the filter bandwidth was a further concern and was considered to be one of the principal limiting factors. To account for fabrication and temperature tolerances, a few percent larger coupling factor would in fact be desirable. Materials with larger coupling are ferroelectrics. They are in general - however - not exploitable for microwave applications since their mechanical losses are too large. From a

theoretical point of view $KNbO_3$ thin films bear a potential of high coupling for BAW applications, since this material is more rigid than other ferroelectrics. With this perspective in mind we developed a deposition process for the fabrication of $KNbO_3$ films. We were able to deposit successfully and for the first time orthorhombic, stoichiometric and crystalline {100} and {111} pseudocubic textured $KNbO_3$ films on Pt/Si and IrO_2/Pt/Si substrates. We chose RF magnetron sputtering, which allows for deposition on large substrates, with $KNbO_3$ ceramic targets enriched with 25-40% excess potassium at substrate temperatures of 530°C in an Ar atmosphere. The films were piezoelectric with a saturated $d_{33,f}$ value of 24pm/V and a relative dielectric constant ϵ_r of 420. This is the first time that piezoelectric properties were measured on $KNbO_3$ thin films on platinized silicon substrates. From these values a thickness extensional coupling coefficient of 2.8% can be derived. This is low compared to the 47% calculated for a perfectly (101) textured film. The main reason for this low value was identified in the large (010) domain fraction. These domains do not contribute to piezoelectric coupling and moreover reduce the overall film coupling due to their large permittivity. It remains an open question whether these domains could be reduced by a hot poling procedure.

The principal impacts of the first part of my thesis work for the field of BAW filters, which was very applied and industry oriented, may be summarized as

- the demonstration in simulation and experiment of AlN BAW filters for the 8GHz range with low insertion losses, large bandwidth and low ripple, which show the prospect of achieving future industrial viable BAW filters at frequencies as high as 12GHz.

- the investigation and proposition of alternative metals which have to satisfy stringent electric conductivity, acoustic property and seed/nucleation constraints.

The second part of my thesis work was more speculative in the way that an alternative material, which had not been considered for microwave BAW applications before, was selected, and a possible processing way was developed to a point were thin films could be deposited and characterized electrically. This second part has taken the knowledge of non-lead based piezo- and ferroelectric thin films a step ahead by

- demonstrating for the first time the deposition of $KNbO_3$ films on platinized silicon substrates using rf magnetron sputtering. These first steps open the way for its integration onto silicon substrates which are a prerequisite for device processing.

- measuring for the first time piezoelectric properties of $KNbO_3$ films deposited on platinized silicon substrates. The piezoelectric constant measured by AFM on single crystalline $KNbO_3$ grains has a very high magnitude and exceeds by a factor 10 the values measured on small PZT self assembled single crystals.

- allowing for a better assessment of the risks and merits of this material.

The knowledge on $KNbO_3$ thin film fabrication is relatively new compared with AlN and PZT thin films which have been studied for the last 20 to 30 years. The growth of stoichiometric and well textured $KNbO_3$ thin films proved to be very delicate using magnetron sputtering. However, the theoretical properties and the high piezoelectric values measured justify a further research of this materials. For further continuation of this work, it will be necessary to dispose of a deposition method that is more apt to overcome the difficulties of $KNbO_3$ processing, for example using high density targets or co-sputtering.

Today it is not yet clear whether $KNbO_3$ could yield a viable material for passive FBAR filters. More effort is need to investigate this interesting material with its large potential. (Na,K)NbO_3 should also be considered as an alternative material with similar properties to $KNbO_3$ and might be easier to manufacture.

List of publications

[1] R. Lanz, M.-A. Dubois, and P. Muralt. Solidly mounted BAW filters for the 6 to 8 GHz range based on AlN thin films. In *IEEE International Ultrasonics Symposium*, pages 843–846, 2001.

[2] R. Lanz, P Carazzetti, and P. Muralt. Surface micromachined BAW resonators based on AlN. In *IEEE International Ultrasonics Symposium*, pages 981–983, 2002.

[3] R. Lanz and P. Muralt. 8 GHz microwave filters based on bulk acoustic waves in piezoelectric AlN thin films. In *13th IEEE International Symposium on Applications of Ferroelectric*, Nara, Japan, 2002. ISAF.

[4] R. Lanz and P. Muralt. Solidly mounted BAW filters for 8GHz based on AlN thin films. In *IEEE International Ultrasonics Symposium*, Honolulu, Hawaii, USA, 2003.

[5] A. Reinhardt, V. Laude, R. Lanz, P. Muralt, M. Solal, S. Ballandras, and W. Steichen. Design of coupled resonator filters using admittance and scattering matrices. In *IEEE International Ultrasonics Symposium*, Honolulu, Hawaii, USA, 2003.

Curriculum vitae

Roman LANZ
25 February 1972, Swiss citizen

Work experience

2000 – 2004	Research assistant and Ph.D. student at *Ceramics Laboratory*, *EPF Lausanne*, Switzerland.
1998 – 2000	Project manager at *EMPA Dübendorf*, Switzerland.

University studies

1997 – 1998	Diploma work at the *Korean Institute of Aeronautical Technology, KIAT*, Taejon, South Korea.
1993 – 1998	Study of Material Science Engineering, *EPF Lausanne*, Switzerland.

Gymnasium

1987 – 1993	High school, Typ C, at *Kantonsschule Solothurn*, Switzerland.
1989 – 1989	Exchange student at *Warilla High School* during 1 year, NSW, Australia.